

©Copyright 2024

Kristian Davidsen



Tools to investigate aspartate limited proliferation  
of cancer cells

Kristian Davidsen

A dissertation  
submitted in partial fulfillment of the  
requirements for the degree of

Doctor of Philosophy

University of Washington

2024

Reading Committee:

Lucas B Sullivan, Chair

Arvind R Subramaniam

Dana L Miller

Program Authorized to Offer Degree:

Molecular and cellular biology



University of Washington

## **Abstract**

Tools to investigate aspartate limited proliferation  
of cancer cells

Kristian Davidsen

Chair of the Supervisory Committee:  
Assistant Professor Lucas B Sullivan  
Fred Hutch Cancer Center, Human Biology

Cellular aspartate levels are tightly linked to cell proliferation rate. But how aspartate limitation decreases proliferation is unknown and could be related to its role as an amino acid as well as a substrate in multiple metabolic reactions. In this dissertation, the role of each of the metabolic fates of aspartate is interrogated. Surprisingly, it was not possible to rescue proliferation during aspartate limitation by providing the fates of aspartate, neither were there any evidence of insufficiency for protein synthesis. It is hypothesized that nucleotide imbalance is responsible and that this would elude efforts to rescue proliferation through complementation. Nevertheless, these results prompted the development of better tools to measure aspartate and the consequences of aspartate limitation. Towards that end, an aspartate biosensor was developed and tested, enabling increased throughput of non-invasive aspartate measurements under relevant growth conditions. Also, a highly accurate method for measuring tRNA aminoacylation using sequencing was developed. This tRNA-Seq method was tested on human tRNAs with a titration of charge levels, its measurements were determined to be quantitative and with enough accuracy and precision to detect small ( $\sim 5\%$ ) effects on tRNA charge.



## TABLE OF CONTENTS

	Page
List of Figures . . . . .	iii
List of Tables . . . . .	vii
Chapter 1: Aspartate's role in cellular metabolism of the proliferating cell . . . . .	2
1.1 Introduction . . . . .	2
1.2 The metabolic rational for aerobic glycolysis . . . . .	3
1.3 Environmental limitations to cancer cell proliferation . . . . .	5
1.4 Cellular metabolism requires redox balance . . . . .	6
1.5 Aspartate fates . . . . .	10
1.6 Which aspartate fate controls proliferation . . . . .	15
Chapter 2: Molecular mechanisms of aspartate limitation . . . . .	17
2.1 Introduction . . . . .	17
2.2 Results . . . . .	18
2.3 Discussion . . . . .	34
2.4 Methods and Materials . . . . .	36
Chapter 3: An engineered biosensor enables dynamic aspartate measurements in living cells . . . . .	52
3.1 Introduction . . . . .	53
3.2 Results . . . . .	54
3.3 Discussion . . . . .	65
3.4 Methods and Materials . . . . .	67
3.5 Acknowledgement . . . . .	76
3.6 Funding . . . . .	76

Chapter 4: Robust method for measuring aminoacylation through tRNA-seq . . . . .	77
4.1 Introduction . . . . .	78
4.2 Results . . . . .	81
4.3 Discussion . . . . .	93
4.4 Methods and Materials . . . . .	95
4.5 Acknowledgments . . . . .	110
4.6 Funding . . . . .	110
Chapter 5: Future directions . . . . .	111
5.1 Aspartate limitation and nucleotide synthesis . . . . .	111
5.2 Aspartate sensor . . . . .	115
5.3 Further development and applications of tRNA-Seq . . . . .	116
Bibliography . . . . .	119
Appendix A: Chapter 1 appendix . . . . .	137
A.1 Mathematical description of simple labelling flux . . . . .	137
A.2 Pig serum nucleoside/base concentrations . . . . .	141
A.3 Fumarate regeneration to aspartate . . . . .	142
Appendix B: Chapter 2 appendix . . . . .	143
B.1 Packed cell volume is an overestimate in common cancer cell lines . . . . .	143
B.2 Mitochondrial inhibition induces a titratable aspartate limitation . . . . .	145
B.3 Nucleoside, nucleobase and amino acid quantification after acid hydrolysis .	146
B.4 <sup>15</sup> N Gln tracing in 143B and H1299 . . . . .	151
B.5 ETC inhibitor rescue with purines is blunted in serine free media . . . . .	155
B.6 Aspartate to proliferation curves . . . . .	156
B.7 tRNA charge over time . . . . .	160
B.8 Figures related to integrated stress response . . . . .	161
B.9 Antimycin induced metabolic changes . . . . .	165
Appendix C: Aspartate sensor supplementary figures . . . . .	167
Appendix D: tRNA-Seq supplementary figures . . . . .	175

## LIST OF FIGURES

Figure Number	Page
1.1 NCI-60 cancer cell line doubling time in cell culture vs. xenografts. . . . .	6
1.2 Biomass accumulation requires NAD <sup>+</sup> regeneration. . . . .	8
1.3 Aspartate rescues proliferation but not the NAD <sup>+</sup> /NADH ratio. . . . .	10
1.4 Metabolic fates of aspartate. . . . .	12
1.5 Aspartate metabolism fluxes. . . . .	14
1.6 Two hypotheses for aspartate to proliferation correlation. . . . .	16
2.1 Aspartate, NAD <sup>+</sup> /NADH ratio over time after rotenone. . . . .	19
2.2 Aspartate levels correlates with proliferation rate. . . . .	19
2.3 Aspartate and NAD <sup>+</sup> /NADH ratios are correlated. . . . .	20
2.4 Media amino acid uptake. . . . .	21
2.5 Asparagine consumption fluxes. . . . .	22
2.6 Amino acid and pyrimidine total cell concentration. . . . .	23
2.7 Relative consumption towards each fate of aspartate. . . . .	24
2.8 Salvage into purines. . . . .	25
2.9 Inferred synthesis paths into purines. . . . .	26
2.10 Salvage into asparagine and pyrimidines. . . . .	27
2.11 Rescuing aspartate limitation with aspartate fates. . . . .	28
2.12 H1299 rotenone titration aspartate to proliferation. . . . .	30
2.13 ETC inhibitor in H1299/143B, effect on tRNA charge. . . . .	31
2.14 Mitochondrial inhibitor induced ATF4 is rescued by Asn. . . . .	33
2.15 Antimycin induced ISR correlates with Asn depletion. . . . .	34
3.1 Protein engineering and <i>in vitro</i> characterization. . . . .	57
3.2 . . . . .	61
3.2 jAspSnFR3 resolves temporal aspartate changes in live cells. . . . .	62
3.3 jAspSnFR3 signal predicts LCMS measured intracellular aspartate concentration. . . . .	65

4.1	Charge tRNA-Seq method summary . . . . .	80
4.2	Figure caption below . . . . .	85
4.2	Optimizing the chemistry of charge tRNA-Seq . . . . .	86
4.3	Masking of the reference sequences improves alignment performance . . . . .	88
4.4	Barcode replicates show high precision and limited barcode bias . . . . .	89
4.5	Charge titration shows linearity over the full range of charge measurements . . . . .	91
4.6	Measuring aminoacylation half-life using charge tRNA-Seq . . . . .	93
5.1	Mitochondrial inhibitors increase cell size . . . . .	113
5.2	Rotenone induced cell size increase over time . . . . .	114
5.3	Proliferation rate correlation with cell volume . . . . .	114
5.4	Chk1/2 phosphorylation after rotenone/antimycin treatment . . . . .	114
A.1	Mass balance diagram for metabolite labelling . . . . .	138
A.2	Pig serum nucleoside/base concentrations . . . . .	141
A.3	Fumarate regeneration to aspartate . . . . .	142
B.1	Packed cell volume vs. Coulter counter . . . . .	144
B.2	Rotenone concentration over time . . . . .	145
B.3	Redox metabolite over time after rotenone . . . . .	145
B.4	Amino acid stability in HCl . . . . .	148
B.5	Nucleobase stability in HCl . . . . .	149
B.6	Nucleoside, nucleobase and amino acid, hydrolysis saturation . . . . .	149
B.7	Hydrolyzed amino acids normalized with internal standards . . . . .	150
B.8	Isotope dilution calibration curves . . . . .	150
B.9	Purine metabolism $^{15}\text{N}$ -amide Gln tracing overview . . . . .	151
B.10	Gln amide to alpha $^{15}\text{N}$ transfer . . . . .	152
B.11	Glu alpha- $^{15}\text{N}$ tracing into Asp, HpX and ATP . . . . .	153
B.12	Salvage as a function of Urd/HpX concentration . . . . .	153
B.13	No evidence of arginine synthesis in DMEM . . . . .	154
B.14	ETC inhibitor purine rescue in serine free media . . . . .	155
B.15	H1299 rotenone titration aspartate to proliferation . . . . .	156
B.16	H1299 metformin titration aspartate to proliferation . . . . .	157
B.17	HCT116 metformin titration aspartate to proliferation . . . . .	158
B.18	143B metformin titration aspartate to proliferation . . . . .	159

B.19	Antimycin time-series in 143B, effect on tRNA charge.	160
B.20	ATF4 reporter, media change vs. spike-in.	161
B.21	Mitochondrial inhibitor, ATF4 western.	162
B.22	ATF4 reporter, drug titrations.	163
B.23	Mito inhibitor induced ATF4 is rescued by Asn, other clones.	164
B.24	GOT DKO western blot validation.	164
B.25	.	165
B.25	Metabolic changes in HT1080 after antimycin treatment.	166
C.1	Aspartate specificity and excitation/emission spectra.	168
C.2	Decoy, temperature and pH sensitivity.	169
C.3	Stopped-flow kinetics.	170
C.4	mRuby3 interaction with histidine tag.	171
C.5	Rotenone titration in different cell lines.	172
C.6	Plots related to glutamine limitation.	173
C.7	jAspSnFR3 signal does not correlate with glutamate concentration.	174
D.1	Whitfeld reaction scheme.	175
D.2	Optimizing lysine induced cleavage.	176
D.3	Measurement bias in charge tRNA-Seq using blunt-end ligation.	177
D.4	tRNA-adapter blunt-end ligation attempted optimization.	178
D.5	Splint assisted ligation is highly efficient.	179
D.6	Ligation tests, related to panel E.	180
D.7	RT readthrough comparing TGIRT to Maxima.	181
D.8	Sequenced controls.	182
D.9	tRNA homology requires careful PCR conditions.	183
D.10	Reference masking effect on RPM and charge levels.	184
D.11	Anticodon modification mcm5s2U is detected in periodate oxidized samples.	185
D.12	Charge and RPM deviation at the transcript level.	186
D.13	Best and worst barcode replicates.	186
D.14	Best and worst fitting transcripts for charge titration.	187
D.15	Error binned by sequencing run and titration sample.	187
D.16	Spike-in control for 50% charge.	188
D.17	RNA integrity and comparison to previous half-life values.	188

D.18 Best and worst transcript half-life estimates. . . . .	189
-------------------------------------------------------------	-----

## **LIST OF TABLES**

Table Number	Page
2.1 CRISPR guides. . . . .	39
3.1 CRISPR guides. . . . .	72



## **ACKNOWLEDGMENTS**

I would like to acknowledge all the people that I have been working with for the past five and a half years. My lab mates, current and previous members of the Sullivan lab: Jen Crainic, Ian Engstrom, Madeleine Hart, Ayaha Itokawa, Adam Krol, Oliver Newsom, Evan Quon, David Sokolov, Anna-Lena Vigil and PI Lucas Sullivan. My previous PI Erick Matsen and members of his group: Arman Bilge, Will DeWitt, Amrit Dhar, Jean Feng, Eli Harkins, Andy Magee, Branden Olson, Duncan Ralph and David Shaw. The members on my committee: Taran Gujral, Dana Miller, Daniel Raftery and Arvind (Rasi) Subramaniam. Various collaborators, rotations labs and helpful people: Kristin Anderson, Alicia Darnell and the Vander Heiden lab, Liangcai Gu and the Gu lab, Jonathan Marvin, JP McNevin, Brian Milles, Vladimir Minin, Smita Yadav and the Yadav lab. And my wife Giang Tra Le.

And as prescribed by the ancient cliché in all acknowledgement sections, a dedication or a person for which “this work could not have been completed without” must be identified. Well, I hereby declare that this work is dedicated to all US taxpayers - you paid for it!

## Chapter 1

# ASPARTATE'S ROLE IN CELLULAR METABOLISM OF THE PROLIFERATING CELL

*Metabolism, the sum of chemical reactions occurring inside living organisms.*

### 1.1 *Introduction*

Most of metabolism is *cellular metabolism*, occurring within the confines of a cell, to bring together metabolites and enzymes at a sufficient concentration to enable production of energy and large biomolecules such as proteins, DNA/RNA and lipids. It follows, that *cancer metabolism* is metabolism occurring inside cancer cells. However, most often the term is used comparatively to highlight the differences between metabolism in healthy and cancerous cells, with the assumption that such differences can be targeted therapeutically to provide anti-cancer treatments [154, 53, 95, 158]. Cancer metabolism is most often associated with the “Warburg effect”, an observation made during the 1920s by Otto Warburg that cancer cells in the presence of ample oxygen ferment glucose to lactate and therefore also known as “aerobic glycolysis” [160, 21]. Since then, many researchers have rediscovered this phenomenon and attempted to explain this squandering of glucose in many ways. At present it suffices to say that aerobic glycolysis in cancer cells is not due to mitochondria dysfunction and that other non-cancerous rapidly proliferation cells like T and embryonic stem cells also engage in abundant lactate production.

In the context of this thesis the Warburg effect serves as an illustration that little, if any, difference can be observed between metabolism of the cancer cell and an appropriately matched proliferating cell. This is the Achilles’ heel of the therapeutic ambitions of cancer metabolism, but it also suggests that many lessons about basic cellular metabolism can be

learned by studying cancer cells. Indeed, this is becoming increasingly popular because of the large palette of well characterized cancer cell lines that are rapidly dividing, easy to passage and commercially available. Thus, making gene knockouts, protein over-expression, inhibitor treatments, CRISPR screens etc. available with relative ease. In this thesis, cancer cell lines are also used in such way, with the objective of more broadly generalizing about cellular metabolism of proliferating cells.

## 1.2 *The metabolic rational for aerobic glycolysis*

Many reasons have been provided to rationalize the apparent energetic waste of aerobic glycolysis [155, 111, 68, 177, 119]. Interesting parallels have been drawn between proliferating cells of unicellular and multicellular origin as a way of rationalizing aerobic glycolysis [155]. In the context of yeast, aerobic glycolysis is also known as the Crabtree effect; a feature displayed by some strains but not by others [28]. The effect is also found in bacteria where acetate is secreted in what is known as the acetate switch [167]. A hypothetical explanation of the Crabtree effect in unicellular organisms was proposed by modeling the protein synthesis cost and pathway efficiency to derive an estimate of ATP produced per unit time per unit protein required [107]. In this “proteome allocation” hypothesis, the cost of ATP production through aerobic glycolysis is lower than oxidative phosphorylation because glycolytic enzymes are few and fast whereas oxidative phosphorylation requires many more enzymes with slower conversion rates. Although ATP production per glucose through aerobic glycolysis is 2 vs. approximately 36 for oxidative phosphorylation, the cost of enabling oxidative phosphorylation in human cells is enormous with around 50 proteins required for complex I structure and assembly [130], 11 subunits in complex III [72], 14 subunits in complex IV [134], 29 proteins in ATPase [56] and a long list of regulatory proteins. Indeed, it was later experimentally determined that aerobic glycolysis was approximately twice as efficient as oxidative phosphorylation when comparing the protein demands in *E.coli* [9]. However, this simple conclusion is likely more complicated since some Crabtree positive and negative yeast strains have a similar growth rates; an observation that has been explained by different

translation efficiencies caused by usage of different ribosomal subunit variants [97].

The parallels between aerobic glycolysis in unicellular and multicellular organisms are many but so are the differences. Multicellular organisms have evolved towards a high degree of regulation at the expense of efficiency and their metabolism is often compartmentalized such that some tissues handle the waste of others e.g. the Cori cycle of lactate and the urea cycle of ammonia. Human cells also experience a constant supply of amino acids from the blood and thus do not incur the same cost of protein synthesis as a yeast cell growing with ammonium as the sole source of nitrogen. Therefore, it is unclear if the proteome allocation hypothesis even applies to cancer cells.

Rather than being ATP limited, cancer cells appear to be oversupplied with ATP [129]. High ATP shifts the balance between ATP and AMP which inhibits the glycolytic enzyme phosphofructokinase (PFK) [35]. Conversely, limiting ATP synthesis from ATPase using oligomycin leads to lower ATP/ADP, resulting in enhanced forward driving force of glycolysis [114]. Tumor up-regulated genes leading to increased ATP consumption through ER UDPase relieves the cell of high ATP and increase both glycolysis and proliferation [44, 71]. It has also been shown that when pyruvate oxidation is pharmacologically induced in cancer cells it leads to lower NAD<sup>+</sup>/NADH levels, increased mitochondrial membrane potential and lower proliferation that can all be reversed by uncoupling the mitochondrial membrane potential using an ionophore [96]. The proposed mechanism is that the ATP/ADP (or ATP/AMP) ratio is high at baseline and that more mitochondrial NADH and proton pumping leads to higher membrane potential because ATPase is substrate limited due to low ADP supply. That proliferation can be rescued by relieving the mitochondrial membrane potential directly through uncoupling or increasing the ATP consumption through increased ATP hydrolysis by Na<sup>+</sup>/K<sup>+</sup>-ATPase demonstrates that ATP is not limiting for cancer cell proliferation.

Consensus among contemporary research indicates that cancer cells maintain high flux through glycolysis to drive the pentose-phosphate pathway, serine synthesis and generation of NADPH, and as a side-product an abundance of lactate is produced to regenerate the NAD<sup>+</sup> cofactor consumed by glycolysis [156, 21].

### 1.3 Environmental limitations to cancer cell proliferation

The cellular metabolism of proliferating cells must be calibrated to provide components for cell copying. Ordered by biomass abundance, these components are amino acids, nucleotides and fatty acids followed by the plethora of lower abundance molecules that make up a cell. In culture, protein and lipid biomass is mostly scavenged by uptake of amino acids and lipids from the media, whereas nucleotides are primarily derived from glucose metabolism [66].

For the NCI-60 set of cancer cell lines, proliferation data exists both for cells in culture and cells transplanted into immunodeficient mice (figure 1.1). For the cells in culture, they tend to double once a day, while when xenografted it takes approximately five times as long. Some of which have grown in culture for decades, so it is not surprising that they prefer the cell culture environment over being under the skin of a mouse. Could some of this difference be explained by metabolic differences? One piece of evidence in support of this is that cancer cell lines engineered with the ability to scavenge aspartate from the environment outgrow their non-aspartate scavenging counterparts when grown as tumors in mice but not in culture [141, 48]. This would suggest that aspartate availability is limiting tumor growth, thus explaining some of the difference observed in figure 1.1.

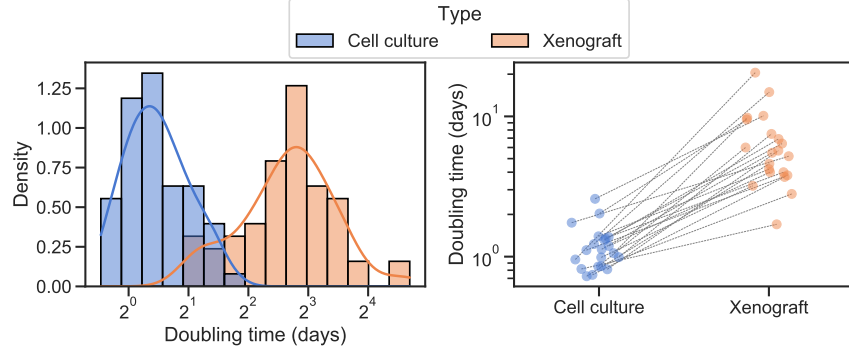


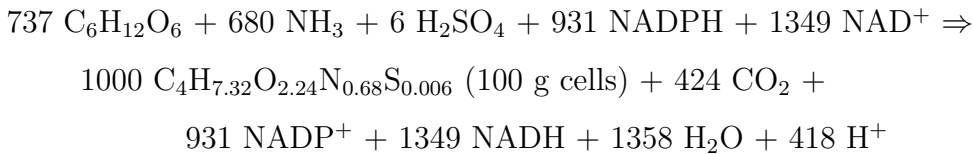
Figure 1.1: NCI-60 cancer cell line doubling time in cell culture vs. xenografts. Left plot: distribution of doubling time of all NCI-60 cells in culture vs. those with data in xenografts. Right plot: paired doubling times for those cell lines with data in xenografts. Paired data connected by dashed lines. Cell culture data from NCI [70], xenograft data from Charles River [87].

#### 1.4 Cellular metabolism requires redox balance

A well-known metabolic difference between cells in culture and in a tumor is the oxygen tension. Cells in culture experience oxygen levels close to atmospheric air whereas cells in tissues experience 2-10 fold lower oxygen [6]. Due to poor vascularization, cells in a tumor experience another 2-10 fold lower oxygen than their host tissue [102]. For mammalian cells oxygen is the principal electron acceptor and thus this profound decrease in oxygen tension could lead to decreased respiration. Lower respiration results in lower ATP production from oxidative phosphorylation and lower capacity to regenerate  $\text{NAD}^+$ . As noted previously, ATP production does not appear to limit proliferation; however, redox imbalance could.

Cellular redox is governed by the co-factors  $\text{NADP}^+$  and  $\text{NAD}^+$  and their redox status defined by the ratio of oxidized to reduced:  $\text{NAD(P)}^+/\text{NAD(P)H}$ . The two redox pools are separate due to the absence of transhydrogenase activity and tight regulation around metabolic reactions ending in conversion. Generally speaking,  $\text{NAD}^+$  is consumed in catabolic reactions such as glycolysis and TCA cycling and  $\text{NADPH}$  is consumed in anabolic reactions such as amino acid, fatty acid and nucleotide synthesis.  $\text{NADPH}$  is primarily generated through

the pentose-phosphate pathway [22, 49, 174]. NAD<sup>+</sup> is generated in several reactions in the TCA cycle and glycolysis and regenerated through respiration. For yeast, biosynthesis of 100 g cells from glucose and ammonia has been estimated to leads to a net production of NADH and a net consumption of NADPH described by the following stoichiometry [16, 153]:



However, besides glucose, mammalian cells have access to fatty acids and amino acids from the blood supply and therefore most of the NADPH consumption for anabolic processes can be avoided. Nucleosides and nucleobases on the other hand are not abundant in serum [147] (appendix A.2) and thus need to be synthesized. Most amino acids are available in serum and can be taken up to fulfill the protein synthesis demand of cancer cells; however, aspartate is an exception due to low cell permeability and low serum concentrations. Glutamate has similar low cell permeability but is readily generated through deamination by the enzyme glutaminase. Aspartate is neither cell permeable nor generated through asparagine deamination in most cell lines [141] and thus has to be synthesized from either glucose or glutamine with a net consumption of NAD<sup>+</sup> (figure 1.2).

Under standard cell culture conditions, respiration is sufficient to regenerate NAD<sup>+</sup> to allow unconstrained aspartate synthesis; however, the mitochondrial electron transport chain can be inhibited with various drugs (figure 1.2) to constrain aspartate production and limit proliferation. The redox imbalance created by inhibited respiration can conveniently be rescued by providing an exogenous electron acceptor such as pyruvate or alpha-ketobutyrate and these tools have been frequently used to study redox imbalance and its effect on aspartate synthesis [12, 140, 13, 51, 48, 3, 30, 171, 96, 47].

Aspartate synthesis appears to be at the nexus of redox imbalance due to its inability to be scavenged from the environment and thus the aspartate level, the NAD<sup>+</sup>/NADH ratio and cell proliferation is coupled together. This coupling has been observed when progres-

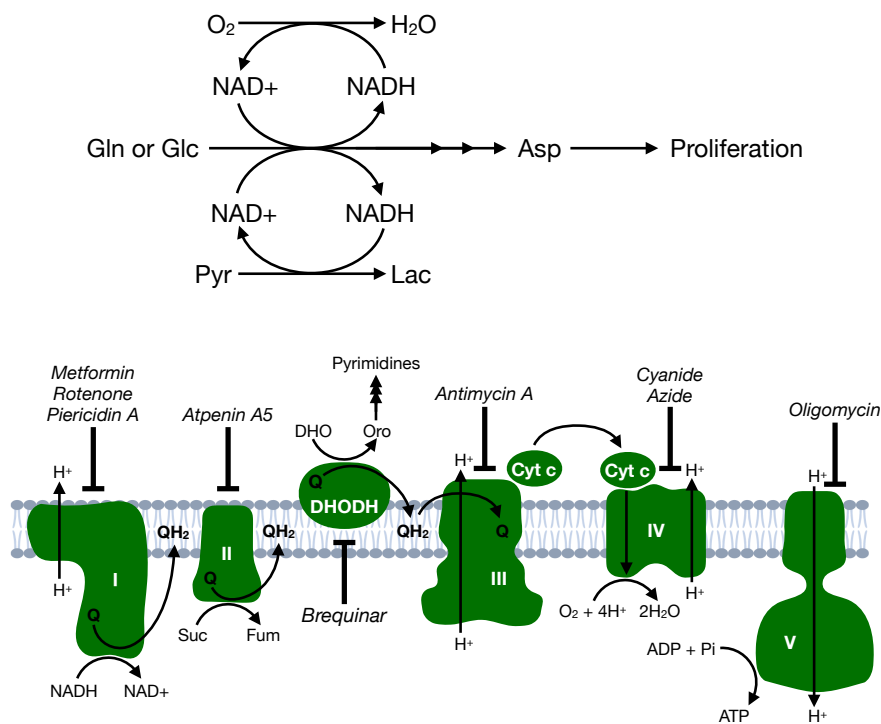


Figure 1.2: Biomass accumulation requires  $\text{NAD}^+$  regeneration. Top diagram: glutamine or glucose is converted into aspartate with consumption of  $\text{NAD}^+$ . Aspartate synthesis is necessary for cell proliferation as it cannot be scavenged from the environment, therefore  $\text{NAD}^+$  regeneration is required either through respiration using oxygen or with an electron acceptor such as pyruvate. Bottom diagram: the mitochondrial electron transport chain regenerates  $\text{NAD}^+$  through respiration of oxygen and many inhibitors exist to probe the effect of each component in the chain.

sively inhibiting respiration such that the NAD<sup>+</sup>/NADH ratio decreases from baseline. A sigmoidal relationship between NAD<sup>+</sup>/NADH ratio and proliferation is observed; however, the NAD<sup>+</sup>/NADH ratio is also tightly correlated with intracellular aspartate levels [51]. This raises the question of causality: is proliferation decrease cause by aspartate or the NAD<sup>+</sup>/NADH ratio?

The evidence is now clear that aspartate is the cause of limited proliferation. Large parts of the proliferation defects caused by inhibiting respiration can be rescued by directly supplying the cells with aspartate either through supraphysiological concentrations (20-40 mM) [51, 13, 140, 84] or expression of an aspartate transporter or an asparaginase enzyme [13, 116, 48, 141]. Respiratory deficient cells, either depleted of mitochondrial DNA ( $\rho^0$ ) or having a frameshift deletion in cytochrome B (CytB), have also been rescued using aspartate [140, 13]. Aspartate limitation can also be induced through complex II inhibition which prevents succinate oxidation to fumarate and thus stops TCA cycling and mitochondrial aspartate synthesis. In this case, when cells are provided with an electron acceptor like pyruvate, the cytoplasmic NAD<sup>+</sup>/NADH ratio is rescued but proliferation is not, and it is only by increasing the intracellular aspartate concentration that proliferation is rescued [54], thus uncoupling the NAD<sup>+</sup>/NADH ratio from proliferation.

In figure 1.3 such uncoupling experiment is repeated by expression of the Glu/Asp transporter SLC1A3 after which aspartate can be delivered by media addition. Using complex I inhibitor rotenone to suppress respiration and thus decreasing proliferation and the NAD<sup>+</sup>/NADH ratio, proliferation was almost fully rescued by aspartate delivery, thus confirming that proliferation is limited by aspartate and not NAD<sup>+</sup>.

In summary, aspartate synthesis is required for cell proliferation due to its impermeability, its synthesis consumes NAD<sup>+</sup> thereby coupling it to respiration, it appears to be insufficiently synthesized by tumors limiting their growth and it is limiting cell proliferation during respiration deficiency. This has prompted us to investigate which fate of aspartate is responsible for limiting tumor growth and cell proliferation.

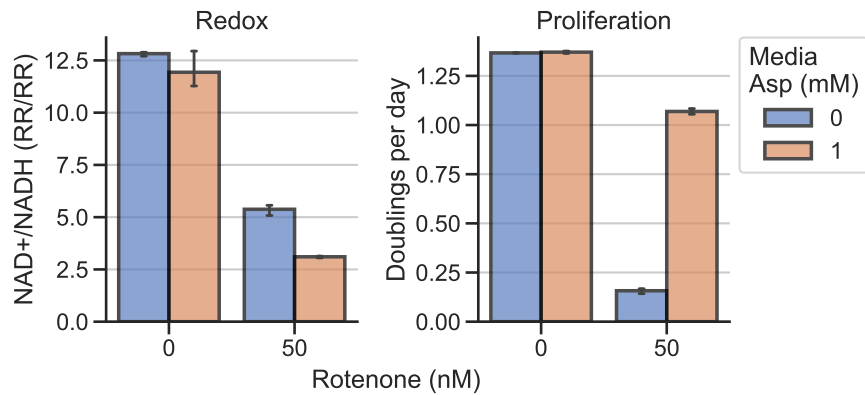


Figure 1.3: Aspartate rescues proliferation but not the NAD<sup>+</sup>/NADH ratio. Uncoupling NAD<sup>+</sup>/NADH and aspartate's effect on proliferation using 143B cells with stable expression of the Glu/Asp transporter SLC1A3, treated with/without 1 mM media aspartate and with-/without 50 nM rotenone. NAD<sup>+</sup>/NADH ratio measured using LCMS as a ratio between two internal standard normalized response ratios (RR/RR).

## 1.5 Aspartate fates

Amino acids can be divided into two groups: terminal amino acids such as asparagine, threonine, valine, leucine, histidine, tryptophan etc. which only fate is protein synthesis and metabolized amino acids such as serine and methionine in the folate and methionine cycles, glutamate as a substrate for anaplerosis and glutamine as a nitrogen donor. However, notice that this grouping will change depending on the cell context e.g. in certain cells and conditions valine, leucine and isoleucine will be consumed as a substrate for anaplerosis, tryptophan will fuel the kynurenine pathway etc. Therefore, when discussing the fates of an amino acid, or any metabolite, the cell context must be considered to focus attention on relevant pathways and avoid getting lost in the vast metabolic network.

For aspartate the relevant fates are asparagine and nucleotide synthesis (figure 1.4). For nucleotide synthesis, aspartate is consumed to make pyrimidine precursor carbamoyl-aspartate, in the purine synthesis pathway to make purine precursor IMP and in the conversion of IMP to AMP. Aspartate fates can be divided into two classes: fates consuming the aspartate carbon backbone and fates where only the nitrogen is donated, and the carbon

backbone is returned in the form of fumarate. The distinction is important as fumarate has the same redox state as aspartate and can be recycled back into aspartate with no net consumption of NAD<sup>+</sup>(appendix A.3). On the other hand when aspartate is consumed for asparagine, pyrimidine or protein synthesis it must be replenished by synthesis from glucose or glutamine at the cost of NAD<sup>+</sup> consumption.

Aspartate is a nitrogen donor in the urea cycle, required to convert citrulline into arginine. For cells synthesizing their own arginine, this is drained from the urea cycle which is then replenished by ornithine synthesis from glutamate and subsequent conversion to citrulline by ornithine transcarbamylase to close the cycle. However, ornithine transcarbamylase is almost exclusively expressed in the liver and gastrointestinal tract, with no expression in most cancer cell lines; therefore, non-hepatic cell lines have no net arginine synthesis and are arginine auxotrophs unless provided with exogenous citrulline.

N-acetylaspartate is another potential aspartate fate found abundantly in brain tissue but also to some extend in adipocytes; however, most other tissues and cancer cell lines do not produce appreciable amounts of N-acetylaspartate. This correlates with lacking expression of NAT8L, the enzyme responsible for its synthesis [46]. Therefore, in the context of cancer cell lines, N-acetylaspartate does not consume a meaningful amount of aspartate, nor is it a metabolite that appear to influence cell proliferation.

Finally, although not a net consumption term, aspartate is used as a shuttle metabolite in the aspartate-malate shuttle to transfer electrons generated in the cytoplasm into the mitochondrial matrix.

### *1.5.1 Aspartate metabolism fluxes*

Each aspartate fate is responsible for a fraction of the total cellular aspartate consumption, a consumption rate also known as a flux. These aspartate consumption fluxes could change in different conditions such as during mitochondrial inhibition or when aspartate fates can be salvaged from the environment and thus measuring each flux would be useful tool. Flux measurements are often done using stable isotope tracing and are routinely applied using

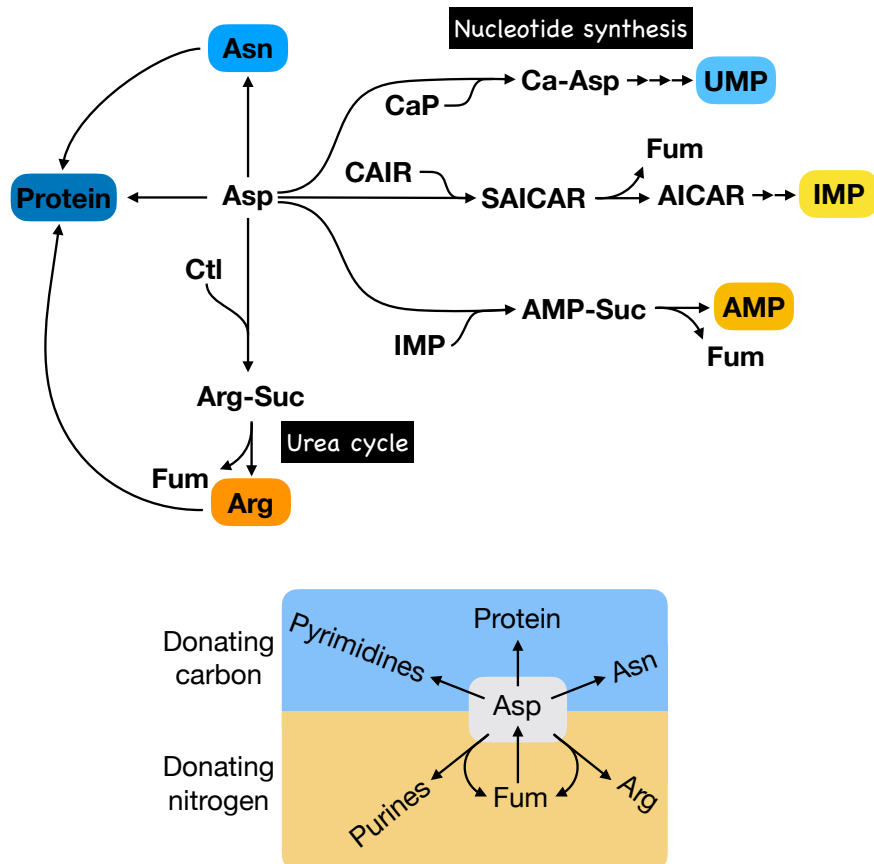


Figure 1.4: Metabolic fates of aspartate. Top diagram: aspartate is used as a substrate for protein synthesis directly and indirectly as a precursor of asparagine and arginine. Aspartate is also a substrate for all pyrimidine synthesis, synthesis of purine precursor IMP and conversion of IMP to AMP. Bottom diagram: aspartate fates can be divided into those where aspartate is donating its carbon backbone and thus requiring NAD<sup>+</sup> consumption to resynthesize aspartate (pyrimidine, protein and asparagine synthesis) and those where aspartate is donating its amino group nitrogen to yield fumarate which can be recycled back to aspartate in a redox neutral way.

<sup>13</sup>C-labelled glucose, glutamine or other amino acids [172, 113, 73, 8].

As such, flux can easily be calculated by measuring label incorporation over time e.g. if labelled metabolite  $A$  is introduced at time zero and consumed to synthesize labelled metabolite  $B$  then the label incorporation is described by an exponential with the rate  $r_{AB}$  and pool size  $[B]$ :

$$B_{\text{labelled}}(t) = [B] - [B]e^{-r_{AB}t}$$

The synthesis flux is defined as:  $F_{syn} = [B]r_{AB}$  and controls the time before half of the pool is labelled:

$$t_{1/2} = \frac{[B]}{F_{syn}} \ln(2)$$

A detailed treatment of this example can be found in appendix A.1.

In these simple flux measurements, it is assumed that the reaction is irreversible, but it is trivial to extend the mathematical model to a reversible reaction; however, it is not always trivial to measure the flux of such reversible reactions. Unfortunately, this is the case for the fates of aspartate which has several challenges. Firstly, the impermeability makes it impractical to use aspartate directly as a tracer, and secondly, aspartate fates both involve carbon and nitrogen. Potentially, both of these issues could be solved using U-<sup>13</sup>C, U-<sup>15</sup>N glutamine but the number of relevant reaction rates is very large (figure 1.5) and to solve such system it would be necessary to measure protein, DNA and RNA abundance and breakdown rates. This makes aspartate fate flux very difficult to measure directly using time-series of isotopic labelling and therefore were not attempted. Instead, fluxes were estimated using measurements of total amino acids and nucleotides at a steady-state proliferation rate (detailed in chapter 2).

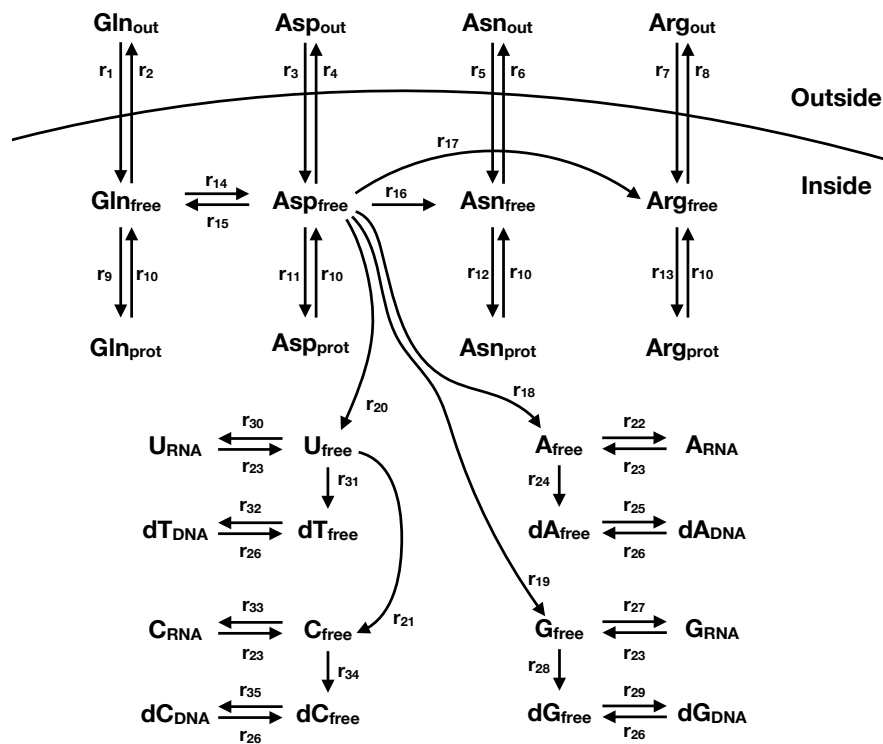


Figure 1.5: Aspartate metabolism fluxes as they would appear from glutamine labelling with enumerated conversion rates. Amino acids are either outside the cell (out), inside the cell (free) or bound in protein (prot). Nucleotides are either as (d)NTP, (d)NDP, (d)NMP free or bound in RNA/DNA.

### **1.6 Which aspartate fate controls proliferation**

Based on the fates of aspartate it can be speculated which of these, if any, is “the first-degree effect” responsible for the relationship between aspartate and proliferation. As tumor growth is aspartate limited it seems likely that tumors are also experiencing this first-degree effect of aspartate limitation, whatever it may be. Several of the metabolic fates of aspartate can be salvaged from the environment e.g. asparagine, uridine, hypoxanthine and adenine to complement asparagine, pyrimidine IMP and AMP synthesis, respectively. And thus, if depletion of any one of the salvageable aspartate fates is the first-degree effect of aspartate limitation, then it can be added to the media to either rescue proliferation or induce a further aspartate depletion resulting in a “second degree effect” which then controls proliferation. In both cases the aspartate to proliferation rate correlation would be shifted to reflect that proliferation is no longer mediated by the first-degree effect.

Initially, the effect of all salvageable fates of aspartate can be tested with a “Salvage mix” containing these at a sufficient concentration. This tests the hypothesis that one of the aspartate fates is the first-degree effect of aspartate limitation. Thus, if this fate is scavenged through salvage mix supplementation it enables proliferation at lower a aspartate concentration (figure 1.6). If true, this fate can be isolated by attempting proliferation rescue with single components from the salvage mix. If false, none of the salvageable fates is the first-degree effect of aspartate limitation, leaving aspartate consumption to protein.

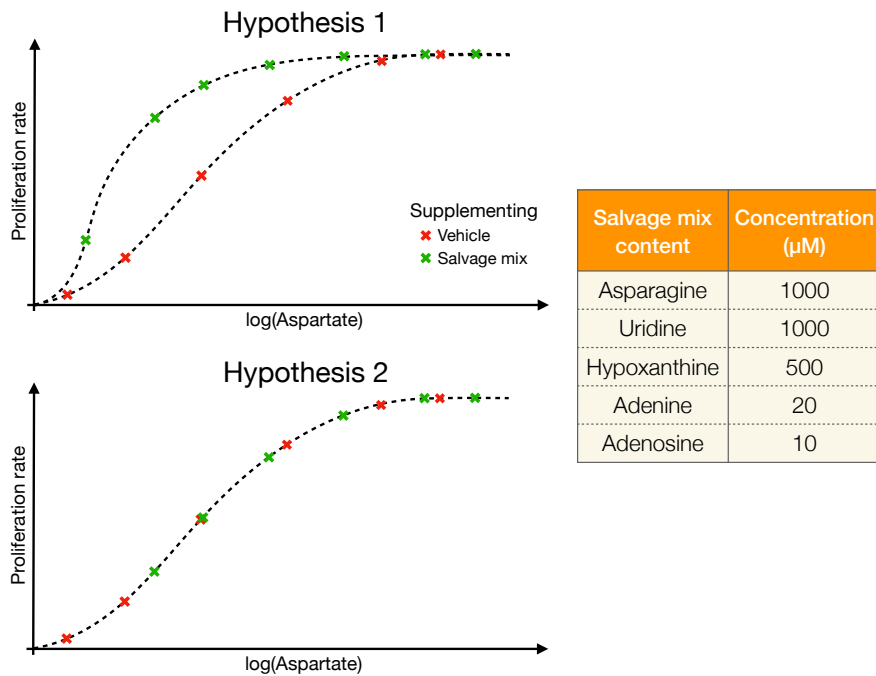


Figure 1.6: Two hypotheses for aspartate to proliferation correlation. Hypothesis 1 posits that some fate of aspartate is the direct cause of aspartate limited proliferation and thus if this fate is scavenged through salvage mix supplementation it enables proliferation at a lower aspartate concentration. Hypothesis 2 posits that no such fate exists, or that it cannot be scavenged through salvage mix supplementation.

## Chapter 2

# MOLECULAR MECHANISMS OF ASPARTATE LIMITATION

*Aspartate limitation, a level of aspartate insufficient to sustain maximal cell proliferation.*

### 2.1 *Introduction*

Cells require aspartate for protein synthesis and as a metabolic substrate to fuel proliferation. However, unlike most amino acids, aspartate levels are dictated by cellular metabolism and are influenced by many perturbations that alter said metabolism. Metabolic perturbations leading to a small decrease in aspartate synthesis capacity does not result in full aspartate depletion; rather, it results in a downwards adjustment of the aspartate level as well as cell proliferation. This aspartate to proliferation correlation has been observed in several cell lines using various ways of constraining aspartate synthesis [140, 13, 51]. Many of these constraints also result in decreased NAD<sup>+</sup>/NADH ratio; however, aspartate levels can be uncoupled from the NAD<sup>+</sup>/NADH ratio to show a causal link between aspartate levels and cell proliferation [141, 48].

Interestingly, aspartate levels are not only related to cell proliferation but has also been associated with modifications to cell function in multiple biological processes, including stem cells [146, 5], immune cells [7], endothelial cells [29], and cancer [59]. The sum of these observations provide impetus for studying the underlying reasons for the ability of aspartate levels to “control” proliferation rate. Aspartate’s role as a substrate for asparagine and nucleotide synthesis is known, its requirement for protein synthesis is self-evident and simultaneously it is cycled between the cytoplasm and the mitochondrial matrix to transfer electrons into the matrix via. the malate-aspartate shuttle. It is unknown if these roles of aspartate are involved in its coupling to proliferation, but this knowledge would be useful to establish the

mechanism of aspartate limitation.

In this chapter the concept of aspartate limitation is investigated. A stable correlation between intracellular aspartate levels and proliferation is established, the flux towards the different fates of aspartate is estimated, a mix of salvageable fates of aspartate is characterized and their individual influence on rescuing aspartate limitation is determined. Finally, aspartate limitation's effect on tRNA aminoacylation levels is measured and its effect on integrated stress response is surveyed.

## 2.2 Results

### 2.2.1 Mitochondrial inhibition induces a titratable aspartate limitation

Aspartate limitation was induced with complex I inhibitor rotenone in two experiments measuring intracellular aspartate and the NAD<sup>+</sup>/NADH ratio alongside cell counts to calculate the proliferation rate between time zero and 2, 3, 4 and 5 days (figure 2.1). Proliferation rate adjusts in accordance with the rotenone dose and can be partially rescued with pyruvate. For the highest dose of rotenone, proliferation decreases over time, reflecting the time it takes before steady-state proliferation is reached.

Intracellular aspartate decreases to correlate with proliferation rate (figure 2.2) but then recovers slightly over time, likely due to media conditioning and rotenone breakdown (appendix figure B.2). Intracellular asparagine appear to be affected similarly to aspartate (appendix figure B.3). Throughout the experiment intracellular aspartate and NAD<sup>+</sup>/NADH ratio correlate as expected (figure 2.3).

### 2.2.2 Quantifying the metabolic fates of aspartate

The relevant metabolic fates of aspartate are: protein, arginine, asparagine pyrimidines and purines. It is desirable to know the consumption flux of each aspartate fate as a way of ranking their importance during aspartate limitation. To achieve this, first amino acid uptake and release was determined for wildtype (WT) 143B cells and its double knockout of

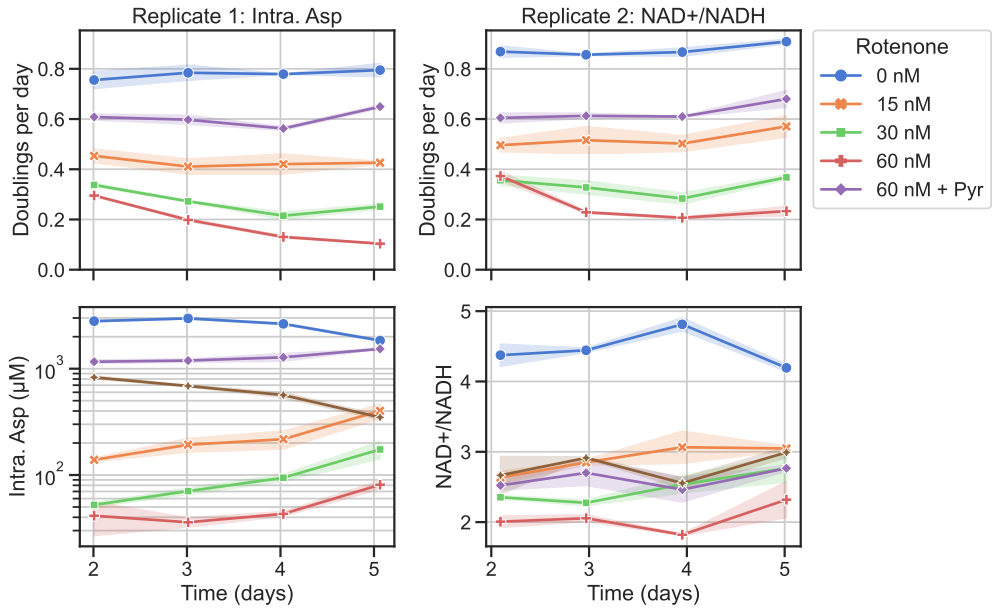


Figure 2.1: Rotenone induces aspartate limitation in H1299 cells. In replicate one (left column), proliferation rate and intracellular aspartate concentration were determined over time. In replicate two (right column), proliferation rate and the NAD<sup>+</sup>/NADH ratio were determined over time. For rescue, 2 mM pyruvate was used.

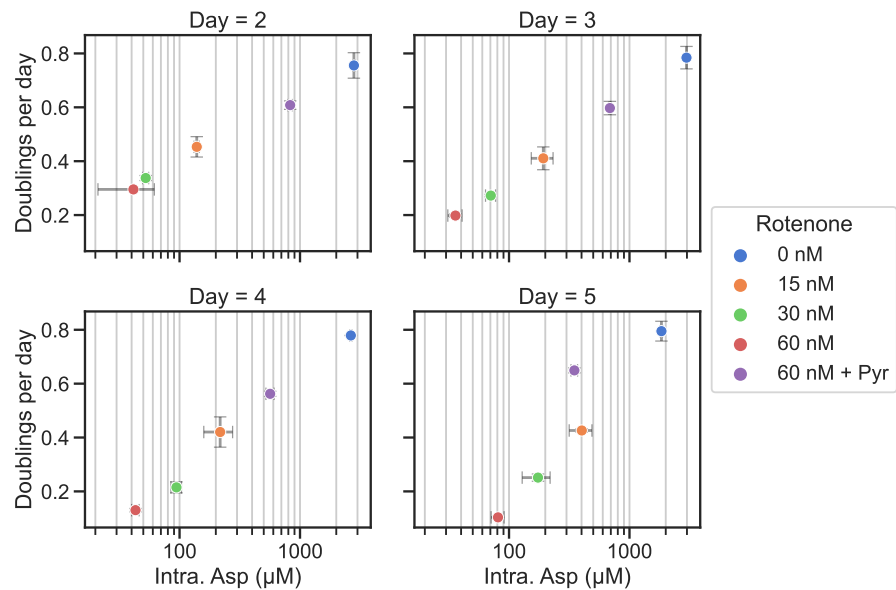


Figure 2.2: Correlation between the intracellular aspartate concentration and proliferation rate for data in figure 2.1.

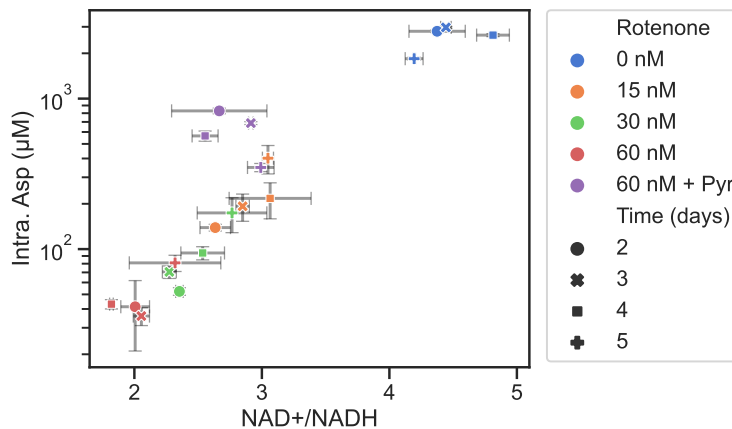


Figure 2.3: Correlation between the intracellular aspartate concentration and the  $\text{NAD}^+/\text{NADH}$  ratio for data in figure 2.1.

the aspartate synthesis genes glutamic oxalacetic transaminases 1 and 2 (GOT DKO) (figure 2.4). The GOT DKO cells have abolished aspartate synthesis, relying on aspartate import via. the SLC1A3 transporter and thus total aspartate consumption can be determine. It was observed that highly consumed amino acids like glutamine have high uptake flux while rare amino acids like tryptophan like have low uptake, in accordance with previous measurements [66]. Permeable amino acids, not present in DMEM like asparagine and proline, are released. In this experiment, isotopically labelled asparagine was added to the media to quantify its uptake and at the final timepoint intracellular metabolites were extracted to determine the ratio of labelled to unlabelled asparagine inside the cells. With the flux measurements for unlabelled asparagine release and labelled asparagine uptake, and the intracellular labelling ratio, the other asparagine fluxes could be solved by application of flux conservation (figure 2.5a; see methods for details).

Asparagine efflux must be calculated as an initial value because progressive accumulation of asparagine in the media will lead to lower efflux over time. Thus calculated, the initial efflux of asparagine is close to 2.5 mM/h while asparagine consumption by protein synthesis is 1.5-2 mM/h (figure 2.5b). The measured efflux is in good agreement with asparagine efflux

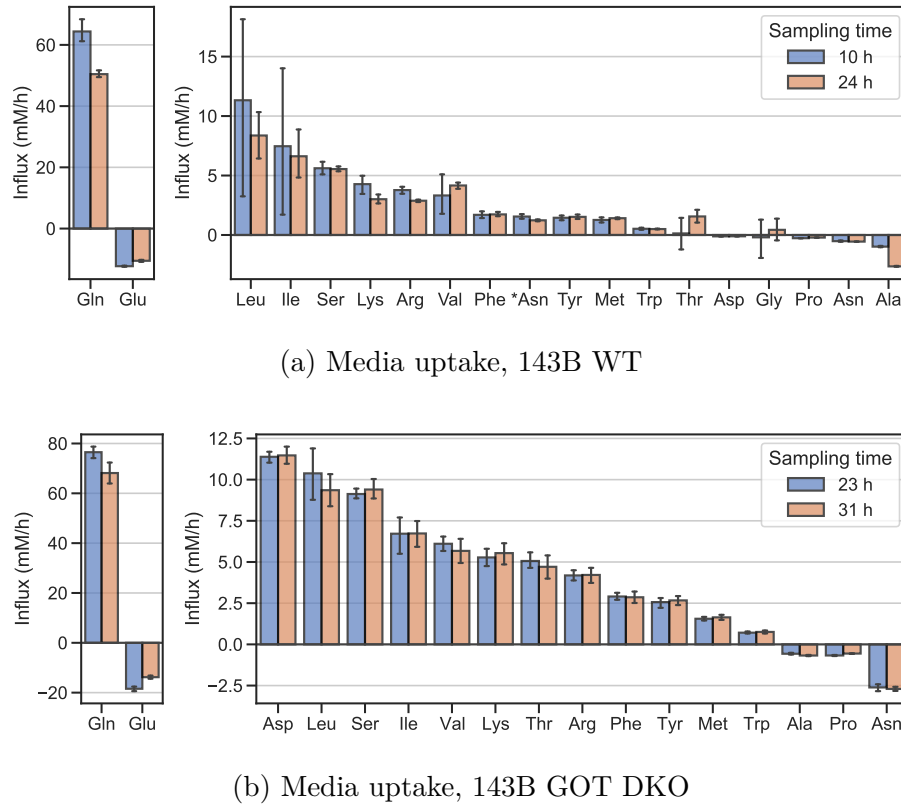


Figure 2.4: Amino acid influx/efflux from DMEM media. For 143B WT in (a), media was spiked with U-<sup>13</sup>C Asn (\*Asn in the plot) to measure asparagine uptake. For 143B GOT DKO in (b), cells expressing Glu/Asp transporter SLC1A3, media was spiked with 500  $\mu$ M aspartate to measure its uptake.

measured in GOT DKO cells with did not receive isotopically labelled asparagine 2.4b).

To determine aspartate consumption by protein and pyrimidine synthesis, 143B and H1299 cells were hydrolyzed to measure all aspartate, asparagine and arginine bound in protein and all pyrimidines bound in DNA and RNA (figure 2.6). Both cell lines show similar total amino acid concentrations, with 143B cells appearing slightly denser than H1299. Since asparagine and glutamine are entirely deaminated to aspartate and glutamate during acid hydrolysis (appendix figure B.4) the sum of asparagine and aspartate is measured. Similarly, purines are susceptible to acid hydrolysis and cannot be accurately quantified (appendix

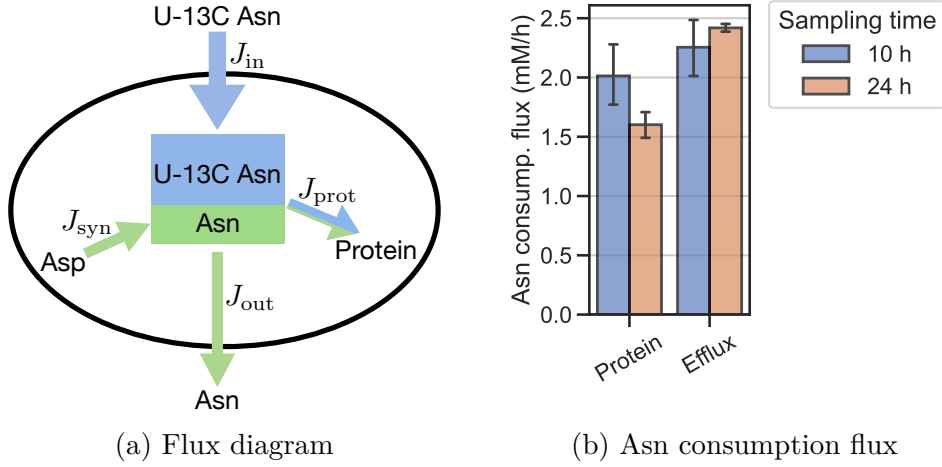


Figure 2.5: (a) Diagram of asparagine fluxes in a cell. Net influx of U-<sup>13</sup>C labelled Asn ( $J_{in}$ ), net efflux of unlabelled Asn ( $J_{out}$ ), net deposition of Asn into protein ( $J_{prot}$ ) and Asn synthesis from Asp ( $J_{syn}$ ). Unlabelled metabolites symbolized by green and U-<sup>13</sup>C labelling symbolized by blue. (b) Measured asparagine consumption fluxes in 143B cells using the media uptake data from figure 2.4a. Asn is consumed into protein synthesis (Protein) and leaked into the media (Efflux). Efflux is calculated as the initial rate i.e. assuming no Asn is provided in the media.

figure B.5). Therefore, the total concentration of purines was estimated equal to that of pyrimidines, based on published measurements on rat liver RNA [92].

Taken together, the flux of each aspartate fate in 143B cells can be inferred (figure 2.7). These fluxes shows that protein synthesis is the biggest consumer of aspartate but also that asparagine efflux is a large sink, dependent on media conditions. The total aspartate consumption flux in DMEM, i.e. with arginine but without asparagine, is estimated to be 10.4 mM/h. This is close to the aspartate uptake in 143B GOT DKO cells which was measured at 11.4 mM/h (figure 2.4b). The difference can be accounted for by considering that total pyrimidine/purine levels underestimate synthesis flux by discounting recycling (figure appendix B.9) and because 143B GOT DKO cells maintain a higher intracellular concentration of aspartate due to expression of the SLC1A3 aspartate transporter.

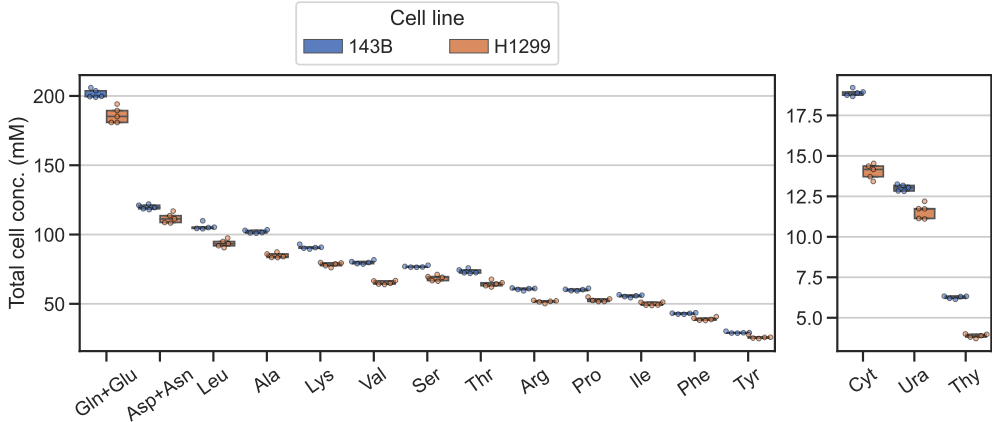


Figure 2.6: Total amino acids and pyrimidines liberated by acid hydrolysis of 143B and H1299 cells, normalized by total cell volume (Total cell conc.). Gln and Asn is converted during acid hydrolysis to Glu and Asp, respectively. Glycine is not shown because it is also produced from purine hydrolysis [98].

### 2.2.3 Salvage can fulfill all the non-protein metabolic fates of aspartate

Media complementation of aspartate fates could be used to identify the mechanisms of aspartate limitation. Towards this end, isotope tracing was employed to test the ability of cells to divert consumption of aspartate into its metabolic fates by providing a salvageable alternative. Steady-state tracing was performed with both amide-<sup>15</sup>N and alpha-<sup>15</sup>N labelled glutamine to measure the salvage fraction for asparagine, uridine, hypoxanthine, adenine and guanine. For purines traced with Gln amide-<sup>15</sup>N, *de novo* synthesis results in GTP with three label incorporations (<sup>15</sup>N3) and ATP with two (<sup>15</sup>N2), whereas the number of labels decreases if purines are salvaged (figure 2.8). The resulting isotopologue distributions for 143B cells show that hypoxanthine salvage is fully substituting *de novo* purine synthesis to the point of IMP. Interestingly, a similar results is shown for adenine, likely due to deamination and recycling back to IMP (appendix figure B.9). Guanine is also salvaged into GTP, but less efficiently at around 20%, and it is only recycled back into IMP at a small degree apparent by the small changes in ATP labelling. For H1299, the isotopologue distributions are more complex because of Gln amide to alpha <sup>15</sup>N transfer (appendix figure B.10); however,

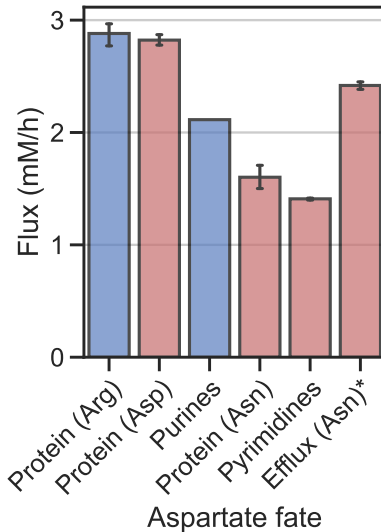


Figure 2.7: Relative consumption towards each fate of aspartate in 143B cells, estimated using best estimates from figure 2.5b and 2.6. Synthesis of purines was assumed equal to pyrimidines and thus aspartate consumption towards purines was estimated 1.5 times the consumption towards pyrimidines to account for two aspartate consumed for AMP and one for GMP (see appendix figure B.9). \* Asn efflux is calculated as the initial rate for cells are grown in asparagine free media.. Blue bars indicate the aspartate fate is a nitrogen donation yielding fumarate, red bars indicate the fate consumes aspartate carbons.

when taking this into account the results are similar to the 143B cells except that guanine is salvaged more efficiently, at higher than 90%, as well as recycled back into IMP at a higher degree.

These results can be summarized by the relative contribution of each synthesis path into ATP and GTP in cells receiving adenine or guanine, respectively (figure 2.9). In summary, for both 143B and H1299, 100  $\mu$ M adenine is sufficient to displace aspartate consumption for purine synthesis by salvage of adenine directly into AMP and by its recycling into hypoxanthine/IMP.

Salvage of asparagine and pyrimidines can also be measured using Gln amide- $^{15}\text{N}$  tracing. Asparagine synthesis leads to one label incorporation (15N1) and thus the salvage fraction can be measured by comparing the abundance of unlabelled and 15N1 labelled intracellular

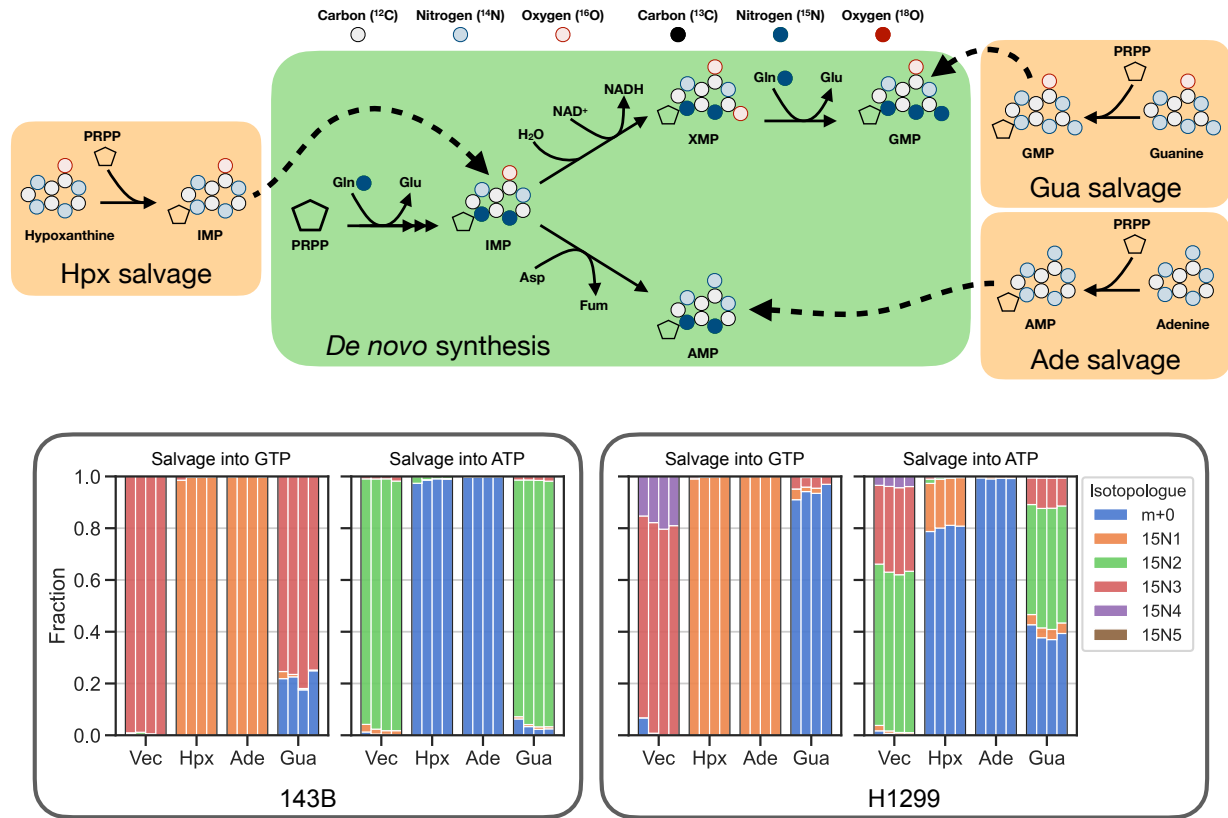


Figure 2.8: Salvage into purines. Top diagram shows Gln amide-<sup>15</sup>N label incorporation into purines and the resulting changes following salvage of hypoxanthine (Hpx), adenine (Ade) or guanine (Gua). Bottom isotopologue distributions show Gln amide-<sup>15</sup>N label incorporation into GTP and ATP at steady-state for cell lines 143B and H1299 grown in DMEM supplemented with vehicle (Vec) or 100  $\mu$ M Hpx, Ade or Gua. The four replicates are plotted as grouped bars.

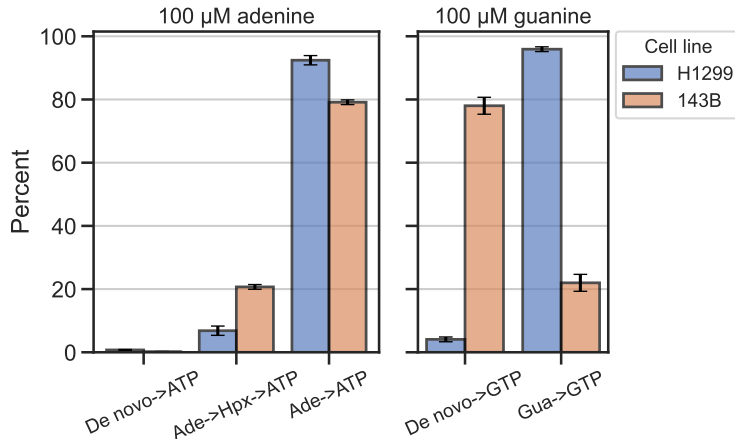


Figure 2.9: Inferred synthesis paths into ATP and GTP when cells receive 100  $\mu\text{M}$  adenine or guanine, respectively. ATP and GTP are either derived from *de novo* synthesis or salvage. ATP can be salvaged from adenine directly or through hypoxanthine/IMP as a product of adenine deamination.

asparagine (figure 2.10). Gln amide to alpha  $^{15}\text{N}$  transfer in H1299 causes asparagine to be doubly labelled from both glutamine and partially from aspartate. Consistent with the high permeability of asparagine [141], its salvage fraction is high in both 143B and H1299 when provided at 500  $\mu\text{M}$  in the media (figure 2.10). A small fraction of unlabelled asparagine persists which indicates continued synthesis; however, uptake is likely sufficient for cellular demands thus making residual synthesis non-essential. The labelling pattern for UTP synthesis is similar, with one label incorporation (15N1) and a possible second label in H1299 cell from aspartate due to Gln amide to alpha  $^{15}\text{N}$  transfer. Taking amide to alpha  $^{15}\text{N}$  transfer into account, the salvage fraction of 200  $\mu\text{M}$  uridine is around 95% for both 143B and H1299 (figure 2.10).

Taken together, salvage of asparagine and uridine is efficient and using a mixture of adenine, uridine and asparagine should be able to fulfill all the non-protein metabolic fates of aspartate. In such mixture, concentrations must be chosen to be low enough to be non-toxic but high enough to avoid insufficient salvage and depletion. This could be achieved using a mix of 500  $\mu\text{M}$  asparagine, 200  $\mu\text{M}$  uridine and 100  $\mu\text{M}$  adenine; however, salvage

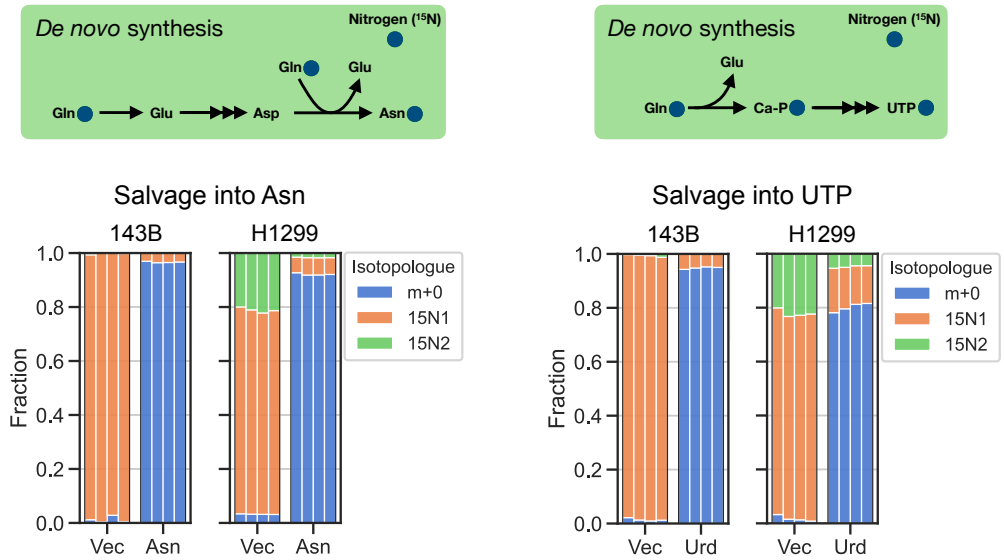


Figure 2.10: Salvage into asparagine and pyrimidines. Top diagram shows Gln amide-<sup>15</sup>N label incorporation into asparagine (left) and pyrimidines (right). Bottom isotopologue distributions show Gln amide-<sup>15</sup>N label incorporation into Asn and UTP at steady-state for cell lines 143B and H1299 grown in DMEM supplemented with vehicle (Vec), 500 µM Asn or 200 µM Urd. The four replicates are plotted as grouped bars.

appear to be efficient even at lower concentrations (appendix figure B.12). Finally, aspartate consumption by arginine synthesis was also measured using Gln alpha-<sup>15</sup>N tracing and found to be non-existing (appendix figure B.13), as expected given the non-hepatic origin of the cell lines used.

If any of the metabolic fates of aspartate is the cause of decreased proliferation during aspartate limitation, then adding it back via. salvage could restore proliferation. In H1299 cells, aspartate limitation was induced using metformin or rotenone and then rescued using the above established routes for salvage (figure 2.11). As a positive control pyruvate shows a robust rescue while each salvaged metabolite shows a small but positive effect of proliferation. The effect of uridine relative to asparagine is consistent with the relative consumption fluxes (figure 2.7), suggesting that they exert their effect by diverting aspartate consumption. It would be tempting to suggest a similar explanation for the rescues made with hypoxanthine

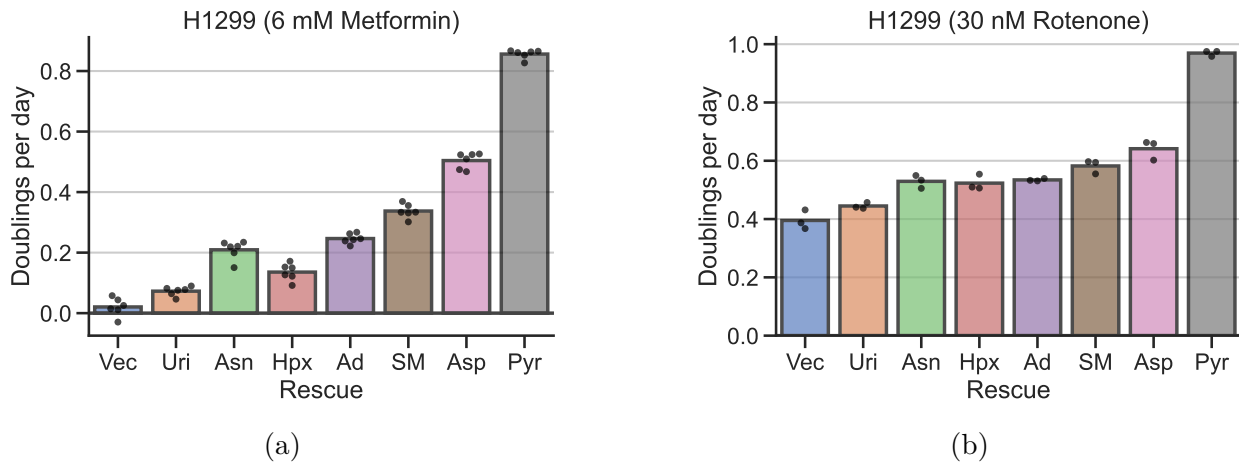


Figure 2.11: Rescuing aspartate limitation with aspartate fates. In (a) inducing aspartate limitation with 6 mM metformin and in (b) with 30 nM rotenone. Rescuing with vehicle (Vec), 200  $\mu$ M uridine (Urd), 500  $\mu$ M asparagine (Asn), 100  $\mu$ M hypoxanthine (Hpx), 100  $\mu$ M adenine (Ad), salvage mix (SM), 20 mM aspartate (Asp) or 2 mM pyruvate (Pyr). Salvage mix contain: 500  $\mu$ M asparagine, 200  $\mu$ M uridine and 100  $\mu$ M adenine.

and adenine; however, aspartate consumption in purine synthesis is for nitrogen donation and the resulting fumarate can readily be recycled back to aspartate with no net consumption of NAD<sup>+</sup>. Therefore, the partial rescue of hypoxanthine and adenine is more likely a result of diverting consumption of 10-formyl-THF which is consumed twice during purine synthesis. This is because 10-formyl-THF production by the folate cycle consumes NAD<sup>+</sup> thereby enhancing the effect of complex I inhibition [171]. This explanation is also consistent with results showing that metformin rescue by hypoxanthine and adenine is blunted in serine free media with sodium formate, where the folate cycle no longer consumes NAD<sup>+</sup> (appendix figure B.14).

#### 2.2.4 Proliferation is not controlled by the non-protein metabolic fates of aspartate

The salvageable fates of aspartate partially rescues proliferation. Two models can be proposed to explain this: Model 1, the decrease in proliferation during aspartate limitation is

controlled by the one metabolic fate of aspartate which becomes limiting first. When this fate is salvaged, proliferation is partially restored until a second metabolic fate of aspartate becomes limiting at a lower aspartate level etc. In this model, providing salvageable metabolites for the metabolic fates of aspartate should partially rescue proliferation and enable cells to maintain proliferation at lower aspartate levels. Model 2, the decrease in proliferation during aspartate limitation is not controlled by any of the salvageable fates of aspartate. Thus, provided with salvageable fates of aspartate, proliferation is partially restored only by diverting aspartate consumption, but it does not allow proliferation at lower aspartate levels. In model 1, when cells are provided with a “salvage mix” to fulfill the metabolic fates of aspartate, the aspartate to proliferation relationship must shift leftwards to reflect proliferation at lower aspartate concentrations. For model 2, the aspartate to proliferation relationship should remain, or at least not shift leftwards. When performing this experiment in H1299 cells the aspartate to proliferation relationship does not shift leftwards, but slightly rightwards, upon addition of salvage mix (figure 2.12). The reason for the rightwards shift is unknown; however, assuming that tRNA<sup>Asp</sup> aminoacylation is not limiting, the results rule out model 1. It is concluded that proliferation is not controlled by the non-protein metabolic fates of aspartate.

Interestingly, when cells are supplied with salvage mix, the intracellular aspartate level at 50% proliferation is stable between 380-570  $\mu\text{M}$  across different complex I inhibitors and cell lines (appendix section B.6). In this condition, only aspartate consumption towards protein synthesis should be required and thus this concentration is surprisingly high considering that aspartate-tRNA ligase has a  $K_M$  for aspartate between 16 and 29  $\mu\text{M}$  [14, 42, 103].

#### *2.2.5 Depleted tRNA charge is not required for aspartate limitation*

None of the salvageable fates of aspartate could relax the aspartate to proliferation relationship, but it remains to be tested if proliferation is limited by protein synthesis directly through uncharged tRNA<sup>Asp</sup>. This possibility was tested on H1299 and 143B cells, treated with inhibitors of electron chain complexes I, II, III and V that are known to causes as-

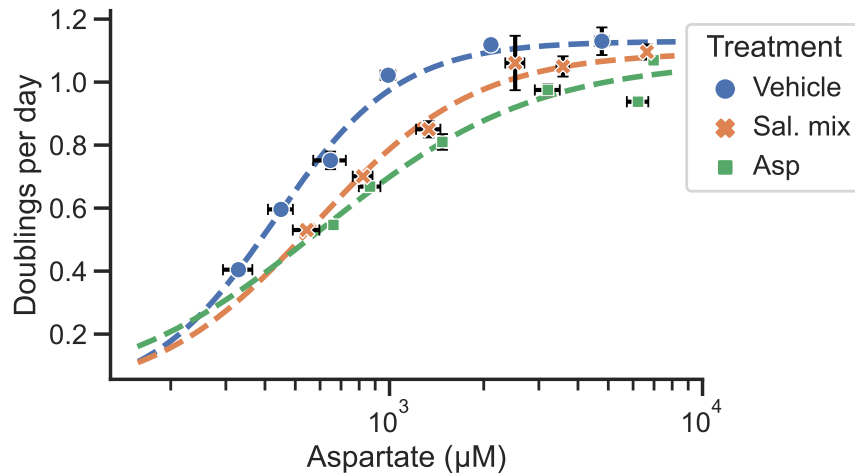


Figure 2.12: Aspartate to proliferation relationship for H1299 using rotenone to induce aspartate limitation. Aspartate concentration at 50% proliferation is 430, 570 and 610  $\mu\text{M}$  for Vehicle, Sal. mix and Asp treatments, respectively. Condition with salvage mix (Sal. mix) contains: 1 mM asparagine/uridine, 0.5 mM hypoxanthine, 20  $\mu\text{M}$  adenine and 10  $\mu\text{M}$  adenosine.

partate limitation [140, 54]. tRNA charge was determined at steady-state using tRNA-seq (see chapter 4) and inhibitors were used at concentrations that result in very little or no proliferation. The resulting tRNA charges show that some inhibitors do indeed cause a decrease in charge, for example antimycin has a strong effect on tRNA charge in 143B cells (figure 2.13). However, since all the inhibitor treated conditions experience strong aspartate limitation, it can be concluded that depleted tRNA charge is not a defining feature. This is clear for H1299 cells treated rotenone, which at 100 nM should have proliferation close to zero (appendix figure B.15a), but no substantial decrease in tRNA charge is observed. Most inhibitor induced decreases in tRNA charge appear to happen only for mitochondrial tRNAs. This also does not support uncharged tRNA being the driver of aspartate limitation because aspartate limited rho0 cells, devoid of any mitochondrial tRNAs, can still be rescued by aspartate [13]. The possibility of a transient decrease in tRNA charge was also tested, but it appears that tRNA charge decreases monotonically over time after inhibitor treatment (appendix figure B.19).

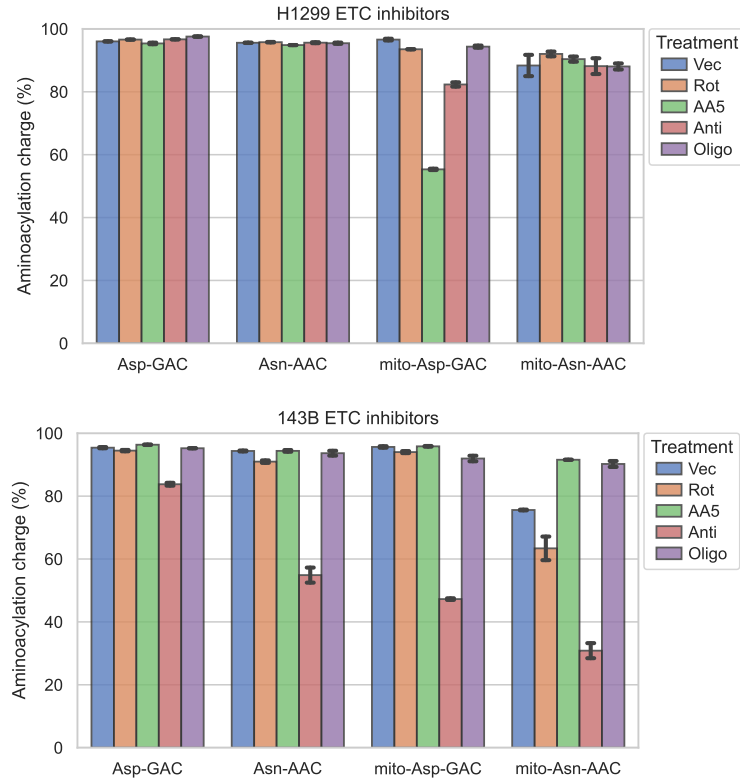


Figure 2.13: Steady-state (30 hours) tRNA charge after mitochondrial inhibitor treatment. (a) H1299 cells treated with vehicle (Vec), rotenone (Rot; 100 nM), atpenin (AA5; 5  $\mu$ M), antimycin (Anti; 5  $\mu$ M) or oligomycin (Oligo; 1  $\mu$ M). (b) 143B cells treated with vehicle (Vec), rotenone (Rot; 50 nM), atpenin (AA5; 5  $\mu$ M), antimycin (Anti; 0.5  $\mu$ M) or oligomycin (Oligo; 0.25  $\mu$ M). For all treatments cells were grown in DMEM, without pyruvate, with dialyzed FBS. For antimycin and oligomycin treatments, 200  $\mu$ M uridine was added to the media. For the atpenin treatment, 1 mM pyruvate was added to the media.

## 2.2.6 Aspartate limitation triggers the integrated stress response through asparagine

With no evidence supporting that proliferation is controlled by the metabolic fates of aspartate, and the relatively high aspartate concentrations required for cells to maintain 50% proliferation rate, it seems more likely that a signaling pathway limits proliferation. The integrated stress response (ISR) is good candidate since it responds to amino acid depletion [27] and has more recently been shown activated by mitochondrial inhibitors rotenone, piericidin, antimycin and oligomycin [52, 104, 25]. Canonical ISR signals through the kinases

GCN2, HRI, PERK and PKR which phosphorylates eIF2alpha to alter translation. The transcription factor ATF4 is a main target and its abundance increase rapidly following ISR. Using both standard western blots and an RFP reporter of ATF4, it was found that mitochondrial inhibitors rotenone, metformin and antimycin induce ISR in a dose-responsive way (appendix figures B.21 and B.22). The ISR activation could be prevented by supplementation with exogenous electron acceptors pyruvate and alpha-ketobutyrate (figures 2.14a and 2.14b). Using complex II inhibitor atpenin to create aspartate limitation, ISR could still be induced without the typical decrease in NAD<sup>+</sup>/NADH ratio (figure 2.14c). Also in this context, using complex I inhibitor rotenone to increase aspartate levels [54] causes a reduction in ISR. And lastly, mitochondrial inhibitor induced ISR requires aspartate synthesis 2.14d), as would be expected if ISR is induced by aspartate limitation and not by other effects of mitochondrial inhibition.

In summary, aspartate limitation clearly triggers ISR. However, unlike aspartate limitation, the ISR induced by rotenone and antimycin could be completely ablated by asparagine supplementation. This is consistent with a recent report using mouse myoblasts which also found that mitochondrial inhibitor induced ISR could be reversed with asparagine [104]. It is also consistent with a rapid drop in intracellular asparagine preceding ATF4 accumulation (figure 2.15).

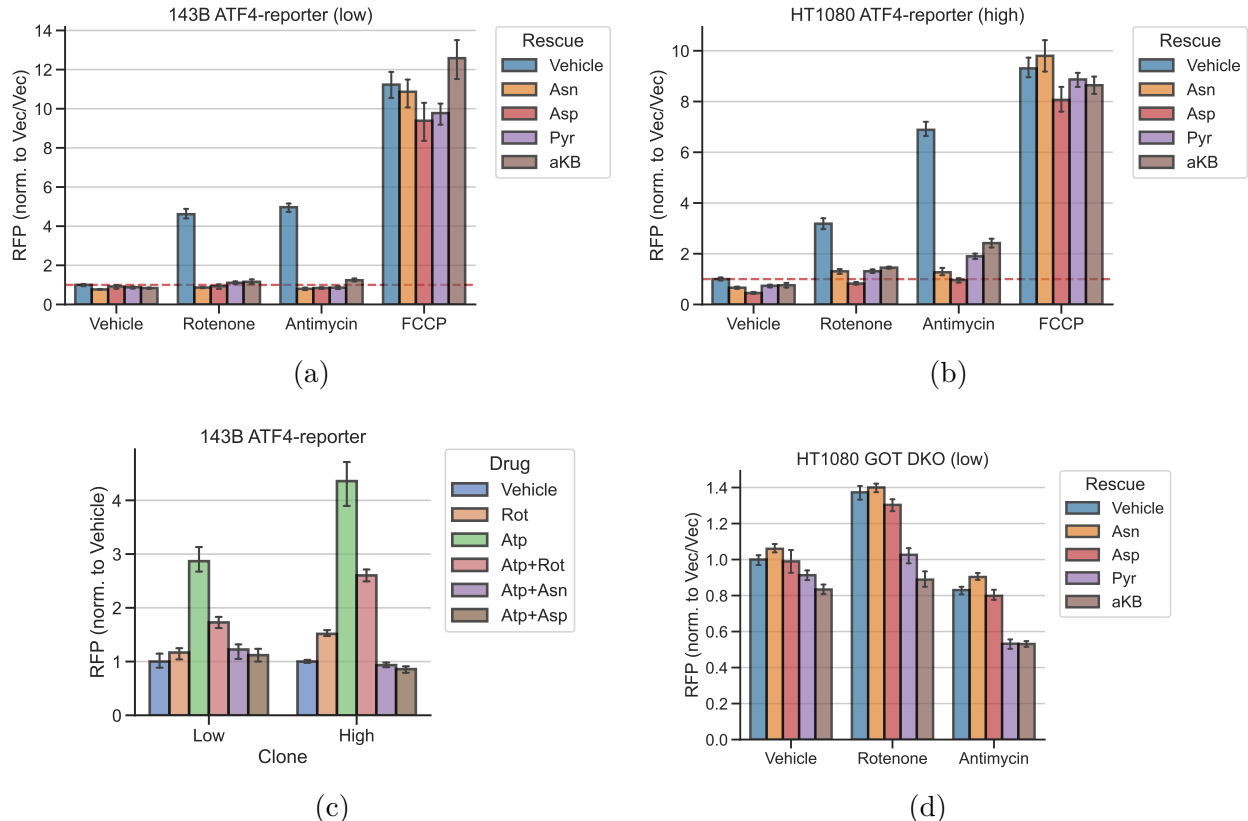


Figure 2.14: Mitochondrial inhibitor induced ATF4 reporter expression is prevented by media asparagine. (a) and (b), data for two clones with low and high reporter expression at baseline. FCCP is a membrane potential uncoupler and used as a positive control. (c) Rotenone can partially prevent ATF4 reporter expression induced by atpenin. (d) GOT DKO cells are not responding to mitochondrial inhibitors; however, they do respond to aspartate depletion (appendix figure B.23d). Similar data for other clones in appendix figure B.23.

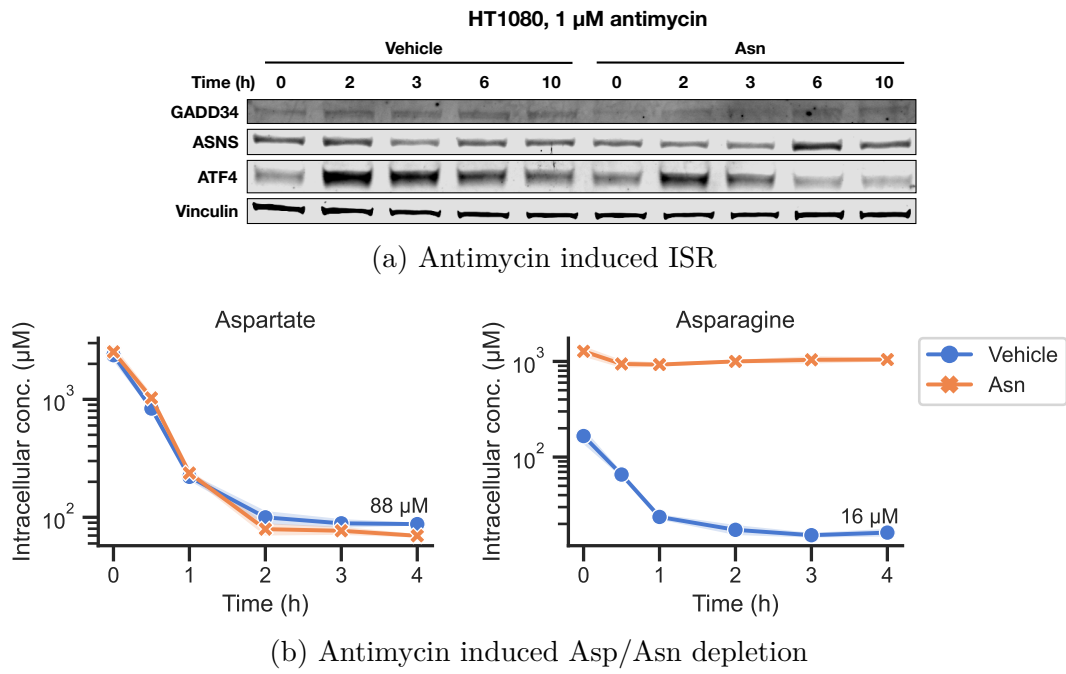


Figure 2.15: Antimycin induced ISR correlates with Asn depletion in HT1080 WT cells. (a) Antimycin (1 μM, media change) induced ATF4 accumulation is partially prevented by media asparagine (100 μM). (b) Intracellular Asp/Asn in HT1080 cells grown and treated in parallel with the cells used for (a).

### 2.3 Discussion

Despite the efforts presented in this chapter it is still unclear what causes proliferation decrease during aspartate limitation. However, the current data highlights several important aspects of aspartate limitation that were not previously known. First, the aspartate consumption fluxes revealed the importance of asparagine efflux as a larger consumption flux than asparagine consumption by protein synthesis. This could help explain the relatively large proliferation rescue observed upon asparagine supplementation to complex I inhibited cells in culture and the compounding anti-tumor effect of *in vivo* asparagine depletion using asparaginase and complex I inhibitor metformin [84]. Second, a strategy was validated for complementation of non-protein metabolic fates of aspartate. Previously, purine bases have

been used for complementation of aspartate limited cells but with no validation that these were consumed and provided at sufficient concentrations [140]. Third, aspartate to proliferation curves were generated with quantification of intracellular aspartate concentrations at steady-state, as opposed to ion counts after 8 hours of treatment [51]. This revealed a surprisingly high intracellular aspartate concentration of 380-570  $\mu\text{M}$  necessary to maintain proliferation rate at 50% while receiving salvage mix to cover all non-protein metabolic fates of aspartate. Fourth, for the first time tRNA charge data is presented for cells during aspartate limitation. In line with the high intracellular aspartate concentrations required for proliferation, uncharged tRNAs do not appear to be required for aspartate limitation. And lastly, it was shown that while the integrated stress response is turned on upon aspartate limitation it can be ablated with asparagine and thus it is not relevant for aspartate's ability to control proliferation.

So how then does aspartate limit proliferation? One possibility is nucleotide imbalance, which could occur even when metabolic fates of aspartate are provided through a salvage mix. The balance of nucleotides has large effects on cell proliferation and imbalance causes suppression of DNA synthesis and limits progression through S phase of the cell cycle [31]. Indeed, aspartate limitation causes a great increase in IMP [140] which could be due to decreased conversion of IMP to AMP by the aspartate consuming enzyme adenylosuccinate synthase. Complex III inhibition also appears to increase IMP levels as well as increasing the guanine to adenine ratios (GMP/AMP, GDP/ADP and GTP/ATP; appendix figure B.25), again pointing towards adenylosuccinate synthase. For human adenylosuccinate synthase the  $K_M$  for aspartate has been reported to be 950  $\mu\text{M}$  [152], whereas for other mammals it has been reported between 230 and 1500  $\mu\text{M}$  [136]. This is within the range of intracellular concentrations that causes aspartate limitation and thus nucleotide imbalance should be further explored in the future.

## 2.4 Methods and Materials

### 2.4.1 Cell culture

Cell lines were acquired from ATCC (143B, H1299, HT1080) and tested to be free from mycoplasma (MycoProbe, R&D Systems). Cells were maintained in Dulbecco's Modified Eagle's Medium (DMEM) (Gibco, 50-003-PB) supplemented with 3.7 g/L sodium bicarbonate (Sigma, S6297), 10% fetal bovine serum (FBS) (Gibco, 26140079) and 1x penicillin-streptomycin solution (Sigma, P4333). Cells were incubated in a humidified incubator at 37°C with 5% CO<sub>2</sub>.

### 2.4.2 Western blots

Protein lysates were harvested in RIPA buffer (Sigma, R0278) supplemented with Halt protease and phosphatase inhibitor cocktail (Fisher, PI78443) and 5 mM EDTA. Protein concentration was determined using a BCA assay (Fisher, 23225) using bovine serum albumin (BSA) as a protein standard. Equal amounts of protein were added to LDS sample buffer (ThermoFisher, B0008) with 5% 2-Mercaptoethanol (Sigma, M3148), denatured at 95°C for 5 min, loaded onto 4–12% SDS-polyacrylamide gels (Invitrogen, NW04122BOX) along with a prestained protein ladder (ThermoFisher, 26616) and run 35 min at 180V in MES buffer (ThermoFisher, B000202). Proteins were dry transferred onto a 0.2 µm nitrocellulose membrane using the iBlot2 device (ThermoFisher, IB21001) with the P0 system setting and associated transfer stacks (Fisher, IB23001). Membranes were blocked with 5% bovine serum albumin (Sigma, A4503) in tris-buffered saline with 0.1% Tween-20 (TBS-T) and incubated at 4°C overnight with the following antibodies: anti-ATF4 (Cell Signaling, 11815S, 1:500), anti-ASNS (Cell Signaling, 92479T, 1:1000), anti-GADD34 (Proteintech, 10449-1-AP, 1:500), anti-GOT2 (Proteintech, 14800-1-AP, 1:750), anti-GOT1 (Cell Signaling, 34423 S, 1:1000), anti-Vinculin (Sigma, SAB4200729; 1:10,000) and anti-Tubulin (Sigma, T6199; 1:10,000). Membranes were washed with TBS-T and the following secondary antibodies were added in blocking buffer: 800CW Goat anti-Mouse IgG (LiCOR, 926-32210; 1:15,000) and/or 680RD

Goat anti-Rabbit IgG (LiCOR, 926–68071; 1:15,000) and incubated for 1 hour. Membranes were washed with TBS-T, incubated for 10 min in TBS-T, washed in deionized water and imaged on a LiCOR Odyssey Near-Infrared imaging system.

#### *2.4.3 Proliferation assays*

Cells were trypsinized (Corning, 25,051 CI), resuspended in seeding media, counted (Beckman Coulter Counter Multisizer 4) and seeded overnight onto 6/12/24 well dishes (Corning, 3516;3513;3524) with an initial seeding density of 10,000 cells/mL and a volume of 4, 2 and 1 mL, respectively. After overnight incubation, 3–6 wells were counted for a starting cell count at the time of treatment. Treatment was initiated either by media switch or by spike-in of drug/metabolite from a 20-50x stock. For both seeding and treatment, experiments were conducted in DMEM without pyruvate (Corning 50–013-PB) supplemented with 3.7 g/L sodium bicarbonate, 10% dialyzed fetal bovine serum (Sigma, F0392) and 1x penicillin-streptomycin solution, with or without sodium pyruvate (Pyr) (Sigma, P8574), 2-ketobutyric acid (AKB) (Sigma, K401), aspartate (Asp) (Sigma, A7219), asparagine (Asn) (Sigma, A7094), uridine (Urd) (Sigma, U3003), hypoxanthine (Cayman Chemical, 22254), adenine (Ade) (Sigma, A2786), guanine (Gua) (Sigma, 51030) or sodium formate (Sigma, 71539) with concentration noted when relevant. Drug treatments included rotenone (Sigma, R8875), metformin (Sigma, D150959), atpenin A5 (Cayman Chemical, 11898; AdipoGen, AG-CN2-0110; Abcam, ab144194; or Enzo Life Sciences, ALX-380–313), antimycin A (Sigma, A8674), oligomycin A (Sigma, 495455), FCCP (Cayman Chemical, 15218-10), BAM15 (Cayman Chemical, 17811) and DMSO vehicle (Sigma, D2650). Cells were incubated in a humidified incubator at 37°C with 5% CO<sub>2</sub>, then counted after 4–6 days. Proliferation rate was reported as doublings per day and determined using the time and fold count difference between the starting and final counts, assuming a constant proliferation rate throughout the assay.

#### 2.4.4 Generation of nuclear RFP cell lines

Nuclear RFP cell lines were generated using 1e5 transducing units of EF1A-nuclear RFP lentivirus (Cellomics Technology, PLV-10205-50) by spinfection. Cells were seeded at 50% confluence on 6 well dishes, lentivirus was added to fresh media with 8 µg/µL polybrene, then added to cells and followed by centrifugation (900g, 90 mins, 30°C). Two days after infection, cells were sorted for high RFP expression using fluorescence-activated cell sorting (FACS). High RFP cells were then expanded and single-cell cloned by limiting dilution, plating 0.5 cells/well on a 96 well plate. Plates were then screened for RFP expression and localization using Incucyte S3 (Sartorius) and a suitable clone chosen, expanded, and used for all subsequent experiments.

#### 2.4.5 Lentiviral production and stable cell line generation

The following plasmids were obtained: pLenti6.3-V5 DEST\_SLC1A3 (DNASU Plasmid Repository) and ATF4 reporter pXG237 (Addgene, 141281). Genes were first cloned into entry vector pENTR1A (Fisher, A10462) using NEBuilder HiFi DNA Assembly Cloning Kit (New England BioLabs, E2621). These donor constructs were then used to transfer their insert into destination vectors: pLX304-CMV-Blast (Addgene, 25890) or pLenti-CMV-Hygro (w117-1) (Addgene, 17454 a gift from Eric Campeau & Paul Kaufman) using LR Clonase II (Fisher, 11791100). Each plasmid sequence was verified by whole plasmid sequencing (Plasmidsaurus). Lentivirus was generated by co-transfection of HEK293T cells with destination vector plasmid DNA and the packaging plasmids pMDLg/pRRE (Addgene, 12251), pRSV-Rev, (Addgene, 12253) and pMD2.G (Addgene, 12259) using FuGENE transfection reagent (Fisher, PRE2693) in DMEM (Fisher, MT10017CV) without FBS or penicillin-streptomycin. The supernatant containing lentiviral particles was filtered through a 0.45 µM membrane (Fisher, 9720514) and was supplemented with 8 µg/µL polybrene (Sigma, TR-1003-G) prior to infection. For infection, cells were seeded at 50% confluence in 6 well dishes and centrifuged with lentivirus (900g, 90 mins, 30°C). After 24 hours the media was replaced with

fresh media and after 48 hours cells were treated with either 1 µg/mL blasticidin (Fisher, R21001) or 150 µg/mL hygromycin (Sigma, H7772-1G) and maintained in selection media until all uninfected control cells died. After selection, cells were expanded and single-cell cloned by limiting dilution, plating 0.5 cells/well using 96 well plates. These clones were expanded and screened by either western blot or presence of RFP signal using Incucyte S3 (Sartorius) to validate expression. From this, a single clone was chosen, expanded and used for all subsequent experiments.

#### *2.4.6 Generation of knockout cells*

Protocol and guide RNA generation was identical to that described in Hart et al. [54]. Briefly, three chemically synthesized 2'-O-methyl 3'phosphorothioate-modified single guide RNAs (sgRNA) with sequences targeting the gene of interest were purchased (Synthego; table 2.1). A pool of all three sgRNAs (or all six for GOT1/GOT2 double knockout) were resuspended in nuclease-free water, combined with SF buffer (Lonza, V4XC-2032), and sNLS-spCas9 (Aldevron, 9212). 200,000 cells were resuspended in the resulting solution containing ribonucleoprotein complexes (RNPs) and electroporated using a 4D-Nucleofector (Amaxa, Lonza). Nucleofected cells were then expanded and single-cell cloned by limiting dilution by plating 0.5 cells/well on a 96 well plate. Gene knockout was confirmed using western blots.

Table 2.1: CRISPR guides.

Gene	sgRNA sequence (5'-3')
GOT1	CAGUCAUCCGUGCGAU AUGC
	GCACGGAUGACUGCCAUC CCC
	CGAUCUUCUCCAUCUGGGAA
GOT2	UUUCUCAUUUCAGCUCCUGG
	CGGACGCUAGGCAGAACGUA
	UCCUUCCACUGUUCGGACG

#### 2.4.7 Enzymatic NAD<sup>+</sup>/NADH ratio measurement

NAD<sup>+</sup>/NADH measurements were done using a modified version of the enzymatic NAD-/NADH Glo assay (Promega, G9071), similar to Sullivan et al. 2015 [140]. Cells were plated and treated like a proliferation experiment. At the time of harvest, cells on a parallel plate were counted to estimate the total cell volume. The volume of lysis buffer used was adjusted to be between 500-2000 times the total cell volume. Extractions were performed by washing three times with ice cold saline, followed by thorough aspiration and addition of ice-cold lysis buffer (0.5% DTAB (Sigma, D5047), 0.1 M NaOH in PBS). Cells were scraped and frozen at -80°C until further processing. At processing, lysate was thawed one ice and 2x40 µL was move to two PCR tubes. To break down NADH under basic conditions, one tube was incubated at 75°C for 30 min and then neutralize with 40 µL 0.25 M Tris base in 0.2 M HCl. To break down NAD<sup>+</sup> under acidic conditions, the other tube was added 40 µL 0.4 M HCl, incubated at 60°C for 15 min and then neutralize with 80 µL neutralization buffer (0.25 M Tris base, 0.25% DTAP, 0.05 M NaOH). Titrations with pure standards of NAD<sup>+</sup> (Sigma, N1511) and NADH (Sigma, N8129) were also made, diluted in lysis buffer and processed in parallel to generate calibration curves. To measure NAD<sup>+</sup>, NADH and the derived ratio, 25 µL of the acid/base treated samples were moved to a white 96 well plate (ThermoFisher, 236105) whereafter 25 µL of the LDR mix was quickly added using a multi channel pipette to start the luminescent reaction. The reactions were mixed by shaking, then luminescence was measured every 5 minutes using 0.5 second integration and 0.5 second settle time on a Tecan Infinite 200 M Plex microplate reader. The measurements were performed with technical replicates and the average of these were used in further analysis.

#### 2.4.8 Polar metabolite extraction

For polar metabolite extraction, a plate was move to ice and the media was thoroughly aspirated. Wells were washed thrice with cold saline (Fisher, 23293184), 1 mL 80% HPLC grade methanol in HPLC grade water was added, cells were scraped with the back of a

P1000 pipet tip and transferred to tubes. Tubes were centrifuged (17,000g, 15 mins, 4°C) and a fraction of the supernatant containing polar metabolites was transferred to a new centrifuge tube and placed in a centrivap until dry. The fraction of supernatant transferred was adjusted to correspond to that extracted from a 1 µL cell volume e.g. 50% was transferred if the total cell volume extracted from was 2 µL. The total cell volume extracted from was determined by counting cells and sizes on a parallel plate using a Coulter counter. This way of determining the total cell volume was found to be superior to packed cell volume (see appendix B.1). Dried samples were reconstituted with 40 µL 80% HPLC grade methanol, containing internal standards when appropriate, and transferred to vials for measurement by LCMS.

#### *2.4.9 Media metabolite extraction*

For media metabolite extraction, 10 µL media was sampled, added to 990 µL 80% HPLC grade methanol in HPLC grade water and incubated at -20°C for 30 min. Tubes were centrifuged (17,000g, 15 mins, 4°C), 400 µL of the supernatant containing media metabolites was transferred to a new tube and placed in a centrivap until dry. Dried samples were reconstituted with 40 µL 80% HPLC grade methanol, containing internal standards when appropriate, and transferred to vials for measurement by LCMS.

#### *2.4.10 Absolute quantification by isotope dilution*

Dried samples were reconstituted with 40 µL 80% HPLC grade methanol containing 5 µM U-<sup>13</sup>C, U-<sup>15</sup>N labelled canonical amino acid mix (Cambridge Isotope Laboratories, MSK-CAA-1) and transferred to vials for measurement by LCMS. For pyrimidine nucleobase/nucleoside quantification a U-<sup>13</sup>C internal standard was made by partial hydrolysis (12 hours in 6 M HCl at 90°C) of U-<sup>13</sup>C spirulina whole cells lyophilized powder (Cambridge Isotope Laboratories, CLM-8400-PK). The peak area for each compound was divided by its labelled standard to derive the response ratio. The response ratio was then mapped to a calibration curve to infer the compound concentration in the vial. The sample concentration

was calculated by correcting for each step introducing a dilution which for the intracellular concentrations, included using of the total cell volume. To make the calibration curves a non-labelled amino acid mixture was made from an analytical amino acid standard without glutamine and asparagine (Sigma, A9906-1ML) and added glutamine (Sigma, 76523-100MG) and asparagine (Sigma, 51363-100MG) to match the concentration of the other amino acids. For pyrimidine nucleobase/nucleoside quantification this pool was also mixed with equimolar uracil (Sigma, U1128), uridine (Sigma, U3003), 2 -deoxyuridine (Sigma, D5412), thymine (Sigma, T0376), cytosine (Sigma, C3506) and cytidine (Cayman Chemical, 29602). Using this mix, three replicates of a 12 point 2-fold dilution series was made with a maximum concentration of 500  $\mu$ M and a volume per dilution of 40  $\mu$ L. These were placed in a centrifavap until dry and reconstituted with 40  $\mu$ L 80% HPLC grade methanol containing the appropriate isotopic internal standard and transferred to vials for measurement by LCMS. The peak area for each compound was divided by its labelled standard to derive the response ratio, then the best fitting calibration curves for each compound were chosen among either linear, power or a second-degree polynomial. Each calibration curve was manually inspected for proper fit and measurements below or above the concentration range of the dilution series were discarded.

#### *2.4.11 Liquid Chromatography-Mass Spectrometry (LCMS)*

Metabolite quantitation was performed using a Q Exactive HF-X Hybrid Quadrupole-Orbitrap Mass Spectrometer equipped with an Ion Max API source and H-ESI II probe, coupled to a Vanquish Flex Binary UHPLC system (Thermo Scientific). Mass calibrations were completed at a minimum of every 5 days in both the positive and negative polarity modes using LTQ Velos ESI Calibration Solution (Pierce). Polar Samples were chromatographically separated by injecting a sample volume of 1  $\mu$ L into a SeQuant ZIC-pHILIC Polymeric column (2.1 x 150 mm 5 mM, EMD Millipore). The flow rate was set to 150 mL/min, autosampler temperature set to 10°C, and column temperature set to 30°C. Mobile Phase A consisted of 20 mM ammonium carbonate and 0.1% (v/v) ammonium hydroxide, and Mobile Phase B

consisted of 100% acetonitrile. The sample was gradient eluted (%B) from the column as follows: 0-20 min.: linear gradient from 85% to 20% B; 20-24 min.: hold at 20% B; 24-24.5 min.: linear gradient from 20% to 85% B; 24.5 min.-end: hold at 85% B until equilibrated with ten column volumes. Mobile Phase was directed into the ion source with the following parameters: sheath gas = 45, auxiliary gas = 15, sweep gas = 2, spray voltage = 2.9 kV in the negative mode or 3.5 kV in the positive mode, capillary temperature = 300°C, RF level = 40%, auxiliary gas heater temperature = 325°C. Mass detection was conducted with a resolution of 240,000 in full scan mode, with an AGC target of 3,000,000 and maximum injection time of 250 msec. Metabolites were detected over a mass range of 70-850 m/z. Quantitation of all metabolites was performed using Tracefinder 4.1 (Thermo Scientific) referencing an in-house metabolite standards library using 5 ppm mass error. For samples subjected to stable isotope tracing, peak areas were natural abundance corrected with IsoCor [105], using experimentally determined tracer purity values.

#### 2.4.12 Media uptake flux

The cells were first passaged in DMEM with dialyzed FBS and the tracer and/or metabolites used during the uptake experiment. For 143B GOT DKO cells expressing SLC1A3, 500 µM sodium aspartate was added. For 143B WT cells, 100 µM U-<sup>13</sup>C Asn was added to achieve a steady-state label fraction in the proteome. To start the experiment, cells were seeded on 6 well dishes at 1e5 cells/well. On the next day fresh media was added and t=0 media samples were collected. Cells were then incubated and subsequent media samples collected at the indicated time. After the last media collection, the residual media volume was quantified to correct for evaporation. For U-<sup>13</sup>C Asn tracing the labelling ratio was determined by extracting intracellular metabolites after the last media collection. Two dishes were run in parallel and used for counting to determine proliferation rates and cell volume measurement using a Coulter counter.

#### 2.4.13 Acid hydrolysis to measure amino acids and pyrimidines

Two 12 well plates were seeded in parallel in DMEM without pyruvate, with dialyzed FBS. At 90% confluency, plates were washed thrice with saline, then to one plate 1 mL 6 M HCl (Sigma, 84429) was added to each well. The plate was sealed with adhesive PCR plate seal (ThermoFisher, AB0558) and placed in an incubator at 90°C for 20 hours for hydrolysis. Meanwhile, each well on the other plate was trypsinized and counted on a Coulter counter. At the end of the 20 hour incubation, the hydrolysate was moved to a tube followed by thrice washing with 1 mL HPLC grade water to collect all material. This was dried down and reconstituted again in 0.5 mL 6 M HCl following another incubation at 90°C for 48 hours to complete the hydrolysis. Tubes were dried and reconstituted again in 0.5 mL 6 M HCl, then a volume equivalent to 20,000 cells was moved to a fresh tube and dried down. To remove water insoluble material, tubes were reconstituted with 1 mL HPLC grade water and centrifuged (17,000g, 15 mins) before moving 0.5 mL to a fresh tube and drying. Dried samples were reconstituted with 40  $\mu$ L 80% HPLC grade methanol, containing internal standards for both amino acids and nucleotides/nucleobases.

To ensure correct quantification, amino acid and nucleobase stability and solubility was tested. These tests are documented in appendix section [B.3](#).

#### *Flux calculation*

Cell counts over time is assumed to be exponential,  $y(t)$ , with proliferation rate  $K$  and cell count at  $t = 0$  being  $y_0$ :

$$y(t) = y_0 2^{Kt} \quad (2.1)$$

Assuming amino acid uptake into a cell is constant, the uptake rate (also called influx) can be defined as the total molar uptake over a time range, divided by the total area under the cell count curve of the same time range. Formally, the flux of a compound  $i$  is:

$$F_i = \frac{n_i(t_1) - n_i(t_2)}{\int_{t_1}^{t_2} y(t) dt} \quad (2.2)$$

With  $F_i$  being the flux of compound  $i$ ,  $n_i(t)$  being its molar quantity, and  $t_1$  and  $t_2$  being the first and second timepoint, respectively.

Using  $\Delta$  to indicate the difference between  $t_1$  and  $t_2$ , we can simplify the above:

$$F_i = \frac{\Delta n_i}{\int_{t_1}^{t_2} y(t) dt} = \frac{\Delta n_i}{\frac{y_0 2^{Kt_2}}{K \ln(2)} - \frac{y_0 2^{Kt_1}}{K \ln(2)}} = \frac{\Delta n_i}{\frac{y_0 (2^{Kt_2} - 2^{Kt_1})}{K \ln(2)}} \quad (2.3)$$

The denominator is the area under the cell count curve from  $t_1$  to  $t_2$  and is sometimes referred to as “cell hours” because of its unit is time, typically hours.

Using cell hours it is possible to calculate the molar quantity taken up per cell per hour, typically as:  $\frac{\text{fmol}}{\text{cell} \times h}$ . However, this makes it hard to compare across cell lines because of variability in cell size. To fix this, simply redefine the problem from integrating the area under the cell count curve to the area under the cell volume curve. The cell volume curve is defined using a volume per cell multiplier ( $V_c$ ):

$$V(t) = y(t)V_c = V_c y_0 2^{tK} \quad (2.4)$$

Assuming cell volume is unchanged throughout the experiment,  $V_c$  is a constant that is not integrated and we get:

$$F_i = \frac{\Delta n_i}{\frac{V_c y_0 (2^{Kt_2} - 2^{Kt_1})}{K \ln(2)}} \quad (2.5)$$

Since  $V_c$  is a volume, we have a denominator with a typical unit of  $\frac{L}{h}$ . We could call this “volume hours”, and dividing a molar quantity onto this we typical get a unit of  $\frac{\text{mM}}{h}$ , which is comparable across cell lines with different sizes.

Sometimes it can be useful to convert the influx of a compound to its accumulated intracellular concentration, also referred to as “total cell concentration”. The accumulated intracellular concentration of a compound can be understood intuitively as the total molar uptake divided by the total increase in cell volume. To convert flux to total cell concentration

for compound  $i$  ( $C_i$ ) observe the following rearrangement of equation 2.5:

$$F_i = K \ln(2) \frac{\Delta n_i}{V_c y_0 (2^{Kt_2} - 2^{Kt_1})} \quad (2.6)$$

The fraction is the total cell concentration for compound  $i$  and thus we have:

$$F_i = K \ln(2) C_i \Rightarrow C_i = \frac{F_i}{K \ln(2)} \quad (2.7)$$

#### *Net asparagine consumption*

Human cells do not have any appreciable asparagine deaminase activity [141] and thus asparagine is a terminal metabolite that does not get converted or used as a substrate in other metabolic reactions. This makes the asparagine fluxes suitable for isotope tracing if we make the explicit assumption that asparagine can be generated from synthesis using aspartate but not recycled back. Figure 2.5a shows the net asparagine fluxes when U-<sup>13</sup>C labelled Asn is added to the media. Each net flux is the sum of fluxes in both directions e.g. U-<sup>13</sup>C Asn is net influxed because it is consumed while unlabelled Asn is net effluxed because it is absent from media at the initial conditions.

Influx and efflux can be measured by media sampling and using the ratio of labelled to unlabelled Asn inside the cell, the remaining fluxes can be solved. Observe that the labelling ratio is defined by the influx ( $J_{\text{in}}$ ), efflux ( $J_{\text{out}}$ ) and synthesis flux ( $J_{\text{syn}}$ ):

$$\frac{\text{U-}^{13}\text{C Asn}}{\text{Asn}} = \frac{J_{\text{in}}}{J_{\text{syn}} - J_{\text{out}}} \quad (2.8)$$

Isolate the synthesis flux:

$$J_{\text{syn}} = \frac{\text{Asn}}{\text{U-}^{13}\text{C Asn}} J_{\text{in}} + J_{\text{out}} \quad (2.9)$$

Introduce flux balance:

$$J_{\text{in}} + J_{\text{syn}} = J_{\text{prot}} + J_{\text{out}} \Rightarrow J_{\text{prot}} = J_{\text{in}} + (J_{\text{syn}} - J_{\text{out}}) \quad (2.10)$$

Isolate the flux of Asn deposition into protein ( $J_{\text{prot}}$ ) and insert  $J_{\text{syn}}$  from equation 2.9:

$$J_{\text{prot}} = J_{\text{in}} + \left( \frac{\text{Asn}}{\text{U-}^{13}\text{C Asn}} J_{\text{in}} + J_{\text{out}} - J_{\text{out}} \right) \quad (2.11)$$

Simplify:

$$J_{\text{prot}} = J_{\text{in}} \left( 1 + \frac{\text{Asn}}{\text{U-}^{13}\text{C Asn}} \right) \quad (2.12)$$

The efflux of asparagine when none is provided in the media, can be inferred by scaling  $J_{\text{out}}$  according to the labelling ratio:

$$\text{Efflux} = J_{\text{out}} \left( 1 + \frac{\text{U-}^{13}\text{C Asn}}{\text{Asn}} \right) \quad (2.13)$$

### *Aspartate consumption fluxes*

For 143B cells, asparagine fluxes (efflux and protein) and total cell concentration of amino acids and pyrimidines were measured. Total cell concentrations of aspartate+asparagine and pyrimidines were converted to flux using equation 2.7. From this, the aspartate flux towards protein was isolated by subtracting the contribution from asparagine. Potential aspartate consumption towards arginine was determined from the media uptake data. The total cell concentration of purines could not be determined due to their sensitivity to hydrolysis (appendix figure B.5). Therefore, purine abundance was estimated to be equal to pyrimidine abundance which is consistent with published measurements using rat liver RNA [92]. *De novo* purine synthesis consumes aspartate in one step towards IMP but also in the conversion of IMP to AMP. It was assumed that AMP and GMP synthesis flux is equal and thus the total aspartate consumption by *de novo* purine synthesis is 1.5 times that of pyrimidine synthesis.

#### 2.4.14 Nitrogen-15 tracing

##### *Salvage fraction of individual components*

The fractional contribution of individual components into their respective aspartate consuming fate was determined in 143B and H1299 cells for the salvageable metabolites asparagine (Asn), uridine (Urd), hypoxanthine (Hpx), adenine (Ade) and guanine (Gua) along with a vehicle treatment (Vec). The salvageable metabolites were spiked-in from a 20x stock solution to achieve a final concentration of: 500  $\mu$ M Asn, 200  $\mu$ M Urd, 100  $\mu$ M Hpx, 100  $\mu$ M Ade or 100  $\mu$ M Gua. The fraction of salvage was determined by stable isotope tracing, performed using both Gln amide-<sup>15</sup>N (Cambridge Isotope Laboratories, NLM-557-PK) and Gln alpha-<sup>15</sup>N (Cambridge Isotope Laboratories, NLM-1016-PK) in separate reactions and added to DMEM without glucose, glutamine, pyruvate and phenol red (Sigma, D5030) supplemented with 10% dialyzed FBS, 1x penicillin-streptomycin and 25 mM glucose (Sigma, G7528). The combination of cell lines, salvageable metabolites and tracers gave 2x6x2=24 conditions which were labelled to steady-state by culturing for four passages with a 1/20 split at each passage. At the end of the last passage each condition was split into four technical replicates and plated on 24 well plates. Upon reaching confluence, polar metabolites were extracted and submitted to LCMS.

The relative contribution of guanine salvage into the GTP pool was determined using the m+0 vs. m+3 GTP isotopologue fractions from the Gln amide-<sup>15</sup>N labelled samples. The relative contribution of both adenine and hypoxanthine salvage into the ATP pool was determined using the m+0 ATP isotopologue fraction from the Gln amide-<sup>15</sup>N labelled samples and the direct contribution from adenine was determined using the m+1 isotopologue fractions of aspartate compared to ATP from the Gln alpha-<sup>15</sup>N labelled samples (see appendix figure B.11).

### *Salvage fraction as a function of concentration*

H1299 and 143B cells were seeded at 5,000 and 10,000 cells/well on a 6 well dish in DMEM containing Gln amide-<sup>15</sup>N as described above. Then added an equimolar mix of hypoxanthine and uridine from a 40x stock to a final concentration of 10, 20, 30, 40, 50, 60  $\mu$ M in each of the 6 wells. Fresh media was then added every four days and upon reaching confluence, polar metabolites were extracted and submitted to LCMS.

### *Aspartate to proliferation curves*

Cell seeding on 6 well plates, starting counts and drug treatment was performed as described for proliferation assays. A titration of rotenone or metformin was added by media change to each plate and used to induce a wide degree of aspartate depletion. Media change was made every 5 days and metabolites were harvested when cells reached near confluence. For each plate, three wells were used for metabolite extraction and three wells were used for cell counts to calculate the total cell volume and the proliferation rate. Proliferation rate as a function of the intracellular aspartate concentration,  $f(c)$ , was fitted by an increasing Hill curve:

$$f(c) = t - \frac{t}{1 + (c/m)^s}$$

Whereas the proliferation rate as a function of the drug concentration was fitted by a decreasing Hill curve:

$$f(c) = \frac{t}{1 + (c/m)^s}$$

With  $t$  being the top of the curve, describing the upper asymptotes of proliferation rate and fixed at the observed proliferation rate with no drug treatment. The curve slope is described by  $s$ , also known as the Hill coefficient, and the midpoint ( $m$ ) describes the intracellular aspartate concentration at half maximum proliferation rate. The curve parameters,  $s$  and  $m$ , were fitted to the data using the Broyden–Fletcher–Goldfarb–Shanno (BFGS) algorithm.

#### 2.4.15 ATF4 reporter measurements

First monoclonal cells lines expressing the RFP-based ATF4 reporter described in Guo et al. [52] were made. Clones of high and low basal expression were selected and typically tested in parallel. Cells were seeded onto 24 well plates at 50,000 cells per well in 1 mL of DMEM without pyruvate, with dialyzed FBS. For GOT DKO cells, 20 mM sodium aspartate was added to the seeding media. At 70-90% confluence, drugs were spiked in as a 10x solution as this was found to yield similar reporter measurements as media change (appendix figure B.20). Final drug concentrations were: vehicle (DMSO), 100 nM rotenone, 1  $\mu$ M antimycin and 10  $\mu$ M FCCP. For experiments with atpenin and/or rotenone, atpenin was added to a final concentration of 5  $\mu$ M and rotenone to 50 nM. For aspartate depletion in GOT DKO cells, wells were washed once with aspartate free media before adding media with the reported aspartate concentration and the metabolite rescue. For all plates, metabolite rescues were spiked in as a 20x solution 1-2 hours before adding drugs or media change. The final concentration of these were: vehicle (water), 100  $\mu$ M asparagine, 30 mM aspartate, 2 mM pyruvate and 1 mM alpha-ketobutyrate. Reporter expression was measured on an Incucyte S3 using the RFP channel with default exposure time and 20x magnification. Using the associated Incucyte software the total RFP signal was extracted and exported. Continuous measurements were taken but only a single measurement between 17-21 hours was reported for better clarity. Measurements were normalized to the no drug, no rescue condition, or in the case of GOT DKO cells, to the 20 mM aspartate, no rescue condition.

#### 2.4.16 tRNA aminoacylation levels

Aminoacylation levels, referred to as “charge”, were measured using the method described in chapter 4. For the antimycin time-series charge, 143B cells were grown to 40% confluence on 6 cm dishes in DMEM without pyruvate, with dialyzed FBS and 200  $\mu$ M uridine. Treatment was initiated by spiking in 10x antimycin to a final concentration of 1  $\mu$ M. Cells were harvested by moving the dish onto ice, quickly aspirating the media and adding 0.5 mL of

Trizol to cover the whole surface. Cells were scraped, moved to a tube on ice and frozen in liquid nitrogen. Sample tubes were stored in a vapor phase liquid nitrogen freezer until further processing. For steady-state charge, 143B and H1299 cells grown on 6 well plates in DMEM, without pyruvate, with dialyzed FBS. For antimycin and oligomycin treatments, 200  $\mu$ M uridine was added to the media. For the atpenin treatment, 1 mM pyruvate was added to the media. At 50% confluence, cells were treated with drugs in replicates for 30 hours before harvesting similarly to the time-series samples. H1299 cells were treated with vehicle (DMSO), rotenone (100 nM), atpenin (5  $\mu$ M), antimycin (5  $\mu$ M) or oligomycin (1  $\mu$ M). 143B cells were treated with vehicle (DMSO), rotenone (50 nM), atpenin (5  $\mu$ M), antimycin (0.5  $\mu$ M) or oligomycin (0.25  $\mu$ M).

#### *2.4.17 Plotting and statistics*

Plots were made using matplotlib and/or Seaborn [162]. Error bars are either bootstrapped 95% confidence intervals or +/- standard deviation.

## Chapter 3

# AN ENGINEERED BIOSENSOR ENABLES DYNAMIC ASPARTATE MEASUREMENTS IN LIVING CELLS

Kristian Davidsen<sup>1,2</sup>, Jonathan S Marvin<sup>3\*</sup>, Abhi Aggarwal<sup>3</sup>, Timothy A Brown<sup>3</sup>,  
Lucas B Sullivan<sup>1\*</sup>

This chapter is based on a manuscript published in eLife [[link](#)]. It is reprinted here in a reformatted version with no substantial changes to the text and figures and thus contains method subsections similar to those in other chapters.

### Abstract

Intracellular levels of the amino acid aspartate are responsive to changes in metabolism in mammalian cells and can correspondingly alter cell function, highlighting the need for robust tools to measure aspartate abundance. However, comprehensive understanding of aspartate metabolism has been limited by the throughput, cost, and static nature of the mass spectrometry based measurements that are typically employed to measure aspartate levels. To address these issues, we have developed a GFP-based sensor of aspartate (jAspSnFR3), where the fluorescence intensity corresponds to aspartate concentration. As a purified protein, the sensor has a 20-fold increase in fluorescence upon aspartate saturation, with dose dependent fluorescence changes covering a physiologically relevant aspartate concentration range and no significant off target binding. Expressed in mammalian cell lines, sensor intensity

---

<sup>1</sup>Human Biology Division, Fred Hutchinson Cancer Center, Seattle, WA, USA

<sup>2</sup>Molecular and cellular biology program, University of Washington, Seattle, WA, USA

<sup>3</sup>Howard Hughes Medical Institute (HHMI), Janelia Research Campus, Ashburn, VA, USA

\*For correspondence: marvinj@janelia.hhmi.org (JSM), lucas@fredhutch.org (LBS)

correlated with aspartate levels measured by mass spectrometry and could resolve temporal changes in intracellular aspartate from genetic, pharmacological, and nutritional manipulations. These data demonstrate the utility of jAspSnFR3 and highlight the opportunities it provides for temporally resolved and high throughput applications of variables that affect aspartate levels.

### **3.1 Introduction**

The primary tool used by metabolism researchers, mass spectrometry (MS) coupled with either gas chromatography (GCMS) or liquid chromatography (LCMS), involves extracting pools of thousands of cells and measuring the liberated metabolites. This approach is powerful but has significant drawbacks; it requires highly specialized equipment, it is expensive, and sample preparation by chemical extractions homogenizes metabolic differences that may occur amongst different cells in complex samples or across subcellular compartments. Metabolite extraction also consumes precious samples that might otherwise be desirable to analyze over time or with additional outputs. Development of genetically encoded protein sensors (biosensors) over the past two decades has provided new opportunities to visualize the release, production, and depletion of important signaling molecules and metabolites with subsecond and subcellular resolution (reviewed in Kostyuk et al. and Koveal et al. [82, 83]). Thus, with the trade-off of only monitoring one metabolite per sensor, biosensors provide a solution to many of the problems inherent to metabolite extraction and MS.

Aspartate is amongst the most concentrated metabolites in cells [113], yet it is one of only two amino acids that is not predominantly acquired from the environment. While the other, glutamate, is made from glutamine by the enzyme glutaminase, no analogous enzyme exists in humans to convert asparagine to aspartate [141]. Instead, aspartate must be synthesized by transamination of the tricarboxylic acid (TCA) cycle metabolite oxaloacetate by the cytosolic enzyme GOT1 or the mitochondrial enzyme GOT2. Notably, aspartate synthesis can occur from multiple metabolic sources *via* complex metabolic reactions occurring in both the cytosol and mitochondria, rendering aspartate levels at the whole cell and subcellular lev-

els dependent on multiple metabolic variables. For example, impairments to mitochondrial respiration can deplete aspartate levels and aspartate restoration can reestablish proliferation in cells with defective mitochondria [140, 13, 18, 54]. Alterations to aspartate levels are associated with modifications to cell function in multiple biological processes, including stem cells [146, 5], immune cells [7], endothelial cells [29], and cancer [59]. In addition, genetic methods to elevate intracellular aspartate can impact biology *in vivo*, increasing tumor growth [141, 48] and improving hematopoietic function [121]. Therefore, our understanding of metabolism in multiple biological systems could be improved with the availability of an aspartate biosensor.

We have previously developed a biosensor for glutamate (iGluSnFR) using the *E.coli* glutamate/aspartate binding domain (GltI) linked to circularly permuted GFP [99], and subsequently optimized it by modulating its affinity, kinetics, color, and total fluorescence change (SF-iGluSnFR and iGluSnFR3) [100, 1]. Since the GltI domain also binds aspartate, albeit at lower affinity than glutamate [67], we reasoned that subtle modifications to the ligand binding site could switch the relative aspartate/glutamate specificity. We achieved this using a small mutagenesis screen on a precursor to iGluSnFR3 (Supplementary file 1), guided by the crystal structure of glutamate-bound GltI. The resulting biosensor, jAspSnFR3, was characterized *in vitro* and in cells with matched LCMS determined aspartate levels, showing that it accurately reports genetic, pharmacological, and nutritional manipulation of intracellular aspartate.

### 3.2 Results

#### 3.2.1 Protein engineering

We observed that the glutamate sensor, iGluSnFR, binds both glutamate and aspartate, with higher affinity for the former [99]. To shift the relative affinities of the two ligands, we evaluated the structure of the binding pocket [67], and sampled all possible amino acid substitutions of residue S72, which interacts with the side-chain carboxylate of bound glu-

tamate (figure 3.1, panel A). By expressing mutant sensors in bacteria and measuring the fluorescence of bacterial lysate in response to aspartate and glutamate, we identified S72A and S72P as having switched specificity from glutamate to aspartate. S72T, identified in a faster version of iGluSnFR [58], also preferentially binds aspartate over glutamate.

As an improved glutamate sensor (iGluSnFR3) was being developed [1], we took a variant from that process and queried the effect of S72A, S72T, and S72P on aspartate/glutamate affinity. In bacterial cell lysate, S72P maintained the expected shift to a preference for aspartate when inserted into a iGluSnFR3 precursor, and had a higher fluorescence fold increase ( $\Delta F/F$ ) than either S72A or S72T (figure 1 - figure supplement C.1, panel A). To further increase specificity of the S72P mutant, we sampled mutations at S27, which also interacts with the carboxylate of bound glutamate. One of those, S27A, had lower affinity for glutamate while mostly maintaining affinity for aspartate (figure 1 - figure supplement C.1, panel A). We then moved forward with this variant, and since it is built from a precursor of iGluSnFR3, named it Janelia-developed Aspartate-Sensing Fluorescent Reporter (jAspSnFR3). Since we expected to be using this sensor in cell culture studies, and potentially *in vivo*, over the course of hours or even days, we added a C-terminal red fluorescence protein, mRuby3, to enable correction for expression. All biochemical characterization is reported with jAspSnFR3-mRuby3. For jAspSnFR3 signal normalization in cells we used a mix of jAspSnFR3-mRuby3 and nuclear localized mRuby2.

Further characterization of the sensor found it is yellow-shifted in excitation and emission compared to typical GFP-based sensors, since its chromophore is formed by the triad of GYG and has the T203Y pi-stacking mutations of the Venus yellow fluorescent protein. This yellow-shift facilitates observation deeper into tissues using 2-photon microscopy, as the sensor has high signal fold change and significant 2-photon cross-section at 1040 nm (figure 1 - figure supplement C.1, panel B). It has a  $K_D$  for aspartate of about 50  $\mu\text{M}$  and binds glutamate and asparagine with  $K_D$  greater than 5 mM (figure 3.1, panel B). The sensor also does not appreciably change its green fluorescence in response to other amino acids (figure 1 - figure supplement C.2, panel A) or to other decoys considered relevant to aspartate

metabolism, including pharmacological treatments (figure 1 - figure supplement C.2, panel B). We performed rapid-mixing stopped-flow fluorescence spectroscopy to determine the aspartate binding kinetics and measured an on-rate of  $0.8 \mu\text{M}^{-1} \text{ sec}^{-1}$  and an off-rate of  $26 \text{ sec}^{-1}$ , resulting in a  $K_D$  of  $33 \mu\text{M}$  in agreement with equilibrium measurements (figure 1 - figure supplement C.3). The off-rate corresponds to a time to equilibrium of 130 msec. when defined using five half-lives [74].

Surprisingly, the mRuby3 fluorescence of affinity-purified jAspSnFR3.mRuby3 responds to some amino acids at high millimolar concentrations, indicating a non-specific effect (figure 1 - figure supplement C.4, panel A). This was determined to be due to an unexpected interaction with the C-terminal histidine tag and could be reproduced with other proteins containing mRuby3 and purified via the same C-terminal histidine tag (figure 1 - figure supplement C.4, panel B and C). Interestingly, a structurally related, non-amino acid compound, GABA, does not elicit a change in red fluorescence; indicating, that only amino acids are interacting with the histidine tag (figure 1 - figure supplement C.4, panel D). Nevertheless, most of our cell culture experiments were performed with nuclear localized mRuby2, which lacks a C-terminal histidine tag, and these measurements correlated with those using the histidine tagged jAspSnFR3-mRuby3 construct (figure 1 - figure supplement C.5, panel D).

A recently described and concurrently developed biosensor for aspartate is reported to be adversely affected by temperatures higher than  $30^\circ\text{C}$ , causing lower maximum  $\Delta F/F$  [60]. Our aspartate sensor appears unaffected by temperature up to  $37^\circ\text{C}$ , with the same maximum  $\Delta F/F$  at  $37^\circ\text{C}$  as compared to  $30^\circ\text{C}$  (figure 1 - figure supplement C.2, panel C). Like all cpGFP-based sensors, it is sensitive to pH but changes in fluorescence due to aspartate far exceed what one might expect from changes in fluorescence due to physiologically attainable changes in intracellular pH (figure 1 - figure supplement C.2, panel D). To determine whether it had the potential to serve as an aspartate biosensor in mammalian cells, we expressed jAspSnFR3 in H1299 cells along with nuclear-RFP. Expression of jAspSnFR3 had no obvious toxic effects and H1299 jAspSnFR3 cells had visible fluorescence in the green channel (figure 3.1, panel C). As it is the primary substrate for aspartate production, glutamine removal is

expected to deplete aspartate levels. Indeed, we found that 24 hours of glutamine withdrawal abolished GFP signal while leaving RFP unchanged. These findings therefore supported the further testing of jAspSnFR3 as a method to quantify aspartate levels over time in live mammalian cells.

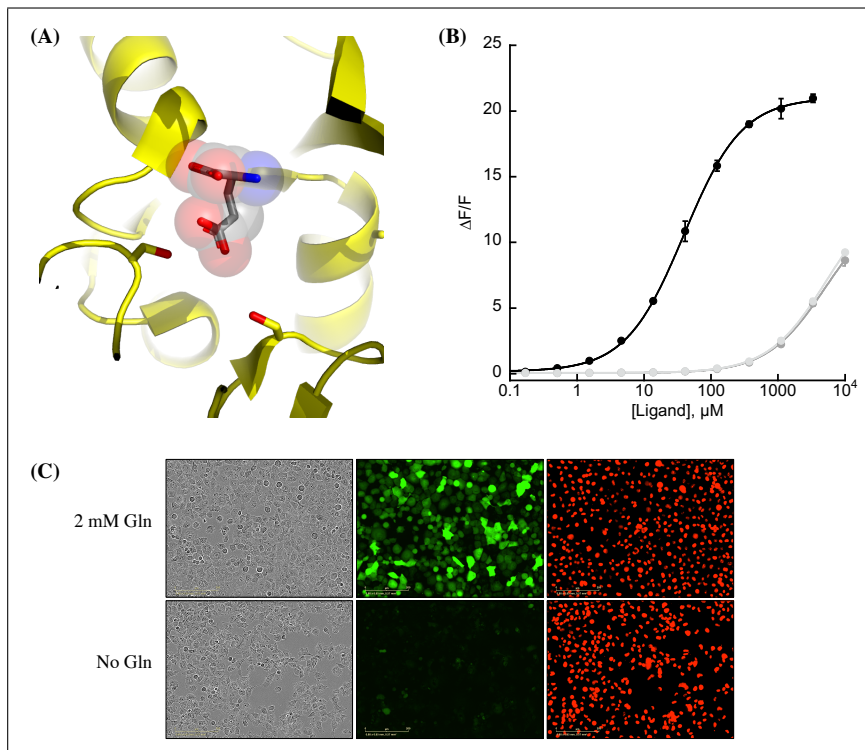


Figure 3.1: Protein engineering and *in vitro* characterization. (A) Structure of the binding pocket of glutamate-bound GltI (2VHA.pdb) with residues S72 (left) and S27 (right) shown as sticks and bound glutamate as sticks inside transparent spheres. (B) Fluorescence response of purified jAspSnFR3-mRuby3 when titrated with aspartate (black) or glutamate or asparagine (grey tones). Ex. 485 nm (20 nm bandpass), Em. 535 nm (20 nm bandpass). Error bars are s.d. of three technical replicates. (C) Live cell imaging in the phase contrast, GFP and RFP channels of H1299 Nuclear-RFP cells expressing jAspSnFR3 after 24 hours with/without glutamine.

### 3.2.2 *jAspSnFR3 reveals the temporal dynamics of aspartate limitation*

Having shown that jAspSnFR3-mRuby3 protein can measure the concentration of aspartate *in vitro*, we wanted to test the usefulness of the sensor in cells. To that end, we generated stable cell lines with constitutive expression of jAspSnFR3-mRuby3 or jAspSnFR3 and nuclear localized RFP, and generated single cell clones from each to yield cell lines with uniform expression. In each case, we then normalized GFP sensor signal to RFP signal to control for expression differences within and across cell lines. We also noted that normalization with nuclear RFP and RFP fusion were highly correlated, enabling jAspSnFR3 sensor applications where nuclear RFP labeling is desirable e.g. for counting cells at multiple timepoints using live cell imaging (figure 2 - figure supplement C.5, panel D). An important motivation for using a biosensor for tracking aspartate changes is to enable temporal measurements on the same subset of live cells, therefore we used an Incucyte S3 which performs live cell imaging under native cell line growth conditions.

Cellular aspartate levels depend on the availability of metabolic precursors and the activity of several metabolic processes. One such process is the generation of a sufficiently large intracellular NAD<sup>+</sup>/NADH ratio to drive aspartate precursor synthesis, a process normally maintained through mitochondrial respiration or, in its absence, by treatment with exogenous electron acceptors like pyruvate (figure 3.2, panel A). Genetic alterations and pharmacological treatments that disrupt mitochondrial respiration can decrease NAD<sup>+</sup>/NADH and aspartate levels, both of which can be partially restored by supplementation with pyruvate [140, 13]. We thus tested the ability of jAspSnFR3 to quantify depletion of intracellular aspartate abundance upon treatment with the mitochondrial complex I inhibitor rotenone and the partial rescue of aspartate by supplementing cells with pyruvate. Titrating rotenone in H1299 cells, we observed a dose dependent decrease in sensor fluorescence with increased rotenone, corresponding to the expected decrease in aspartate synthesis capacity, and a partial restoration of fluorescence in cells co-treated with pyruvate (figure 3.2, panel B). This observation was extended to different cell lines with different rotenone sensitivities, corrobor-

rating the observation of decreased sensor fluorescence upon rotenone treatment and rescue by pyruvate supplementation (figure 2 - figure supplement C.5, panel A, B and E). Furthermore, we tested and confirmed the ability of pyruvate to rescue aspartate levels after an initial depletion phase with rotenone, thus confirming that the sensor is also able to measure the reverse kinetics of aspartate restoration (figure 2 - figure supplement C.5, panel C).

We next evaluated the ability of the sensor to measure changes in aspartate without requiring treatment with a mitochondrial inhibitor. To this aim, we used CRISPR/Cas9 to generate an H1299 cell line with a double knockout (DKO) of the genes glutamic oxaloacetic transaminases 1 and 2 (GOT1/2 DKO), which renders cells unable to synthesize aspartate and therefore dependent on aspartate uptake from the media [47]. Using these H1299 GOT1/2 DKO cells, we titrated media aspartate and observed that sensor fluorescence decreased upon aspartate withdrawal, approaching a steady-state after approximately 11 hours, that corresponded to the aspartate availability in the media (figure 3.2, panel C). We note that 10 mM media aspartate, a higher concentration than any other amino acid in media, is still unable to rescue sensor signal significantly above aspartate depleted media. This confirm previous observations that aspartate has poor cell permeability and often requires concentrations of 20 mM or more to robustly contribute to intracellular aspartate pools [141].

Finally, we evaluated the ability of the sensor to measure rapid decreases/increases in aspartate levels. In most cancer cell lines, intracellular aspartate is derived primarily from glutamine oxidation, thus making glutamine depletion and restoration an entry point for affecting aspartate levels. Glutamine withdrawal from H1299 cells showed a rapid depletion in sensor fluorescence with a low level steady-state reached after approximately 12-16 h (figure 3.2, panel E). In the same cells, glutamine repletion, after different times of glutamine depletion, caused an initial rapid increase in sensor fluorescence followed by a slower adjustment phase before reaching baseline. Particularly interesting is the sensor readings for cells repleted with glutamine 6 h after withdrawal, showing a rapid increase followed by a decrease, before a slow increase to baseline. We concurrently measured the cell count over

time by counting RFP fluorescent nuclei and the cell confluence (figure 2 - figure supplement C.6, panel A and B). These data confirm that cells remain viable 12 h after glutamine withdrawal and that proliferation rates are first fully recovered when aspartate levels reach baseline. Interestingly, the proliferation rate undergoes a similar multi-phase recovery as the aspartate sensor signal. We suspect these phases to be driven by low aspartate causing S-phase arrest during glutamine deprivation [115], and although more evidence is necessary to prove this suspicion, our data show that an aspartate sensor is an excellent tool towards this end.

#### *Metformin has slower inhibitor kinetics compared to rotenone*

Metformin is a commonly used diabetes treatment that has been shown to act as a mitochondrial complex I inhibitor [112, 38, 4, 164] and can decrease intracellular aspartate levels in a dose responsive way [51]. Whereas rotenone is a lipophilic molecule that can cross the cell membrane and act rapidly, metformin is hydrophilic and poorly permeable to most cells, resulting in comparatively delayed kinetics for metformin to decrease mitochondrial respiration in intact cells. As rotenone and metformin are often used interchangeably as complex I inhibitors, we wondered whether they have an equivalent temporal effect on aspartate or if the delayed effects of metformin on mitochondrial inhibition would similarly delay its effects on aspartate levels. To test this, we treated cells with two doses each of rotenone and metformin with roughly equivalent aspartate lowering effects and followed the sensor signal over time (figure 3.2, panel F). We observed that the aspartate depleting effects of metformin acted slower than rotenone, with 30 nM rotenone reaching steady-state after ~20 hours and 2 mM metformin reaching a similar sensor response after almost 40 hours. These data therefore provide orthogonal confirmation of the differential kinetics of these drugs on cell metabolism and highlight the temporal opportunities enabled by measuring aspartate levels by jAspSnFR3.

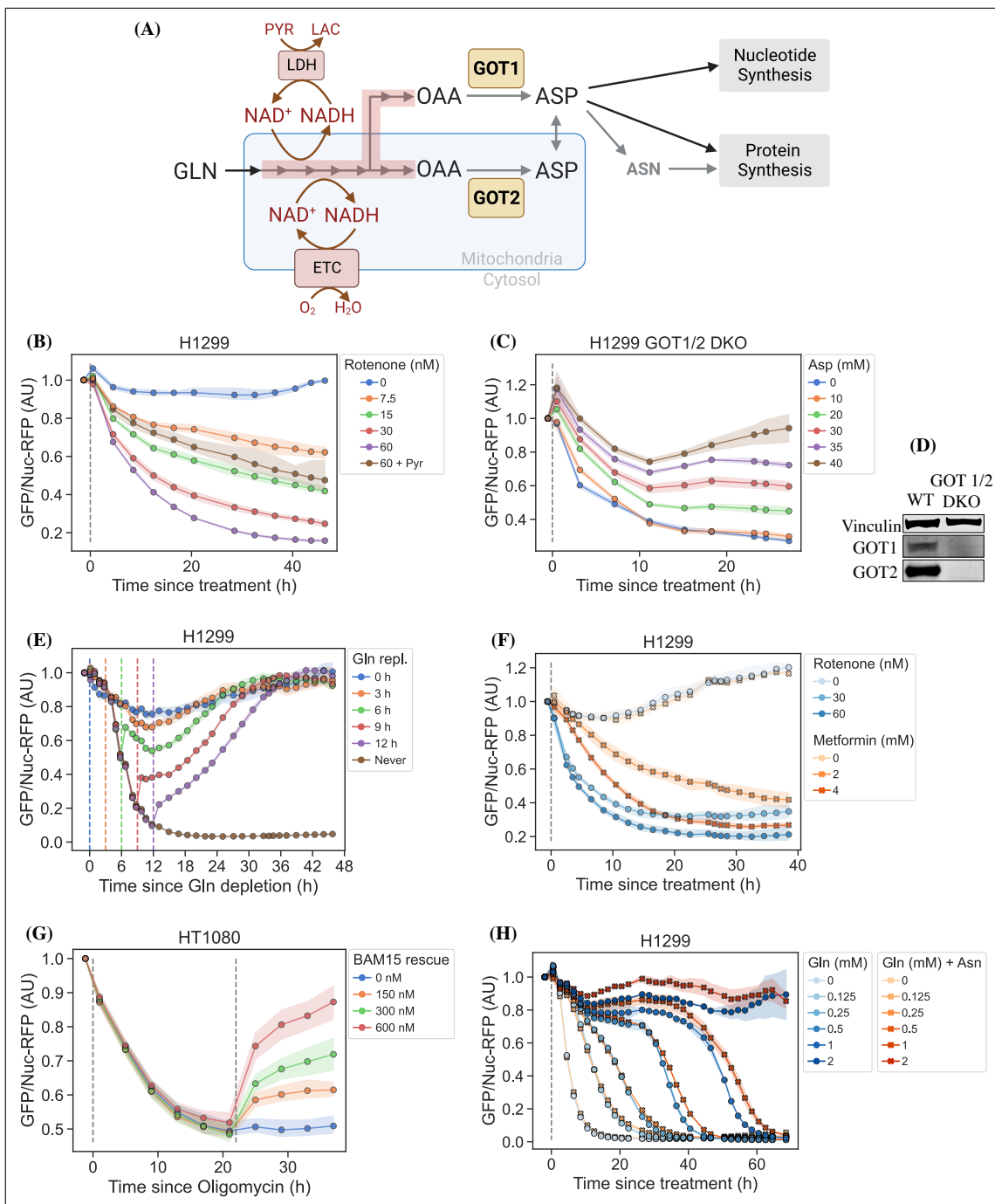


Figure 3.2: jAspSnFR3 resolves temporal aspartate changes in live cells. (A) Overview of aspartate metabolism, highlighting how glutamine depletion, mitochondrial inhibition, GOT1/2 knockout and pyruvate/asparagine supplementation can impact aspartate levels. (B) H1299 cells treated with a rotenone titration and rescued by co-treatment with pyruvate. (C) H1299 GOT1/2 double knockout cells grown in media with 40 mM aspartate, washed thrice in media without aspartate and then changed into media with a titration of aspartate. (D) Western blot verification of H1299 GOT1/2 double knockout. (E) H1299 cells changed into media without glutamine and then glutamine repleted (repl.) at the different timepoints. (F) H1299 cells treated with either rotenone or metformin to compare inhibitor kinetics. (G) HT1080 cells treated with oligomycin A and after 22 h rescued with a titration of mitochondrial uncoupler BAM15. (H) H1299 cells changed into media with a titration of glutamine with or without 1 mM asparagine. For (B), (C), (E), (F), (G) and (H) sensor signal over time shown as RFP normalized jAspSnFR3 signal following various perturbations of live cells. All experiments shown are normalized to a pre-treatment scan and then treated with the specified drug or amino acid. Grey dashed lines indicate the time of treatment. Colored dashed lines indicate the time of treatment for multiple treatments in the same plot. Markers indicate the average using available well replicates and are superimposed on a bootstrapped 95% confidence interval colored using the same color code as the markers. GLN, glutamine. ETC, electron transport chain. LDH, lactate dehydrogenase. OAA, oxaloacetic acid. ASP, aspartate. ASN, asparagine. AU, arbitrary unit.

*Oligomycin induced decrease in aspartate can be rescued by uncoupling the mitochondrial membrane potential*

Oligomycin A binds to and inhibits the proton coupled rotation of ATP synthase [143]. This inhibition leads to a slowing of the electron transfer in the mitochondrial electron transport chain by hyperpolarizing the membrane potential [15] and it has previously been shown that the cellular effects of oligomycin can be rescued by partial uncoupling of the mitochondrial membrane potential [140, 145]. We used our aspartate sensor to show that oligomycin induces a decrease in aspartate and that the mitochondrial membrane potential specific uncoupler BAM15 [79] can partially restore this aspartate level (figure 3.2, panel G), thus confirming previous observations and illustrating the versatility of the our sensor.

### *Asparagine salvage diverts glutamine consumption*

It has previously been reported that asparagine, a product of aspartate metabolism, becomes essential upon glutamine starvation [116, 173]. We hypothesize that asparagine becomes essential in these conditions because glutamine starvation decreases synthesis of aspartate, slowing asparagine production, and because asparagine supplementation spares aspartate consumption, allowing it to be redirected into other essential fates. However, it has been difficult to measure metabolic changes during glutamine limitation because continuous glutamine consumption during the course of the experiment will result in progressive glutamine depletion and further developing metabolic effects. One solution to this problem is to measure the temporal changes in aspartate levels over the course of glutamine starvation and, indeed, we found that full glutamine depletion has a rapid and drastic effect on sensor signal (figure 3.2, panels E and H and figure 2 - figure supplement C.6, panel C). Interestingly, aspartate signal did not robustly correlate with the concentration of glutamine in the media in the short term, but instead we found that higher amounts of glutamine in the media delayed the time until aspartate depletion, presumably corresponding to the time at which glutamine is fully depleted and unable to support further aspartate synthesis. Furthermore, we found that adding 1 mM asparagine delayed the decrease in sensor signal, suggesting that when asparagine can be salvaged from the media it diverts glutamine consumption that would otherwise be purposed for asparagine synthesis via aspartate consumption. We note that, as this data is produced in real-time, the method can be used to dynamically find the optimal sampling times to measure and compare intracellular levels of other metabolites relevant to glutamine starvation using mass spectrometry.

#### *3.2.3 jAspSnFR3 signal correlates with intracellular aspartate concentration*

It is an important requirement for an aspartate sensor that it reflects the intracellular concentration of aspartate over a biologically relevant range for several cell lines. Reference points for the intracellular aspartate concentration can be generated using metabolite ex-

traction and LCMS, but it is important to note that this technique reports the total amount of aspartate summed across all compartments, which can differ in their aspartate concentration [23]. The LCMS derived concentration also does not reflect protein crowding, aspartate binding to enzymes, or other factors that would affect the free aspartate concentration. Nevertheless, LCMS is the standard approach in studying metabolism and has previously been used to correlate aspartate levels with cell proliferation [51, 54]. Thus, we titrated mitochondrial inhibitors of complex I (rotenone and metformin) and complex III (antimycin A), with or without pyruvate rescue, in three different cell lines and waited 24 hours until aspartate had reached near steady-state levels before conducting a final measurement of sensor fluorescence, followed by immediate metabolite extraction and quantitative LCMS measurements of aspartate levels using isotope dilution. We then compared sensor signals to LCMS derived aspartate concentrations and fitted a Hill curve to infer the intracellular aspartate concentrations at half-maximum sensor signal (figure 3.3). For all three cell lines, we observe a monotonically increasing relationship between sensor signal and intracellular aspartate concentration, covering around two orders of magnitude. We also observe no relationship between sensor signal and intracellular glutamate levels (figure 3 - figure supplement C.7). These observations validate the utility of our sensor in a biologically relevant range of aspartate concentrations without interference from glutamate.

Interestingly, the intracellular aspartate concentrations at half-maximum sensor fluorescence is more than 17 fold higher than the aspartate  $K_D$  determined by *in vitro* characterization of the sensor. While the numbers inferred for intracellular aspartate are only point estimates, it is highly unlikely that they are inaccurate to this degree. We speculate that the apparent cytosolic aspartate concentration is likely lower than the total aspartate concentration summed across all compartments. This suggests that binding of aspartate by jAspSnFR3 is in competition with other proteins and highlights that another advantage of using a biosensor is that measurements are made relative to their native environment.

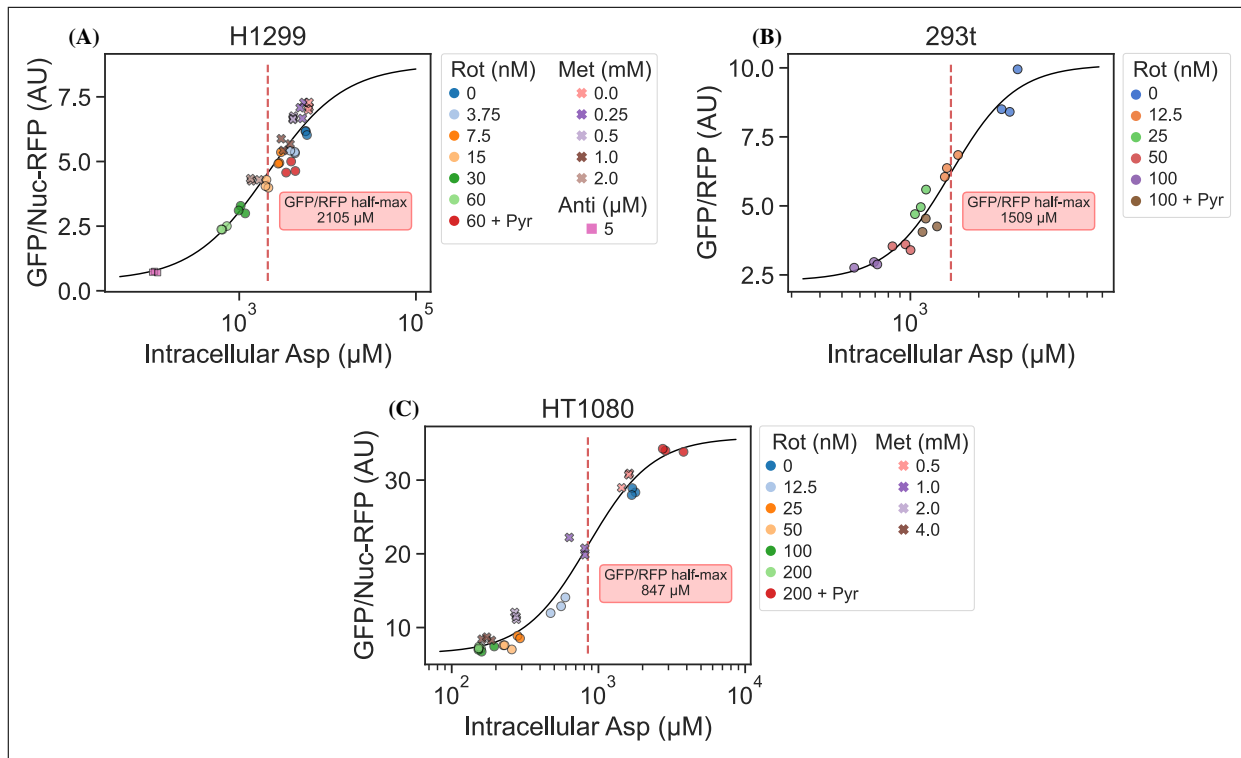


Figure 3.3: jAspSnFR3 signal predicts LCMS measured intracellular aspartate concentration. A Hill equation with top and bottom asymptotes, midpoint and slope as free variables is fitted to the datapoints and shown by the black line. The intracellular aspartate concentration at the inferred half maximum of RFP normalized jAspSnFR3 signal is reported in the red inserts. (A) Rotenone, metformin and antimycin A titrations in H1299 cells. (B) Rotenone titration in HEK293t cells. (C) Rotenone and metformin titrations in HT1080 cells. Markers indicate a single well from which both LCMS and jAspSnFR3 data was collected. Replicate wells have identical color and marker shape. AU, arbitrary unit.

### 3.3 Discussion

A biosensor for aspartate is an important step towards improved understanding of aspartate metabolism. We have shown that our jAspSnFR3 sensor can resolve temporal changes in intracellular aspartate to answer questions that would be impractical using LCMS. In most studies involving aspartate metabolism, metabolite extraction is performed 6-16 hours after treatment with the implicit assumption that this is enough time to reach metabolic steady-

state. Using our sensor, we have shown that the time to reach steady-state can be much longer and depends on the treatment. Future studies seeking to understand the effects of treatments affecting aspartate levels can therefore use real-time measurements using jAspSnFR3 to determine when cells have reached steady-state and then perform metabolite extraction for LCMS.

Recently, a concurrently developed aspartate sensor based on SF-iGluSnFR was reported by another group [60]. That aspartate sensor started with the S72A mutation, but then included 6 additional mutations identified by a combination of targeted screening and deep mutational scanning. Our design differs from the one by Hellweg et al. [60] by 25 mutations (Supplementary file 1). Notably, we achieved aspartate selectivity by generating only two mutations in the binding pocket of its precursor, and so the majority of these amino acid differences derive from us building off the next generation precursor for iGluSnFR3, which has increased  $\Delta F/F$  compared to iGluSnFR. Indeed, the sensor described here appears to have a larger signal change both *in vitro* and in live cells, although head-to-head comparisons have not been performed. Importantly, while the sensor from Hellweg et al. [60] is adversely affected by temperature at 37°C, our sensor is not, allowing us to perform cell culture experiments at standard incubation conditions. Another difference is that our jAsp-SnFR3 sensor has a higher affinity for all three relevant ligands (aspartate, asparagine, and glutamate); however, we found no discernible effect of treatment with 1 mM asparagine on sensor signal in cell culture experiments and found no correlation between intracellular glutamate concentration and sensor fluorescence across treatment conditions (figure 3 - figure supplement C.7). Collectively, we conclude that the jAspSnFR3 aspartate sensor reported here has biochemical features that makes it ideal for measuring intracellular aspartate levels in live cells.

In summary, we report a novel fluorescence based biosensor that enables dynamic measurements of aspartate. This tool is free of significant interference from relevant metabolites in physiological intracellular systems and can resolve changes in aspartate from diverse treatment conditions in live cells over time. This approach to measuring aspartate will also have

advantages compared to LCMS based metabolomics, including enabling high throughput experiments to identify variables that affect aspartate levels, such as testing the effects of a drug library on cells in multiwell plates or using FACS based selection during genetic screens. Another potential use for this sensor would be to dissect compartmentalized metabolism, with mitochondria being a critical target, although incorporating the influence of pH on sensor fluorescence will be an important consideration in this context. Altogether, adoption of jAsp-SnFR3 to measure aspartate levels will therefore provide novel opportunities to understand this critical node of cell metabolism.

### **3.4 Methods and Materials**

#### *3.4.1 Sensor engineering and screening*

The starting template for jAspSnFR3 was a variant along the path of making iGluSnFR3 (sequence information in Supplementary file 1). Site saturation mutagenesis at positions S72 and S27 was achieved by the uracil template method [86]. Mutant libraries (maximum theoretical diversity of 20 each) were transformed into T7 express cells. Individual colonies were picked into a 96-well plate containing auto-induction media [139] and shaken at 30°C for 18-24 hours, then harvested by centrifugation. Cell pellets were resuspended in PBS and repelleted by centrifugation 5 times over, then frozen as pellets overnight. The frozen 96-well plate was thawed by addition of room temperature PBS, agitated by vortexing to resuspend and lyse cells, and then pelleted again. 100  $\mu$ L clarified lysate was added to each of two black 96-well plates and its fluorescence was measured. Aspartate or glutamate was added (final concentration 100  $\mu$ M) and fluorescence was measured again. Wells that had a higher  $\Delta F/F$  for aspartate than glutamate were isolated, titrated with aspartate and glutamate, and sequenced. After confirming that S72P was the most selective variant for aspartate from a library of S72X, a library of S27X was made in the background of S72P. The selection process was repeated, and S72P+S27A was identified as the "best" aspartate sensor and named jAspSnFR3. mRuby3 was subsequently cloned at the C-terminus and this construct

was named jAspSnFR3-mRuby3.

### *3.4.2 Protein expression and purification*

For large scale protein expression and purification, jAspSnFR3-mRuby3 was transformed into T7 express cells and a single colony was grown in 300 mL auto-induction media [139] at 30°C for ~18 hours. Cells were pelleted by centrifugation at 6000g, resuspended in PBS and 1 M NaCl and frozen. The resuspended cell pellet was thawed, sonicated on ice (5 sec on, 5 sec off, 10 min), and centrifuged at 6000g to remove cellular debris. The lysate was further clarified by centrifugation at 35,000g for 1 hour, and then purified by IMAC on a HisTrap FF column, with a 2 mL/min flow rate and elution from 0 to 200 mM imidazole over 120 mL. Untagged mRuby2 and mRuby3 were partially purified by DEAE anion exchange. Fluorescent fractions were pooled, concentrated by ultrafiltration, and dialyzed in PBS to remove endogenously bound ligands. Protein concentration was determined by alkaline denaturation, and measurement at A447 (Ext. Coeff. 44,000 M-1 cm-1).

### *3.4.3 Sensor biochemical characterization*

*In vitro* fluorescence measurements were performed on a Tecan Spark plate reading fluorimeter at ~28°C, with the exception of the controlled temperature measurement, in which a BioTek Cytation 5 was used. Concentrated jAspSnFR3-mRuby3 protein was diluted to 0.2 μM in PBS for all measurements. Decoy amino acids and pharmacologues were purchased from Sigma-Aldrich and solvated as 100 mM stocks in PBS, with the exception of rotenone, which was resuspended in DMSO. Titrations were performed by making serial dilutions (1:2) of the stock compound into PBS, and adding 10 μL of that to 100 μL of 0.2 μM protein solution. Fluorescence was measured before addition of compound, and ΔF/F was calculated as (F(treatment)-F(initial))/F(initial).

Two-photon cross sections were collected for 1 μM solutions of protein in PBS with or without 10 mM aspartate, excited by pulses from a mode-locked Ti:Sapphire laser (Chameleon

Ultra, Coherent, 80 MHz, 140 fs pulse width, 1 mW power at the focus). Emission was detected by an avalanche photodiode (PDM Series, Micro Photon Devices) with a 550 nm filter (88 nm bandpass).

Stopped-flow kinetics of binding were determined by mixing equal volumes of 0.2  $\mu\text{M}$  jAspSnFR3 protein (in PBS, pH 7.4) with varying concentrations of aspartate in an Applied Photophysics SX20 stopped flow fluorimeter with 490 nm LED excitation and 515 nm long pass filter at room temperature (22°C). The increase in fluorescence upon mixing was observed with 1000 data points over the course of 1 sec (1 msec per data point) and equilibrium was reached within 100 msec. Each mixing was repeated five times and averaged. Standard deviations are excluded from the plots as the error bars are nearly the same size as the data markers. The first 3 observations were discarded to remove mixing artefacts and account for the dead time of the instrument. Data were plotted and time courses were fit to a single rising exponential ( $y - \text{intercept} + \text{total rise} * (1 - \exp(-k_{obs} * t))$ ) using Kaleidagraph (version 5.01). To determine the kinetic rates,  $k_{obs}$  was plotted as a function of aspartate concentration and the linear portion of that graph was fitted. The slope, corresponding to the on-rate  $k_1$ , was found to be 0.8  $\mu\text{M}^{-1} \text{ sec}^{-1}$  and the y-intercept, corresponding to the off-rate  $k_{-1}$ , was found to be 26  $\text{sec}^{-1}$ , resulting in a  $K_D$  of 33  $\mu\text{M}$ .

#### 3.4.4 Cell culture

Cell lines were acquired from ATCC (HEK293T, H1299, HT1080) and tested to be free from mycoplasma (MycoProbe, R&D Systems). Cells were maintained in Dulbecco's Modified Eagle's Medium (DMEM) (Gibco, 50-003-PB) supplemented with 3.7 g/L sodium bicarbonate (Sigma-Aldrich, S6297), 10% fetal bovine serum (FBS) (Gibco, 26140079) and 1% penicillin-streptomycin solution (Sigma-Aldrich, P4333). Cells were incubated in a humidified incubator at 37°C with 5% CO<sub>2</sub>.

### 3.4.5 Generation of nuclear RFP cell lines

Nuclear RFP cell lines were generated using 1e5 transducing units of EF1A-nuclear RFP lentivirus (Cellomics Technology, PLV-10205-50) by spinfection. Cells were seeded at 50% confluence in 6 well dishes, lentivirus was added to fresh media with 8  $\mu\text{g}/\mu\text{L}$  polybrene, then added to cells and followed by centrifugation (900g, 90 mins, 30°C). Two days after infection, cells were sorted for high RFP expression using fluorescence-activated cell sorting (FACS). High RFP cells were then expanded and single-cell cloned by limiting dilution, plating 0.5 cells/well on a 96 well plate. Plates were then screened for RFP expression and localization using Incucyte S3 (Sartorius) and a suitable clone chosen, expanded, and used for all subsequent experiments.

### 3.4.6 Lentiviral production and stable cell line generation

jAspSnFR3 and jAspSnFR3-mRuby3 were first cloned into entry vector pENTR1A (Fisher, A10462) using NEBuilder HiFi DNA Assembly Cloning Kit (New England BioLabs, E2621). These donor constructs were then used to transfer their insert into destination vectors: pLX304-CMV-Blast (Addgene, 25890), pLenti-CMV-Hygro (w117-1) (Addgene, 17454 a gift from Eric Campeau & Paul Kaufman), or pLX304-CAG-Blast using LR Clonase II (Fisher, 11791100). pLX304-CAG-Blast was generated in house by swapping the CMV promoter region of pLX304-CMV-Blast with a CAG promoter provided on synthetic DNA (Integrated DNA Technologies). Each plasmid sequence was verified by whole plasmid sequencing (Plasmidsaurus). Lentivirus was generated by co-transfection of HEK293T cells with destination vector plasmid DNA and the packaging plasmids pMDLg/pRRE (Addgene, 12251), pRSV-Rev, (Addgene, 12253) and pMD2.G (Addgene, 12259) using FuGENE transfection reagent (Fisher, PRE2693) in DMEM (Fisher, MT10017CV) without FBS or penicillin-streptomycin. The supernatant containing lentiviral particles was filtered through a 0.45  $\mu\text{M}$  membrane (Fisher, 9720514) and was supplemented with 8  $\mu\text{g}/\mu\text{L}$  polybrene (Sigma, TR-1003-G) prior to infection. For infection, cells were seeded at 50% confluence in 6 well dishes and cen-

trifuged with lentivirus (900g, 90 mins, 30°C). After 24 hours the media was replaced with fresh media and after 48 hours cells were treated with either 1 µg/mL blasticidin (Fisher, R21001) or 150 µg/mL hygromycin (Sigma-Aldrich, H7772-1G) and maintained in selection media until all uninfected control cells died. After selection, cells were expanded and single-cell cloned by limiting dilution, plating 0.5 cells/well using 2-3 96 well plates. These clones were incubated until 10-30% confluence and screened for high GFP and RFP signal using Incucyte S3 (Sartorius). The highest expressing monoclonal cells were selected and further expanded on 6 well plates and again screened for fluorescence using the Incucyte. From this a single clone was chosen, expanded and used for all subsequent experiments. Different cell lines received different vector-sensor combinations: HEK293T cells were infected with pLX304-CAG-jAspSnFR3-mRuby3 (blasticidin), HT1080 with pLenti-jAspSnFR3-mRuby3 (hygromycin) and HT1080, H1299 and H1299 GOT1/2 DKO cells expressing nuclear RFP were infected with pLenti-jAspSnFR3 (hygromycin).

#### *3.4.7 Generation of GOT1/2 double knockout (DKO) cells*

Protocol and guide RNA generation was identical to that described in Hart et al. [54]. Briefly, three chemically synthesized 2'-O-methyl 3'phosphorothioate-modified single guide RNA (sgRNA) sequences targeting GOT1 and GOT2 were purchased (Synthego; table 3.1). A pool of all six sgRNAs for GOT1 and GOT2 were resuspended in nuclease-free water, combined with SF buffer (Lonza, V4XC-2032), and sNLS-spCas9 (Aldevron, 9212). 200,000 H1299 cells were resuspended in the resulting solution containing ribonucleoprotein complexes (RNPs) and electroporated using a 4D-Nucleofector (Amaxa, Lonza). Nucleofected cells were then expanded and single-cell cloned by limiting dilution by plating 0.5 cells/well in a 96 well plate. Gene knockout was confirmed using western blots.

#### *3.4.8 Intracellular jAspSnFR3 measurements*

Experiments were conducted in DMEM without pyruvate (Corning 50-013-PB) supplemented with 3.7 g/L sodium bicarbonate 10% dialyzed fetal bovine serum (FBS) (Sigma-

Table 3.1: CRISPR guides.

Gene	sgRNA sequence (5'-3')
GOT1	CAGUCAUCCGUGCGAUAUGC
	GCACGGAUGACUGCCAUCCC
	CGAUCUUCUCCAUCUGGGAA
GOT2	UUUCUCAUUUCAGCUCCUGG
	CGGACGCUAGGCAGAACGUA
	UCCUUCCACUGUUCCGGACG

Aldrich, F0392) and 1% penicillin-streptomycin solution. To start an experiment, cells were trypsinized (Corning, 25051CI), resuspended in media, counted using a coulter counter (Beckman Coulter, Multisizer 4) and seeded onto 24-well dishes (Nunc, 142475) with an initial seeding density of 50,000, 70,000, 70,000 or 150,000 cells/well for H1299, H1299 GOT1/2 DKO, HT1080 and HEK293T, respectively. After 24h (H1299, HT1080, HEK293T) or 48h (H1299 GOT1/2 DKO) incubation, treatment was added and plates moved into an Incucyte S3 (Sartorius) live cell imaging platform inside a humidified incubator at 37°C with 5% CO<sub>2</sub>. Rotenone (Sigma-Aldrich, R8875), metformin (Sigma-Aldrich, D150959), antimycin A (Sigma-Aldrich, A8674), oligomycin A (Sigma-Aldrich, 495455) and BAM15 (Cayman Chemical, 17811) treatments were spiked-in as 20x solutions in water and the 2 mM pyruvate (Sigma-Aldrich, P8574) was added as 500x stock in water. For treatments with varying media aspartate (Sigma-Aldrich, A7219) or glutamine (Sigma-Aldrich, G5792), wells were washed thrice and filled with media deplete of the given amino acid, then it was added as a spike-in at the specified concentration from a 20x solutions in water. For plates receiving asparagine (Sigma-Aldrich, A7094), this was added to 1 mM from a 20x solution in water, with vehicle wells receiving water. Live cell imaging was performed on the Incucyte S3 using the GFP and RFP channels with default exposure times. Images were processed using the associated Incucyte software to subtract background, define areas of cell confluence and GFP/RFP signal and extract the sum of the fluorescence signal in these areas. The data for the GFP signal, RFP signal, GFP/RFP ratio and confluence for each well at each timepoint

was exported and used for further data processing using Python code. The jAspSnFR3 signal (GFP channel) was normalized to an RFP signal, either as a stably expressed nuclear localized RFP (Nuc-RFP) or mRuby3 C-term fusion to jAspSnFR3. For some experiments the Nuc-RFP was used to estimate cell counts per well by counting the number of nuclear foci in each field of view when scanning in the RFP channel. Cell confluence was determined with the phase contrast scans using the associated Incucyte software. For some experiments a pre-treatment scan was made shortly prior to treatment to normalize the data to this point. For temporal measurements without a pre-treatment scan, the first scan was made 30 min after treatment with subsequent scans indicated on relevant plots. For comparisons of near steady-state measurements of GFP/RFP versus mass spectrometry based metabolite measurements, a single scan was made 24 h after treatment, the plate was then quickly moved to ice and metabolite extraction performed (see below). Another plate was processed in parallel for cell volume determination using a coulter counter and averaging across three replicate wells. The normalized jAspSnFR3 signal as a function of intracellular aspartate concentration,  $f(c)$ , was fitted by a baseline shifted Hill curve:

$$f(c) = t + \frac{b - t}{1 + (c/m)^s}$$

With  $t$ ,  $b$  being the top and bottom of the curve, respectively, describing the upper and lower asymptotes of normalized jAspSnFR3 signal. The curve slope is described by  $s$ , also known as Hill coefficient, and the midpoint ( $m$ ) describes the intracellular aspartate concentration at half maximum jAspSnFR3 signal. The curve parameters were fitted to the data using the Broyden–Fletcher–Goldfarb–Shanno (BFGS) algorithm with an upper bound constraint on the top of the curve of 1.2 times the maximum observed normalized jAspSnFR3 signal in any of the conditions on the same plot. Note that this curve is not intended to represent a mechanistic model of the binding kinetics, rather the purpose is to infer a reasonable estimate of the intracellular aspartate concentration at half maximum jAspSnFR3 signal.

### 3.4.9 Metabolite extraction

For polar metabolite extraction, a plate was move to ice and the media was thoroughly aspirated. For H1299 and HT1080 cells, wells were washed once with cold saline (Fisher, 23293184). For HEK293T cells, washing was omitted due to weak cell adherence. Then, 1 mL 80% HPLC grade methanol in HPLC grade water was added, cells were scraped with the back of a P1000 pipet tip and transferred to Eppendorf tubes. Tubes were centrifuged (17,000g, 15 mins, 4°C) and 800  $\mu$ L of the supernatant containing polar metabolites was transferred to a new centrifuge tube and placed in a centrivap until dry.

### 3.4.10 Intracellular amino acid concentration measurements by isotope dilution

Dried samples were reconstituted with 40  $\mu$ L 80% HPLC grade methanol containing 5  $\mu$ M U-13C, U-15N labelled canonical amino acid mix (Cambridge Isotope Laboratories, MSK-CAA-1) and transferred to vials for measurement by LCMS. The peak area for each amino acid was divided by its labelled standard to derive the response ratio. The response ratio was then mapped to a calibration curve to infer the amino acid concentration and finally the intracellular concentration was calculated by correcting for each step introducing a dilution, including the use of the total cell volume. To make the calibration curves a non-labelled amino acid mixture was made from an analytical amino acid standard without glutamine and asparagine (Sigma-Aldrich, A9906-1ML) and added glutamine (Sigma-Aldrich, 76523-100MG) and asparagine (Sigma-Aldrich, 51363-100MG) to match the concentration of the other amino acids. Using this mix, three replicates of a 12 point 2-fold dilution series was made with a max concentration of 500  $\mu$ M and a volume per dilution of 40  $\mu$ L. These were placed in a centrivap until dry and reconstituted with 40  $\mu$ L 80% HPLC grade methanol containing 5  $\mu$ M U-13C, U-15N labelled canonical amino acid mix (Cambridge Isotope Laboratories, MSK-CAA-1) and transferred to vials for measurement by LCMS. The peak area for each amino acid was divided by its labelled standard to derive the response ratio, then the best fitting calibration curves for each amino acid were chosen among either linear, power

or a second-degree polynomial. Each calibration curve was manually inspected for proper fit and measurements below or above the concentration range of the dilution series were discarded.

#### *3.4.11 Liquid Chromatography-Mass Spectrometry (LCMS)*

Metabolite quantitation was performed using a Q Exactive HF-X Hybrid Quadrupole-Orbitrap Mass Spectrometer equipped with an Ion Max API source and H-ESI II probe, coupled to a Vanquish Flex Binary UHPLC system (Thermo Scientific). Mass calibrations were completed at a minimum of every 5 days in both the positive and negative polarity modes using LTQ Velos ESI Calibration Solution (Pierce). Polar Samples were chromatographically separated by injecting a sample volume of 1  $\mu$ L into a SeQuant ZIC-pHILIC Polymeric column (2.1 x 150 mm 5 mM, EMD Millipore). The flow rate was set to 150 mL/min, autosampler temperature set to 10 °C, and column temperature set to 30°C. Mobile Phase A consisted of 20 mM ammonium carbonate and 0.1% (v/v) ammonium hydroxide, and Mobile Phase B consisted of 100% acetonitrile. The sample was gradient eluted (%B) from the column as follows: 0-20 min.: linear gradient from 85% to 20% B; 20-24 min.: hold at 20% B; 24-24.5 min.: linear gradient from 20% to 85% B; 24.5 min.-end: hold at 85% B until equilibrated with ten column volumes. Mobile Phase was directed into the ion source with the following parameters: sheath gas = 45, auxiliary gas = 15, sweep gas = 2, spray voltage = 2.9 kV in the negative mode or 3.5 kV in the positive mode, capillary temperature = 300°C, RF level = 40%, auxiliary gas heater temperature = 325°C. Mass detection was conducted with a resolution of 240,000 in full scan mode, with an AGC target of 3,000,000 and maximum injection time of 250 msec. Metabolites were detected over a mass range of 70-850 m/z. Quantitation of all metabolites was performed using Tracefinder 4.1 (Thermo Scientific) referencing an in-house metabolite standards library using  $\leq$  5 ppm mass error.

### *3.4.12 Data analysis and plotting*

All data processing, curve fitting, plotting and statistics for experiments involving jAsp-SnFR3 expressed in cell lines was made using Python code and data available on Github:  
[www.github.com/krdav/Aspartate-sensor](https://www.github.com/krdav/Aspartate-sensor)

### *3.4.13 Plasmid availability*

Submitted to Addgene under article ID 28238106.

## **3.5 Acknowledgement**

We would like to acknowledge Kaspar Podgorski for pre-publication plasmid access to iGluS-nFR3 variants and Ronak Patel for the 2P spectral analysis.

## **3.6 Funding**

This research was supported by the Proteomics & Metabolomics Shared Resource of the Fred Hutch/University of Washington/Seattle Children's Cancer Consortium (P30 CA015704). L.B.S. acknowledges support from the National Institute of General Medical Sciences (NIGMS; R35GM147118). J.S.M. and T.A.B. are funded by the Howard Hughes Medical Institute.

## Chapter 4

# ROBUST METHOD FOR MEASURING AMINOACYLATION THROUGH tRNA-SEQ

Kristian Davidsen<sup>1,2</sup>, Lucas B Sullivan<sup>1\*</sup>

This chapter is based on a manuscript published in eLife [[link](#)]. It is reprinted here in a reformatted version with no substantial changes to the text and figures.

### Abstract

Current methods to quantify the fraction of aminoacylated tRNAs, also known as the tRNA charge, are limited by issues with either low throughput, precision, and/or accuracy. Here, we present an optimized charge tRNA-Seq method that combines previous developments with newly described approaches to establish a protocol for precise and accurate tRNA charge measurements. We verify that this protocol provides robust quantification of tRNA aminoacylation and we provide an end-to-end method that scales to hundreds of samples including software for data processing. Additionally, we show that this method supports measurements of relative tRNA expression levels and can be used to infer tRNA modifications through reverse transcription misincorporations, thereby supporting multipurpose applications in tRNA biology.

---

<sup>1</sup>Human Biology Division, Fred Hutchinson Cancer Center, Seattle, WA, USA

<sup>2</sup>Molecular and cellular biology program, University of Washington, Seattle, WA, USA

\*For correspondence: lucas@fredhutch.org (LBS)

#### 4.1 Introduction

Quantification of transfer RNA (tRNA) aminoacylation, also referred to as charge, has been performed using radiolabeling [168], Northern blotting [63, 157, 137], DNA microarrays [32] and high-throughput sequencing [43]. While radiolabeling is highly accurate, it is limited to purified tRNAs undergoing lab manipulation. Northern blotting uses differential migration of acylated tRNA during electrophoresis to measure acylation levels but has many known limitations such as cross-binding probes, low sensitivity, low throughput on multiple tRNAs, insufficient band separation etc. Chemical differentiation of acylated tRNAs combined with DNA microarrays were introduced to circumvent the problems with Northern blotting, but has since been superseded by high-throughput sequencing approaches that enable quantification on all tRNAs in one experiment.

Chemical differentiation of acylated tRNAs is achieved using the Malaprade reaction to attack the 2,3-dihydroxyls on the 3' ribose of deacylated tRNA, causing ring opening and destabilization. The destabilized base is then eliminated using high pH and heat, resulting in a one base truncated 3' sequence of uncharged tRNAs compared to those protected by aminoacylation. This sequence of reactions was characterized and used extensively in the past in an effort to sequence RNA molecules [166, 165, 80, 109], and while futile for RNA sequencing, the single base truncation has proven highly useful to "tag" deacylated tRNAs. We shall refer to this reaction sequence as the "Whitfeld reaction" (figure 1 - figure supplement D.1).

The accuracy and robustness of aminoacylation measurements depend on two parts: the completeness of the Whitfeld reaction and the quality of tRNA sequencing (tRNA-Seq). A major problem in tRNA-Seq is base modifications known to be numerous on tRNAs. These can lead to stalling, misincorporation, skipping or falloff during the reverse transcription (RT) step of the sequencing protocol [108]. The RT polymerase is most severely affected by base modifications disrupting the Watson–Crick base pairing, while other modifications are often less impactful or silent [159, 127]. To increase RT readthrough the demethylase AlkB

has been used [175, 26], while more recently optimization of incubation conditions, including low salt and extended incubation time, can similarly increase readthrough [10]. Several other factors can also lead to errors in tRNA-Seq such as low RNA integrity, incomplete deacylation prior to adapter ligation, adapter ligation bias, PCR amplification bias and errors in read alignment, necessitating further protocol optimization to overcome these issues.

Adapter ligation bias is another well documented problem in small RNA sequencing [45, 176], but receives little attention in most tRNA-Seq protocols where it is particularly problematic because adapters often incorporate a barcode for sample multiplexing. The problem is further exacerbated when tRNA-Seq is coupled with the Whitfeld reaction, because this creates different sequence contexts for ligation of aminoacylated and deacylated tRNAs. One solution is to optimize conditions such that the ligation goes to completion. To that end, the tRNA secondary structure provides a useful opportunity as it contains four nucleotides on the 3' end that do not participate in the basepairing of the acceptor stem. These are the discriminator base followed by the invariant CCA-end (figure 4.1). These free nucleotides can be engaged in basepairing by an oligo splint designed to guide the ligation of the adapter and can improve tRNA specificity and ligation efficiency [131, 135].

Read mapping is another known problem for tRNA-Seq. It arises due to the high error-rate of the RT polymerase when reading through modified bases in addition to frequent falloff. In combination, reads will often not have any continuous stretch of more than 15 nt. that perfectly match its reference. This is a problem for almost all alignment algorithms because they rely on some variation of subsequence matching to enable speed-up. The problem has been addressed by clustering of the reference sequences [64] as well as masking known modified positions in the reference sequences [10].

In recent years many variations of the tRNA-Seq method have been published [159, 175, 26, 131, 40, 144, 94, 120, 161, 170], but only few couple it with the Whitfeld reaction to probe aminoacylation levels [43, 10, 163] and little is known about the precision and accuracy of these measurements. Here, we present an up-to-date method for charge tRNA-Seq that integrates new and existing developments, including improved Whitfeld reaction chemistry,

splint assisted ligation, high readthrough RT-PCR and improved read mapping, enabling us to measure tRNA charge, expression and modifications (figure 4.1). We perform tests of the quantitative capabilities of the method and determine its precision and accuracy. Finally, we provide an open-source code repository, enabling others to use our read processing, mapping and statistical tools on their own data (<https://github.com/krdav/tRNA-charge-seq>).

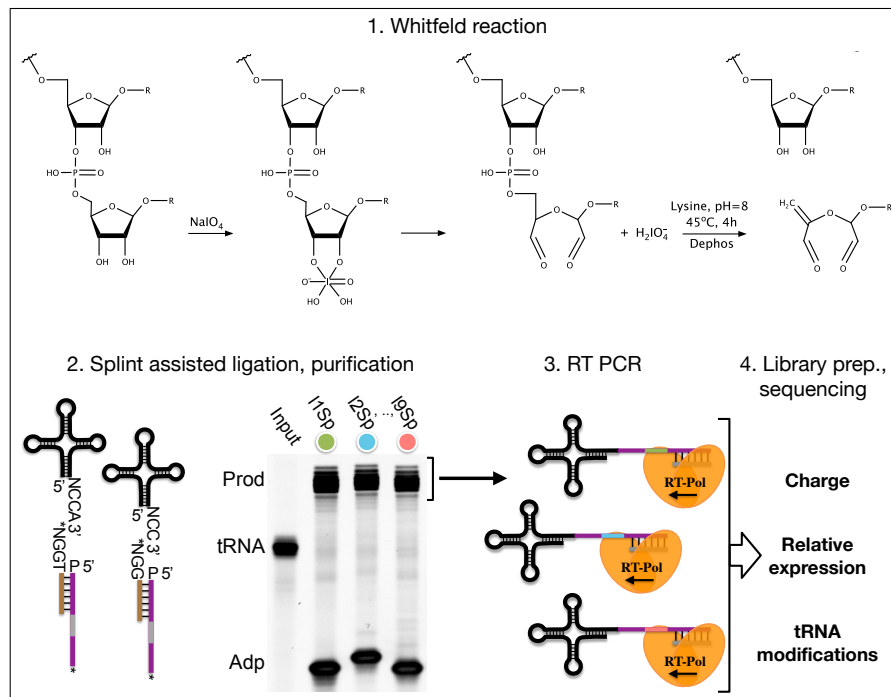


Figure 4.1: Summary illustrating the steps of the charge tRNA-Seq method we used to measure aminoacylation, relative expression and tRNA modification levels. First, the Whitfeld reaction (detailed in figure 1 - figure supplement D.1) is used to discriminate between tRNAs with and without an aminoacylation by cleaving off the 3' base of deacylated tRNA. Second, the tRNA secondary structure exposes the discriminator base (N) followed by the CCA/CC-end, creating a sticky-end for splint assisted ligation to a barcoded adapter. Stars (\*) on the 3' end of splint and adapter oligos indicate modifications to block self-ligation. Third, using the purified ligation product, RT-PCR is used to generate cDNA. Fourth, the cDNA is converted into a dsDNA library and sequenced to determine tRNA charge, expression and modifications.

## 4.2 Results

### 4.2.1 Optimizing the Whitfeld reaction for charge tRNA-Seq

The use of periodate oxidation to discriminate aminoacylated tRNA by sequencing was first used by Dittmar et al. [32] for microarray measurements and then elegantly adapted to high-throughput sequencing by Evans et al. [43]. However, we found noticeable differences between the conditions reported optimal for periodate oxidation in biochemical assays in the past [80, 109, 81, 37] and those used in charge tRNA-Seq today [43, 10, 163, 117, 148]. We therefore reasoned that it would be valuable to find a set of optimal conditions for the Whitfeld reaction when applied to charge tRNA-Seq. To do this, we used an E.coli tRNA-Lys-CCA oligo and measured conversion to its 1 nt. truncated product.

Periodate oxidation of cis-glycols is known to occur rapidly, even at low temperature [37]; therefore, we tested if oxidation could be performed on ice to protect tRNA aminoacylations prone to hydrolysis. We found that complete oxidation is achieved after just 5 min (figure 4.2, panel A) and therefore chose 10 min as optimal, with incubation on ice and in the dark because sunlight induces periodate oxidation side-reactions [41].

Oxidation of deacylated tRNA yields a dialdehyde on the terminal ribose which enables the phosphoric ester linkage to be broken in a *beta*-elimination reaction [122, 151], yielding an unsaturated product (figure 1 - figure supplement D.1). While this cleavage reaction is complex, involving several semi-stable intermediates and different pathways depending on the pH, it appears to be induced by high pH and the presence of a primary amine [150]. Lysine has been identified as a good source of primary amine and incubation at 45°C has been found optimal [80, 109]. In previous charge tRNA-Seq methods, a borax buffered solution at pH=9.5 has been used to induce cleavage, instead we wanted to test using lysine at pH=8 to improve RNA stability. We found complete cleavage after just 10 min (figure 4.2, panel B); however, this step also serves as deacylation step and some aminoacylations were still measurable after up to 90 min of lysine cleavage (figure 2 - figure supplement D.2, panel A). Therefore, we settled on a 4 h incubation time, but even with this extended incubation, the

decrease in pH made a large improvement on RNA integrity (figure 4.2, panel C).

Finally, we wanted to perform the Whitfeld reaction as a one-pot reaction as shown by Watkins et al. [163]. However, we found that the typical quenchers used to remove unreacted periodate ( glucose or ribose) are not compatible with lysine induced cleavage (figure 2 - figure supplement D.2, panel C). This is likely due to the generation of dialdehydes that cross-link lysines; therefore, we chose to use ethylene glycol which forms formaldehyde upon periodate quenching. Additionally, ethylene glycol reacts fast and can be added in high molar excess without negatively affecting subsequent steps, thus enabling the whole Whitfeld reaction in one tube (figure 4.2, panel D).

#### *4.2.2 Blunt-end adapter ligation introduces charge measurement bias*

Following the Whitfeld reaction tRNAs must be sequenced in order to measure aminoacylation levels. To achieve this with enough throughout, we chose to ligate the samples to barcoded adapters to enable sample pooling before the RT-PCR step [101]. We followed the protocol of Behrens et al. [10], with minor modifications to the oligo design, but found that the measured charge was highly variable between replicates and that the measurements were biased by the barcode identity to an unacceptable degree (figure 2 - figure supplement D.3). We hypothesized that this is due to ligation bias commonly encountered in blunt-end ligation [45, 176, 75] and reasoned that increasing ligation efficiency could mitigate the bias. However, our attempts to improved ligation efficiency failed as we were never able to reach more than ~50% ligation of the input tRNA (figure 2 - figure supplement D.4).

#### *4.2.3 Splint assisted ligation improves efficiency*

Inspired by Smith et al. [135] and Shigematsu et al. [131] we turned to splint assisted ligation. This approach utilizes that tRNAs have four nucleotides protruding from the 3' end and therefore available for basepairing: the discriminator base, which can be any of the four RNA nucleotides, followed by the invariant CCA-end. The splint oligo is designed to bind both the 3' end of tRNAs and the 5' end of an adapter (figure 4.1), thus bringing the

two into proximity and increasing ligation efficiency. However, whereas earlier uses of splint assisted ligation could assume that all tRNAs end on CCA, we have a mix of CCA and CC-ending tRNAs and therefore needed to use two splints. As tRNAs compete for ligation it is imperative that CCA-ending tRNAs, with stronger interaction with the splint, is not favoured over CC-ending tRNAs. Fortunately, we observed a near complete ligation between all of our nine barcoded adapters and both CCA-ending human tRNA and a CC-ending E. Coli tRNA-Lys oligo (figure 2 - figure supplement D.5, panel A and B). The ligation was specific as it was fully dependent on complementarity between the tRNA and the splint (figure 2 - figure supplement D.5, panel C). As we are only interested in ligation between tRNA and adapter, we block all other possible ligations through dephosphorylation of the 5' tRNA nucleotide and oligo modifications blocking the 3' end of adapter and splint oligos. This affords us the advantage of using a pure DNA splint without any RNA nucleotides as those used in previous publications [135, 131, 120, 161, 144, 94].

Importantly, we validated that tRNA processed using the one-pot Whitfeld reaction could be effectively used as substrate in the ligation reaction (figure 4.2, panel E and figure 2 - figure supplement D.6, panel A). We noted that a small amount of unligated tRNA appeared in reactions with tRNA oxidized with periodate. This unligated tRNA is of unknown origin and largely refractory to further ligation (figure 2 - figure supplement D.6, panel B); however, as shown later using charge titration, this did not have a measurable impact on the accuracy of the aminoacylation measurement.

#### 4.2.4 Combining optimizations results in a robust method for measuring tRNA charge

After combining the optimized Whitfeld reaction with subsequent splint assisted ligation, we used the RT-PCR method proposed by Behrens et al. [10] using the TGIRT polymerase [106] to maximize the readthrough of modified nucleotides. We later found that almost as high readthrough could be achieved using Maxima RT polymerase (figure 2 - figure supplement D.7). The RT-PCR was primed by an oligo containing a 10 nt. unique molecular identifier (UMI) to diversify the sequence context for the subsequent circular ligation and

allow collapsing of reads derived from the same tRNA molecule during data analysis. A final PCR was performed to attach Illumina barcodes to pool samples for multiplex sequencing.

Using this as our final charge tRNA-Seq method, we use the E.coli tRNA-Lys-CCA oligo as a spike-in control before the Whitfeld reaction to validate near complete conversion to its CC-end product, suggesting efficient periodate oxidation (figure 2 - figure supplement D.8, panel A). Similarly, we validated the completeness of deacylation using deacylated controls and the integrity of the tRNA CCA-end using non-oxidized controls (figure 2 - figure supplement D.8, panel B and C). We then measured the baseline charge of H1299 cells grown in DMEM using four replicates, observing excellent repeatability and high charge for most codons except tRNA<sup>Ser</sup> codons and a tRNA<sup>Glu</sup> codon, validating observation by Evans et al. [43] (figure 4.2, panel F).

#### *4.2.5 Reference masking improves read mapping*

It has previously been noted that alignment of tRNA reads is challenging due to RT misincorporations and falloff [64, 10]. Most commonly, the Bowtie1 or Bowtie2 aligners have been applied using various settings to accommodate short reads and the many mismatches [26, 175, 24, 43, 120]. However, while these are ultra-fast and widely used for RNA-Seq, Bowtie1 does not support alignments with insertions or deletions, and although Bowtie2 does, it does not guarantee that the best alignment is returned [90, 89]. We reasoned that many users of tRNA-Seq would rather sacrifice computational speed than mapping accuracy and therefore we apply a full all-against-all local alignment using the Smith-Waterman algorithm to provide the guaranteed best alignment(s). This is possible because the set of tRNA transcripts in a typical species is only a few hundred sequences and thus we are able to align 1e8 tRNA-Seq reads to a human tRNA reference with 457 sequences in less than 8 h on an Intel Core i7-8700K Processor (12 threads, 4.70 GHz).

In addition to the choice of read alignment method, Behrens et al. [10] found that using a SNP-tolerant alignment substantially improved mapping when modified positions causing RT misincorporations were defined as SNPs. We adapted this approach by masking modified

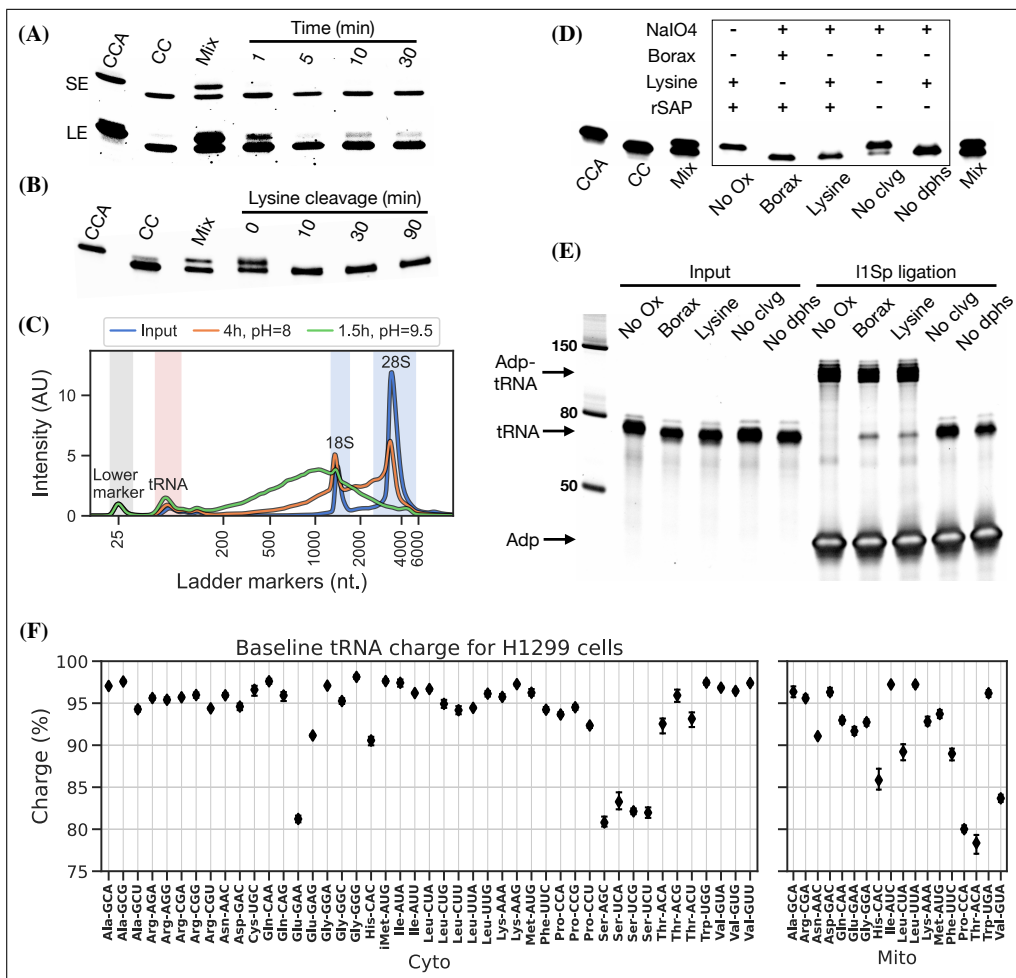


Figure caption below.

positions in the reference to "N"; however, we cannot rely solely on annotated modifications because these are incomplete and their effect on RT misincorporation rates is hard to predict. Instead, we used the misincorporation information embedded in the sequencing data, extracting it after a first pass alignment and then using mismatch frequencies to pick positions for reference masking. As such, this is an iterative process because the alignment will change slightly with a new masked reference. In addition to the number of iterations, masking is only applied on positions with a minimum mismatch frequency (`min_mut_freq`) and frequency is calculated either including or excluding reads with multiple transcript alignments

Figure 4.2: Optimizing the chemistry of charge tRNA-Seq. **(A)** Time required to complete periodate oxidation of the E.coli tRNA-Lys-CCA oligo on ice. Following oxidation, RNA was processed similar to Evans et al. [43] to cleave off the 3' adenosine. Successful cleavage produce E.coli tRNA-Lys-CC. CCA, input oligo. CC, product oligo. Mix, 50/50 mix of CCA and CC. SE, short exposure. LE, long exposure. **(B)** Time required to complete lysine cleavage of the E.coli tRNA-Lys-CCA oligo (CCA) at 45°C, pH=8. Cleavage at time 0 is likely due to the heat denaturation step performed in RNA loading buffer prior to running the gel. **(C)** TapeStation electropherogram comparing stability of whole cell RNA before and after 4 h lysine cleavage at pH=8 or 1.5 h borax cleavage at pH=9.5. tRNA range marked by red background, 18/28S by blue. See figure 2 - figure supplement D.2, panel B for RNA stability timecourse as it occurs on a gel. **(D)** Effect of individual components on cleavage of the E.coli tRNA-Lys-CCA oligo (CCA). All samples were processed as a one-pot reaction, except the borax sample which was processed similar to Evans et al. [43]. rSAP, shrimp alkaline phosphatase. **(E)** Ligation test comparing the effect of RNA processing. Deacylated and gel purified human tRNA was processed identically as in panel (D), then ligated to adapter l1Sp. Other adapters were tested with similar results (figure 2 - figure supplement D.6, panel A). **(F)** Baseline tRNA aminoacylation charge in H1299 cells grown in DMEM (4 replicates, bootstrapped 95% confidence interval of the mean). Charge on tRNA<sup>His</sup> is possibly erroneously low because the discriminator base is shielded by base pairing [57], creating a steric hindrance for the splint assisted ligation.

(`unique_anno_float`). Furthermore, a parameter (`frac_max_score`) controls the sharing of a mask to highly similar transcripts. To find the optimal combination of parameters for reference masking we performed a grid search with the objective of finding the masking that resulted in the least number of reads assigned to transcripts with multiple codons (figure 4.3, panel A). This lead to 533 positions in the 455 sequence reference getting masked and resulting in an alignment improvement, reducing the reads with multiple codon alignments from 11.71% to 5.09%.

Masked positions do not contribute to the alignment score and thus possibly lowering it below the minimum threshold; however, we observed no trade-off between optimized reference masking and read mapping percentage (figure 4.3, panel B). Like Behrens et al. [10], we observe a striking difference in the mapping of certain tRNA transcripts with inosine at the first position of the anticodon (position 34; I34). For example, transcripts decoding the Ser-

UCU codon (IGA anticodon) (figure 4.3, panel C). Generally, reference masking appears to increase annotations for around a dozen transcripts but a substantial mapping change only occurs for six codons (figure 3 - figure supplement D.10, panel a). The effect of reference masking on the charge measurements was low as expected because this is a relative number (figure 3 - figure supplement D.10, panel B).

#### *tRNA modifications are reflected in mismatches, gaps and RT stops*

Our computational method also supports using misincorporation data for inference of nucleotide modifications, which is typically only valid for modifications that disrupt Watson–Crick base pairing such as methylations [24, 10]. As such the 5-methoxycarbonylmethyl-2-thiouridine (mcm5s2U) modification should be silent; however, thionucleosides are sensitive to periodate treatment, which oxidizes them to sulfonates and makes them sensitive to nucleophilic attack [178, 123]. When periodate oxidation of mcm5s2U is followed by lysine cleavage it would presumably result in a lysine adduct [178], thus disrupting Watson–Crick base pairing. We verified this by comparing the misincorporation signature in samples processed with/without periodate oxidation, focusing on the human tRNAs Lys-UUU, Gln-UUG, Glu-UUC and Arg-UCU shown by Lentini et al. [91] to carry the mcm5s2U modification (figure 3 - figure supplement D.11). Large changes in the misincorporation signature is observed upon periodate oxidation, but curiously some tRNAs respond with a large decrease in RT readthrough while others have an increased mutation and/or gap frequency. Similar observations were recently showed by Katanski et al. [78].

#### *4.2.6 Barcode replicates show high precision*

To assess measurement precision, we performed our charge tRNA-Seq protocol on the same tRNA sample using all nine barcoded adapters. We used partially deacylated RNA to achieve a representative spread of aminoacylation levels within a single sample (figure 4 - figure supplement D.13, panel A) and then extracted differences compared to the median barcode

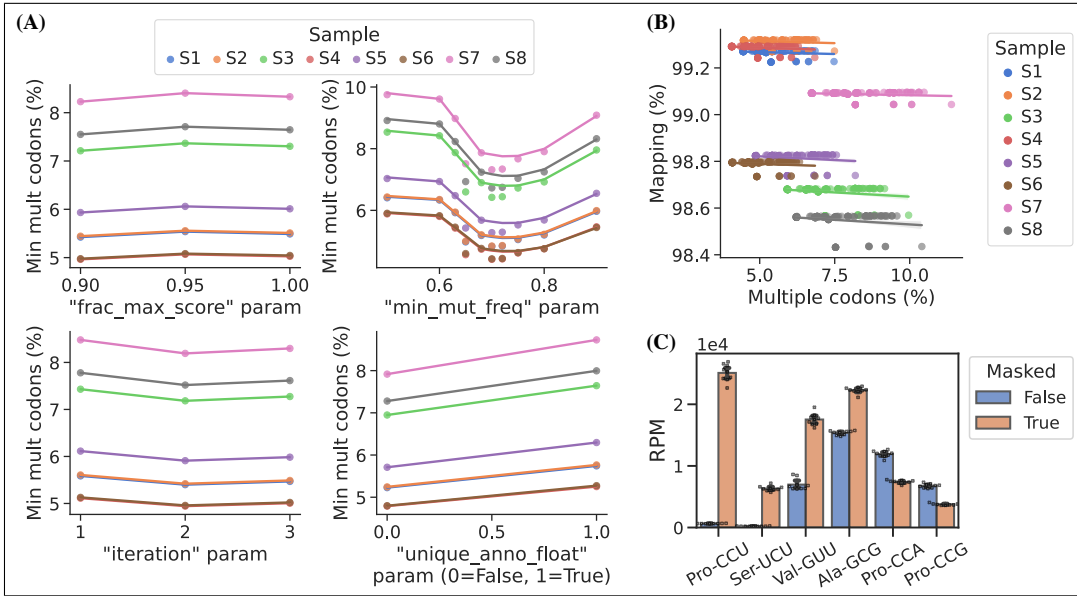


Figure 4.3: Masking of the reference sequences improves alignment performance. (A) Grid search optimization of parameters determining the extent of reference masking (see method section for details). Each subplot shows the mean effect of one tuning parameter when combined with the combination of all the other three. Parameters used for reference masking are chosen to minimize the percentage of reads assigned to tRNAs with multiple codons. (B) There is no trade-off between sequence mapping success and minimizing multiple codon mapping. (C) Reference masking increase relative expression levels of select codons. Reads per million (RPM) levels of the codons shown was found before and after optimized reference masking. Error bars are bootstrapped 95% confidence interval of the mean over the 9 barcode replicate samples.

replicate measurement. When comparing charge measurements binned by barcode, we observed that most were narrowly distributed with the median close to zero indicating little or no barcode bias (figure 4.4, panel A). Adapter l4Sp is the exception that proves why barcode bias needs to be investigated, because it is consistently overestimating charge levels, with a median overestimate of  $\sim 3$  percentage points. Overall however, charge measurements show high precision with a standard deviation from the median of just 1.7 percentage points, with similar results at the transcript level (figure 4 - figure supplement D.12, panel A).

For RPM values, some barcode replicates were more narrowly distributed than others.

However, these differences are small and with a standard deviation from the median of 5.1 percentage we consider the RPM measurements to be precise (figure 4.4, panel B and figure 4 - figure supplement D.12, panel B).

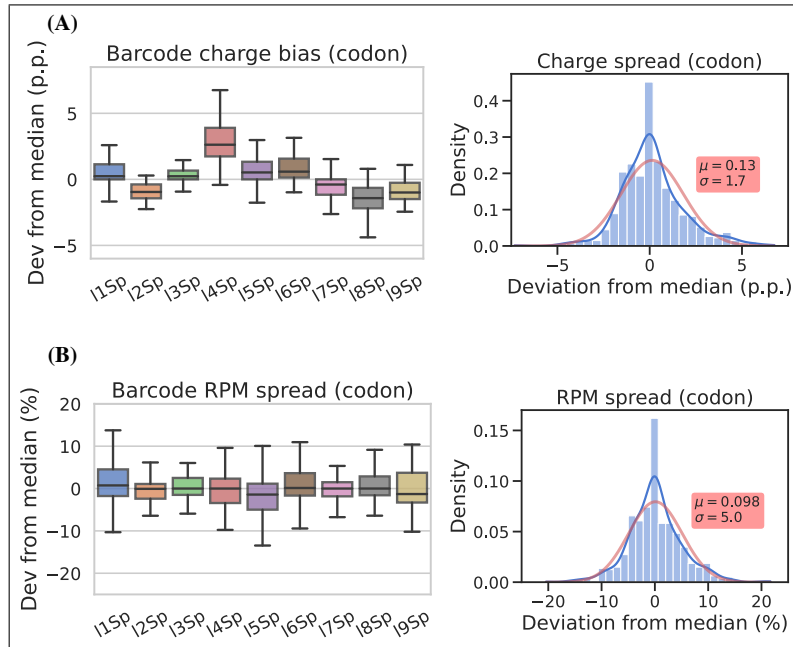


Figure 4.4: Barcode replicates show high precision and limited barcode bias. Each of the nine adapters were ligated to the same sample containing a heterogeneous mix of CC and CCA-ending tRNAs. Ligations were then pooled and submitted to the remainder of the charge tRNA-Seq protocol. **(A)** The percentage point deviation from the median charge at the codon level, grouped by barcode identity (left) or shown summarized as a density plot (right). **(B)** The percentage deviation from the median RPM at the codon level, grouped by barcode identity (left) or shown summarized as a density plot (right). Density plots are provided with kernel density estimate (KDE) in blue, normal distribution estimate in red and inserts with mean ( $\mu$ ) and standard deviation ( $\sigma$ ). For plots of transcript level data see figure 4 - figure supplement D.12.

#### 4.2.7 Charge titration shows high accuracy

Testing the accuracy of charge measurements is a much harder problem. Spiking in a defined ratio of CC and CCA-ending oligo to the ligation reaction is a common approach, but this

ignores the possible incompleteness of the Whitfeld reaction. It is also possible to compare to charge measured by Northern blotting, but this presents a different set of issues with probe annealing, band resolution etc. As an alternative, we made a charge titration by mixing different proportions of intact and deacylated RNA allowing us to predict and measure charge levels of over 150 transcripts (figure 4.5, panel A). The results showed excellent proportionality between predicted and measured charge across the full range of values (figure 4.5, panel B), thus indicating that the charge measurements are highly accurate. This experiment also confirmed our previous observations that barcode bias is limited to the l4Sp adapter, which is consistently overestimating charge (figure 4.5, panel C). Additionally, no bias was found in independently prepared sequencing libraries or any of the different mixing proportions of intact and deacylated RNA (figure 5 - figure supplement D.15).

Inspired by Evans et al. [43], which used radiolabeling techniques to generate a single accurate tRNA charge reference point, we developed a 50% charge control using 3' phosphorylation as protection from periodate oxidation. This control was spiked into samples before the Whitfeld reaction and showed a mean charge of 50.36% and a standard deviation of 1.11 percentage points (figure 5 - figure supplement D.16, panel B), thus further validating the measurement accuracy of our method.

*4.2.8 Charge tRNA-Seq enables measurement of aminoacylation half-lives of native tRNAs*

tRNA aminoacylations are prone to hydrolysis and the effect of pH and temperature on their decay rates has previously been studied [61]. Interestingly, Peacock et al. [118] found that the aminoacylation half-life appeared to be determined solely by the identity of the amino acid attachment and not affected significantly by the tRNA sequence or RNA modifications. However, most of the tRNAs used in this study were derived from in vitro transcription and only a limited set of RNA modifications were tested; additionally, the study did not cover all 20 native amino acids. Having developed an accurate method for measuring tRNA charge on over a hundred samples in a single sequencing run, we wanted to use this to determine the aminoacylation half-lives of tRNA transcripts with their native RNA modifications.

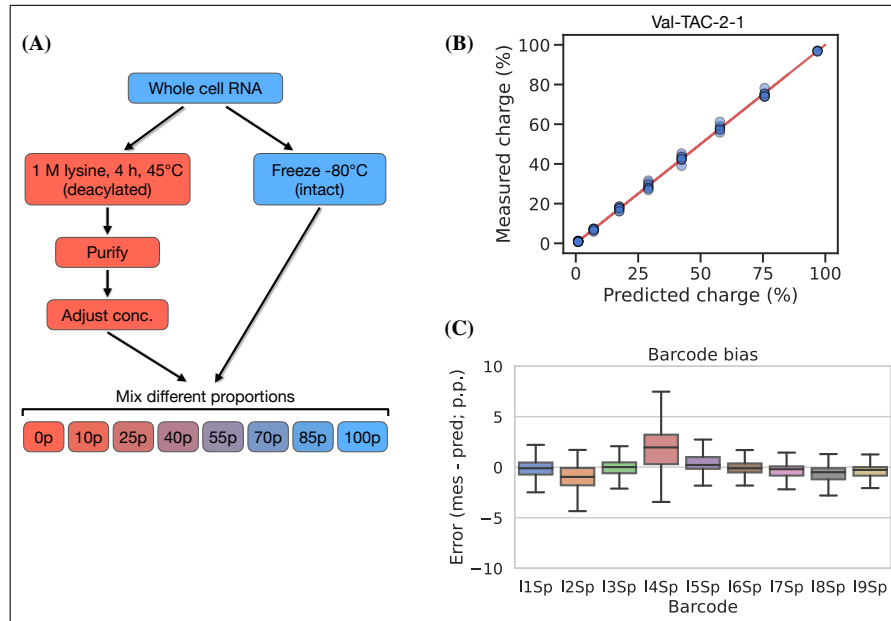


Figure 4.5: Charge titration shows linearity over the full range of charge measurements. **(A)** Schematic illustration of the method to generate samples with predictable charge percentages. **(B)** Titration data for a representative tRNA transcript, Val-TAC-2-1, with the red line indicating proportionality between predicted and measured charge. For reference, the best and worst fitting tRNA transcripts are shown in figure 5 - figure supplement [D.14](#). **(C)** Error binned by adapter barcode. Error is the percentage point difference between the measured vs. predicted charge for all transcripts in the bin.

We used RNA purified from the H1299 cell line, starting at high tRNA charge (figure 4.2, panel F), and tracked the aminoacylation decay over time after switching to physiological buffer (pH=7.2) and incubating at 20°C, similar to Peacock et al. [118]. After sampling 11 timepoints with 4 replicates, charge measurements for each transcript were fitted to a first-order decay function to estimate the half-life of each transcripts (Supplementary file 4), as exemplified by the representative transcript Lys-TTT-3-1 (figure 4.6, panel A). When transcripts were grouped by their cognate amino acid, we could confirm that the half-lives are indeed determined mostly by aminoacylation identity and that they span a 37 fold range (figure 4.6, panel B). Our half-life estimates are highly correlated with those reported by Peacock et al. [118], but surprisingly ours appear to be approximately 4 fold higher despite

using the same incubation temperature and a similar buffer, with only slightly lower pH (7.2 vs. 7.5; figure 6 - figure supplement [D.17](#), panel B).

It seems counterintuitive that the aminoacylation half-life should be completely unaffected by the tRNA sequence; however, as the amino acid is attached to the invariant CCA-end, the nucleotides most proximal to the ester bond are the same for all tRNAs. The most proximal non-invariant nucleotide is the discriminator base. Because we sample all transcripts, we are able to observe that the discriminator base is indeed likely to influence the half-life and that a purine base appears to promote a longer aminoacylation half-life than a uracil (figure [4.6](#), panel C).

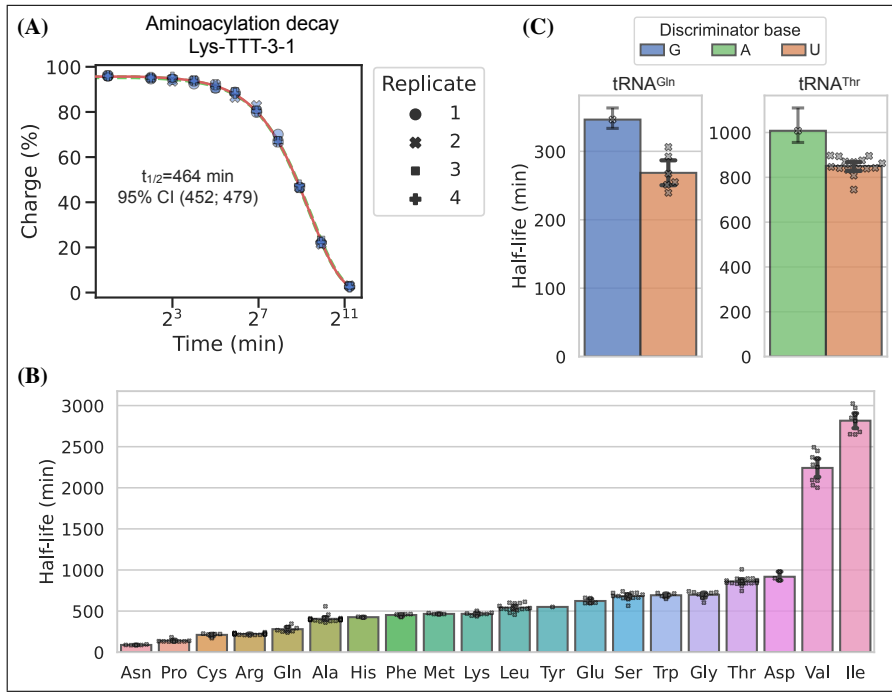


Figure 4.6: Measuring aminoacylation half-life using charge tRNA-Seq. **(A)** Aminoacylation decay for a representative tRNA transcript Lys-TTT-3-1 over the 11 timepoints sampled. For reference, the best and worst fitting tRNA transcripts are shown in figure 6 - figure supplement D.18. The fitted first-order decay to estimate the aminoacylation half-life is shown as a red line. Similar dashed lines are plotted in green for the bootstrapped 95% confidence interval (these are hard to see). **(B)** Aminoacylation half-life estimates grouped by amino acid. Each marker represents one transcript, errorbars are bootstrapped 95% confidence intervals of the mean. **(C)** Distribution of aminoacylation half-life estimates for tRNA<sup>Gln</sup> and tRNA<sup>Thr</sup> transcripts grouped by discriminator base identity. Errorbars are bootstrapped 95% confidence intervals. For the single transcripts with G or A discriminator base the bootstrap is performed on measurement replicates while for the U discriminator base it is performed on the transcript observations.

### 4.3 Discussion

Accurate quantification is a prerequisite for making reliable observations standing the test of time and replication. We have presented a robust method for measuring tRNA charge and extensively validated it in the relevant context of human tRNA. Furthermore, we have quantified the measurement precision of charge and relative expression. Accuracy was only

quantified for charge measurement whereas this is more challenging for expression levels [45]. One step towards accurate expression level measurements is efficient adapter ligation, such as the splint assisted ligation method used herein; however, future versions of tRNA-Seq should strive towards providing better validation and controls for relative expression measurements. In our version of the Whitfeld reaction we use lysine to induce base cleavage at low pH. We later found that ornithine is an even better inducer of cleavage [150] and thus, the pH of the cleavage reaction could be lowered even further and possibly combined with Cu<sup>+2</sup> as a deacylation catalyst [85, 128] to shorten incubation times.

In our experience, as well as others [131], splint assisted ligation is highly efficient compared to blunt-end ligation. In contrast, Behrens et al. [10] achieved high efficiency blunt-end ligation, allowing inclusion of non-mature tRNAs without the normal CCA-end. While the reason for this discrepancy is not obvious, our results highlight the difficulty of using blunt-end ligations for tRNA-Seq and provide an alternative approach of splint assisted ligation to help mitigate those issues. One potential issue with our approach is that the tRNA<sup>His</sup> sequence is not ideal for splint assisted ligation due to the additional G added to the 5' end [57] and thus shielding the discriminator base from base pairing with the splint. Despite this, reads mapping to tRNA<sup>His</sup> are surprisingly abundant and both CC and CCA-ending. In future versions of this method, we see the possibility of combining our optimizations with the on-bead sample processing developed by Watkins et al. [163] to eliminate gel purification steps and achieve faster and cleaner processing.

We solve the tRNA alignment problem by non-heuristic alignment which is guaranteed to return the best alignment. This is computationally demanding but nevertheless quite possible on the small number of tRNA transcript references. A more challenging problem is the application of reference masking to improve the annotation accuracy. We used unique codon annotation as the objective in our optimization, but this is a surrogate as the ground truth is unknown. Further improvements could be achieved by simulation of tRNA reads including realistic RT misincorporations, indels and falloff and optimizing alignment to this simulated ground truth. Additionally, annotation performance could be increased further

using tools, such as hidden Markov models (HMMs), to model complex phenomena such as interaction between modifications [159, 62].

In summary, we report a robust charge tRNA-Seq method that has been thoroughly tested and validated as precise and accurate for charge measurements.

#### 4.4 Methods and Materials

##### 4.4.1 Cell culture and RNA extraction

The human cell line H1299 was acquired from ATCC and tested to be free from mycoplasma (MycoProbe, R&D Systems). Cells were maintained in Dulbecco's Modified Eagle's Medium (DMEM) supplemented with 3.7 g/L sodium bicarbonate, 10% fetal bovine serum (FBS) and 1% penicillin-streptomycin solution. Cells were incubated in a humidified incubator at 37°C with 5% CO<sub>2</sub>.

For RNA extraction, cells were seeded onto a 15 cm dish and grown in DMEM until confluence. The cells were then removed from the incubator, placed on a slope on ice and media was quickly and thoroughly aspirated before adding 3 mL Trizol to cover all the cells. From this point onward, everything was kept ice cold to prevent hydrolysis of the aminoacetylation. After a 2 mins incubation, the cell material was scraped down the slope mixing it with the Trizol, then 2x1.5 mL was transferred to 2 mL Eppendorf tubes and 0.3 mL chloroform was added. The tubes were vortexed 2 min and then centrifuged (17,000g, 5 mins). From each tube, 0.75 mL of the upper layer was transferred to a tube with 0.8 mL isopropanol (IPA), then mixed and incubated 60 mins at -20°C. Tubes were then centrifuged (17,000g, 15 mins) and RNA pellets were washed twice with 1 mL 80% IPA containing 100 mM sodium acetate (pH=4.5). These washing steps are critical because Trizol contains glycerol which will react with and inhibit the subsequent periodate oxidation step. A last wash was performed using 1 mL 100% IPA and after removing the supernatant the RNA pellets were air-dried at room temperature, then stored dry at -80°C.

#### 4.4.2 Charge tRNA-Seq using blunt-end ligation

For charge tRNA-Seq using blunt-end ligation shown in figure 2 - figure supplement D.3 the protocol described by Behrens et al. [10] was followed with the exception of using different adapter sequences, a UMI containing RT oligo (Supplementary file 1), more rounds of amplification and gel based size selection for the final sequence library and using paired-end sequencing. Briefly, whole cell RNA was extracted, reconstituted in 100 mM sodium acetate (pH=4.5) and concentration adjusted to 1 g/ L. A 20 L sample was move to a new tube and submitted to periodate oxidation and 3' base elimination using sodium borate as described by Evans et al. [43]. After purification and reconstitution in water, 8 ng of a 50/50 mix of E.coli tRNA-Lys-CCA and E.coli tRNA-Lys-CC oligo was added as a CCA/CC ratio control. The true ratio of these oligos is hard to control because each contain a different fraction of truncated oligos that will not contribute to the number of mapped reads; however, the sequenced CCA/CC ratio is an important measure of the sample to sample variance. Then the RNA was 3' dephosphorylated using T4 PNK and after another round of RNA purification the tRNA fraction was isolated on a 10% Urea-TBE gel using SYBRGold staining and a blue light transilluminator for visualization. After gel elution and reconstitution in water, 100 ng tRNA was transferred to a PCR tube and ligated to 20 pmol pre-adenylated adapter (l1, l2, l3 or l4) in 25% PEG-8000, 1xT4 RNA ligase buffer using 1 L T4 RNA ligase 2 (truncated KQ) and 1 L SuperaseIn. Prior to ligation adapters were adenylated using the NEB 5' DNA Adenylation Kit following the manufacturers instruction. After purification, adapter adenylation was verified using differential gel migration. Ligation reactions were incubated 6 h at 25°C, pooled by adapter barcode and purified, followed by isolation of the ligation product from unligated tRNA using a 10% Urea-TBE gel.

After gel elution and reconstitution in water, the RT-PCR reaction was performed as described by Behrens et al. [10] using a similar RT oligo but with an extra 9 random nucleotides at the 5'-end to act as a unique molecular identifier (UMI). After the RT-PCR incubation, the remainder of the sample processing follows the charge tRNA-Seq sample processing de-

scribed below, including cDNA circularization, Illumina P7/P5 sequence attachment and sequencing.

#### 4.4.3 Charge tRNA-Seq method optimization

Optimization of the oxidation, cleavage and dephosphorylation, collectively called the Whitfeld reaction [166], was done using oligos E.coli tRNA-Lys-UUU-CCA and E.coli tRNA-Lys-UUU-CC (Supplementary file 1; anticodon omitted from name below). Both oligos were gel purified on a 10% Urea-TBE gel to resolve full length from truncated oligos. First, the time required for oxidation was tested, following the same quenching and borax buffered high pH induced cleavage used by Evans et al. [43]. For this, samples of 35 ng E.coli tRNA-Lys-CCA were prepared in 10 L 100 mM sodium acetate (pH=4.5) and used as substrate for the Whitfeld reaction conversion to E.coli tRNA-Lys-CC. Reaction progress was monitored on a 10% Urea-TBE gel by resolving the one nucleotide difference using the substrate, the product and a 50/50 mix as markers. Also using this approach, we tested using lysine induced cleavage [80] by swapping the sodium borate used for cleavage with 1 M lysine (pH=8). The cleavage step also includes deacylation and to verify the completeness of this, four samples of 10 g whole cell RNA were prepared in 10 L 100 mM sodium acetate (pH=4.5) and incubated with 50 L 1 M lysine (pH=8) at 45°C for 5, 30, 90 and 270 min. Then, 1 mL ice cold 80% isopropanol containing 100 mM sodium acetate (pH=4.5) was added, RNA was precipitated, washed twice, dried and reconstituted in 10 L 100 mM sodium acetate (pH=4.5). These deacylated samples were then submitted to the charge tRNA-Seq sample processing described below, except using lysine at pH=9.5 and 90 min incubation at 45°C to ensure complete deacylation. From this, incubation time in lysine (pH=8) was chosen to be 4 h. To compare the RNA integrity after cleavage with lysine vs. borax, samples of 10 g whole cell RNA were prepared in 10 L 100 mM sodium acetate (pH=4.5) and added 50 L of either 1 M lysine (pH=8) or 100 mM sodium borate (pH=9.5). Tubes were incubated 45°C and samples taken at time 0, 1.5, 4 and 8 h. RNA integrity was determined using TapeStation (high sensitivity RNA) and 10% Urea-TBE gel . Upon combining the steps of

the Whitfeld reaction to a one-pot reaction a color change was observed after addition of lysine. To test the effect of the periodate quencher, 10 L of freshly prepared 200 mM NaIO<sub>4</sub> in 100 mM sodium acetate (pH=4.5) was quenched by 10 L 1 M aqueous solution of either ethylene glycol [109], glycerol [2], glucose [43], ribose [163] or water (control) for 10 min at room temperature. Then 100 L 1 M lysine at either pH 8 or 9.5 was added and reactions incubated at 45°C for 4 h before moving to room temperature for visual inspection (figure 2 - figure supplement D.2, panel C).

For ligation optimization human tRNA was isolated from H1299 cells. First, whole cell RNA was isolated as described above, reconstituted in water and deacylation at 45°C in 1 M lysine (pH=8) for 4 h. Then RNA was purified using the Monarch RNA Cleanup Kit (50 g) and run on a 10% Urea-TBE gel to resolve the tRNA from mRNA and rRNA. tRNA was defined as the range between 70 and 85 nt. as approximated by the low range ssRNA ladder. For blunt-end ligations in figure 2 - figure supplement D.4, 40 ng tRNA, either isolated from H1299 cells or as E.coli tRNA-Lys-CC oligo, was ligated to 20 pmol pre-adenylated adapter in a 20 L reaction containing 25% PEG-8000, 200 U T4 RNA ligase 2 (truncated KQ; Rnl2tr KQ), 10 U SUPERaseIn and the vendor provided buffer. For splint assisted ligation in figure 2 - figure supplement D.5, 35 ng tRNA, either isolated from H1299 cells or as E.coli tRNA-Lys-CC oligo, was ligated to 20 pmol annealed adapter:splint partial duplex as described for charge tRNA-Seq sample processing below. For the non-complementary splint test, two splint oligos were made with CAAC and AAC overhangs (Supplementary file 1) and annealed to adapter l1Sp. For the ligation test in figure 4.2, panel E and figure 2 - figure supplement D.6, panel A, 500 ng tRNA isolated from H1299 cells was subjected to the one-pot Whitfeld reaction described for charge tRNA-Seq sample processing below but with a single step removed. For the no oxidation sample NaIO<sub>4</sub> was replaced with NaCl, for the no dephosphorylation sample shrimp alkaline phosphatase (rSAP) was replaced with water and for the no cleavage sample RNA was purified after periodate quenching. These were compared to a sample processed as described in Evans et al. [43]. All samples were purified using the Monarch RNA Cleanup Kit and 35 ng was used per ligation test with adapters l1Sp,

l2Sp and l3Sp using the ligation protocol described for charge tRNA-Seq sample processing below.

#### 4.4.4 Charge tRNA-Seq sample processing

Stepwise description with details in Supplementary file 2. Whole cell RNA was reconstituted in 100 mM sodium acetate (pH=4.5) and keep on ice until the end of the periodate oxidation step. For deacylated control samples, RNA was prepared by first performing a deacylation step on the input RNA by incubation in 1 M lysine (pH=8) at 45°C for 4 h, followed by purification using the Monarch RNA Cleanup Kit (50 g). The RNA concentration was adjusted to 1 g/ L, 10 L was transferred to a fresh tube and 1 L E.coli tRNA spike-in control was added. Initially, the spike-in control contained 5 ng/ L E.coli tRNA-Lys-CCA, later 5 ng/ L of each E.coli tRNA-Thr-CGT CCA-Phos and E.coli tRNA-Thr-CGT CCA was also included. To this 5 L freshly prepared 200 mM NaIO<sub>4</sub> was added following 10 min incubation on ice, in the dark. For non-oxidized control samples, NaCl was used instead of NaIO<sub>4</sub>. The oxidation was quenched by adding 5 L 50% (v/v) ethylene glycol (~9 M) and incubating for 5 min on ice and 5 min at room temperate, in the dark. Then 50 L 1 M lysine (pH=8) with 1 L SuperaseIn was added and tubes were incubate for 4 h at 45°C. To dephosphorylate RNA 8 L 10X rCutSmart Buffer and 1 L rSAP was added followed by 30 min incubation at 37°C. RNA was then purified using the Monarch RNA Cleanup Kit (50 g), eluting with 30 L water. A 6 L sample was then denatured by mixing with 2x urea loading buffer (8 M urea, 30 mM sodium acetate, 2 mM EDTA, 0.02 % (w/v) bromophenol blue and xylene cyanol, pH adjusted to 4.7-5) and incubating 2 min at 90°C. The tRNA fraction was then isolated on a 10% Urea-TBE gel using SYBRGold staining and a blue light transilluminator for visualization. Gel elution was done by crushing the gel with a disposable pestle, adding 200 L gel elution buffer and 1 L SuperaseIn, then snap freezing in liquid nitrogen and incubating at 65°C for 5 mins with shaking. This gel slurry was filtered through a Spin-X filter followed by tRNA purification using the Oligo Clean & Concentrator kit. The concentration of purified tRNA was measured, then it was annealed in NEBuffer

2 by heating to 94°C for 2 min followed by cooling 1°C/s to 4°C. 35 ng of the annealed tRNA was transferred to a PCR tube and to this was added 20 pmol annealed adapter:splint partial duplex, 1 L 10x NEBuffer 2, 2 L 10x T4 RNA ligase buffer, 4 L 50% PEG-8000, 1 L SuperaseIn and 1 L T4 RNA ligase 2. The annealed adapter:splint partial duplex was made by making an equimolar mix of the CCA and CC splint oligos, then using this to make an equimolar mix with the adapter oligo and annealing this in NEBuffer 2 by heating to 94°C for 2 min followed by cooling 0.3°C/s to 4°C. Each ligation reaction was adjusted to 20 L with water, mixed and incubated 1 h at 37°C followed by 24 h at 4°C and heat inactivation at 80°C for 5 min. Samples were pooled by adapter barcode, purified using the Oligo Clean & Concentrator kit and then ligated tRNA was isolated on a gel and purified similarly to the initial tRNA isolation.

Reverse transcription was setup with 60 ng of the purified adapter ligated tRNA as template using the buffer composition, incubation temperature and time suggested by Behrens et al. [10]. To 10 L template in a PCR tube, 2 L 1.25 M RT oligo and 4 L RT buffer was added following denaturation and annealing by incubation at 90°C for 2 min, 70°C for 30 s and cooling 0.2°C/s to 4°C. Then, to each tube 1 L 100 mM DTT, 1 L SuperaseIn and 1 L TGIRT-III RT polymerase (or Maxima H Minus for figure 2 - figure supplement D.7) was added following 10 min incubation at 42°C. Then 1 L 25 mM dNTPs was added and the incubation was resumed at 42°C for 16 h on a thermocycler with the heated lid set to 50°C. The RNA template was hydrolyzed by adding 1 L 5 M NaOH followed by incubation at 95°C for 3 min. The samples were then purified using the Oligo Clean & Concentrator kit and the cDNA was isolated on a gel and purified similarly to the initial tRNA isolation, eluting with 7 L water. cDNA was circularized by transferring 5.5 L cDNA to a PCR tube and adding 2 L 5 M betaine, 1 L 10x CircLigase buffer, 0.5 L 1 mM ATP, 0.5 L 50 mM MnCl<sub>2</sub> and 0.5 L CircLigase. The reaction was incubated at 60°C for 3 h on a thermocycler with a 70°C heated lid, then the enzyme was deactivated by denaturing at 80°C for 10 min.

PCR was used to attach Illumina P7/P5 sequences to flank the tRNA insert. Each PCR reaction was setup to contain 0.6 L circularized cDNA, 1.5 L 10 mM dNTPs, 5

L 10 M P7 oligo, 5 L 10 M P5 oligo, 10 L 5x KAPA HiFi buffer, 1 L KAPA HiFi polymerase and 26.9 L water. The PCR reactions were incubated at 95°C for 3 min followed by 3 cycles of 98°C for 20 s, 68°C for 10 s and 72°C for 15 s, and then followed by X cycles of 98°C for 20 s and 72°C for 15 s, with X being empirically determined (figure 2 - figure supplement D.9, panel A). The optimal number of PCR cycles were determined by preparing three PCR reactions, incubating them with X=10, 12 and 14 and running 4 L of each reaction on a 4-12% TBE gel. The PCR reactions with optimal X, resulting in abundant amplification product with little PCR crossover, were purified using the DNA Clean & Concentrator-5 kit and resolved on a 4-12% TBE gel. The gel was stained using SYBRGold and visualized using a blue light transilluminator to isolated the library DNA by cutting out the size range covering all possible insert lengths (170-290 bp). Gel elution was done by crushing the gel with a disposable pestle, adding 300 L TBE, snap freezing in liquid nitrogen and incubating at room temperature overnight with mixing. If necessary, elution time could be decreased by incubation at higher temperature; although, this required adding higher salt concentrations to prevent DNA reannealing (figure 2 - figure supplement D.9, panel B). The gel slurry was filtered through a Spin-X filter following DNA purification using the DNA Clean & Concentrator-5 kit and eluting with 20 L 10 mM Tris (pH=8). DNA with different Illumina P7/P5 barcodes were pooled for multiplexing and sequenced using Illumina paired end sequencing using 2x100 bp reads.

#### *E.coli tRNA spike-in control*

An E.coli tRNA spike-in control was generated from oligos E.coli tRNA-Lys-UUU-CCA and E.coli tRNA-Thr-CGT-CCAA (anticodon sometimes omitted from name). First, 2 g per well of the E.coli tRNA-Lys-CCA oligo was loaded on a 10% Urea-TBE gel to resolve full length from truncated oligos. After gel elution and purification using the Oligo Clean & Concentrator kit the RNA concentration was measured and adjusted such that 5 ng was spiked into each sample of 10 g whole cell RNA before periodate oxidation. Adding the control before periodate oxidation afforded an internal control of the completeness of the

oxidation reaction.

Second, 30 L of 100 M E.coli tRNA-Thr-CCA oligo was submitted to a partial Whitfeld reaction, stopping before the dephosphorylation step. The oxidation reaction was performed by adding 10 L 100 mM sodium acetate (pH=4.5) and 20 L 200 mM NaIO<sub>4</sub> followed by incubation for 30 min at room temperature in the dark. Oxidation was quenched using 20 L 50% ethylene glycol and incubated 30 min at room temperature in the dark. Then buffer exchange was performed using a P-6 gel column pre-equilibrated with 100 mM lysine (pH=8). To the eluate 400 L 1 M lysine (pH=8) and 1 L SuperaseIn was added followed by 5 h incubation at 45°C and purification using the Monarch RNA Cleanup Kit (using two 50 g columns). The product, a 1 nt. truncated and 3' phosphorylated oligo named E.coli tRNA-Thr-CCA-Phos, was resolved on a gel to isolate the full length oligo, as described for the other control. Half of this product was submitted to dephosphorylation using rSAP and purified using the Oligo Clean & Concentrator kit yielding E.coli tRNA-Thr-CCA. Complete phosphorylation of E.coli tRNA-Thr-CCA-Phos and complete dephosphorylation of E.coli tRNA-Thr-CCA was verified using ligation (figure 5 - figure supplement [D.16](#), panel A). Then concentrations of both E.coli tRNA-Thr-CCA-Phos and E.coli tRNA-Thr-CCA was measured to generate an equimolar mix adjusted such that 10 ng was spiked into each sample of 10 g whole cell RNA before periodate oxidation. The 3' phosphorylation protects from periodate oxidation and thus adding it before periodate oxidation afforded an internal control of a 50% charged tRNA, probing the completeness of the whole Whitfeld reaction and potential adapter ligation bias.

#### 4.4.5 Oligo design

For adapters used for blunt-end ligation the design was similar to McGlincy & Ingolia [[101](#)] and Behrens et al. [[10](#)], with a 5' phosphorylation to enable adenylation and a 3' dideoxycytidine to prevent self-ligation and concatemer formation. For adapters l1, l2, l3 and l4 the barcode sequence was 8 nt. starting at the 5', for adapters l1N, l2N and l3N the barcode sequence was truncated to 5 nt. to make space for a preceding six random nucleotides to

diversify the sequence context engaged in ligation.

The design of adapters used for splint assisted ligation was influenced by Smith et al. [135] and Shigematsu et al. [131] but with several important differences listed below. First, we do not use ribonucleotides at any positions in our adapters or splint oligos. This affords us higher quality oligos due to the higher coupling efficiency of deoxyribose during oligo synthesis as well as robustness against hydrolysis of DNA compared to RNA. A primary reason to use ribonucleotides in the adapters and splint oligos is to increase ligation efficiency; however, we achieved ~100% ligation efficiency on isolated human tRNA using our design without ribonucleotides (figure 2 - figure supplement D.5, panel A). Second, instead of ligating the adapter to the 3' and the splint to the 5' of the tRNA, we only ligate the adapter and block the splint from ligating using a 3' C3 spacer, as well as dephosphorylating the 5' of the tRNA. Similar to the blunt-end ligation adapters, a 3' dideoxycytidine is included on all adapters to block self-ligation and concatemer formation. Third, we use two different lengths splint oligos with overhang compatible with NCCA and NCC-ending tRNA. Fourth, our adapters vary in length by the size of their barcodes, from 5 to 8 nt. This is to offset the sequencing reading frame of read P2 (P7) as it progresses into the 3' end of the tRNA, thus increasing the sequence diversity and base calling quality.

The RT-PCR oligo was designed in a similar way as McGlincy & Ingolia [101] and Behrens et al. [10] with a 5' phosphorylation for subsequent circular ligation of the cDNA and an 18-atom hexa-ethyleneglycol spacer (iSp18) to terminate the polymerase extension and avoiding rolling-circle amplification during the PCR to attach Illumina P7/P5 sequences. The RT oligo has a random purine base on the 5' to increase circular ligation efficiency. We added an additional 9 random nucleotides following this purine to increase the diversity of the sequence engaged in circular ligation. These random nucleotides also provide a unique molecular identifier (UMI) with 524288 possible sequences that enable collapsing of reads derived from the same tRNA molecule. The UMI is also used as a general sample quality control by comparing the number of observed UMI sequences with the number expected.

The expected number unique UMI observations is calculated as:

$$E[X] = n \left[ 1 - \left( \frac{n-1}{n} \right)^k \right] \quad (4.1)$$

With  $E[X]$  being the expected number of unique UMI observations,  $n$  being the number of reads for the particular sample and  $k$  being the number of possible UMIs.

The final dsDNA library was designed as an Illumina TruSeq dual index library with combined i5 and i7 indices attached by PCR with P7/P5 oligos. These oligos were synthesized with a phosphorothioate bond between the last two nucleotides to prevent degradation by the KAPA HiFi polymerase. An overview of the RNA/DNA manipulations including ligation of adapters, RT-PCR, circularization and library PCR is provided in Supplementary file 3.

#### 4.4.6 Read processing

Reads were first demultiplexed according to their i7/i5 barcodes. Read pairs were then trimmed and merged using AdapterRemoval:

```
AdapterRemoval --preserve5p --collapse --minalignmentlength 10 --adapter1
    AGATCGGAAGAGCACACGTCTGAACTCCAGTCAC<P7_index>ATCTCGTATGCCGTCTCTGCTTG --
    adapter2 AGATCGGAAGAGCGTCGTAGGGAAAGAGTGT<P5_index>
    GTGTAGATCTCGGTGGTCGCCGTATCATT --minlength <MIN_LEN>
```

With `<P7_index>` and `<P5_index>` defined by the i7/i5 index sequences for the given sample and `<MIN_LEN>` set to 25 for charge tRNA-Seq using blunt-end ligation and 39 for charge tRNA-Seq using splint assisted ligation. Each file with merged reads were then split based on adapter barcode. A read was assigned to a particular adapter barcode if its 3' end had a substring within a hamming distance of one to the barcode sequence, including the region complementary to the splint. The adapter sequence was then trimmed off the 3' end; similarly, the 10 nt. UMI was located, saved and trimmed off the 5' end, leaving only the tRNA sequence with possible 5' non-template bases introduced during RT-PCR. Finally,

samples with an excess of 2e6 reads were downsampled to 2e6 reads.

Trimmed reads were aligned to a masked reference as described below using the Smith-Waterman algorithm implemented by SWIPE [124]:

```
swipe --symtype 1 --outfmt 7 --num_alignments 3 --num_descriptions 3 --
      eval 0.00000001 --strand 1 -G 6 -E 3 --matrix <SCORE_MATRIX>'
```

With an input score matrix (<SCORE\_MATRIX>) defining a match score of 1, a mismatch score of -3 and a score for alignment to a masked reference position (N) of 0.

Alignment results were processed to extract three key data: 1) tRNA charge, 2) relative expression level and 3) mismatches, gaps and RT truncations. First the alignment was parsed to extract transcript annotation(s), alignment score and other relevant information. A read was assigned the annotation with the highest alignment score and upon ties up to three annotations were merged. When reporting data on the transcript level, a unique annotation was required for filtering, when reporting at the codon level multiple annotations were allowed but a unique anticodon was required and similarly for data on the amino acid level. Relative expression levels were calculated as reads per million (RPM) with a count correction such that reads with identical sequence and UMI were only counted once. Charge was calculated using uncorrected counts as this is a relative number. Mismatches, gaps and RT truncations were extracted by redoing the Smith-Waterman alignment between the read and its unmasked transcript annotation using a match score of 1, a mismatch score of -2, a gap opening score of -3 and a gap extension score of -2. Using this new alignment, mismatched, gaps and the index at the end of the alignment were extracted. Then for each transcript the fraction of reads having mismatches and gaps at a given position was calculated and the percentage drop in coverage at each position, referred to here as RT stops. For both mutation, gap fractions and RT stops the UMI corrected read count was used. We provide a boilerplate example of the whole read processing workflow on GitHub: [https://github.com/krdav/tRNA-charge-seq/blob/main/projects/example/process\\_data.ipynb](https://github.com/krdav/tRNA-charge-seq/blob/main/projects/example/process_data.ipynb).

#### 4.4.7 Reference masking

A human tRNA transcript reference for alignment was made from hg38 annotations in GtRNADB [20]. These sequences were deduplicated and mitochondrial tRNAs and spike-in control sequences were appended. Then a BLAST database was generated, as required by SWIPE, using the `makeblastdb` application. To further improve the alignment specificity, a masked reference was made by converting positions with high likelihood of mismatch to Ns such that these have no negative contribution on the alignment score. Position-wise mismatch frequency was found as described above and filtered using a minimum of 200 transcript observations and 100 observations on each position. These were then turned into a masked reference using four tuning parameters for picking the positions to mask. `unique_anno`: Only count reads with a unique transcript annotation. `min_mut_freq`: The minimum mismatch frequency to trigger masking. `frac_max_score`: The minimum fraction of the maximum alignment score between two reference sequences to expand the masked positions in one reference to another, requiring both positions to have the same nucleotide and the acceptor position to have less than 100 observations. The purpose is for an abundant transcript to donate its masking to a highly similar, but less abundant, transcript likely having the same RNA modifications. `iteration`: The number of masking iterations to perform. When changing the reference for alignment by masking the annotations can change, thus changing the position-wise mismatch frequency and the resulting reference masking. Running multiple iterations of reference masking stabilizes this change.

To find the optimal combination of tuning parameters a grid search was performed, testing all combinations of parameters shown in figure 4.3, panel A. The objective of the search is to minimize the percentage of reads assigned to transcripts with multiple anticodons. Alternatively, the objective could be to minimize the percentage of reads assigned to multiple transcripts; however, this objective can lead the tuning parameters towards masking only a single transcript out of a family of highly similar transcripts, resulting in assignment of unique annotations to truncated reads, which cannot truly distinguish between transcripts

of high similarity. This problem is less concerning using minimization of multiple anticodons since most families of highly similar transcripts have identical anticodons.

#### 4.4.8 Barcode replicate test

For the barcode replicate test shown in figure 4.4, the RNA used was first incubated 8 h at 20°C in intracellular physiological buffer, similar to the 8 h timepoint described in the aminoacylation half-life section below. This provided tRNA containing a spectrum of charge levels, spanning from almost fully acylated isoleucine tRNAs to almost fully deacylated asparagine tRNA. A single 10 g sample of this RNA was then subjected to the one-pot Whitfeld reaction and subsequent tRNA isolation and ligation to each of the nine adapters as described for charge tRNA-Seq sample processing above.

#### 4.4.9 Charge titration test

Whole cell RNA was reconstituted with 100 mM sodium acetate (pH=4.5) and adjusted to 1 g/ L while keeping the RNA cold throughout. Half of this was moved to a fresh tube and deacylated by adding 5x volumes of 1 M lysine (pH=8), incubating at 45°C for 4 h and purifying using the Monarch RNA Cleanup Kit. Meanwhile, the other half was stored at -80°C. The concentration of the deacylated RNA was adjusted to 1 g/ L and mixtures of intact and deacylated RNA was made using the following percentages of intact/deacylated RNA: 100/0, 85/15, 70/30, 55/45, 40/60, 25/75, 10/90, 0/100. Then these mixtures were subjected to the charge tRNA-Seq sample processing protocol described above with between 4 to 8 barcode replicates across independently prepared sequencing libraries, sequenced on different flow cells.

Reads were processed and the aminoacylation charge of each transcript was extracted to relate the measured with the predicted charge. However, the actual mixing ratios may deviate from the ones noted above due to inaccuracies in measuring the RNA concentration of intact and deacylated RNA, and due to depletion of certain tRNA species during the deacylation process, for example tRNAs sensitive to hydrolysis or depurination. We address

this using a correction factor,  $F_i$ , described below. To calculate the predicted charge let  $A$  represent intact RNA,  $B$  represent deacylated RNA and the index  $i$  represent the transcript. Now, define the concentration,  $C$ , of a tRNA transcript  $i$  in the intact RNA as 1, while letting the concentration of the same tRNA transcript in the deacylated RNA be a fraction,  $F_i$ , of the intact RNA:

$$\begin{aligned} C_i^A &= 1 \\ F_i = \frac{C_i^B}{C_i^A} &\Leftrightarrow C_i^B = F_i \end{aligned} \tag{4.2}$$

Then, define  $T_i^A$  as the measured charge of the intact tRNA of a transcript  $i$  averaged over the replicates, and similarly  $T_i^B$  for deacylated RNA:

$$\begin{aligned} T_i^A &= \text{Avg charge}(A_i) \\ T_i^B &= \text{Avg charge}(B_i) \end{aligned} \tag{4.3}$$

Now, the predicted charge of a mixture of  $A$  and  $B$  can be defined using  $p$  to describe the percentage of  $A$  in the mixture:

$$T_i^{AB}(p) = \frac{pT_i^A + (100 - p)T_i^B F_i}{p + (100 - p)F_i} \tag{4.4}$$

In the above, only  $F_i$  is unknown. The titration was made with 8 different mixing ratios, two of which are used to calculating  $T_i^A$  and  $T_i^B$ , thus leaving 6 mixing ratios, each with several barcode replicates, to fit  $F_i$ . Fitting was performed by minimizing the sum of squared differences between predicted and measured charge using the Broyden–Fletcher–Goldfarb–Shanno (BFGS) algorithm with upper and lower bound constraints of 4 and 0.25. Then equation 4.4 was used to calculate the predicted charge and the difference to the measured charge was found and broken down by adapter barcode to investigate ligation bias.

#### 4.4.10 Aminoacylation half-life

Whole cell RNA was reconstituted with 1 mM sodium acetate (pH=4.5) and adjusted to 1.5 g/ L while keeping the RNA cold throughout. A zero timepoint was then taken and 80 L was transferred to a PCR tube after which the experiment was started by adding 20 L room temperature 5x buffer, quickly mixing and placing the tube on a thermocycler set to 20°C. The buffer used was an intracellular physiological buffer at 1x containing: 19 mM NaCl, 125 mM KCl, 0.33 mM CaCl<sub>2</sub>, 1.4 mM MgCl<sub>2</sub>, 0.5 mM spermidine, 30 mM HEPES, adjusted to pH=7.2 with KOH. Time from start of incubation was tracked and samples drawn at the following timepoints: 4 min, 8 min, 16 min, 32 min, 1 h, 2 h, 4 h, 8 h, 16 h and 40 h. For the 40 h timepoint, two samples were drawn: one standard and one receiving sham (NaCl) oxidation. Sample were taken by removing 8 L, mixing it in a prepared tube with 2 L ice cold 500 mM sodium acetate (pH=4.5) and storing it at -80°C until all timepoints were collected. This was repeated four times to generate independent replicates. Then samples were processed similar to the charge tRNA-Seq protocol described above, but with the three 5 min incubation times during periodate oxidation and quenching increased to 30 min each due to the lower periodate solubility in the presence of potassium ions.

After read processing and alignment, data integrity was verified by checking that the E.coli tRNA spike-in control and the non-oxidized 40 h samples conformed to expectations. RNA integrity at the end of the experiment was also verified on a gel (figure 6 - figure supplement D.17, panel A). The aminoacylation charge was then calculated at the codon level and the data fitted to an equation describing first-order decay:

$$N(t) = N_0 \left( \frac{1}{2} \right)^{\frac{t}{t_{1/2}}} + N_\infty \quad (4.5)$$

Where  $N(t)$  is the charge of a given codon as a function of time,  $N_0$  is the charge at time zero and  $t_{1/2}$  is the decay half-life. We added the  $N_\infty$  parameter to model the lower asymptote of charge to accommodate the small fraction of tRNAs that still presents with a CCA-end after full deacylation. The three parameters were fitted to the data by minimizing the sum of

squared errors using the Broyden–Fletcher–Goldfarb–Shanno (BFGS) algorithm with upper and lower bound constraints for  $N_0$  between 100 and 0 percent, for  $t_{1/2}$  between 1e5 and 1 min and for  $N_\infty$  between 3.5 and 0 percent. A point estimate for the three parameters were found using all timepoints and replicates and a 95% confidence interval was found using bootstrapping (N=1000) by sampling a single time-series made up of random draws from the replicates (Supplementary file 4).

#### *4.4.11 Data availability*

Raw data and code for processing and recreating plots were uploaded to Zenodo: <https://doi.org/10.5281/zenodo.8200907>

Python code is available on Github: <https://github.com/krdav/tRNA-charge-seq>

### **4.5 Acknowledgments**

We would like to acknowledge Arvind Rasi Subramaniam for suggesting we setup charge tRNA-Seq, Alicia Darnell for sharing relevant samples and data and David Sokolov for help with early method optimization.

### **4.6 Funding**

L.B.S. acknowledges support from the National Institute of General Medical Sciences (NIGMS; R35GM147118).

## Chapter 5

## FUTURE DIRECTIONS

In this last chapter a perspective is offered on the three key contributions presented in chapter 2, 3 and 4.

### **5.1 Aspartate limitation and nucleotide synthesis**

As mentioned in chapter 2, some evidence points to nucleotide imbalance being a driver of aspartate limitation. This warrants further investigation into the role of AMP synthesis by adenylosuccinate synthase. Adding to this evidence, in chapter 3 it was shown how glutamine depletion induces a rapid decrease in intracellular aspartate, much akin to mitochondrial inhibitor induced aspartate limitation. Such glutamine depletion has previously been shown to cause cells to get arrested in S-phase, in a phenotype that could be rescued both with addition of aspartate and a mix of nucleosides [115]. However, which of the nucleosides that were causing S-phase arrest during glutamine depletion was never tested and, as shown in chapter 2, the aspartate to proliferation relationship does not shift upon supplementation with adenine. Thus, a better explanation for decreased proliferation during aspartate limitation would be nucleotide imbalance since this can also occur while nucleotides are being supplemented.

Diehl et al. [31] did a detailed study of nucleotide imbalance by media supplementation of nucleosides/nucleobases and likewise found S-phase arrest to be a hallmark of nucleotide imbalance. They furthermore found that nucleotide imbalance led to large change in the dNTP pools, with both increases and decreases, and that this correlated with Chk1/2 phosphorylation by the single-stranded DNA break detector kinase ATR. Interestingly, cells under nucleotide imbalance did not stop protein synthesis and thus their size increased. In fact,

when nucleotide imbalance was titrated it led to progressively decreased proliferation that was highly correlated with increased cell size. This is reminiscent of titratable aspartate limitation with mitochondrial inhibitors, but Diehl et al. claim that inhibitors rotenone and oligomycin do not elicit nucleotide imbalance as determine by cell size as a readout. However, when revisiting their data, it was found that both rotenone and oligomycin did in fact lead to cell size increases compared to baseline, albeit these increases were smaller compared to those cause by imbalanced nucleoside/nucleobase supplementation.

A quick test on H1299 and 143B cells was performed and showed that five different mitochondrial inhibitors known to cause aspartate limitation all lead to increased cell size compared to vehicle (figure 5.1). This prompted a reanalysis of previous aspartate limitation proliferation data, revealing a remarkable time dependent increase in cell size that was highly correlated with the proliferation rate (figure 5.2). This bears resemblance to nucleotide imbalance described by Diehl et al. The correlation between proliferation rate and cell size was robust and could not be broken by partial proliferation rescue with salvageable fates of aspartate (figure 5.3). Lastly, it was shown that Chk1 is phosphorylated during rotenone and antimycin exposure, indicating single-stranded DNA breaks (figure 5.4). In this, thymidine is a positive control for nucleotide imbalance and its effect should be rapid, aspartate limitation on the other hand takes about 1 day to reach a low steady-state (see chapter 3), thus explaining the timing difference in Chk1 phosphorylation.

In summary, there is compelling evidence for further pursuing the nucleotide imbalance hypothesis. It would be informative to know the correlation between aspartate limitation and S-phase arrest as well as the change in dNTP levels. It would also be useful to look at the aspartate to proliferation relationship with increasing adenine levels for AMP synthesis complementation; although, this would be complicated by adenine deamination and competing salvage into GMP as observed in chapter 2. Therefore, it may be necessary to isolate the effect of nucleotide imbalance by generating an adenylosuccinate synthase, IMP dehydrogenase double knockout that is fully relying on guanine and adenine salvage.

Interestingly, if aspartate limitation works by decreasing adenylosuccinate synthase ac-

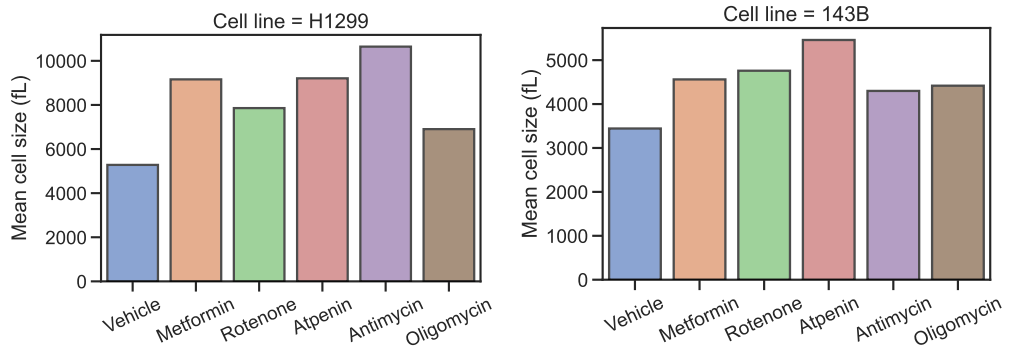


Figure 5.1: A panel of mitochondrial inhibitors all lead to cell size increase in H1299 and 143B cells. For H1299 drug treatments: vehicle (DMSO), metformin (6 mM), rotenone (50 nM), atpenin (5  $\mu$ M, 1 mM pyruvate), antimycin (5  $\mu$ M) and oligomycin (1 nM). For 143B drug treatments: vehicle (DMSO), metformin (2 mM), rotenone (50 nM), atpenin (5  $\mu$ M, 1 mM pyruvate), antimycin (100 nM) and oligomycin (5 nM). Cell size measured using a Coulter counter 3 days after drug treatment.

tivity it should phenocopy the effect of the adenylosuccinate synthase inhibitor hadacidin. Hadacidin is an aspartate analog but it is a much stronger inhibitor against adenylosuccinate synthetase than other aspartate consuming enzymes, and thus at concentrations suppressing ATP synthesis, pyrimidine and protein synthesis are intact [133, 132]. As hadacidin is a competitive inhibitor, lowering intracellular aspartate levels by complex I inhibition amplify its toxicity [110]. Similar to the hypothesized nucleotide imbalance during aspartate limitation, hadacidin treatment increases cell size causes cells to arrest in S-phase [88]. Hadacidin was found unsuitable for its original purpose as a chemotherapy [149], but it could possibly be repurposed as a tool for studying aspartate limitation.

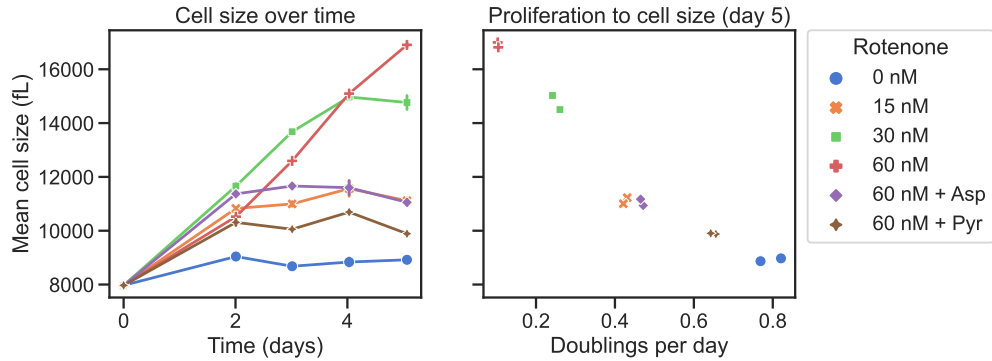


Figure 5.2: Rotenone induces an increase in H1299 cell size over time and after 5 days a linear correlation between cell size and proliferation rate is observed. Data from replicate 1 proliferation experiment shown in chapter 2, figure 2.1.

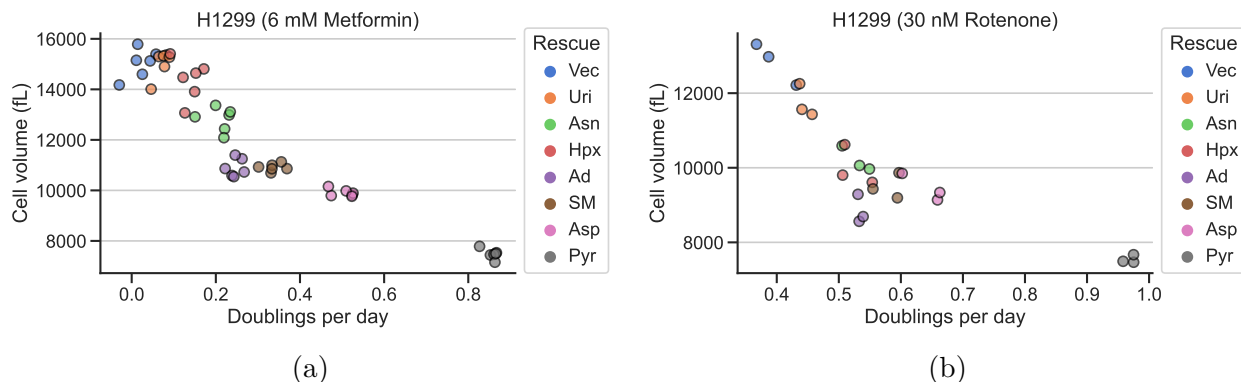


Figure 5.3: Proliferation rate correlates with cell volume across a panel of metabolites partially rescuing aspartate limitation induced with metformin or rotenone. Cell volumes in (a) and (b) from endpoint counts from figures 2.11a and 2.11b, respectively.

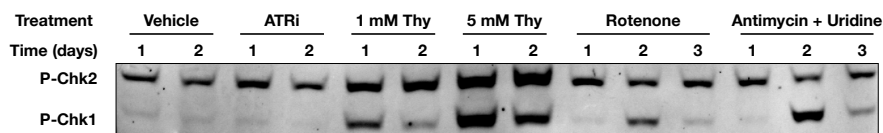


Figure 5.4: Chk1/2 phosphorylation in H1299 cells over time. Treatments: vehicle (untreated), ATRi (50 nM, AZ20), thy (1 and 5 mM thymidine), rotenone (200 nM), antimycin+uridine (5  $\mu$ M + 200  $\mu$ M).

## 5.2 Aspartate sensor

Mass spectrometry is the workhorse for detection and quantification of metabolites because of its unrivaled sensitivity and specificity while maintaining versatility. But alas, the versatility of measuring thousands of metabolites, is traded for the destructivity of sample ionization. Protein based sensors offer the inverse trade with sample preservation but low versatility and thus these approaches have the potential of being complementary.

In the study of aspartate limitation, such a biosensor can be a very useful tool. For example, in parts of chapter 2 a hypothesis is put forth about the expected intracellular aspartate level necessary to sustain proliferation with and without salvage complementation of the non-protein fates of aspartate. To generate these aspartate to proliferation curves, a large number of samples had to be collected and processed for mass spectrometry only to measure aspartate. Using the aspartate sensor, similar measurements can now be performed with much less work.

Further development and characterization could make this sensor more useful e.g. a better approach to normalization and development of expression systems tested on more cell lines. While nuclear RFP normalization appears to work quite well in practice, it remains unsatisfactory to normalize to a protein which expression is decoupled from that of the sensor's. Another unsolved issue is robust sensor expression which was good for some cell lines but poor in others. In the future, it should be exciting to use the sensor for measurement of compartmentalized aspartate pools; specifically, the mitochondria are relevant due to their role in aspartate synthesis. A particularly interesting opportunity offered by a biosensor is the ability to combine intracellular aspartate measurements with genetic screening tools. CRISPR-based screens of gene knockouts and expression induction and suppression have become widely available and often coupled to flow cytometry assisted cell sorting to select for phenotypes other than proliferation. A similar approach might not be directly applicable for the aspartate sensor because of difficulties preserving intracellular metabolite levels while cell sorting and therefore such an effort may have to use laser tagging to mark the cells before

sorting [11, 55].

### 5.3 Further development and applications of tRNA-Seq

The method presented in chapter 4 improves on two main aspects of tRNA-Seq: 1) enabling the measurement of aminoacylation quantitatively and 2) showing that non-heuristic alignment can be applied in practice. In the limit of perfect alignment performance, heuristic alignment algorithms like Bowtie, BWA, STAR, GSNAP, SHRIMP etc. become equal to the deterministic Smith-Waterman alignment. The sole reason for using heuristics is to improve efficiency i.e. reduce runtime to a manageable level, which is very important when aligning billions of reads containing hundreds of billions of nucleotides against a 3.2 billion nucleotide genome. Compare this to tRNA-Seq which produces of few dozen million reads containing a few billion nucleotides that must be aligned against a 40,000 nucleotide tRNA reference set and you get an alignment problem reduced by approximately one million fold. This, along with continued improvement of CPU speed, makes it possible to use all-against-all Smith-Waterman alignment for tRNA-Seq data. So, it is possible, it has a clear theoretic justification and it can even be used in practical settings, but is it necessary? The question is not answered in chapter 4 and currently there is no good benchmark. A good approach for such benchmark would be a simulation study to establish a ground truth and test the influence of the various parameters e.g. RT-PCR readthrough, tRNA modifications, reference set size etc. A tRNA-Seq read simulator was actually made and is available on Github ([link](#)).

Since our method was submitted, another tRNA-Seq method was published by Sun et al. [142]. Herein they use nanopore sequencing to generate reads but otherwise their data is like that generated using Illumina sequencing. They reach a similar conclusion regarding alignment and substantiate it by pointing to examples of misalignment when using BWA. These misalignments were caused by the high degree of RT-PCR generated misincorporations and could be resolved using Smith-Waterman alignment. Furthermore, they employ a statistical model to infer tRNA modifications from RT-events. This can be advantageous

because it offers a principled way of comparing differences in tRNA modification status e.g. as a response to nutritional change, drug treatments etc. Another way of modelling these RT-events would be as a Markov chain in which the tRNA modification probabilities would be described by a hidden Markov model [36].

On the chemistry side of things there are many possible improvements to be made. Past efforts have been made to improve RT-PCR readthrough, but these are far from exhaustive. Therefore, there is an opportunity to systematically test different RT polymerases, buffers, temperatures and other incubation conditions. It may even be possible to couple these tests to a selection method and develop a screen. If successful, a better readthrough would have a large impact on the method by improving read mapping and expanding the coverage of inferred tRNA modifications. Improved and expanded detection of tRNA modifications could also be achieved by using chemical treatments to “activate” a modified residue, thereby enhancing its propensity to generate an RT-event as observed for periodate treated 2-thiouridine residues. With efforts to improve detection of tRNA modifications, it will be important to control for batch variations impacting the likelihood of an RT-events, for example small difference in reagents like the dNTP concentration, RT-polymerase, buffers etc. An internal control could be devised and used similarly as the spike-in controls already employed. A convenient source for such control is *E.coli* isolated tRNA, since it has relatively few tRNA transcripts that are all easily distinguishable from human tRNA transcripts. As a control, it would be isolated once and added in small amounts to all samples. The RT-event pattern of the *E.coli* tRNA transcripts would be expected to remain constant across all samples and thus samples with large deviations could be flagged and discarded.

Regarding applications, it would be highly useful to test the method with tissue samples. There is no reason why the method should not be able to work with tissue; however, testing is warranted due to potential issues with glycogen contamination resulting in quenching of the periodate oxidation. With tissue samples, it would be interesting to first survey tRNA charge, expression and modifications across different organs or cell types, particularly those engaged in high protein expression such as pancreatic, endocrine and lymphoid tissues.

Thereafter, the method could be applied to tissues from diseases related to defects in amino acid metabolism and/or translation.

Accurate quantitative tRNA charge measurements also enable several assay developments. For example, when used in conjunction with expression of a library of tRNA sequences, it could be applied to better identify the tRNA sequence requirements of aminoacyl tRNA synthetases. Some of the tRNA elements that specify aminoacylation specificity have already been identified, but with a high-throughput method the resolution of these could greatly increase. The aminoacylation specificity can be described as a tRNA sequence's ability to be aminoacylated or not; however, a better description would be to quantify the changes in the enzyme kinetic parameters. This may be possible by taking measurements over time to make a set of progress curves from which kinetic data can be extracted using numerical integration [77, 76]. Finally, tRNA-Seq can accelerate the development of non-canonical tRNA:aminoacyl tRNA synthetases pairs in several ways. For example, by identification of tRNAs that are compatible with host tRNA processing, while only being aminoacylated upon expression of the cognate aminoacyl tRNA synthetases and not by native host enzymes.

## BIBLIOGRAPHY

- [1] Abhi Aggarwal, Rui Liu, Yang Chen, Amelia J Ralowicz, Samuel J Bergerson, Filip Tomaska, Boaz Mohar, Timothy L Hanson, Jeremy P Hasseman, Daniel Reep, Getahun Tsegaye, Pantong Yao, Xiang Ji, Marinus Kloos, Deepika Walpita, Ronak Patel, Manuel A Mohr, Paul W Tillberg, GENIE Project Team, Loren L Looger, Jonathan S Marvin, Michael B Hoppa, Arthur Konnerth, David Kleinfeld, Eric R Schreiter, and Kaspar Podgorski. Glutamate indicators with improved activation kinetics and localization for imaging synaptic transmission. *Nat. Methods*, 20(5):925–934, May 2023.
- [2] S Alefelder, B K Patel, and F Eckstein. Incorporation of terminal phosphorothioates into oligonucleotides. *Nucleic Acids Res.*, 26(21):4983–4988, November 1998.
- [3] H Furkan Alkan, Katharina E Walter, Alba Luengo, Corina T Madreiter-Sokolowski, Sarah Stryeck, Allison N Lau, Wael Al-Zoughbi, Caroline A Lewis, Craig J Thomas, Gerald Hoefer, Wolfgang F Graier, Tobias Madl, Matthew G Vander Heiden, and Julianne G Bogner-Strauss. Cytosolic aspartate availability determines cell survival when glutamine is limiting. *Cell Metab.*, 28(5):706–720.e6, November 2018.
- [4] Sylvia Andrzejewski, Simon-Pierre Gravel, Michael Pollak, and Julie St-Pierre. Metformin directly acts on mitochondria to alter cellular bioenergetics. *Cancer Metab*, 2:12, August 2014.
- [5] Paige K Arnold, Benjamin T Jackson, Katrina I Paras, Julia S Brunner, Madeleine L Hart, Oliver J Newsom, Sydney P Alibekoff, Jennifer Endress, Esther Drill, Lucas B Sullivan, and Lydia W S Finley. A non-canonical tricarboxylic acid cycle underlies cellular identity. *Nature*, pages 1–5, March 2022.
- [6] Tslil Ast and Vamsi K Mootha. Oxygen and mammalian cell culture: are we repeating the experiment of dr. ox? *Nat Metab*, 1(9):858–860, September 2019.
- [7] Will Bailis, Justin A Shyer, Jun Zhao, Juan Carlos Garcia Canaveras, Fatimah J Al Khazal, Rihao Qu, Holly R Steach, Piotr Bielecki, Omair Khan, Ruaidhri Jackson, Yuval Kluger, Louis J Maher, 3rd, Joshua Rabinowitz, Joe Craft, and Richard A Flavell. Distinct modes of mitochondrial metabolism uncouple T cell differentiation and function. *Nature*, 571(7765):403–407, July 2019.

- [8] Caroline R Bartman, Tara TeSlaa, and Joshua D Rabinowitz. Quantitative flux analysis in mammals. *Nature Metabolism*, pages 1–13, July 2021.
- [9] Markus Basan, Sheng Hui, Hiroyuki Okano, Zhongge Zhang, Yang Shen, James R Williamson, and Terence Hwa. Overflow metabolism in escherichia coli results from efficient proteome allocation. *Nature*, 528(7580):99–104, December 2015.
- [10] Andrew Behrens, Geraldine Rodschinka, and Danny D Nedialkova. High-resolution quantitative profiling of tRNA abundance and modification status in eukaryotes by mim-tRNAsq. *Mol. Cell*, February 2021.
- [11] Loïc Binan, Javier Mazzaferri, Karine Choquet, Louis-Etienne Lorenzo, Yu Chang Wang, El Bachir Affar, Yves De Koninck, Jiannis Ragoussis, Claudia L Kleinman, and Santiago Costantino. Live single-cell laser tag. *Nat. Commun.*, 7:11636, May 2016.
- [12] Kivanç Birsoy, Richard Possemato, Franziska K Lorbeer, Erol C Bayraktar, Prathapan Thiru, Burcu Yucel, Tim Wang, Walter W Chen, Clary B Clish, and David M Sabatini. Metabolic determinants of cancer cell sensitivity to glucose limitation and biguanides. *Nature*, 508(7494):108–112, April 2014.
- [13] Kivanç Birsoy, Tim Wang, Walter W Chen, Elizaveta Freinkman, Monther Abu-Remaileh, and David M Sabatini. An essential role of the mitochondrial electron transport chain in cell proliferation is to enable aspartate synthesis. *Cell*, 162(3):540–551, July 2015.
- [14] Tania Bour, Aziza Akaddar, Bernard Lorber, Sébastien Blais, Christian Balg, Ermanno Candolfi, and Magali Frugier. Plasmoidal aspartyl-tRNA synthetases and peculiarities in plasmodium falciparum. *J. Biol. Chem.*, 284(28):18893–18903, July 2009.
- [15] Martin D Brand and David G Nicholls. Assessing mitochondrial dysfunction in cells. *Biochem. J.*, 435(2):297–312, April 2011.
- [16] P M Bruinenberg, J P Van Dijken, and W A Scheffers. A theoretical analysis of NADPH production and consumption in yeasts. *Microbiology*, 129(4):953–964, April 1983.
- [17] Brian S Bull and Karen L Hay. Is the packed cell volume (PCV) reliable? *Lab. Hematol.*, 7:191–196, 2001.
- [18] Simone Cardaci, Liang Zheng, Gillian MacKay, Niels J F van den Broek, Elaine D MacKenzie, Colin Nixon, David Stevenson, Sergey Tumanov, Vinay Bulusu, Jurre J Kamphorst, Alexei Vazquez, Stewart Fleming, Francesca Schiavi, Gabriela Kalna,

- Karen Blyth, Douglas Strathdee, and Eyal Gottlieb. Pyruvate carboxylation enables growth of SDH-deficient cells by supporting aspartate biosynthesis. *Nat. Cell Biol.*, 17(10):1317–1326, October 2015.
- [19] A Carter, P J Crosland-Taylor, and J W Stewart. Measurement of mean corpuscular and packed cell volumes with a coulter cell counter. *J. Clin. Pathol.*, 21(2):222–224, March 1968.
  - [20] Patricia P Chan and Todd M Lowe. GtRNAdb 2.0: an expanded database of transfer RNA genes identified in complete and draft genomes. *Nucleic Acids Res.*, 44(D1):D184–9, January 2016.
  - [21] Navdeep S Chandel. Metabolism of proliferating cells. *Cold Spring Harb. Perspect. Biol.*, 13(10), October 2021.
  - [22] Li Chen, Zhaoyue Zhang, Atsushi Hoshino, Henry D Zheng, Michael Morley, Zoltan Arany, and Joshua D Rabinowitz. NADPH production by the oxidative pentose-phosphate pathway supports folate metabolism. *Nat Metab*, 1:404–415, March 2019.
  - [23] Walter W Chen, Elizaveta Freinkman, Tim Wang, Kivanç Birsoy, and David M Sabatini. Absolute quantification of matrix metabolites reveals the dynamics of mitochondrial metabolism. *Cell*, 166(5):1324–1337.e11, August 2016.
  - [24] Wesley C Clark, Molly E Evans, Dan Dominissini, Guanqun Zheng, and Tao Pan. tRNA base methylation identification and quantification via high-throughput sequencing. *RNA*, 22(11):1771–1784, November 2016.
  - [25] Kendall J Condon, Jose M Orozco, Charles H Adelmann, Jessica B Spinelli, Pim W van der Helm, Justin M Roberts, Tenzin Kunchok, and David M Sabatini. Genome-wide CRISPR screens reveal multitiered mechanisms through which mTORC1 senses mitochondrial dysfunction. *Proc. Natl. Acad. Sci. U. S. A.*, 118(4), January 2021.
  - [26] Aaron E Cozen, Erin Quartley, Andrew D Holmes, Eva Hrabetá-Robinson, Eric M Phizicky, and Todd M Lowe. ARM-seq: AlkB-facilitated RNA methylation sequencing reveals a complex landscape of modified tRNA fragments. *Nat. Methods*, 12(9):879–884, September 2015.
  - [27] Alicia M Darnell, Arvind R Subramaniam, and Erin K O’Shea. Translational control through differential ribosome pausing during amino acid limitation in mammalian cells. *Mol. Cell*, 71(2):229–243.e11, July 2018.

- [28] R H De Deken. The crabtree effect: a regulatory system in yeast. *J. Gen. Microbiol.*, 44(2):149–156, August 1966.
- [29] Lauren P Diebold, Hyea Jin Gil, Peng Gao, Carlos A Martinez, Samuel E Weinberg, and Navdeep S Chandel. Mitochondrial complex III is necessary for endothelial cell proliferation during angiogenesis. *Nat Metab*, 1(1):158–171, January 2019.
- [30] Frances F Diehl, Caroline A Lewis, Brian P Fiske, and Matthew G Vander Heiden. Cellular redox state constrains serine synthesis and nucleotide production to impact cell proliferation. *Nature Metabolism*, 1(9):861–867, September 2019.
- [31] Frances F Diehl, Teemu P Miettinen, Ryan Elbashir, Christopher S Nabel, Alicia M Darnell, Brian T Do, Scott R Manalis, Caroline A Lewis, and Matthew G Vander Heiden. Nucleotide imbalance decouples cell growth from cell proliferation. *Nat. Cell Biol.*, 24(8):1252–1264, August 2022.
- [32] Kimberly A Dittmar, Michael A Sørensen, Johan Elf, Måns Ehrenberg, and Tao Pan. Selective charging of tRNA isoacceptors induced by amino-acid starvation. *EMBO Rep.*, 6(2):151–157, February 2005.
- [33] Gregory S Ducker, Li Chen, Raphael J Morscher, Jonathan M Ghergurovich, Mark Esposito, Xin Teng, Yibin Kang, and Joshua D Rabinowitz. Reversal of cytosolic One-Carbon flux compensates for loss of the mitochondrial folate pathway. *Cell Metab.*, 23(6):1140–1153, June 2016.
- [34] Gregory S Ducker, Jonathan M Ghergurovich, Nello Mainolfi, Vipin Suri, Stephanie K Jeong, Sophia Hsin-Jung Li, Adam Friedman, Mark G Manfredi, Zemer Gitai, Hahn Kim, and Joshua D Rabinowitz. Human SHMT inhibitors reveal defective glycine import as a targetable metabolic vulnerability of diffuse large b-cell lymphoma. *Proc. Natl. Acad. Sci. U. S. A.*, 114(43):11404–11409, October 2017.
- [35] G A Dunaway. A review of animal phosphofructokinase isozymes with an emphasis on their physiological role. *Mol. Cell. Biochem.*, 52(1):75–91, 1983.
- [36] Richard Durbin, Sean R Eddy, Anders Krogh, and Graeme Mitchison. *Biological sequence analysis: probabilistic models of proteins and nucleic acids*. Cambridge university press, 1998.
- [37] J R Dyer. Use of periodate oxidations in biochemical analysis. *Methods Biochem. Anal.*, 3:111–152, 1956.

- [38] Mohamad-Yehia El-Mir, Véronique Nogueira, Eric Fontaine, Nicole Avéret, Michel Rigoulet, and Xavier Leverve. Dimethylbiguanide inhibits cell respiration via an indirect effect targeted on the respiratory chain complex I \*. *J. Biol. Chem.*, 275(1):223–228, January 2000.
- [39] Ian Engstrom, Kristian Davidsen, and Lucas Sullivan. Packed cell volume is an overestimate in common cancer cell lines. *Bio Protoc.*, 11(21), 2021.
- [40] Lieselotte Erber, Anne Hoffmann, Jörg Fallmann, Heike Betat, Peter F Stadler, and Mario Mörl. LOTTE-seq (long hairpin oligonucleotide based tRNA high-throughput sequencing): specific selection of tRNAs with 3'-CCA end for high-throughput sequencing. *RNA Biol.*, 17(1):23–32, January 2020.
- [41] J W B Erskine, C R N Strouts, G Walley, and W Lazarus. A simple volumetric method for the routine determination of glycerol. *Analyst*, 78(932):630–636, January 1953.
- [42] C Escalante and D C Yang. Expression of human aspartyl-tRNA synthetase in escherichia coli. functional analysis of the n-terminal putative amphiphilic helix. *J. Biol. Chem.*, 268(8):6014–6023, March 1993.
- [43] Molly E Evans, Wesley C Clark, Guanqun Zheng, and Tao Pan. Determination of tRNA aminoacylation levels by high-throughput sequencing. *Nucleic Acids Res.*, 45(14):e133, August 2017.
- [44] Min Fang, Zhirong Shen, Song Huang, Liping Zhao, She Chen, Tak W Mak, and Xiaodong Wang. The ER UDPase ENTPD5 promotes protein n-glycosylation, the warburg effect, and proliferation in the PTEN pathway. *Cell*, 143(5):711–724, November 2010.
- [45] Ryan T Fuchs, Zhiyi Sun, Fanglei Zhuang, and G Brett Robb. Bias in ligation-based small RNA sequencing library construction is determined by adaptor and RNA structure. *PLoS One*, 10(5):e0126049, May 2015.
- [46] H Furkan Alkan, Katharina E Walter, Hubert Hackl, Matthew G Vander Heiden, Tobias Madl, and Juliane G Bogner-Strauss. N-acetylaspartate improves cell survival when glucose is limiting. *bioRxiv*, page 2020.05.28.114629, May 2020.
- [47] Javier Garcia-Bermudez, Michael A Badgley, Sheela Prasad, Lou Baudrier, Yuyang Liu, Konnor La, Mariluz Soula, Robert T Williams, Norihiro Yamaguchi, Rosa F Hwang, Laura J Taylor, Elisa de Stanchina, Bety Rostandy, Hanan Alwaseem, Henrik Molina, Dafna Bar-Sagi, and Kivanç Birsoy. Adaptive stimulation of macropinocytosis overcomes aspartate limitation in cancer cells under hypoxia. *Nat Metab*, 4(6):724–738, June 2022.

- [48] Javier Garcia-Bermudez, Lou Baudrier, Konnor La, Xiphias Ge Zhu, Justine Fidelin, Vladislav O Sviderskiy, Thales Papagiannakopoulos, Henrik Molina, Matija Snuderl, Caroline A Lewis, Richard L Possemato, and Kivanç Birsoy. Aspartate is a limiting metabolite for cancer cell proliferation under hypoxia and in tumours. *Nat. Cell Biol.*, 20(7):775–781, July 2018.
- [49] Jonathan M Ghergurovich, Mark Esposito, Zihong Chen, Joshua Z Wang, Vrushank Bhatt, Taijin Lan, Eileen White, Yibin Kang, Jessie Yanxiang Guo, and Joshua D Rabinowitz. Glucose-6-phosphate dehydrogenase is not essential for K-Ras-driven tumor growth or metastasis. *Cancer Res.*, July 2020.
- [50] Jonathan M Ghergurovich, Juan C García-Cañaveras, Joshua Wang, Emily Schmidt, Zhaoyue Zhang, Tara TeSlaa, Harshel Patel, Li Chen, Emily C Britt, Marta Piqueras-Nebot, Mari Carmen Gomez-Cabrera, Agustín Lahoz, Jing Fan, Ulf H Beier, Hahn Kim, and Joshua D Rabinowitz. A small molecule G6PD inhibitor reveals immune dependence on pentose phosphate pathway. *Nat. Chem. Biol.*, 16(7):731–739, July 2020.
- [51] Dan Y Gui, Lucas B Sullivan, Alba Luengo, Aaron M Hosios, Lauren N Bush, Nadege Gitego, Shawn M Davidson, Elizaveta Freinkman, Craig J Thomas, and Matthew G Vander Heiden. Environment dictates dependence on mitochondrial complex I for NAD<sup>+</sup> and aspartate production and determines cancer cell sensitivity to metformin. *Cell Metab.*, 24(5):716–727, November 2016.
- [52] Xiaoyan Guo, Giovanni Aviles, Yi Liu, Ruilin Tian, Bret A Unger, Yu-Hsiu T Lin, Arun P Wiita, Ke Xu, M Almira Correia, and Martin Kampmann. Mitochondrial stress is relayed to the cytosol by an OMA1–DELE1–HRI pathway. *Nature*, March 2020.
- [53] Robert B Hamanaka and Navdeep S Chandel. Targeting glucose metabolism for cancer therapy. *J. Exp. Med.*, 209(2):211–215, February 2012.
- [54] Madeleine L Hart, Evan Quon, Anna-Lena B G Vigil, Ian A Engstrom, Oliver J Newsom, Kristian Davidsen, Pia Hoellerbauer, Samantha M Carlisle, and Lucas B Sullivan. Mitochondrial redox adaptations enable alternative aspartate synthesis in SDH-deficient cells. *Elife*, 12, March 2023.
- [55] Nicholas Hasle, Anthony Cooke, Sanjay Srivatsan, Heather Huang, Jason J Stephany, Zachary Krieger, Dana Jackson, Weiliang Tang, Sriram Pendyala, Raymond J Monnat, Jr, Cole Trapnell, Emily M Hatch, and Douglas M Fowler. High-throughput, microscope-based sorting to dissect cellular heterogeneity. *Mol. Syst. Biol.*, 16(6):e9442, June 2020.

- [56] Jiuya He, Holly C Ford, Joe Carroll, Corsten Douglas, Evvia Gonzales, Shujing Ding, Ian M Fearnley, and John E Walker. Assembly of the membrane domain of ATP synthase in human mitochondria. *Proc. Natl. Acad. Sci. U. S. A.*, 115(12):2988–2993, March 2018.
- [57] Ilka U Heinemann, Akiyoshi Nakamura, Patrick O’Donoghue, Daniel Eiler, and Dieter Söll. tRNAHis-guanylyltransferase establishes tRNAHis identity. *Nucleic Acids Res.*, 40(1):333–344, January 2012.
- [58] Nordine Helassa, Céline D Dürst, Catherine Coates, Silke Kerruth, Urwa Arif, Christian Schulze, J Simon Wiegert, Michael Geeves, Thomas G Oertner, and Katalin Török. Ultrafast glutamate sensors resolve high-frequency release at schaffer collateral synapses. *Proc. Natl. Acad. Sci. U. S. A.*, 115(21):5594–5599, May 2018.
- [59] Iiro Taneli Helenius, Hanumantha Rao Madala, and Jing-Ruey Joanna Yeh. An asp to strike out cancer? therapeutic possibilities arising from aspartate’s emerging roles in cell proliferation and survival. *Biomolecules*, 11(11), November 2021.
- [60] Lars Hellweg, Martin Pfeifer, Lena Chang, Miroslaw Tarnawski, Andrea Bergner, Jana Kress, Julien Hiblot, Jürgen Reinhardt, Kai Johnsson, and Philipp Leippe. Engineering of a biosensor for intracellular aspartate. *bioRxiv*, 2023.
- [61] D Hentzen, P Mandel, and J P Garel. Relation between aminoacyl-tRNA stability and the fixed amino acid. *Biochim. Biophys. Acta*, 281(2):228–232, October 1972.
- [62] Xavier Hernandez-Alias, Christopher D Katanski, Wen Zhang, Mahdi Assari, Christopher P Watkins, Martin H Schaefer, Luis Serrano, and Tao Pan. Single-read tRNA-seq analysis reveals coordination of tRNA modification and aminoacylation and fragmentation. *Nucleic Acids Res.*, December 2022.
- [63] Y S Ho and Y W Kan. In vivo aminoacylation of human and xenopus suppressor tRNAs constructed by site-specific mutagenesis. *Proc. Natl. Acad. Sci. U. S. A.*, 84(8):2185–2188, April 1987.
- [64] Anne Hoffmann, Jörg Fallmann, Elisa Vilardo, Mario Mörl, Peter F Stadler, and Fabian Amman. Accurate mapping of tRNA reads. *Bioinformatics*, 34(7):1116–1124, April 2018.
- [65] C L Holcomb, M Rastrou, T C Williams, D Goodridge, A M Lazaro, M Tilanus, and H A Erlich. Next-generation sequencing can reveal in vitro-generated PCR crossover products: some artifactual sequences correspond to HLA alleles in the IMGT/HLA database. *Tissue Antigens*, 83(1):32–40, January 2014.

- [66] Aaron M Hosios, Vivian C Hecht, Laura V Danai, Marc O Johnson, Jeffrey C Rathmell, Matthew L Steinhauser, Scott R Manalis, and Matthew G Vander Heiden. Amino acids rather than glucose account for the majority of cell mass in proliferating mammalian cells. *Dev. Cell*, 36(5):540–549, March 2016.
- [67] Yonglin Hu, Cheng-Peng Fan, Guangsen Fu, Deyu Zhu, Qi Jin, and Da-Cheng Wang. Crystal structure of a glutamate/aspartate binding protein complexed with a glutamate molecule: structural basis of ligand specificity at atomic resolution. *J. Mol. Biol.*, 382(1):99–111, September 2008.
- [68] Daphne H E W Huberts, Bastian Niebel, and Matthias Heinemann. A flux-sensing mechanism could regulate the switch between respiration and fermentation. *FEMS Yeast Res.*, 12(2):118–128, March 2012.
- [69] G Hunter. On the hydrolysis of guanine. *Biochem. J*, 30(7):1183–1188, July 1936.
- [70] National Cancer Institute. Nci-60 cancer cell lines. [https://dtp.cancer.gov/discovery\\_development/nci-60/cell\\_list.htm](https://dtp.cancer.gov/discovery_development/nci-60/cell_list.htm). Accessed: 2023-10-27.
- [71] William J Israelsen and Matthew G Vander Heiden. ATP consumption promotes cancer metabolism. *Cell*, 143(5):669–671, November 2010.
- [72] S Iwata, J W Lee, K Okada, J K Lee, M Iwata, B Rasmussen, T A Link, S Ramaswamy, and B K Jap. Complete structure of the 11-subunit bovine mitochondrial cytochrome bc<sub>1</sub> complex. *Science*, 281(5373):64–71, July 1998.
- [73] Cholsoon Jang, Li Chen, and Joshua D Rabinowitz. Metabolomics and isotope tracing. *Cell*, 173(4):822–837, May 2018.
- [74] Inga Jarmoskaite, Ishraq AlSadhan, Pavanapuresan P Vaidyanathan, and Daniel Herschlag. How to measure and evaluate binding affinities. *Elife*, 9, August 2020.
- [75] Anitha D Jayaprakash, Omar Jabado, Brian D Brown, and Ravi Sachidanandam. Identification and remediation of biases in the activity of RNA ligases in small-RNA deep sequencing. *Nucleic Acids Res.*, 39(21):e141, November 2011.
- [76] Kenneth A Johnson. A century of enzyme kinetic analysis, 1913 to 2013. *FEBS Lett.*, 587(17):2753–2766, September 2013.
- [77] Kenneth A Johnson, Zachary B Simpson, and Thomas Blom. FitSpace explorer: an algorithm to evaluate multidimensional parameter space in fitting kinetic data. *Anal. Biochem.*, 387(1):30–41, April 2009.

- [78] Christopher D Katanski, Christopher P Watkins, Wen Zhang, Matthew Reyer, Samuel Miller, and Tao Pan. Analysis of queuosine and 2-thio tRNA modifications by high throughput sequencing. *Nucleic Acids Res.*, 50(17):e99, September 2022.
- [79] Brandon M Kenwood, Janelle L Weaver, Amandeep Bajwa, Ivan K Poon, Frances L Byrne, Beverley A Murrow, Joseph A Calderone, Liping Huang, Ajit S Divakaruni, Jose L Tomsig, Kohki Okabe, Ryan H Lo, G Cameron Coleman, Linda Columbus, Zhen Yan, Jeffrey J Saucerman, Jeffrey S Smith, Jeffrey W Holmes, Kevin R Lynch, Kodi S Ravichandran, Seiichi Uchiyama, Webster L Santos, George W Rogers, Mark D Okusa, Douglas A Bayliss, and Kyle L Hoehn. Identification of a novel mitochondrial uncoupler that does not depolarize the plasma membrane. *Mol Metab.*, 3(2):114–123, April 2014.
- [80] J X Khym and W E Cohn. Amine-induced cleavage of periodate-oxidized nucleotide residues. *J. Biol. Chem.*, 236:PC9–10, March 1961.
- [81] J X Khym and M Uziel. The use of the cetyltrimethylammonium cation in terminal sequence analyses of ribonucleic acids. *Biochemistry*, 7(1):422–426, January 1968.
- [82] Alexander I Kostyuk, Aleksandra D Demidovich, Daria A Kotova, Vsevolod V Belousov, and Dmitry S Bilan. Circularly permuted fluorescent Protein-Based indicators: History, principles, and classification. *Int. J. Mol. Sci.*, 20(17), August 2019.
- [83] Dorothy Koveal, Carlos Manlio Díaz-García, and Gary Yellen. Fluorescent biosensors for neuronal metabolism and the challenges of quantitation. *Curr. Opin. Neurobiol.*, 63:111–121, August 2020.
- [84] Abigail S Krall, Peter J Mullen, Felicia Surjono, Milica Momcilovic, Ernst W Schmid, Christopher J Halbrook, Apisadaporn Thambundit, Steven D Mittelman, Costas A Lyssiotis, David B Shackelford, Simon R V Knott, and Heather R Christofk. Asparagine couples mitochondrial respiration to ATF4 activity and tumor growth. *Cell Metab.*, 33(5):1013–1026.e6, May 2021.
- [85] Harry Kroll. The participation of heavy metal ions in the hydrolysis of amino acid esters1. *J. Am. Chem. Soc.*, 74(8):2036–2039, April 1952.
- [86] T A Kunkel. Rapid and efficient site-specific mutagenesis without phenotypic selection. *Proc. Natl. Acad. Sci. U. S. A.*, 82(2):488–492, January 1985.
- [87] Charles River Laboratories. Charles river tumor model compendium. <https://compendium.criver.com/compendium2/cancertype?species.id=1>. Accessed: 2023-10-27.

- [88] C Ladino, E E Schneeberger, C A Rabito, and R D Lynch. Reduction of adenine nucleotide content of clone 4 MDCK cells: effects on multiplication, protein synthesis, and morphology. *J. Cell. Physiol.*, 140(1):186–194, July 1989.
- [89] Ben Langmead and Steven L Salzberg. Fast gapped-read alignment with bowtie 2. *Nat. Methods*, 9(4):357–359, March 2012.
- [90] Ben Langmead, Cole Trapnell, Mihai Pop, and Steven L Salzberg. Ultrafast and memory-efficient alignment of short DNA sequences to the human genome. *Genome Biol.*, 10(3):R25, March 2009.
- [91] Jenna M Lentini, Jillian Ramos, and Dragony Fu. Monitoring the 5-methoxycarbonylmethyl-2-thiouridine (mcm5s2u) modification in eukaryotic tRNAs via the  $\gamma$ -toxin endonuclease. *RNA*, 24(5):749–758, May 2018.
- [92] R Lipshitz and E Chargaff. Studies on the fractionation of ribonucleic acid. *Biochim. Biophys. Acta*, 42:544–546, August 1960.
- [93] Ling Liu, Xiaoyang Su, William J Quinn, 3rd, Sheng Hui, Kristin Krukenberg, David W Frederick, Philip Redpath, Le Zhan, Karthikeyani Chellappa, Eileen White, Marie Migaud, Timothy J Mitchison, Joseph A Baur, and Joshua D Rabinowitz. Quantitative analysis of NAD Synthesis-Breakdown fluxes. *Cell Metab.*, 27(5):1067–1080.e5, May 2018.
- [94] Morghan C Lucas, Leszek P Pryszcz, Rebeca Medina, Ivan Milenkovic, Noelia Camacho, Virginie Marchand, Yuri Motorin, Lluís Ribas de Pouplana, and Eva Maria Novoa. Quantitative analysis of tRNA abundance and modifications by nanopore RNA sequencing. *Nat. Biotechnol.*, pages 1–15, April 2023.
- [95] Alba Luengo, Dan Y Gui, and Matthew G Vander Heiden. Targeting metabolism for cancer therapy. *Cell Chem Biol*, 24(9):1161–1180, September 2017.
- [96] Alba Luengo, Zhaoqi Li, Dan Y Gui, Lucas B Sullivan, Maria Zagorulya, Brian T Do, Raphael Ferreira, Adi Naamati, Ahmed Ali, Caroline A Lewis, Craig J Thomas, Stefani Spranger, Nicholas J Matheson, and Matthew G Vander Heiden. Increased demand for NAD<sup>+</sup> relative to ATP drives aerobic glycolysis. *Mol. Cell*, 81(4):691–707.e6, February 2021.
- [97] Carl Malina, Rosemary Yu, Johan Björkeroth, Eduard J Kerkhoven, and Jens Nielsen. Adaptations in metabolism and protein translation give rise to the crabtree effect in yeast. *Proc. Natl. Acad. Sci. U. S. A.*, 118(51), December 2021.

- [98] R Markham and J D Smith. A source of error in amino acid analysis. *Nature*, 164(4181):1052, December 1949.
- [99] Jonathan S Marvin, Bart G Borghuis, Lin Tian, Joseph Cichon, Mark T Harnett, Jasper Akerboom, Andrew Gordus, Sabine L Renninger, Tsai-Wen Chen, Cornelia I Bargmann, Michael B Orger, Eric R Schreiter, Jonathan B Demb, Wen-Biao Gan, S Andrew Hires, and Loren L Looger. An optimized fluorescent probe for visualizing glutamate neurotransmission. *Nat. Methods*, 10(2):162–170, February 2013.
- [100] Jonathan S Marvin, Benjamin Scholl, Daniel E Wilson, Kaspar Podgorski, Abbas Kazemipour, Johannes Alexander Müller, Susanne Schoch, Francisco José Urra Quiroz, Nelson Rebola, Huan Bao, Justin P Little, Ariana N Tkachuk, Edward Cai, Adam W Hantman, Samuel S-H Wang, Victor J DePiero, Bart G Borghuis, Edwin R Chapman, Dirk Dietrich, David A DiGregorio, David Fitzpatrick, and Loren L Looger. Stability, affinity, and chromatic variants of the glutamate sensor iGluSnFR. *Nat. Methods*, 15(11):936–939, November 2018.
- [101] Nicholas J McGlincy and Nicholas T Ingolia. Transcriptome-wide measurement of translation by ribosome profiling. *Methods*, 126:112–129, August 2017.
- [102] S R McKeown. Defining normoxia, physoxia and hypoxia in tumours-implications for treatment response. *Br. J. Radiol.*, 87(1035):20130676, March 2014.
- [103] Marie Messmer, Sébastien P Blais, Christian Balg, Robert Chênevert, Luc Grenier, Patrick Lagüe, Claude Sauter, Marie Sissler, Richard Giegé, Jacques Lapointe, and Catherine Florentz. Peculiar inhibition of human mitochondrial aspartyl-tRNA synthetase by adenylate analogs. *Biochimie*, 91(5):596–603, May 2009.
- [104] Eran Mick, Denis V Titov, Owen S Skinner, Rohit Sharma, Alexis A Jourdain, and Vamsi K Mootha. Distinct mitochondrial defects trigger the integrated stress response depending on the metabolic state of the cell. *Elife*, 9:e49178, May 2020.
- [105] Pierre Millard, Baudoin Delépine, Matthieu Guionnet, Maud Heuillet, Floriant Bel-lvert, and Fabien Létisse. IsoCor: isotope correction for high-resolution MS labeling experiments. *Bioinformatics*, 35(21):4484–4487, November 2019.
- [106] Sabine Mohr, Eman Ghanem, Whitney Smith, Dennis Sheeter, Yidan Qin, Olga King, Damon Polioudakis, Vishwanath R Iyer, Scott Hunicke-Smith, Sajani Swamy, Scott Kuersten, and Alan M Lambowitz. Thermostable group II intron reverse transcriptase fusion proteins and their use in cDNA synthesis and next-generation RNA sequencing. *RNA*, 19(7):958–970, July 2013.

- [107] Douwe Molenaar, Rogier van Berlo, Dick de Ridder, and Bas Teusink. Shifts in growth strategies reflect tradeoffs in cellular economics. *Mol. Syst. Biol.*, 5:323, November 2009.
- [108] Yuri Motorin, Sébastien Muller, Isabelle Behm-Ansmant, and Christiane Branolant. Identification of modified residues in RNAs by reverse Transcription-Based methods. In *Methods in Enzymology*, volume 425, pages 21–53. Academic Press, January 2007.
- [109] H C Neu and L A Heppel. NUCLEOTIDE SEQUENCE ANALYSIS OF POLYRIBONUCLEOTIDES BY MEANS OF PERIODATE OXIDATION FOLLOWED BY CLEAVAGE WITH AN AMINE. *J. Biol. Chem.*, 239:2927–2934, September 1964.
- [110] Robert E Neuman and Alfred A Tytell. Inhibitory effects of hadacidin on KB cell cultures. *Proc. Soc. Exp. Biol. Med.*, 112(1):57–61, January 1963.
- [111] Edward J O'Brien, Joshua A Lerman, Roger L Chang, Daniel R Hyduke, and Bernhard Ø Palsson. Genome-scale models of metabolism and gene expression extend and refine growth phenotype prediction. *Mol. Syst. Biol.*, 9:693, October 2013.
- [112] M R Owen, E Doran, and A P Halestrap. Evidence that metformin exerts its anti-diabetic effects through inhibition of complex 1 of the mitochondrial respiratory chain. *Biochem. J.*, 348 Pt 3:607–614, June 2000.
- [113] Junyoung O Park, Sara A Rubin, Yi-Fan Xu, Daniel Amador-Noguez, Jing Fan, Tomer Shlomi, and Joshua D Rabinowitz. Metabolite concentrations, fluxes and free energies imply efficient enzyme usage. *Nat. Chem. Biol.*, 12(7):482–489, July 2016.
- [114] Junyoung O Park, Lukas B Tanner, Monica H Wei, Daven B Khana, Tyler B Jacobson, Zheyun Zhang, Sara A Rubin, Sophia Hsin-Jung Li, Meytal B Higgins, David M Stevenson, Daniel Amador-Noguez, and Joshua D Rabinowitz. Near-equilibrium glycolysis supports metabolic homeostasis and energy yield. *Nat. Chem. Biol.*, 15(10):1001–1008, October 2019.
- [115] Deven Patel, Deepak Menon, Elyssa Bernfeld, Victoria Mroz, Sampada Kalan, Diego Loayza, and David A Foster. Aspartate rescues s-phase arrest caused by suppression of glutamine utilization in KRas-driven cancer cells. *J. Biol. Chem.*, 291(17):9322–9329, April 2016.
- [116] Natalya N Pavlova, Sheng Hui, Jonathan M Ghergurovich, Jing Fan, Andrew M Intlekofer, Richard M White, Joshua D Rabinowitz, Craig B Thompson, and Ji Zhang. As extracellular glutamine levels decline, asparagine becomes an essential amino acid. *Cell Metab.*, 27(2):428–438.e5, February 2018.

- [117] Natalya N Pavlova, Bryan King, Rachel H Josselsohn, Sara Violante, Victoria L Macera, Santosha A Vardhana, Justin R Cross, and Craig B Thompson. Translation in amino-acid-poor environments is limited by tRNAGln charging. *Elife*, 9, December 2020.
- [118] Jacob R Peacock, Ryan R Walvoord, Angela Y Chang, Marisa C Kozlowski, Howard Gamper, and Ya-Ming Hou. Amino acid-dependent stability of the acyl linkage in aminoacyl-tRNA. *RNA*, 20(6):758–764, June 2014.
- [119] T Pfeiffer, S Schuster, and S Bonhoeffer. Cooperation and competition in the evolution of ATP-producing pathways. *Science*, 292(5516):504–507, April 2001.
- [120] Otis Pinkard, Sean McFarland, Thomas Sweet, and Jeff Coller. Quantitative tRNA-sequencing uncovers metazoan tissue-specific tRNA regulation. *Nat. Commun.*, 11(1):4104, August 2020.
- [121] Le Qi, Misty S Martin-Sandoval, Salma Merchant, Wen Gu, Matthias Eckhardt, Thomas P Mathews, Zhiyu Zhao, Michalis Agathocleous, and Sean J Morrison. Aspartate availability limits hematopoietic stem cell function during hematopoietic regeneration. *Cell Stem Cell*, August 2021.
- [122] D H Rammler. Periodate oxidations of enamines. i. oxidation of adenosine 5'-monophosphate in the presence of methylamine. *Biochemistry*, 10(25):4699–4705, December 1971.
- [123] Y S Rao and J D Cherayil. Studies on chemical modification of thionucleosides in the transfer ribonucleic acid of escherichia coli. *Biochem. J.*, 143(2):285–294, November 1974.
- [124] Torbjørn Rognes. Faster Smith-Waterman database searches with inter-sequence SIMD parallelisation. *BMC Bioinformatics*, 12:221, June 2011.
- [125] Maheswaran Rohan, Alastair Fairweather, and Natasha Grainger. Using gamma distribution to determine half-life of rotenone, applied in freshwater. *Sci. Total Environ.*, 527-528:246–251, September 2015.
- [126] Marco A Saraiva, Carlos M Borges, and M Helena Florêncio. Reactions of a modified lysine with aldehydic and diketonic dicarbonyl compounds: an electrospray mass spectrometry structure/activity study. *J. Mass Spectrom.*, 41(2):216–228, February 2006.

- [127] Aldema Sas-Chen and Schraga Schwartz. Misincorporation signatures for detecting modifications in mRNA: Not as simple as it sounds. *Methods*, 156:53–59, March 2019.
- [128] P Schofield and P C Zamecnik. Cupric ion catalysis in hydrolysis of aminoacyl-tRNA. *Biochim. Biophys. Acta*, 155(2):410–416, February 1968.
- [129] Perry Scholnick, Dennis Lang, and Efraim Racker. Regulatory mechanisms in carbohydrate metabolism. *J. Biol. Chem.*, 248(14):5175–5182, July 1973.
- [130] Lokendra K Sharma, Jianxin Lu, and Yidong Bai. Mitochondrial respiratory complex i: structure, function and implication in human diseases. *Curr. Med. Chem.*, 16(10):1266–1277, 2009.
- [131] Megumi Shigematsu, Shozo Honda, Phillip Loher, Aristeidis G Telonis, Isidore Rigoutsos, and Yohei Kirino. YAMAT-seq: an efficient method for high-throughput sequencing of mature transfer RNAs. *Nucleic Acids Res.*, 45(9):e70, May 2017.
- [132] H T Shigeura and C N Gordon. Further studies on the activity of hadacidin. *Cancer Res.*, 22:1356–1361, December 1962.
- [133] H T Shigeura and C N Gordon. The mechanism of action of hadacidin. *J. Biol. Chem.*, 237:1937–1940, June 1962.
- [134] Alba Signes and Erika Fernandez-Vizarra. Assembly of mammalian oxidative phosphorylation complexes I-V and supercomplexes. *Essays Biochem.*, 62(3):255–270, July 2018.
- [135] Andrew M Smith, Robin Abu-Shumays, Mark Akeson, and David L Bernick. Capture, unfolding, and detection of individual tRNA molecules using a nanopore device. *Front Bioeng Biotechnol*, 3:91, June 2015.
- [136] M M Stayton, F B Rudolph, and H J Fromm. Regulation, genetics, and properties of adenylosuccinate synthetase: a review. *Curr. Top. Cell. Regul.*, 22:103–141, 1983.
- [137] Thomas Søndergaard Stenum, Michael A Sørensen, and Sine Lo Svenningsen. Quantification of the abundance and charging levels of transfer RNAs in escherichia coli. *J. Vis. Exp.*, 1(126), August 2017.
- [138] Adolph Strecker. Untersuchungen über die chemischen beziehungen zwischen guanin, xanthin, theobromin, cafféin und kreatinin. *Annal. d. Chem. u. Pharm. CXVII. Bd. 2. Heft.*, 1860.

- [139] F William Studier. Protein production by auto-induction in high density shaking cultures. *Protein Expr. Purif.*, 41(1):207–234, May 2005.
- [140] Lucas B Sullivan, Dan Y Gui, Aaron M Hosios, Lauren N Bush, Elizaveta Freinkman, and Matthew G Vander Heiden. Supporting aspartate biosynthesis is an essential function of respiration in proliferating cells. *Cell*, 162(3):552–563, July 2015.
- [141] Lucas B Sullivan, Alba Luengo, Laura V Danai, Lauren N Bush, Frances F Diehl, Aaron M Hosios, Allison N Lau, Sarah Elmiligy, Scott Malstrom, Caroline A Lewis, and Matthew G Vander Heiden. Aspartate is an endogenous metabolic limitation for tumour growth. *Nat. Cell Biol.*, 20(7):782–788, July 2018.
- [142] Yu Sun, Michael Piechotta, Isabel Naarmann-de Vries, Christoph Dieterich, and Ann E Ehrenhofer-Murray. Detection of queuosine and queuosine precursors in tRNAs by direct RNA sequencing. *Nucleic Acids Res.*, 51(20):11197–11212, November 2023.
- [143] Jindrich Symersky, Daniel Osowski, D Eric Walters, and David M Mueller. Oligomycin frames a common drug-binding site in the ATP synthase. *Proc. Natl. Acad. Sci. U. S. A.*, 109(35):13961–13965, August 2012.
- [144] Niki K Thomas, Vinay C Poodari, Miten Jain, Hugh E Olsen, Mark Akeson, and Robin L Abu-Shumays. Direct nanopore sequencing of individual full length tRNA strands. *ACS Nano*, 15(10):16642–16653, October 2021.
- [145] Tsz-Leung To, Alejandro M Cuadros, Hardik Shah, Wendy H W Hung, Yang Li, Sharon H Kim, Daniel H F Rubin, Ryan H Boe, Sneha Rath, John K Eaton, Federica Piccioni, Amy Goodale, Zohra Kalani, John G Doench, David E Root, Stuart L Schreiber, Scott B Vafai, and Vamsi K Mootha. A compendium of genetic modifiers of mitochondrial dysfunction reveals intra-organelle buffering. *Cell*, 179(5):1222–1238.e17, November 2019.
- [146] Guillaume Tournaire, Shauni Loopmans, Steve Stegen, Gianmarco Rinaldi, Guy Eelen, Sophie Torrekens, Karen Moermans, Peter Carmeliet, Bart Ghesquière, Bernard Thienpont, Sarah-Maria Fendt, Nick van Gastel, and Geert Carmeliet. Skeletal progenitors preserve proliferation and self-renewal upon inhibition of mitochondrial respiration by rerouting the TCA cycle. *Cell Rep.*, 40(4):111105, July 2022.
- [147] T W Traut. Physiological concentrations of purines and pyrimidines. *Mol. Cell. Biochem.*, 140(1):1–22, November 1994.
- [148] Yusuke Tsukamoto, Yumi Nakamura, Makoto Hirata, Ryuichi Sakate, and Tomonori Kimura. i-tRAP (individual tRNA acylation PCR): A convenient method for selective quantification of tRNA charging. *RNA*, 29(1):111–122, October 2022.

- [149] National Cancer Institute (U.S.), National Cancer Institute (U.S.). Division of Cancer Treatment, and National Institutes of Health (U.S.). *Cancer chemotherapy reports. Part 1.* Number v. 52, no. 6 in DHEW publication. U.S. Department of Health, Education, and Welfare, Public Health Service, National Institutes of Health, 1968.
- [150] M Uziel. Amine-catalyzed elimination of beta-phosphoric esters from aldehydes derived from ribonucleic acid and model substrates. *Arch. Biochem. Biophys.*, 166(1):201–212, January 1975.
- [151] Mayo Uziel. Periodate oxidation and amine-catalyzed elimination of the terminal nucleoside from adenylate or ribonucleic acid. products of overoxidation. *Biochemistry*, 12(5):938–942, 1973.
- [152] M B Van der Weyden and W N Kelly. Human adenylosuccinate synthetase. partial purification, kinetic and regulatory properties of the enzyme from placenta. *J. Biol. Chem.*, 249(22):7282–7289, November 1974.
- [153] Johannes P van Dijken and W Alexander Scheffers. Redox balances in the metabolism of sugars by yeasts. *FEMS Microbiol. Rev.*, 32:199–224, 1986.
- [154] Matthew G Vander Heiden. Targeting cancer metabolism: a therapeutic window opens. *Nat. Rev. Drug Discov.*, 10(9):671–684, August 2011.
- [155] Matthew G Vander Heiden, Lewis C Cantley, and Craig B Thompson. Understanding the warburg effect: the metabolic requirements of cell proliferation. *Science*, 324(5930):1029–1033, May 2009.
- [156] Matthew G Vander Heiden and Ralph J DeBerardinis. Understanding the intersections between metabolism and cancer biology. *Cell*, 168(4):657–669, February 2017.
- [157] U Varshney, C P Lee, and U L RajBhandary. Direct analysis of aminoacylation levels of tRNAs in vivo. application to studying recognition of escherichia coli initiator tRNA mutants by glutaminyl-tRNA synthetase. *J. Biol. Chem.*, 266(36):24712–24718, December 1991.
- [158] Karthik Vasan, Marie Werner, and Navdeep S Chandel. Mitochondrial metabolism as a target for cancer therapy. *Cell Metab.*, 32(3):341–352, September 2020.
- [159] Ji Wang, Claire Toffano-Nioche, Florence Lorieux, Daniel Gautheret, and Jean Lehmann. Accurate characterization of escherichia coli tRNA modifications with a simple method of deep-sequencing library preparation. *RNA Biol.*, 18(1):33–46, January 2021.

- [160] O.H. Warburg and Kaiser-Wilhelm-Institut für Biologie. *Über den stoffwechsel der tumoren: arbeiten aus dem Kaiser Wilhelm-institute für biologie*. Springer, 1926.
- [161] Jessica M Warren, Thalia Salinas-Giegé, Guillaume Hummel, Nicole L Coots, Joshua M Svendsen, Kristen C Brown, Laurence Drouard, and Daniel B Sloan. Combining tRNA sequencing methods to characterize plant tRNA expression and post-transcriptional modification. *RNA Biol.*, 18(1):64–78, January 2021.
- [162] Michael Waskom. seaborn: statistical data visualization. *J. Open Source Softw.*, 6(60):3021, April 2021.
- [163] Christopher P Watkins, Wen Zhang, Adam C Wylder, Christopher D Katanski, and Tao Pan. A multiplex platform for small RNA sequencing elucidates multifaceted tRNA stress response and translational regulation. *Nat. Commun.*, 13(1):2491, May 2022.
- [164] William W Wheaton, Samuel E Weinberg, Robert B Hamanaka, Saul Soberanes, Lucas B Sullivan, Elena Anso, Andrea Glasauer, Eric Dufour, Gokhan M Mutlu, Gr Scott Budigner, and Navdeep S Chandel. Metformin inhibits mitochondrial complex I of cancer cells to reduce tumorigenesis. *Elife*, 3:e02242, May 2014.
- [165] P R Whitfeld. A method for the determination of nucleotide sequence in polyribonucleotides. *Biochem. J.*, 58(3):390–396, November 1954.
- [166] P R Whitfeld and R Markham. Natural configuration of the purine nucleotides in ribonucleic acids; chemical hydrolysis of the dinucleoside phosphates. *Nature*, 171(4365):1151–1152, June 1953.
- [167] Alan J Wolfe. The acetate switch. *Microbiol. Mol. Biol. Rev.*, 69(1):12–50, March 2005.
- [168] Alexey D Wolfson and Olke C Uhlenbeck. Modulation of tRNA<sup>Ala</sup> identity by inorganic pyrophosphatase. *Proc. Natl. Acad. Sci. U. S. A.*, 99(9):5965–5970, April 2002.
- [169] Carl Wulff. Beiträge zur kenntniss der nucleinbasen. *physiol. Chem.*, 1892.
- [170] Ryota Yamagami and Hiroyuki Hori. Application of mutational profiling: New functional analyses reveal the tRNA recognition mechanism of tRNA m1a22 methyltransferase. *J. Biol. Chem.*, 299(1):102759, December 2022.

- [171] Lifeng Yang, Juan Carlos Garcia Canaveras, Zihong Chen, Lin Wang, Lingfan Liang, Cholsoon Jang, Johannes A Mayr, Zhaoyue Zhang, Jonathan M Ghergurovich, Le Zhan, Shilpy Joshi, Zhixian Hu, Melanie R McReynolds, Xiaoyang Su, Eileen White, Raphael J Morscher, and Joshua D Rabinowitz. Serine catabolism feeds NADH when respiration is impaired. *Cell Metab.*, 31(4):809–821.e6, April 2020.
- [172] Jie Yuan, Bryson D Bennett, and Joshua D Rabinowitz. Kinetic flux profiling for quantitation of cellular metabolic fluxes. *Nat. Protoc.*, 3(8):1328–1340, 2008.
- [173] Ji Zhang, Jing Fan, Sriram Venneti, Justin R Cross, Toshimitsu Takagi, Bhavneet Bhinder, Hakim Djabballah, Masayuki Kanai, Emily H Cheng, Alexander R Judkins, Bruce Pawel, Julie Baggs, Sara Cherry, Joshua D Rabinowitz, and Craig B Thompson. Asparagine plays a critical role in regulating cellular adaptation to glutamine depletion. *Mol. Cell*, 56(2):205–218, October 2014.
- [174] Zhaoyue Zhang, Tara TeSlaa, Xincheng Xu, Xianfeng Zeng, Lifeng Yang, Gang Xing, Gregory J Tesz, Michelle F Clasquin, and Joshua D Rabinowitz. Serine catabolism generates liver NADPH and supports hepatic lipogenesis. *Nat Metab*, 3(12):1608–1620, December 2021.
- [175] Guanqun Zheng, Yidan Qin, Wesley C Clark, Qing Dai, Chengqi Yi, Chuan He, Alan M Lambowitz, and Tao Pan. Efficient and quantitative high-throughput tRNA sequencing. *Nat. Methods*, 12(9):835–837, September 2015.
- [176] Fanglei Zhuang, Ryan T Fuchs, Zhiyi Sun, Yu Zheng, and G Brett Robb. Structural bias in T4 RNA ligase-mediated 3'-adapter ligation. *Nucleic Acids Res.*, 40(7):e54, April 2012.
- [177] Kai Zhuang, Goutham N Vemuri, and Radhakrishnan Mahadevan. Economics of membrane occupancy and respiro-fermentation. *Mol. Syst. Biol.*, 7:500, June 2011.
- [178] E B Ziff and J R Fresco. Chemical transformation of 4-thiouracil nucleosides to uracil and cytosine counterparts. *J. Am. Chem. Soc.*, 90(26):7338–7342, December 1968.

## Appendix A

### CHAPTER 1 APPENDIX

#### A.1 Mathematical description of simple labelling flux

A common goal of stable isotope tracing is the measurement of flux through a pathway. This requires a mathematical description of the system with a set of associated assumptions. Here such description is provided for a very simple system describing a single metabolic reaction.

The system is illustrated in figure A.1 and contains one or more cells with total volume  $V(t)$ , proliferating with growth rate  $g$  and two metabolites with the concentrations  $A$  and  $B$ .  $A_{out}$  is situated outside of the cell, upon transport into the cell at a rate  $r_{in}$ , it becomes available for conversion into  $B$  at a rate  $r_{AB}$ , whereafter it is exported outside the cell at a rate  $r_{out}$ . These metabolites are either labelled ( $A^L$ ) or unlabelled ( $A^U$ ) and sum describes the total concentration i.e.  $A = A^L + A^U$ .

For this system a number of assumptions are made: 1) cell proliferation is constant, 2) the concentrations  $A_{out}$ ,  $A$  and  $B$  are constant, 3) all reactions (indicated by arrows) are irreversible, 4) the labelling fraction of  $A$  is constant and the same both inside and outside.

The objective is to determine the flux from  $A$  to  $B$  ( $F_{AB} = A r_{AB}$ ) in order to describe  $B^L$  and  $B^U$  over time.

To deal with labelled and unlabelled metabolites the labelling fraction, which is constant for  $A$ , is introduced:

$$\alpha = \frac{A^L}{A^L + A^U} = \frac{A^L}{A} \implies A^L = \alpha A \quad (\text{A.1})$$

For  $B$  the labelling fraction changes over time:

$$\beta(t) = \frac{B^L}{B^L + B^U} = \frac{B^L}{B} \implies B^L = \beta B \quad (\text{A.2})$$

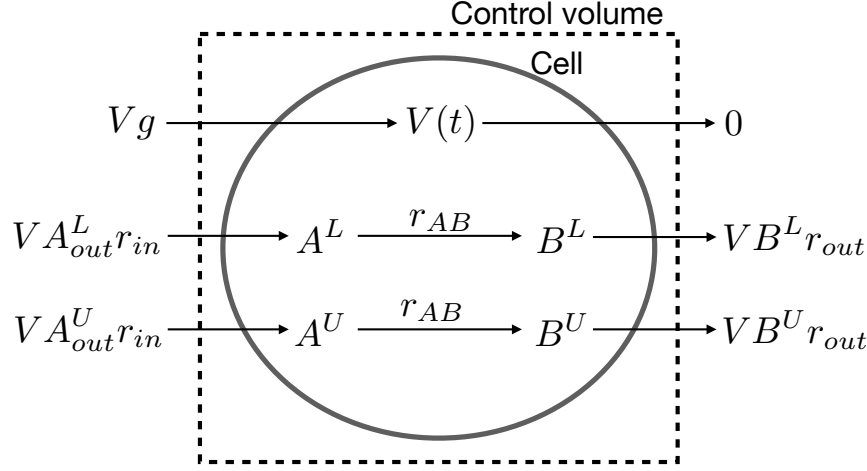


Figure A.1: Mass balance diagram for labelling of metabolite  $B$ . See text for details.

For the cell volume we know that it follows standard exponential growth with initial condition  $V(0) = V_0$  such that:

$$V(t) = V_0 e^{gt} \quad (\text{A.3})$$

This could also be derived from the mass balance, assuming constant cell density.

Now, applying mass balance of the control volume (IN - OUT = ACCUMULATED) on  $A^L$  over a time difference of  $\Delta t$ :

$$V\alpha A_{out} r_{in} \Delta t - V\alpha A r_{AB} \Delta t = (V\alpha A)(t + \Delta t) - (V\alpha A)(t) \quad (\text{A.4})$$

Rearrange:

$$\frac{(V\alpha A)(t + \Delta t) - (V\alpha A)(t)}{\Delta t} = V\alpha A_{out} r_{in} - V\alpha A r_{AB} \quad (\text{A.5})$$

Let  $\Delta t \rightarrow 0$  and the differential quotient emerge:

$$\frac{d}{dt}(V\alpha A) = V\alpha A_{out} r_{in} - V\alpha A r_{AB} = \alpha A \frac{dV}{dt} + V\alpha \frac{dA}{dt} \quad (\text{A.6})$$

From assumption 4) above it is known that  $\frac{dA}{dt} = 0$ , also from the volume equation (equation

A.3) it is observed that  $\frac{dV}{dt} = Vg$ :

$$\alpha AV g = V\alpha A_{out} r_{in} - V\alpha A r_{AB} \implies A_{out} r_{in} = A r_{AB} + A g \quad (\text{A.7})$$

This can be interpreted as influx ( $F_{in}$ ) is equal to consumption flux to B ( $F_{AB}$ ) plus flux to maintain constant concentration  $A$  while cells are replicating ( $F_{rep}^A$ ):

$$A_{out} r_{in} = A r_{AB} + A g \implies F_{in} = F_{AB} + F_{rep}^A \quad (\text{A.8})$$

Similarly, applying mass balance on  $B^L$ :

$$V\alpha A r_{AB} \Delta t - V\beta B r_{out} \Delta t = (V\beta B)(t + \Delta t) - (V\beta B)(t) \quad (\text{A.9})$$

$$\frac{(V\beta B)(t + \Delta t) - (V\beta B)(t)}{\Delta t} = V\alpha A r_{AB} - V\beta B r_{out} \quad (\text{A.10})$$

$$\frac{d}{dt}(V\beta B) = V\alpha A r_{AB} - V\beta B r_{out} = \beta B \frac{dV}{dt} + V B \frac{d\beta}{dt} \quad (\text{A.11})$$

$$\beta B g + B \frac{d\beta}{dt} = \alpha A r_{AB} - \beta B r_{out} \quad (\text{A.12})$$

The flux from  $A$  to  $B$  has already been defined as  $F_{AB} = A r_{AB}$ , also let  $F_{out} = B r_{out}$  and  $F_{rep}^B = B g$ :

$$\beta F_{rep}^B + B \frac{d\beta}{dt} = \alpha F_{AB} - \beta F_{out} \quad (\text{A.13})$$

Rearrange:

$$B \frac{d\beta}{dt} = \alpha F_{AB} - \beta(F_{out} - F_{rep}^B) \quad (\text{A.14})$$

Observe, similar to equation A.8 that  $F_{out} = F_{AB} + F_{rep}^B$  and insert:

$$\frac{d\beta}{dt} = (\alpha - \beta) \frac{F_{AB}}{B} \quad (\text{A.15})$$

By integration the labelling fraction of  $B$  is found:

$$\beta(t) = \alpha + Ce^{-\frac{F_{AB}}{B}t} \quad (\text{A.16})$$

In most cases there will be no labelling of  $B$  at time zero i.e. an initial condition of  $\beta(t) = 0$ , resulting in integration constant  $C = -\alpha$ :

$$\beta(t) = \alpha - \alpha e^{-\frac{F_{AB}}{B}t} \quad (\text{A.17})$$

A useful descriptor is the time to half-max labelling, or more generally the time ( $t_\lambda$ ) to fraction-of-max ( $\lambda \in [0, 1]$ ) labelling:

$$\lambda = \frac{\beta(t_\lambda)}{\beta(\infty)} = \frac{\alpha - \alpha e^{-\frac{F_{AB}}{B}t_\lambda}}{\alpha} \quad (\text{A.18})$$

Isolating the time:

$$t_\lambda = \frac{B}{F_{AB}} \ln \left( \frac{1}{1 - \lambda} \right) \quad (\text{A.19})$$

Finally as an example, glutamine to glutamate synthesis flux is estimate to 30 mM/h and the intracellular pool of glutamate is estimate to a concentration of 5 mM. How long does it take to reach 95% of max labelling from glutamine?

$$\frac{5 \text{ mM}}{30 \text{ mM/h}} \ln \left( \frac{1}{1 - 0.95} \right) \approx 0.5 \text{ h} \quad (\text{A.20})$$

### A.2 Pig serum nucleoside/base concentrations

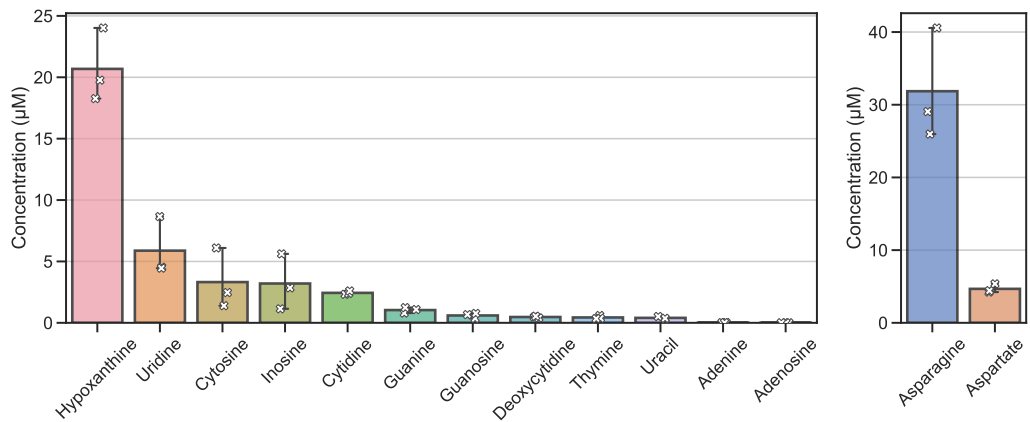


Figure A.2: Left, pig serum nucleoside/base concentrations determined using LCMS isotope dilution. Right, pig serum aspartate/asparagine concentrations determined using LCMS isotope dilution.

### A.3 Fumarate regeneration to aspartate

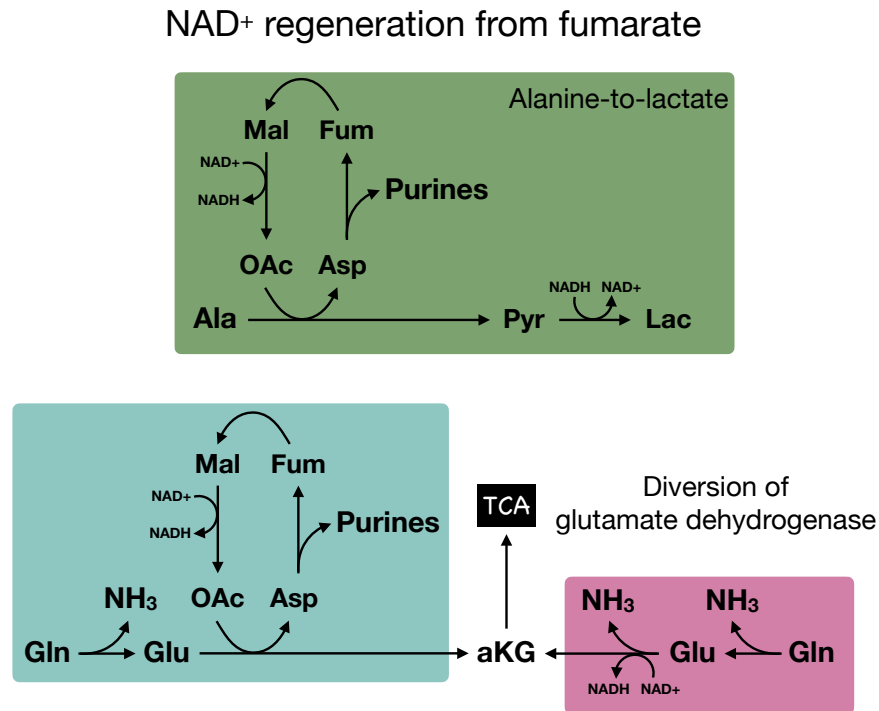


Figure A.3: Fumarate regeneration to aspartate from via. either alanine-to-lactate conversion or diversion of NAD<sup>+</sup> consumption by glutamate dehydrogenase.

## Appendix B

### CHAPTER 2 APPENDIX

#### **B.1 Packed cell volume is an overestimate in common cancer cell lines**

This is an abridged version of the method and results in Engstrom et al. 2021 [39].

Originally developed to determine the volume of red cells in blood, or hematocrit, packed cell volume (PCV) measurements have more recently also been used to determine the volume of adherent cell lines for conversion of intracellular metabolite quantities into concentrations [113, 93, 171, 50]. Another way of determining cell volume is using the Coulter principle which relates particle volume to the change in electrical impedance as the particle passes through an aperture. For blood, PCV is a reliable measurement, proportional to the cell volume determined using the Coulter principle [19, 17]; however, this assumption has not been tested for the diverse set of cell lines used for cell culturing.

We compared PCV with Coulter counter-based cell volume measurements for five cell lines and found that the spin protocol provided by the PCV tube manufacturer (2,500 g for 1 min) lead to an overestimate of cell volume compared to Coulter-based measurements. We hypothesized that this discrepancy is related to incomplete cell packing and that packing efficiency is negatively impacted by “sticky” extracellular matrix proteins found abundantly on adherent cells. This was tested with five different cell lines by increasing the centrifugation speed and time (figure B.1). The results showed that PCV measurements at the lowest centrifugation speed were overestimates of cell volume compared to Coulter-based measurements for all cell lines. Adherent cells had the largest volume discrepancy. PCV measurements decreased with increasing centrifugation speed and time and approached the Coulter-based volume.

In summary, the results indicate that PCV consistently overestimates cell volume com-

pared to measurements using a Coulter counter. This overestimate in PCV is likely due to incomplete packing, which is particularly problematic for adherent cell lines. Therefore, it is advisable for future studies relying on accurate cell volume measurements to use the Coulter principle for cell volume measurement.

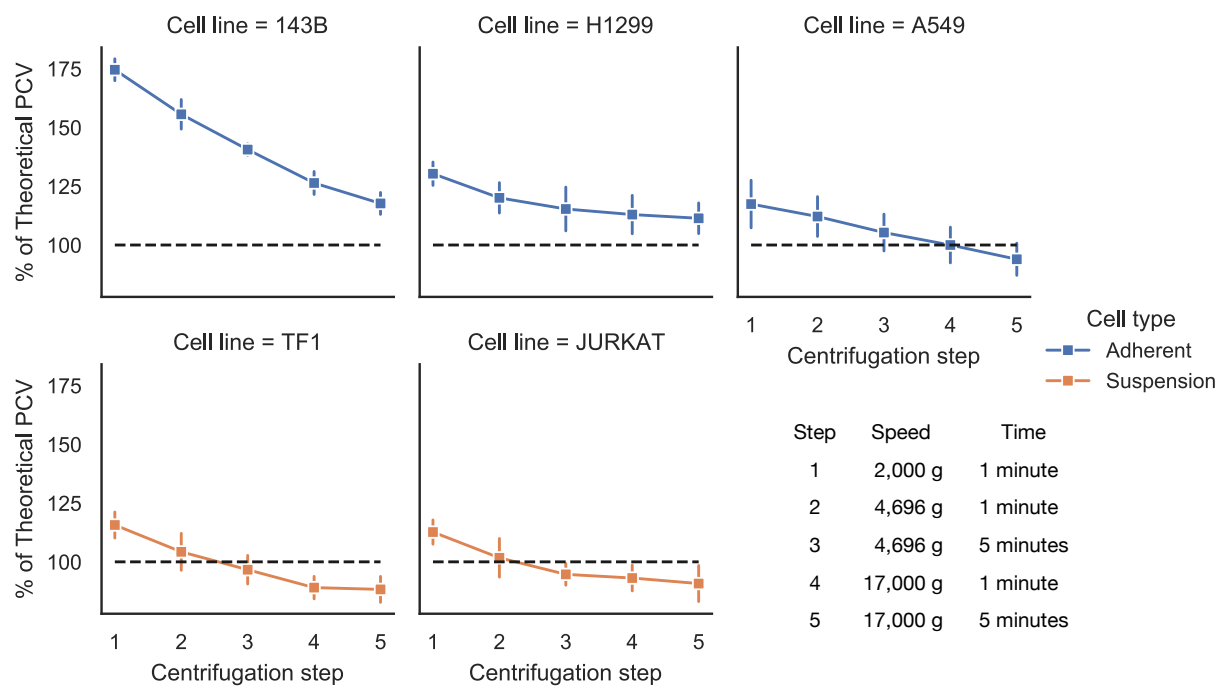


Figure B.1: Packed cell volume (PCV) compared to the theoretical volume as determined by a Coulter counter (Multisizer 4).

## B.2 Mitochondrial inhibition induces a titratable aspartate limitation

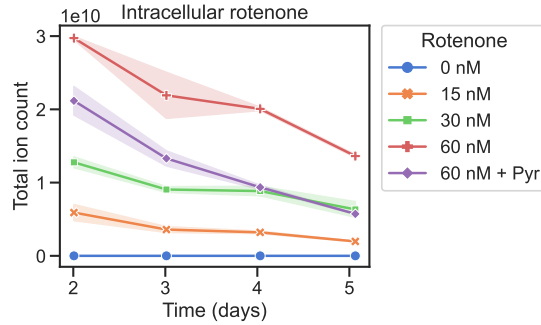


Figure B.2: Rotenone in cell metabolite extract decrease over time after initial treatment indicating degradation. Rotenone is known to be degraded in aqueous solutions [125]. Measured as total ion counts using LCMS. Related to figure 2.1.

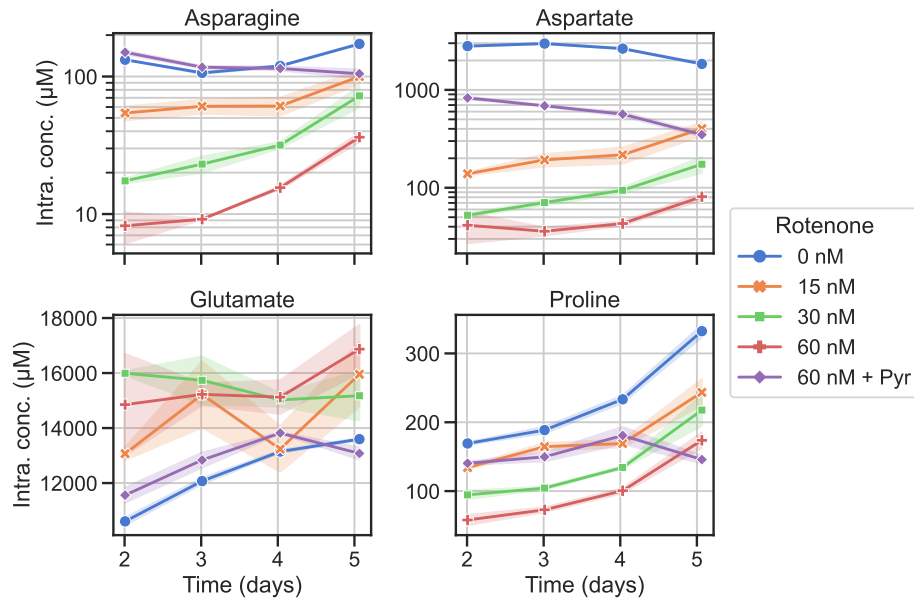


Figure B.3: Intracellular concentration of redox sensitive metabolites over the time course of rotenone treatment. Related to figure 2.1.

### B.3 Nucleoside, nucleobase and amino acid quantification after acid hydrolysis

To quantify cellular nucleotide and amino acid abundance, acid hydrolysis was performed directly on cell material. Since the hydrolysis was performed in regular plastic tubes with ambient air headspace, there is a risk of oxidation and thus underestimation of the true quantities. Therefore, amino acid and nucleobase stability was tested in 6 M HCl with 24 hours incubation at 100°C (figures B.4 and B.5). Samples were prepared with 500 µM amino acid or nucleobase mix and in parallel added either water (MQ) or 6 M HCl. Water samples were set aside at -20°C. Amino acids and nucleobases were then quantified using LCMS and each ion count were normalized to its internal standard yielding a response ratio (RR). For nucleobases, pyrimidines are stable while purines are prone hydrolysis as has been noted previously [138, 169, 69, 98]. For amino acids, asparagine and glutamine are fully deaminated to produce exactly one equivalent of aspartate and glutamate, respectively. Tryptophan also breaks down completely while methionine and cystine are broken down but remain detectable. Note that histidine is missing due to poor chromatographic separation. Thus, acid hydrolysis is compatible with quantification of all pyrimidine nucleobases and all amino acids except asparagine, glutamine, tryptophan, methionine, cystine/cysteine and histidine.

Another potential concern for quantification is low solubility; particularly, of the nucleobases liberated during hydrolysis. Should any compound hit its solubility limit during processing it would precipitate, and its true quantity would be underestimated. To test the bounds of solubility, increasing amounts of cell material was hydrolyzed in 6 M HCl with 24 hours incubation at 100°C. Compounds reaching their solubility limit would be expected to show no increase in peak area with increasing amounts of cell material. This was tested using cell material from a confluent 10 cm dish of 143B cells. Samples were prepared with 30, 5, 1, 0.2 and 0.05% of this material, following hydrolysis, drying and reconstitution with 100 µL 80% LCMS grade methanol. The resulting quantification (figure B.6) shows that none of the measured nucleosides, nucleobases or amino acids reach their solubility limit.

However, it does display abundant ion suppression which can be corrected by normalization to an internal standard (figure [B.7](#)).

The final quantification relies on a calibration curve to convert the internal standard normalized ion count, known as the response ratio, to a concentration. These curves were fitted for all nucleosides, nucleobases and amino acids that had internal standards and show excellent curve fit, generally spanning concentrations of three orders of magnitude (figure [B.8](#)).

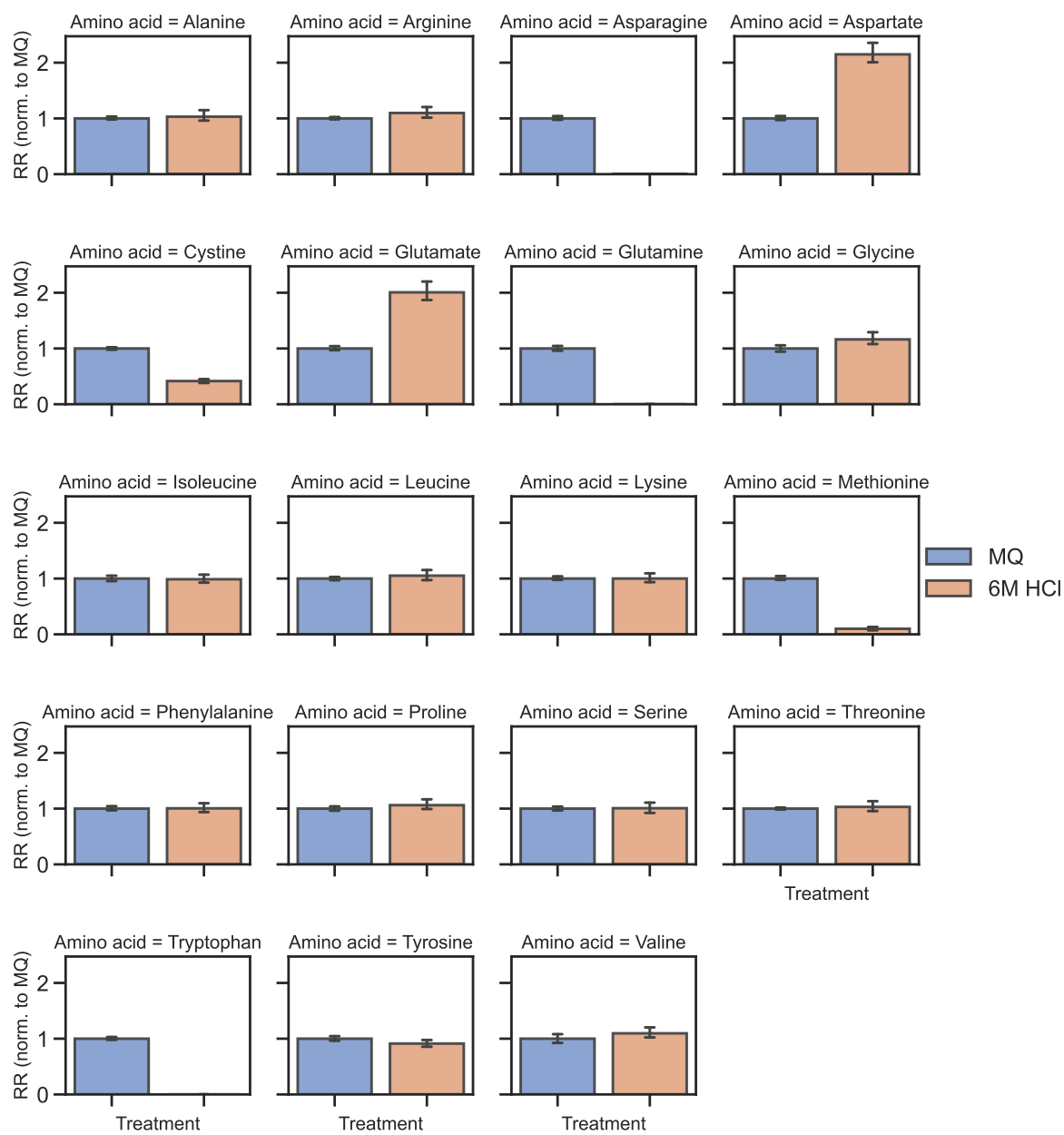


Figure B.4: Amino acid stability in 6 M HCl after 24 hours incubation at 100°C in tubes with ambient air headspace. Incubation in HCl was compared with water (MQ). Ion counts were normalized to their internal standard (RR, response ratio).

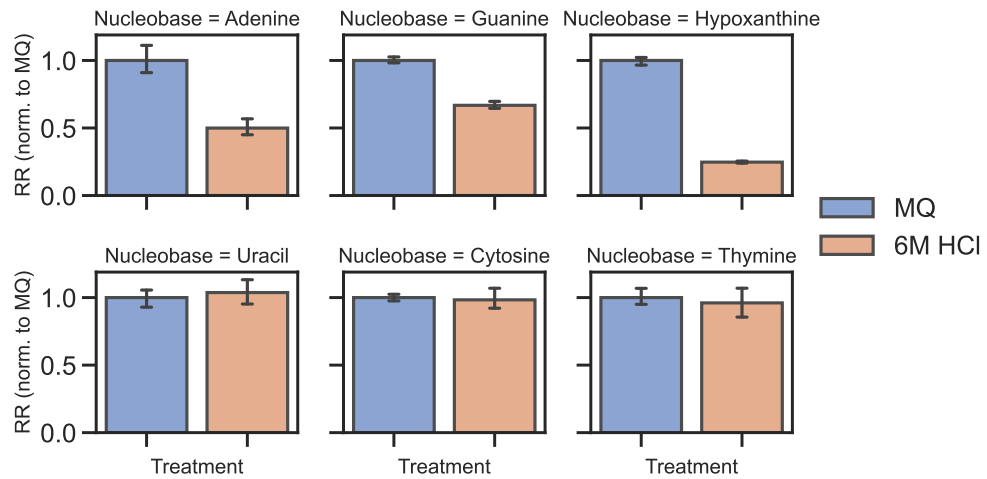


Figure B.5: Nucleobase stability in 6 M HCl after 24 hours incubation at 100°C in tubes with ambient air headspace. Incubation in HCl was compared with water (MQ). Ion counts were normalized to their internal standard (RR, response ratio).

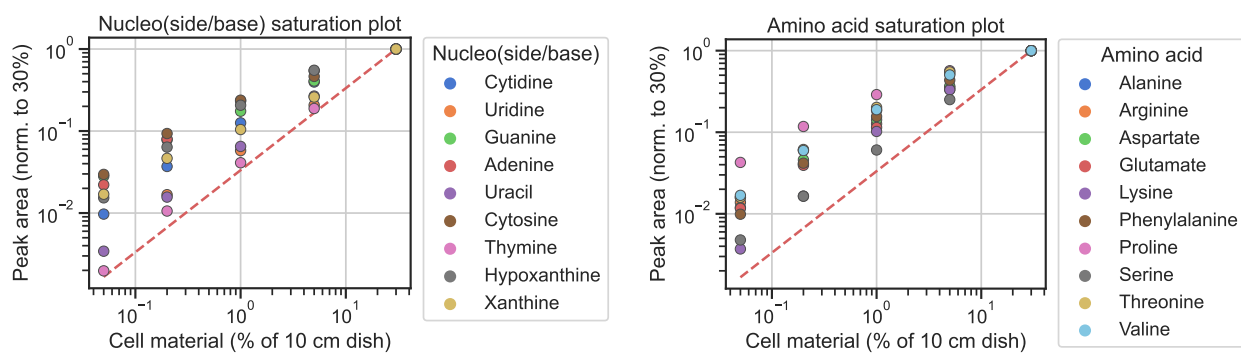


Figure B.6: LCMS measured peak area of nucleosides, nucleobases (left) and amino acids (right) using increasing amounts of cell material as input for acid hydrolysis. The increase in cell material results in an increase in peak area for all compounds, indicating that none have reached their solubility limit. The red dashed line shows direct proportionality using the 30% cell material as reference. Points above this line indicate ion suppression.

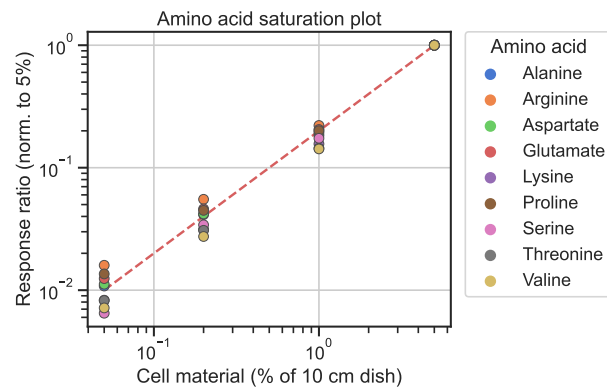


Figure B.7: Ion suppression observed in the above figure B.6 (right panel) can be removed by normalization to the isotopically labelled internal standard for each compound.

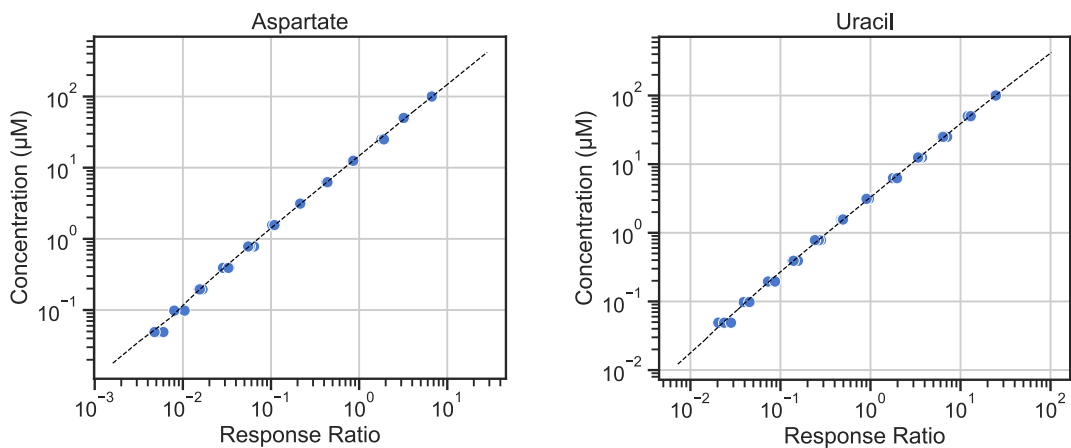


Figure B.8: Examples of calibration curves fitted to three replicates of a compound titration spanning three orders of magnitude.

#### B.4 $^{15}\text{N}$ Gln tracing in 143B and H1299

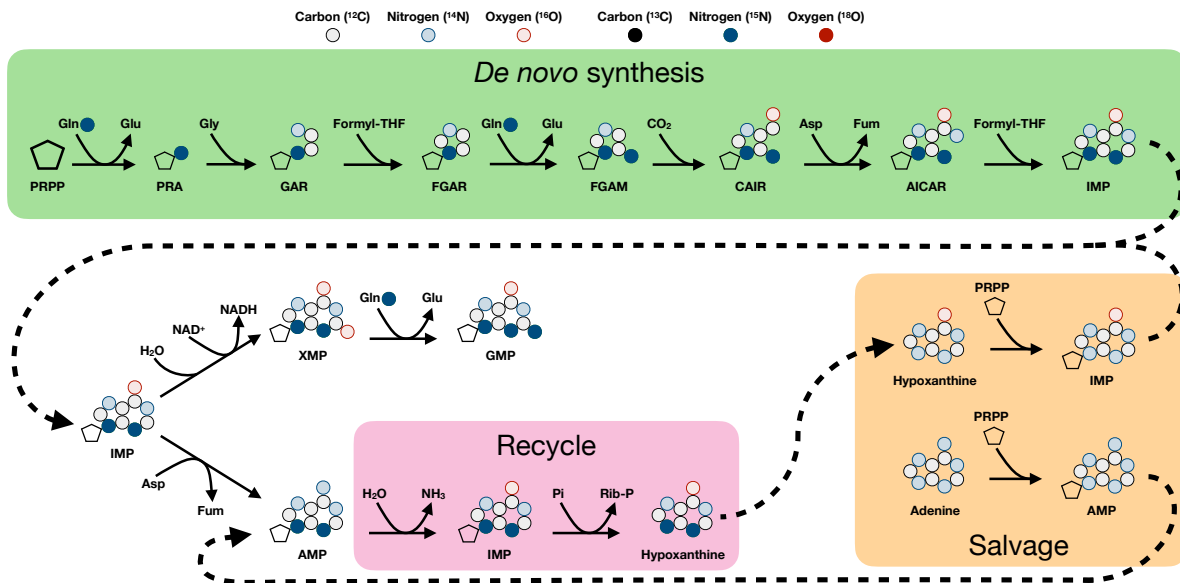


Figure B.9: Overview of Gln  $^{15}\text{N}$ -amide label incorporation in *de novo* purine synthesis. Label incorporation can be affected by salvage of unlabelled hypoxanthine or adenine and recycling.

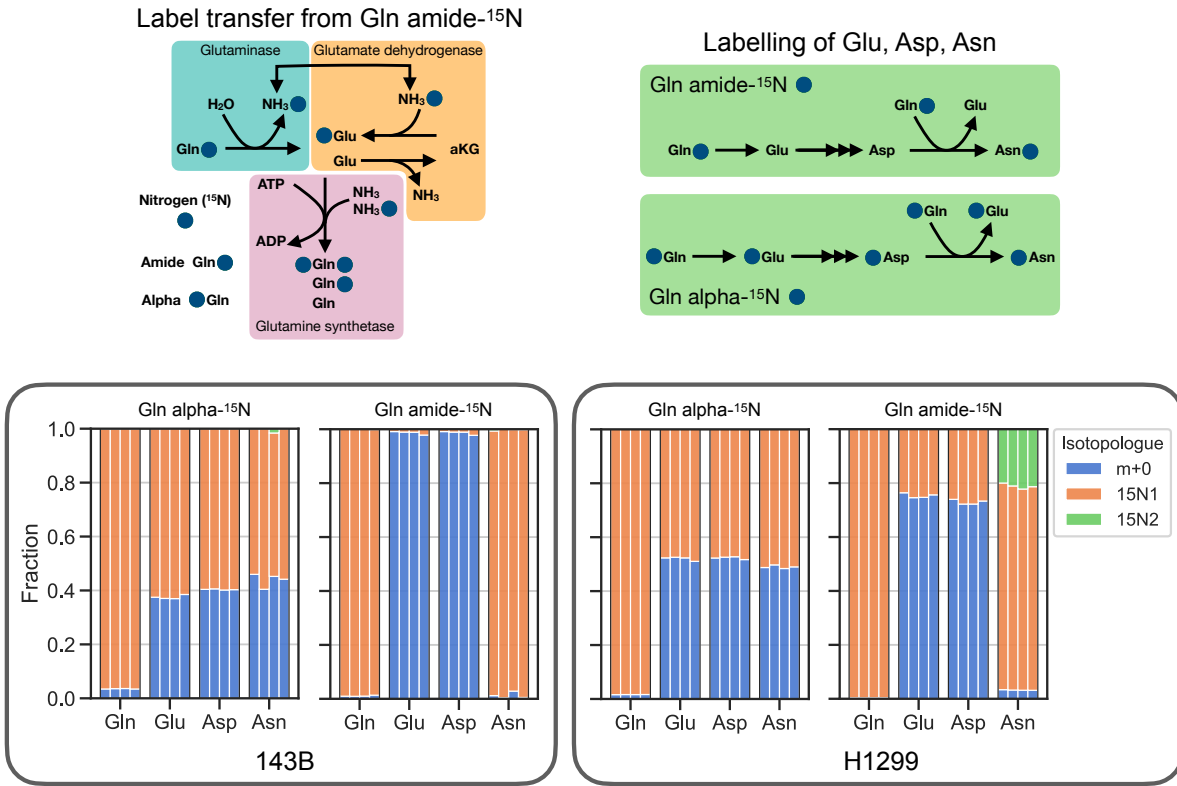


Figure B.10: Gln  $^{15}\text{N}$  on the amide nitrogen can transfer to the alpha nitrogen in H1299 cells but not in 143B cells. Upper left diagram shows how Gln amide and alpha nitrogen labels can transfer. Transfer of amide labelled nitrogen can be achieved by glutaminase catalyzed release of labelled ammonia and its subsequent use as a substrate in the conversion of alpha-ketoglutarate (aKG) to Glu alpha- $^{15}\text{N}$  by glutamate dehydrogenase. The signature of glutamine synthetase activity is the appearance of doubly labelled Gln. Upper right diagram shows how Gln amide and alpha nitrogen labels are transferred to downstream metabolites Glu, Asp and Asn. Lower panel shows the nitrogen isotopologue distribution of Gln, Glu, Asp and Asn in 143B and H1299 at steady-state. The alpha nitrogen label is frequently lost in Glu and downstream, presumably due to transaminase catalyzed exchange with unlabelled amino groups on amino acids such as leucine, isoleucine, valine etc. The amide nitrogen label is partially transferred to the alpha position in H1299, but not in 143B, also indicated by the doubly labelled Asn.

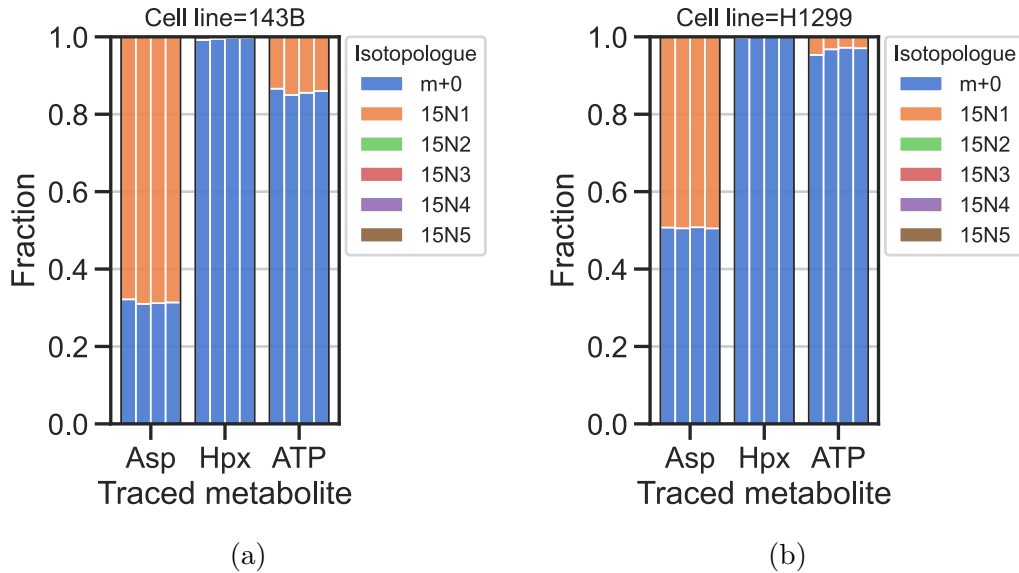


Figure B.11: Glu alpha- $^{15}\text{N}$  tracing into Asp, Hpx and ATP at steady-state for cell lines 143B and H1299 grown in DMEM with 100  $\mu\text{M}$  adenine. *De novo* ATP synthesis and salvage from Hpx results in label incorporation from Asp, while salvage from adenine does not (figure B.9). Therefore, the salvage fraction directly from adenine can be inferred from the fold difference of Asp vs. ATP labelling.

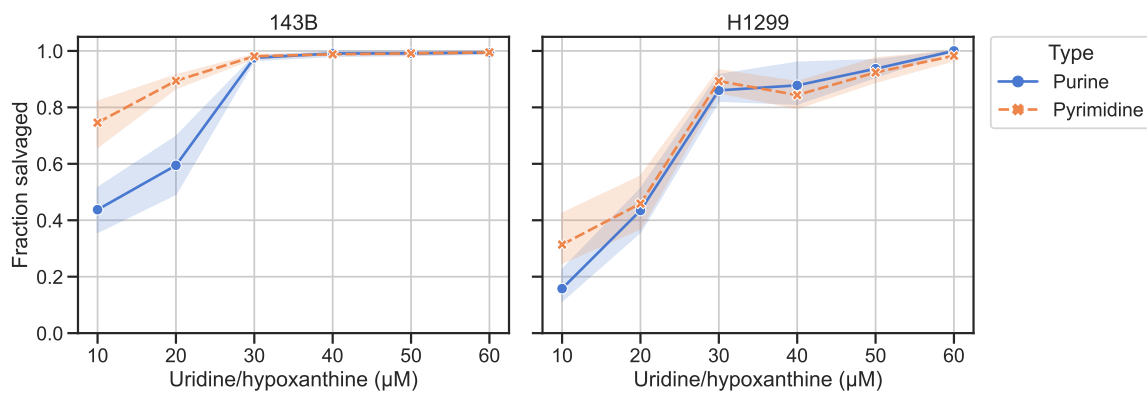


Figure B.12: Fraction of purines (average across GDP, GMP, ADP and AMP) and pyrimidines (average across UDP, UMP, CDP and CMP) derived from salvage when 143B or H1299 cells are cultured in increasing concentrations of uridine/hypoxanthine.

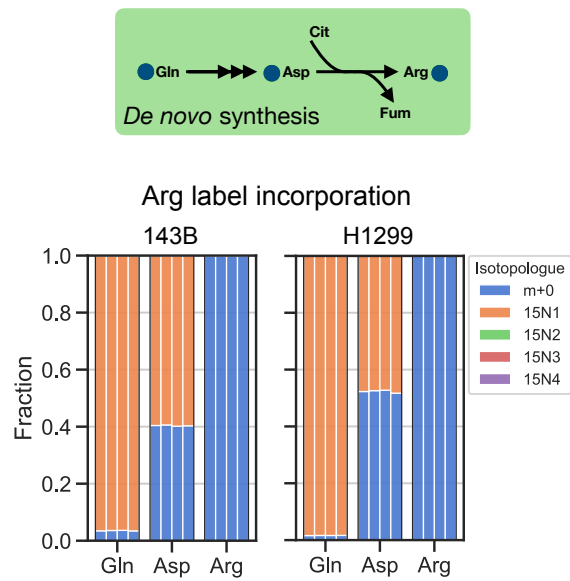


Figure B.13: No evidence of arginine synthesis in DMEM. Top diagram shows Gln alpha-<sup>15</sup>N label incorporation into Asp and subsequently Arg. Bottom isotopologue distributions show Gln alpha-<sup>15</sup>N label incorporation into Gln, Asp and Arg at steady-state for cell lines 143B and H1299 grown in DMEM with no salvageable metabolites added (Vec).

### B.5 ETC inhibitor rescue with purines is blunted in serine free media

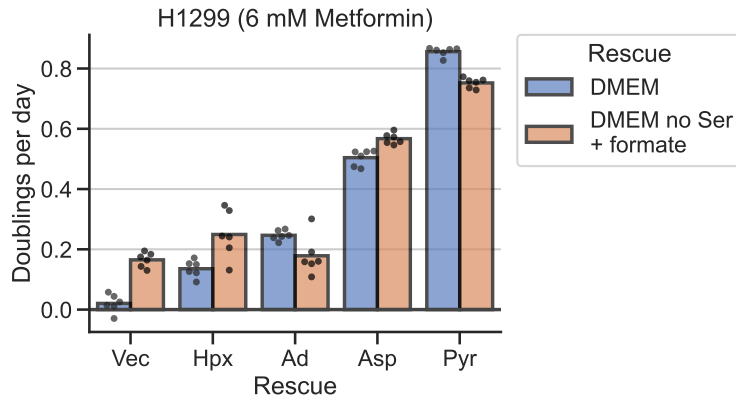


Figure B.14: The small proliferation rescue of hypoxanthine and adenine during 6 mM metformin treatment, is blunted by when repeated in serine free media with 1 mM sodium formate. Serine free media will decrease the mitochondria NADH production by the folate cycle; instead, formate becomes necessary to generate folate species e.g. 10-formyl-THF for purine synthesis [33, 34, 171]. Related to figure 2.11a.

### B.6 Aspartate to proliferation curves

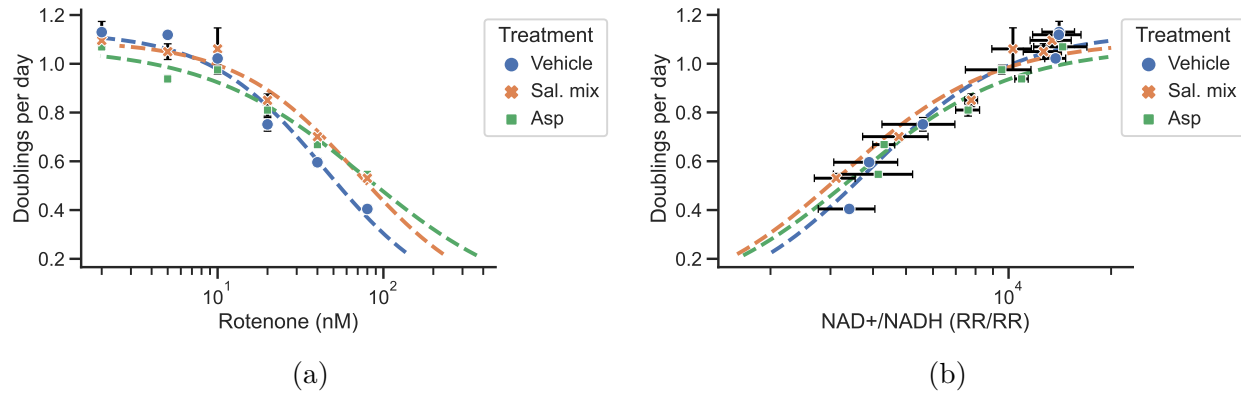


Figure B.15: Supplementary data for figure 2.12. (a) Proliferation as a function of rotenone concentration. Rotenone concentration at 50% proliferation is 40, 70 and 80 nM for Vehicle, Sal. mix and Asp treatments, respectively. (b) Proliferation as a function of the NAD<sup>+</sup>/NADH ratio. The NAD<sup>+</sup>/NADH ratio was made using internal standard normalized LCMS measurements (response ratio/response ratio). Condition with salvage mix (Sal. mix) contains: 1 mM asparagine/uridine, 0.5 mM hypoxanthine, 20  $\mu$ M adenine and 10  $\mu$ M adenosine.

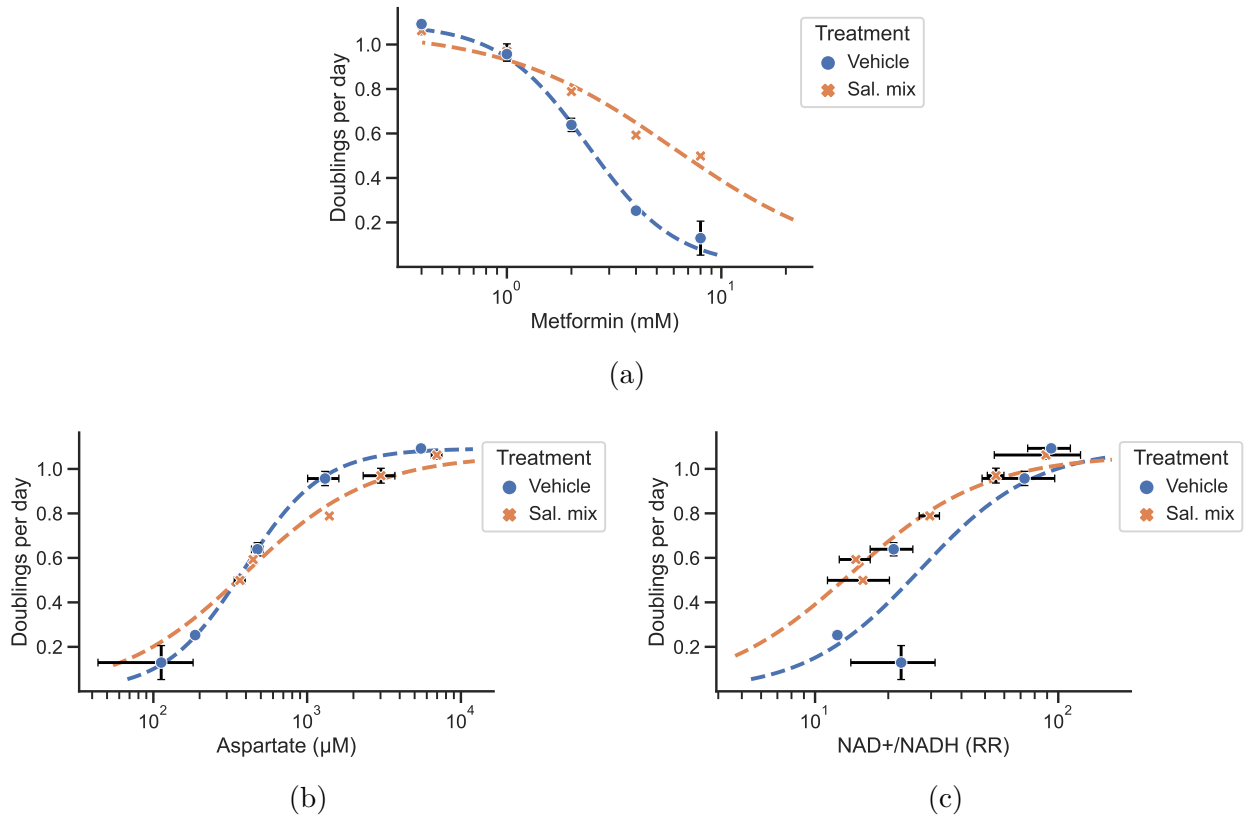


Figure B.16: Aspartate to proliferation relationship for H1299 using metformin to induce aspartate limitation. (a) Proliferation as a function of metformin concentration. Metformin concentration at 50% proliferation is 2.4 and 6.1 mM for Vehicle and Sal. mix treatments, respectively. (b) Proliferation as a function of aspartate concentration. Aspartate concentration at 50% proliferation is 390  $\mu$ M for both Vehicle and Sal. mix treatments. (c) Proliferation as a function of the NAD<sup>+</sup>/NADH ratio. The NAD<sup>+</sup>/NADH ratio was made using internal standard normalized LCMS measurements (response ratio/response ratio). Condition with salvage mix (Sal. mix) contains: 1 mM asparagine/uridine, 0.5 mM hypoxanthine, 20  $\mu$ M adenine and 10  $\mu$ M adenosine.

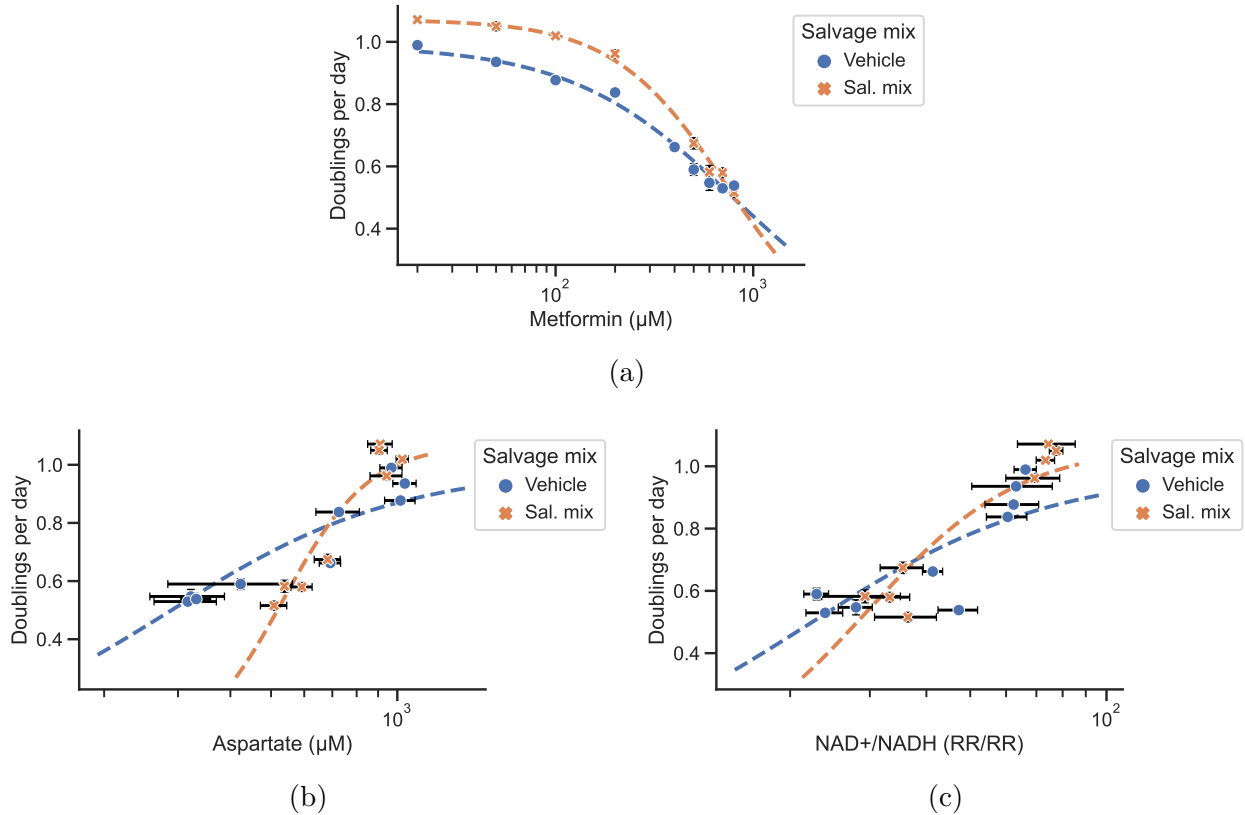


Figure B.17: Aspartate to proliferation relationship for HCT116 using metformin to induce aspartate limitation. (a) Proliferation as a function of metformin concentration. Metformin concentration at 50% proliferation is 810 and 740  $\mu\text{M}$  for Vehicle and Sal. mix treatments, respectively. (b) Proliferation as a function of aspartate concentration. Aspartate concentration at 50% proliferation is 290 and 530  $\mu\text{M}$  for Vehicle and Sal. mix treatments, respectively. (c) Proliferation as a function of the NAD<sup>+</sup>/NADH ratio. The NAD<sup>+</sup>/NADH ratio was made using internal standard normalized LCMS measurements (response ratio/response ratio). Condition with salvage mix (Sal. mix) contains: 1 mM asparagine/uridine, 0.5 mM hypoxanthine, 20  $\mu\text{M}$  adenine and 10  $\mu\text{M}$  adenosine.

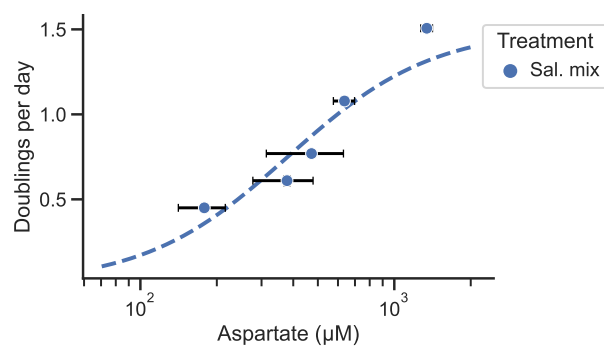


Figure B.18: Aspartate to proliferation relationship for 143B grown in media with salvage mix using metformin to induce aspartate limitation. Aspartate concentration at 50% proliferation is 380  $\mu\text{M}$  for Sal. mix treated cells. Salvage mix (Sal. mix) contains: 1 mM asparagine/uridine, 0.5 mM hypoxanthine, 20  $\mu\text{M}$  adenine and 10  $\mu\text{M}$  adenosine.

### B.7 tRNA charge over time

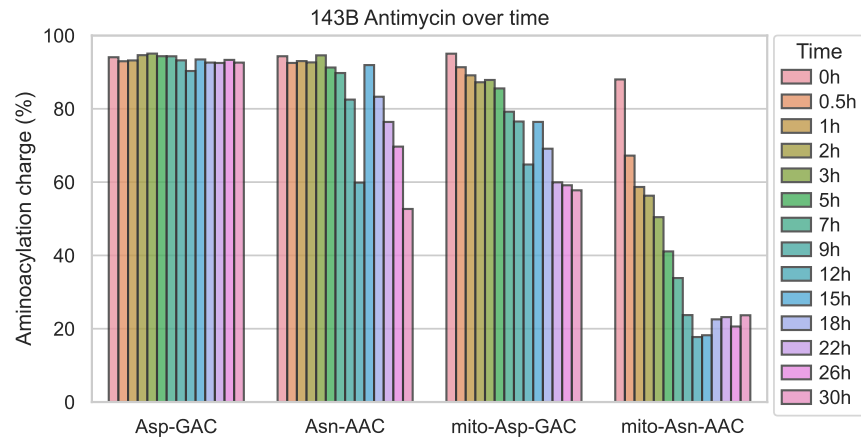


Figure B.19: tRNA charge as a function of time after antimycin treatment (1  $\mu$ M, spike-in) for 143B cells in DMEM, without pyruvate, with dialyzed FBS and 200  $\mu$ M uridine.

### B.8 Figures related to integrated stress response

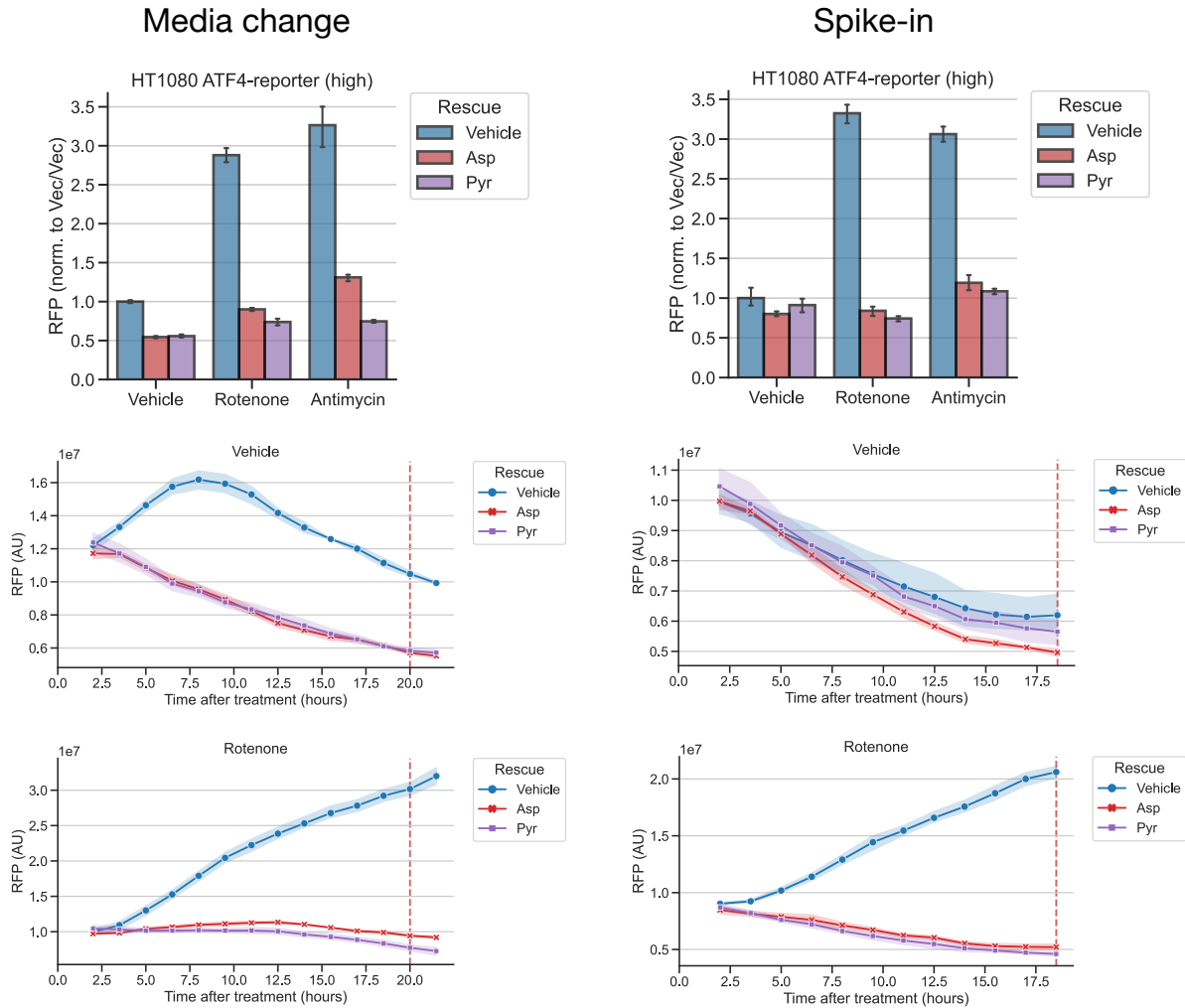


Figure B.20: Mitochondrial inhibitor induced ATF4 reporter, media change vs. spike-in. Left column shows results from an experiment where media change was used to initiate the treatment. Right column shows results from an experiment where the treatment was initiated by a 10x spike-in. Bar plots show results at the time indicated by the red dashed line on the line plots below.

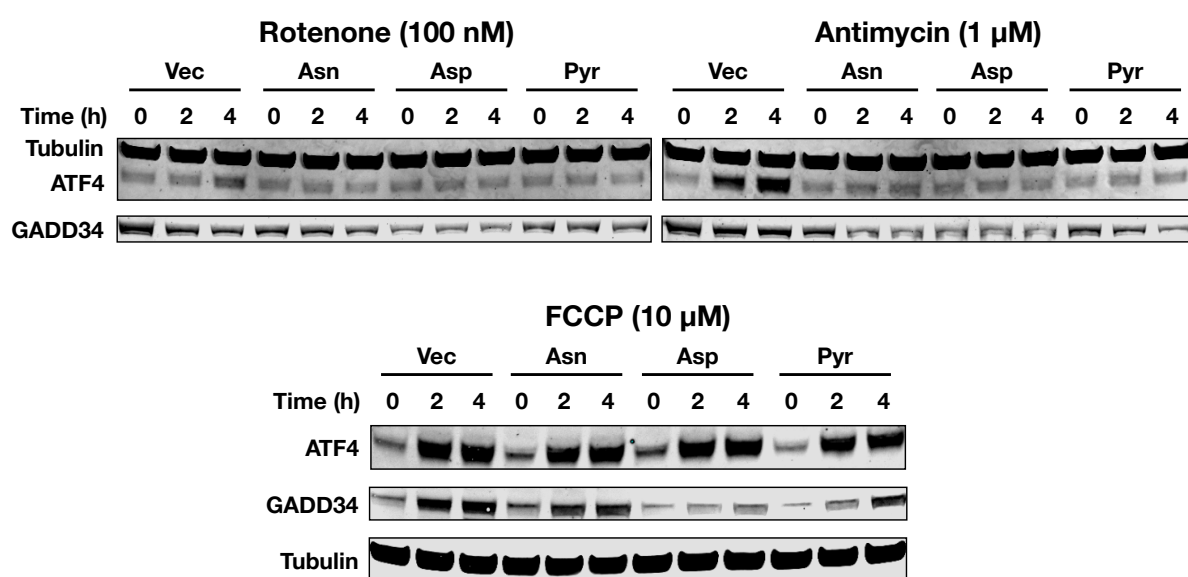


Figure B.21: Western blot validation of ATF4 reporter in HT1080 cells. Treatment and rescue conditions similar to figures 2.14a and 2.14b.

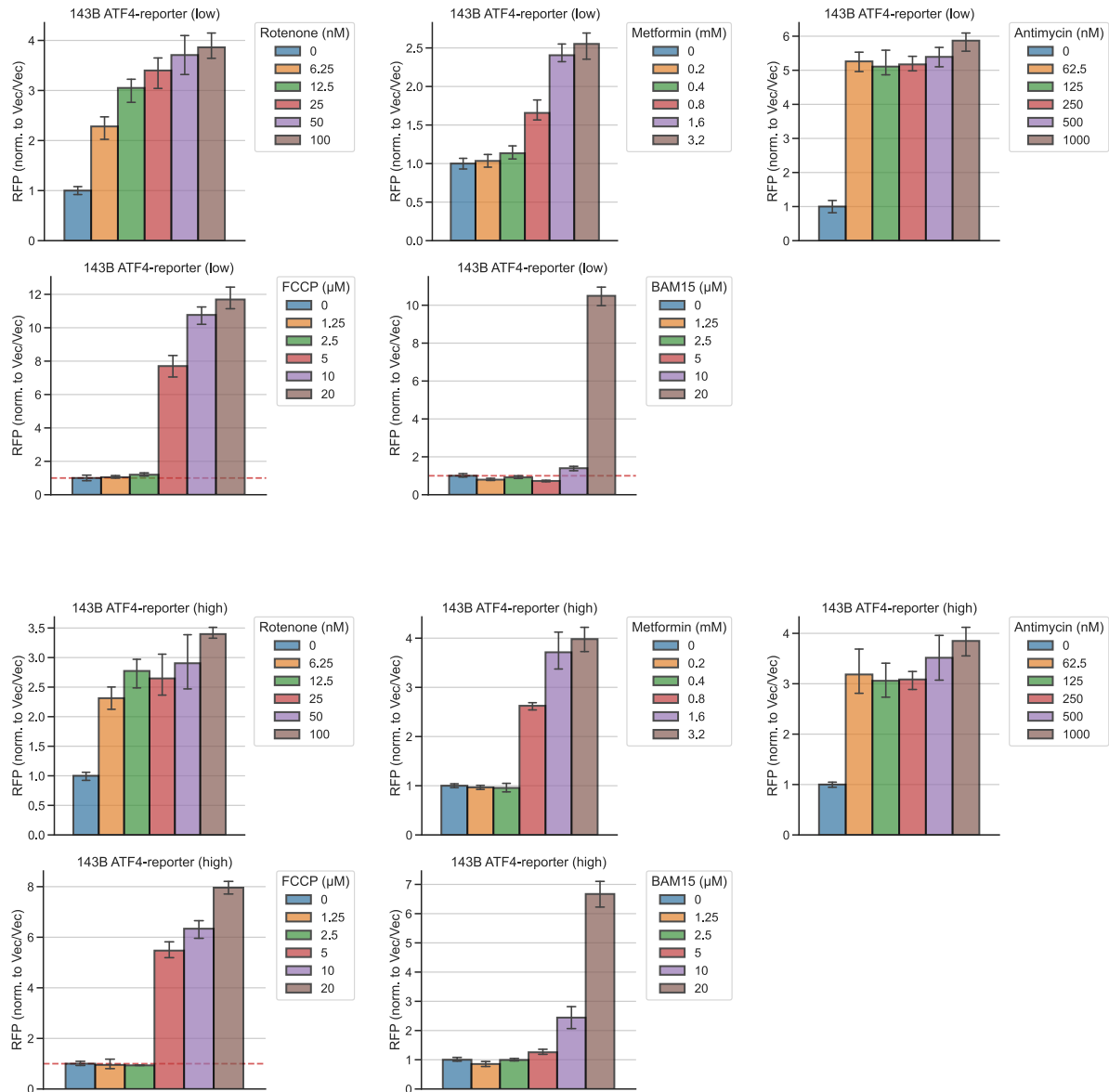


Figure B.22: ATF4 reporter, drug titrations. ATF4 reporter readout at 17.5 h after drug treatments of 143B cells.

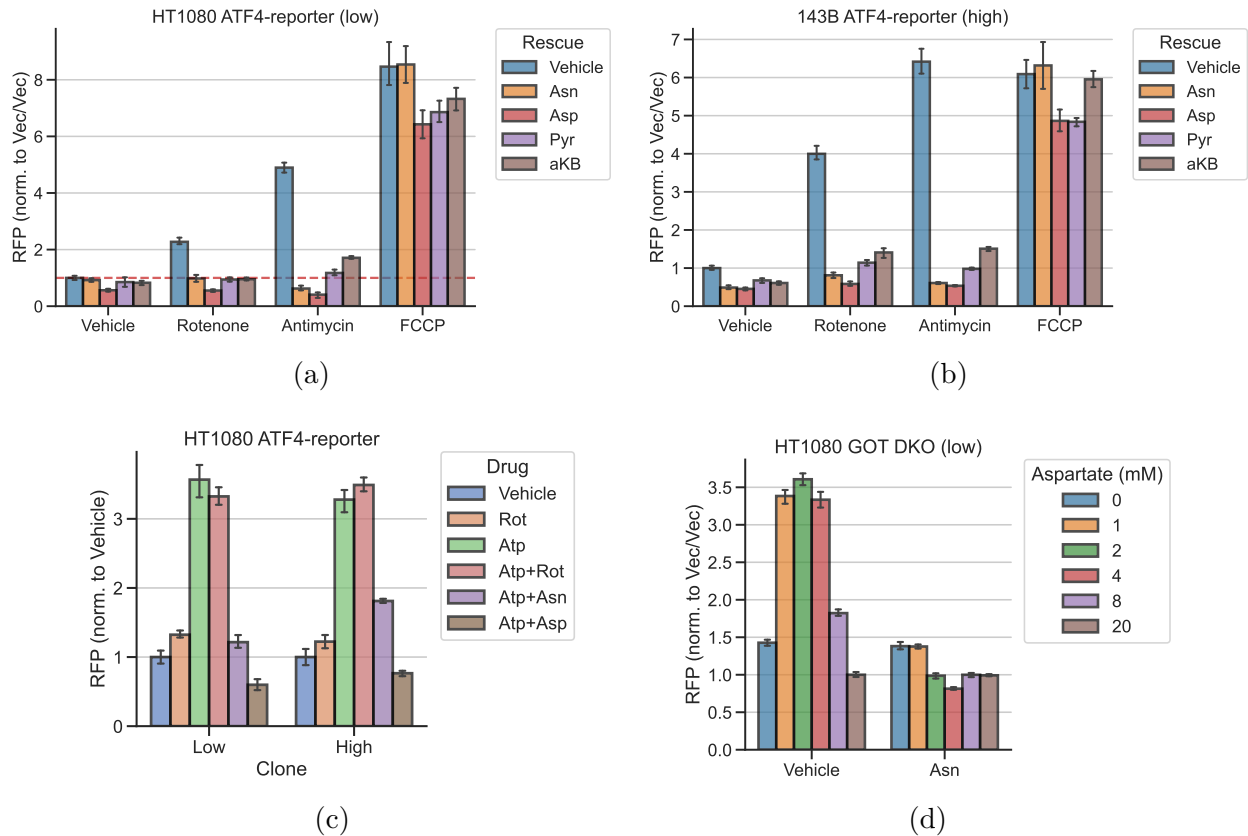


Figure B.23: Panels (a), (b) and (c), related to figure 2.14, here showing data generated for the other clones. Panel (d), GOT DKO cells respond to aspartate depletion. Measured 20.5 h after aspartate depletion. Vec/Vec normalization is normalization to the baseline condition (20 mM Asp, no Asn).

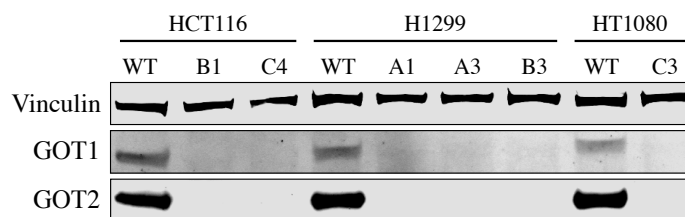
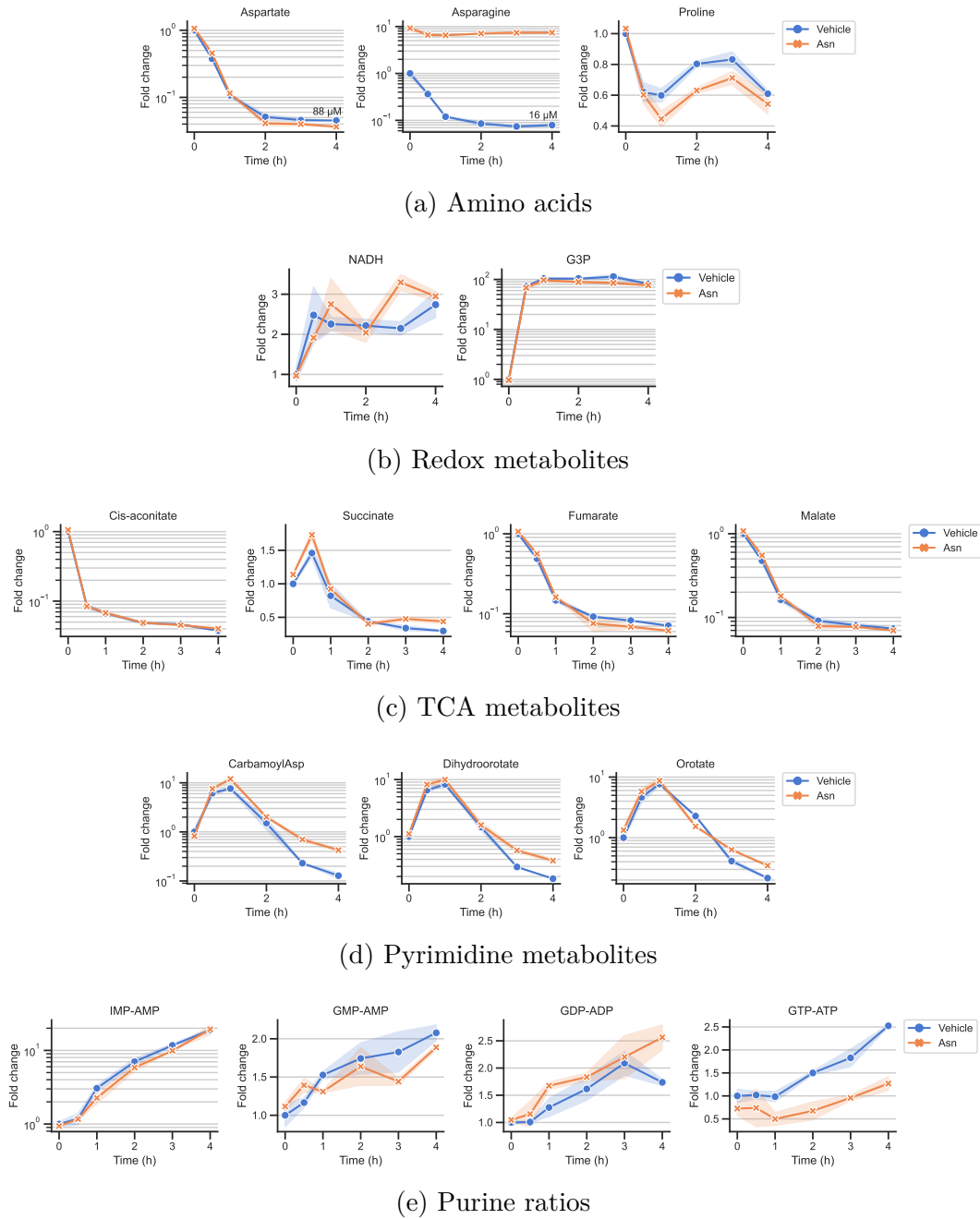


Figure B.24: Western blot validation of GOT DKO single cell clones.

### B.9 Antimycin induced metabolic changes



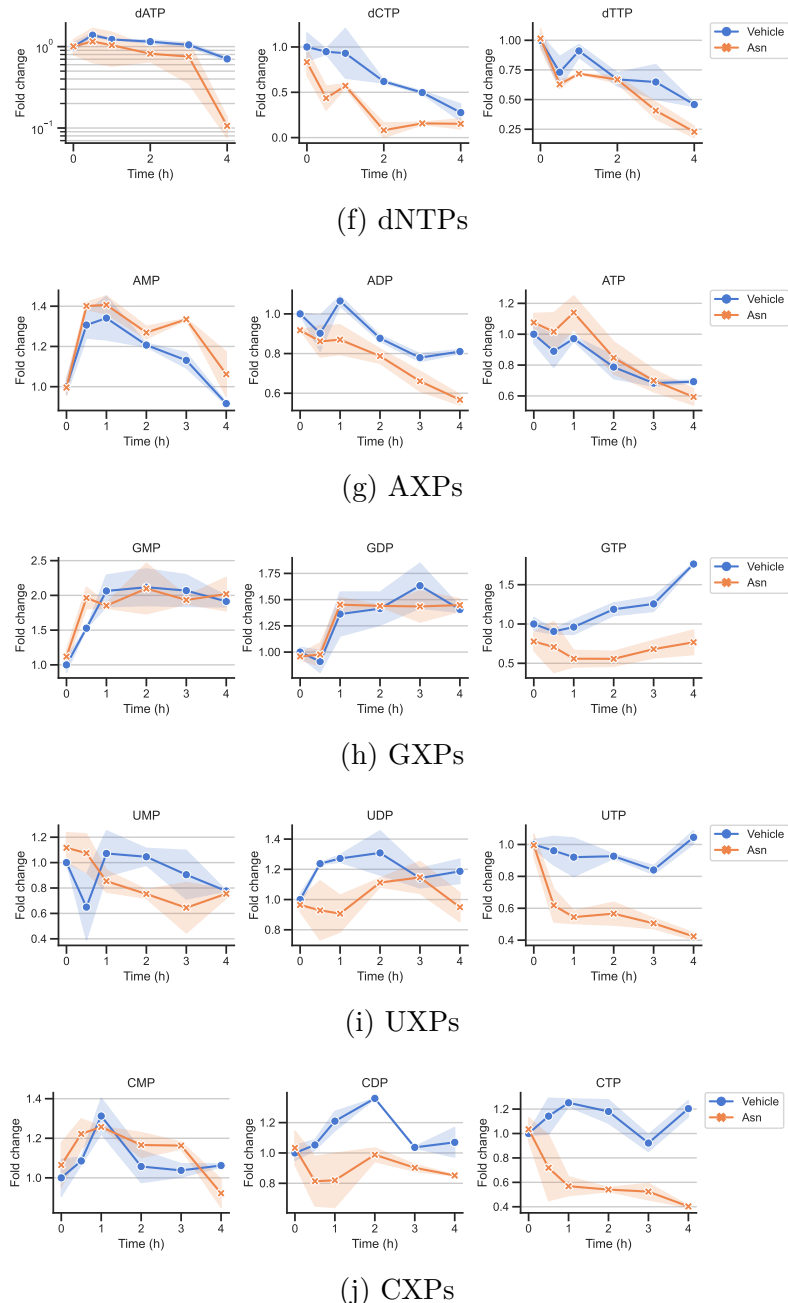


Figure B.25: Metabolic changes in HT1080 WT after antimycin treatment (1  $\mu$ M, media change). From same experiment as figure 2.15.

## Appendix C

### ASPARTATE SENSOR SUPPLEMENTARY FIGURES

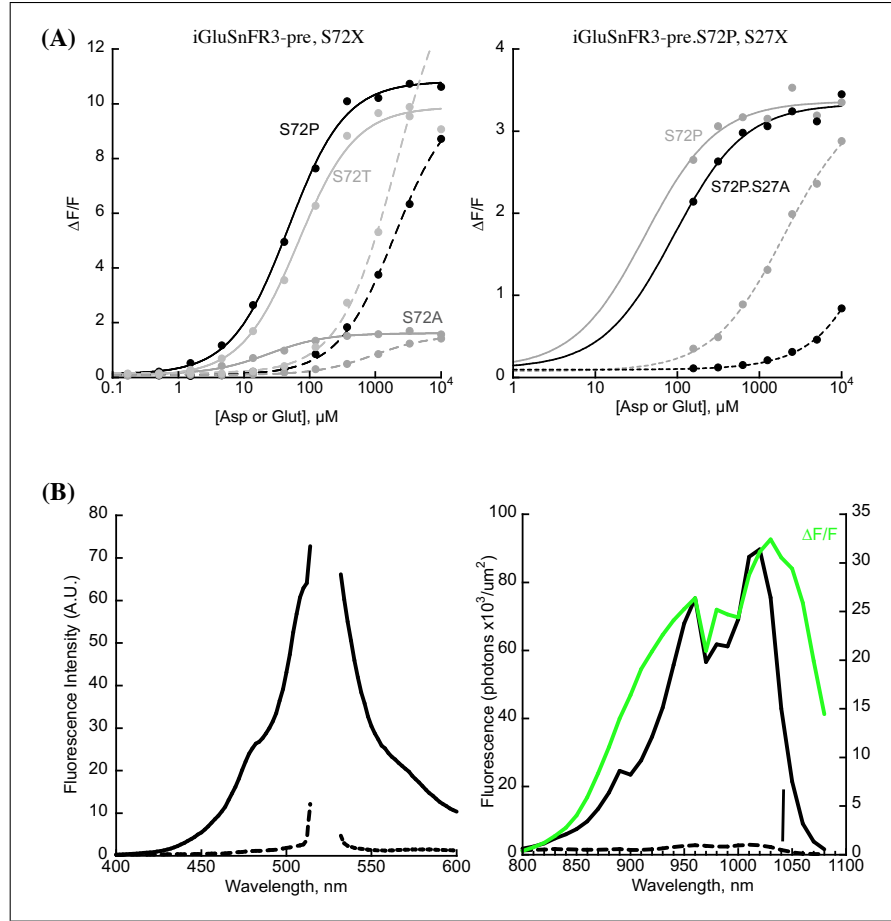


Figure C.1: (A) Switching specificity of the iGluSnFR3 precursor from glutamate to aspartate using S72X library (left) and S72P, S27X library (right). Titrations with aspartate (solid lines) and glutamate (dashed lines) in bacterial lysate. (B) Excitation and emission spectra of jAspSnFR3-mRuby3. Left, 1-photon spectra. Excitation wavelength was varied from 400 nm to 520 nm (7.5 nm bandpass) while observing emission at 535 nm (10 nm bandpass). Emission wavelength was varied from 535 nm to 600 nm (10 nm bandpass) while exciting at 510 nm (7.5 nm bandpass). Fluorescence was measured both in the absence (dashed lines) and presence of 10 mM aspartate (solid lines). Right, 2-photon cross-sections, also  $\pm 10$  mM aspartate, with an overlay of calculated  $\Delta F/F$  (green). Vertical bar indicates 1040 nm.

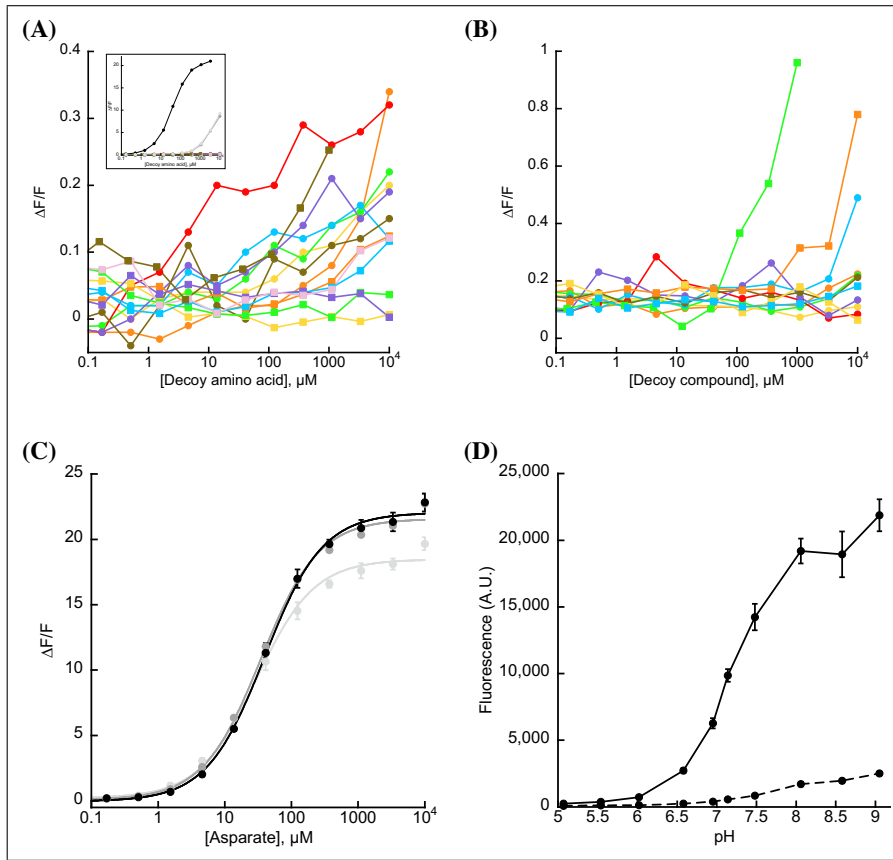


Figure C.2: (A) jAspSnFR3-mRuby3 does not appreciably change its green fluorescence in response to other amino acids (alanine, phenylalanine, glycine, histidine (red line), isoleucine, leucine, methionine, proline, glutamine, arginine, serine, threonine, valine, or tryptophan). Insert with aspartate in black and glutamate/asparagine in grey for comparison. Ex. 485 nm (20 nm bandpass), Em. 535 nm (20 nm bandpass), 0.2  $\mu$ M purified protein in PBS. (B) jAspSnFR3-mRuby3 does not respond to other decoys: citrate, lactate, pyruvate, malate, alpha-ketoglutarate, cis-aconitate, succinate, fumarate, or oxaloacetate (orange squares); nor to relevant pharmacological treatments: rotenone (green squares) or metformin. The small increase in fluorescence from rotenone is likely due to the scattering of a visibly turbid solution; rotenone has very low solubility in water. Ex. 485 nm (20 nm bandpass), Em. 535 nm (20 nm bandpass). (C) jAspSnFR3-mRuby3 is not adversely affected by temperature. Fluorescence as a function of aspartate titration at 23°C (light grey), 30°C (medium grey), and 37°C (black). Error bars are standard deviation of three technical replicates. (D) pH sensitivity of jAspSnFR3-mRuby3 (green component). Ex 485 nm (5 nm bp), Em 515 nm (10 nm bp). Error bars are standard deviation of 5 technical replicates. Solid line is with 3 mM aspartate, dashed line is without aspartate.

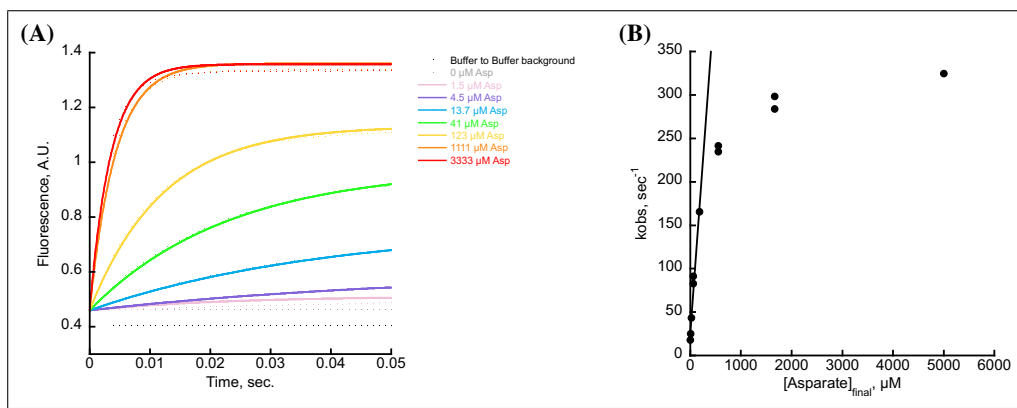


Figure C.3: (A) Stopped-flow kinetics of jAspSnFR3 using different aspartate concentrations for injection. Measurements were performed at a frequency of 1 per msec. and indicated by dots. To each time-series an exponential function was fit, shown as a solid line with matching color. (B)  $k_{obs}$  as a function of aspartate concentration shown for two independent stopped-flow experiments. The line represents the linear function, fitted to the linear range to extract the kinetic rates.

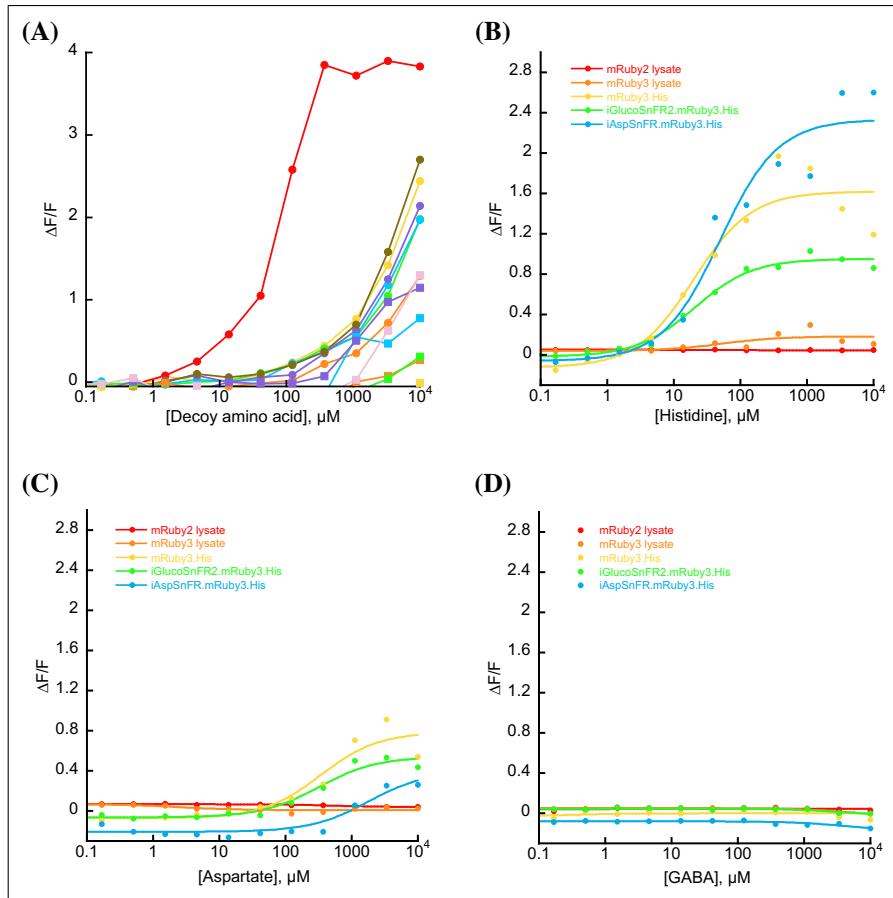


Figure C.4: (A) jAspSnFR3-mRuby3 shows increased red fluorescence at millimolar concentrations of all amino acids (alanine, phenylalanine, glycine, histidine, isoleucine, leucine, methionine, proline, glutamine, arginine, serine, threonine, valine, or tryptophan), with apparent responses to histidine at  $100 \mu M$  (red line). (B) Increased red fluorescence of mRuby3 in response to histidine requires a C-terminal histidine tag. (C) Increased red fluorescence of mRuby3 in response to millimolar concentrations of aspartate requires a C-terminal histidine tag. (D) mRuby, with or without histidine tag, does not increase in fluorescence upon treatment with amino acid related compound gamma-aminobutyric acid (GABA). For all plots Ex. 555 nm (20 nm bandpass), Em. 600 nm (20 nm bandpass).

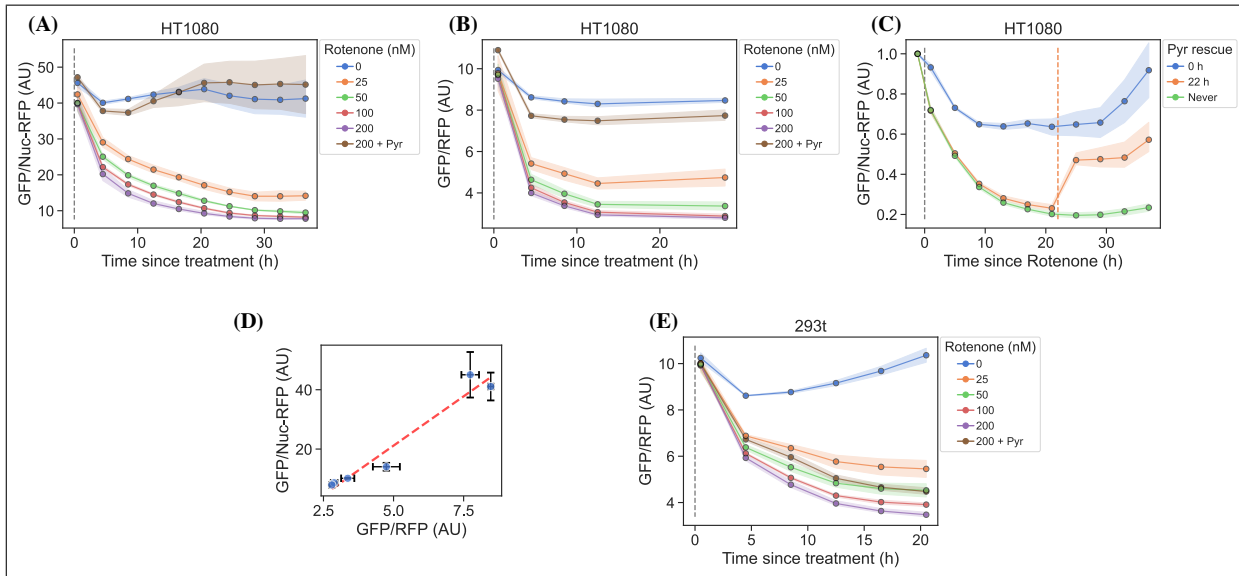


Figure C.5: jAspSnFR3 temporal response after rotenone treatment. (A) HT1080 cells using nuclear RFP to normalize the jAspSnFR3 signal, treated with a rotenone titration. (B) HT1080 cells using an RFP fused to jAspSnFR3 (jAspSnFR3-mRuby3) for normalization, treated with a rotenone titration. (C) HT1080 cells treated with 100 nM rotenone at the start of the experiment (0 h) and then rescued with pyruvate at start, 22 h or never. (D) Comparison between the steady-state signal of (A) and (B) with a linear regression shown as a red dashed line to show that nuclear RFP and RFP fusion normalizations are equivalent. (E) HEK293t cells using an RFP fused to jAspSnFR3 for normalization, treated with a rotenone titration. For plots (A), (B), (C) and (E) markers indicate the average using available well replicates and are superimposed on a bootstrapped 95% confidence interval colored using the same color code as the markers. For plot (D) markers indicate the average using available well replicates and errorbars are drawn as +/- the standard deviation of the replicates. Grey dashed lines indicate the time of treatment. Orange dashed line in panel (C) indicates time of pyruvate addition. AU, arbitrary unit.

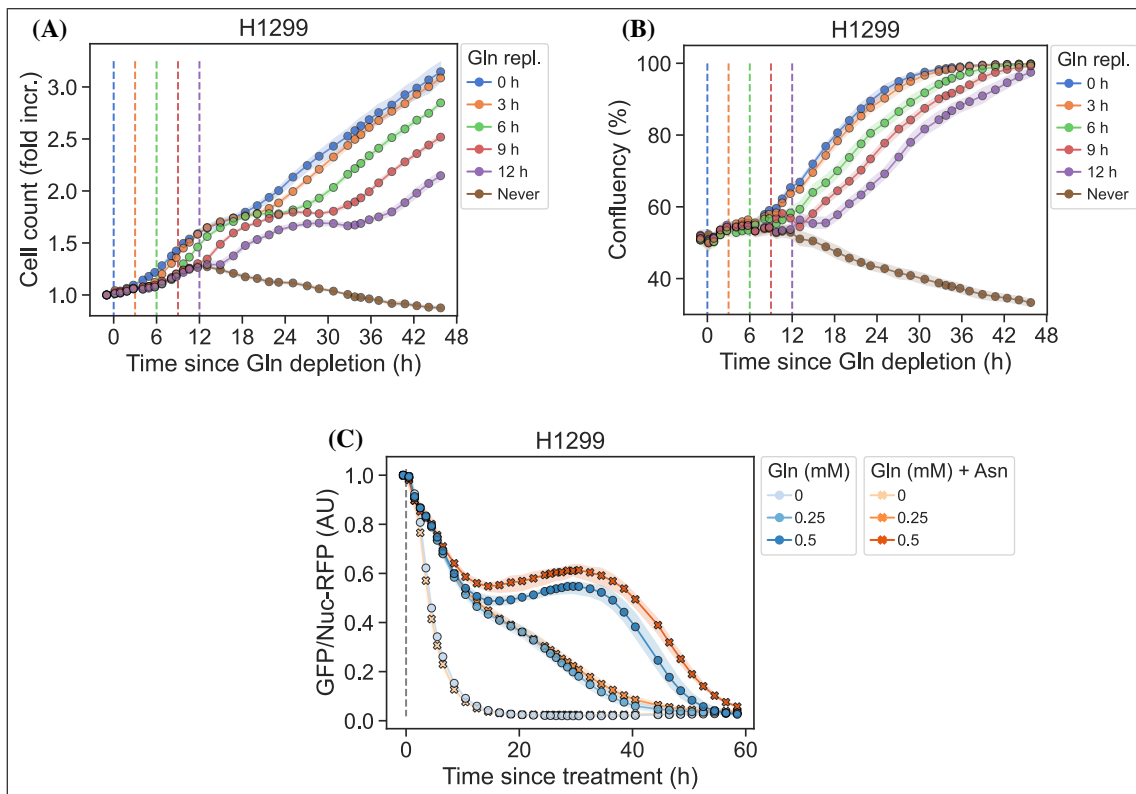


Figure C.6: (A) Nuclei count over time for conditions displayed in figure 3.2, panel E. (B) Cell confluency over time for conditions displayed in figure 3.2, panel E. (C) H1299 cells changed into media with a titration of glutamine with or without 1 mM asparagine. Identical to figure 3.2, panel H but with fewer glutamine concentrations and more well replicates.

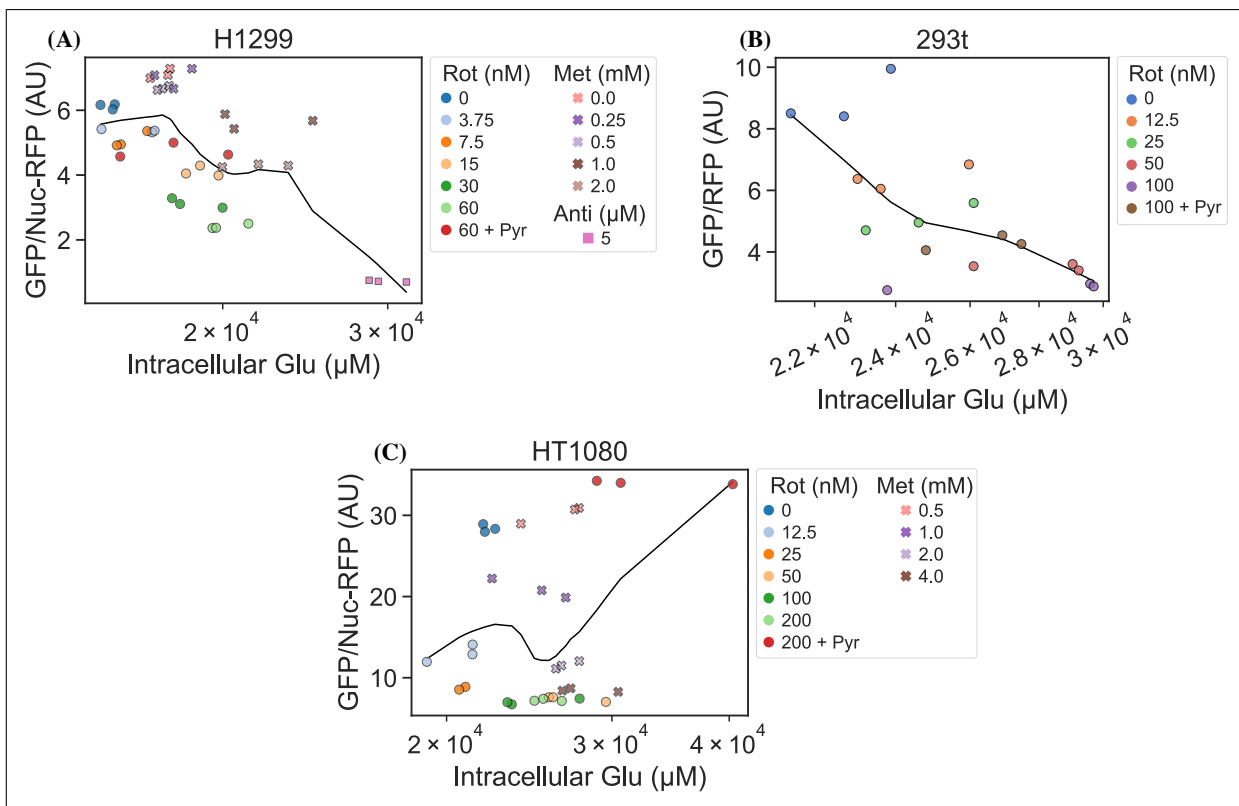


Figure C.7: RFP normalized jAspSnFR3 signal, following various perturbations to live cells, is not correlated with the LCMS measured intracellular glutamate concentration. Datapoints are fitted to a local linear regression, shown by the black line, otherwise, these plots are identical to those in figure 3.3. AU, arbitrary unit.

## Appendix D

### tRNA-SEQ SUPPLEMENTARY FIGURES

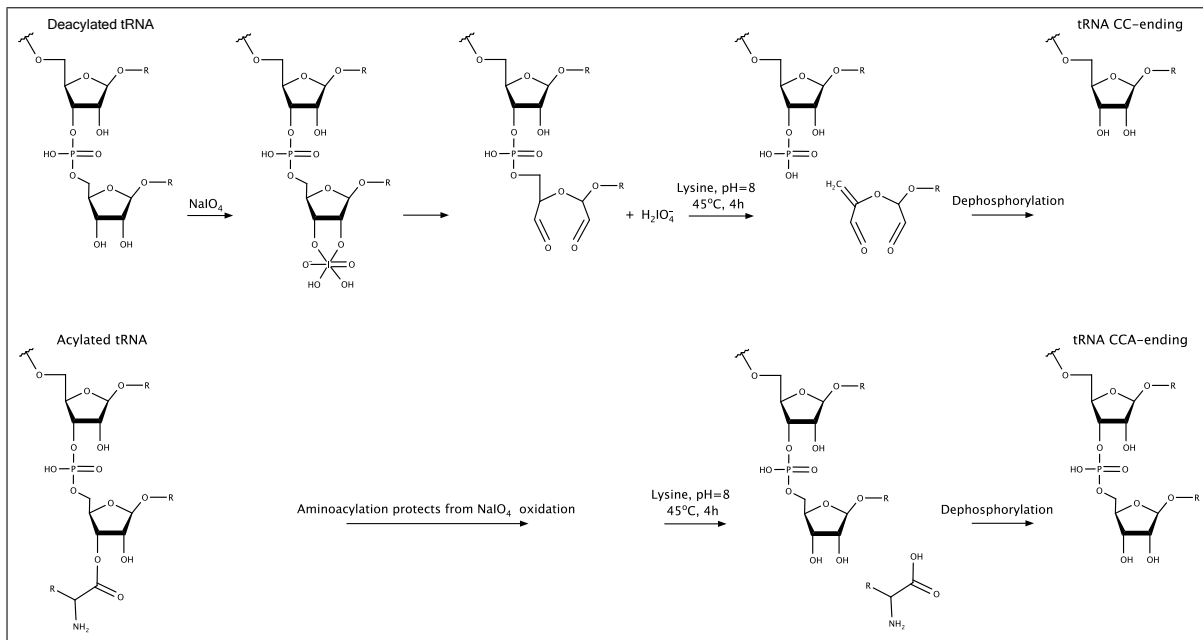


Figure D.1: Schematic of the Whitfeld reaction with acylated and deacylated tRNA leading to generation of CCA and CC-ending tRNAs. For deacylated tRNA, 3' adenine is oxidized by periodate and then cleaved off by lysine induced  $\beta$ -elimination [122, 151]. Acylated tRNA is protected from periodate oxidation but will be deacylated in the subsequent incubation with lysine.

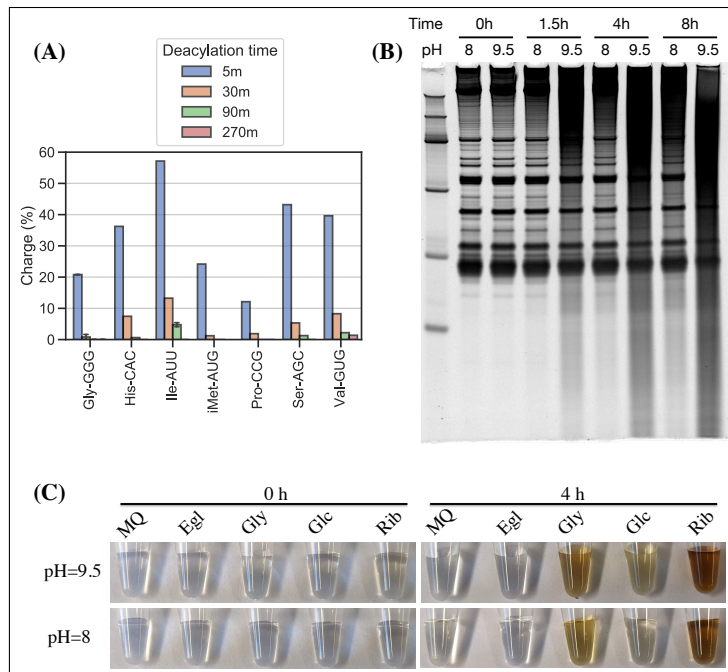


Figure D.2: Optimizing lysine induced cleavage for the charge tRNA-Seq method. **(A)** Aminoacylation remaining after 5, 30, 90 and 270 min of deacylation in 1 M lysine pH=8 at 45°C. After deacylation, RNA was purified and submitted to the Whitfeld reaction using lysine cleavage at pH=9.5 for 90 min at 45°C to ensure complete deacylation. The RNA was then processed using the described charge tRNA-Seq method. **(B)** RNA stability over time for lysine cleavage at pH=8 and borax cleavage at pH=9.5. **(C)** Lysine reacts with dialdehydes forming from quencher oxidation. One-pot Whitfeld reactions were performed at pH=8 and pH=9.5 and quenched with either water (MQ), ethylene glycol (Egl), glycerol (Gly), glucose (Glc) or ribose (Rib). Pictures taken before (0 h) and after (4 h) the lysine cleavage step indicate side product formation consistent with lysine reacting with dialdehydes formed during the periodate quenching [126]. This side product causes problems in the later purification step.

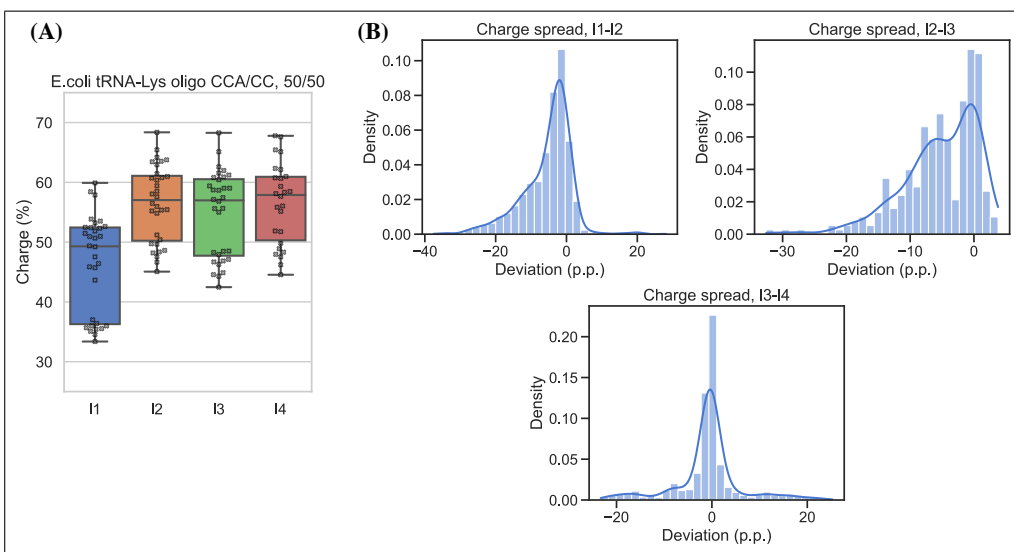


Figure D.3: Measurement bias in charge tRNA-Seq using blunt-end ligation. **(A)** Measured charge of a E.coli tRNA-Lys oligo control spiked into samples processed with four different pre-adenylated adapters using the method described by Behrens et al. [10]. The control was made using a mix of 50% E.coli tRNA-Lys-CCA and 50% E.coli tRNA-Lys-CC and thus simulating 50% charge. Each dot represents a single charge tRNA-Seq sample. **(B)** Distribution of charge differences at the transcript level among samples with two barcode replicates, comparing adapters I1 vs. I2, I2 vs. I3 and I3 vs. I4. Deviation is reported as percentage point differences and the kernel density estimate (KDE) is overlaid.

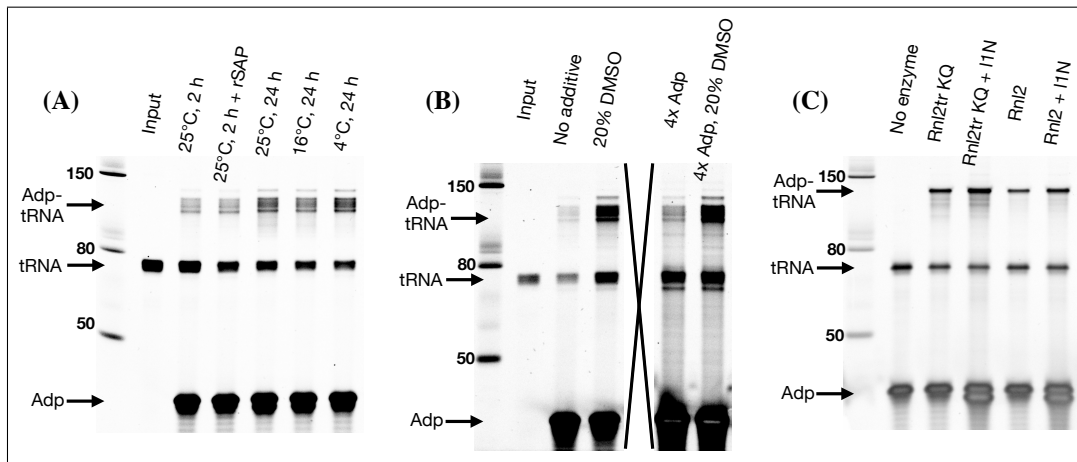


Figure D.4: Despite optimization attempts, high ligation efficiency could not be achieved for blunt-end ligation. **(A)** Effect of incubation temperature, time and addition of a phosphatase (rSAP). Using deacylated and gel purified human tRNA as substrate and pre-adenylated l3N as adapter, otherwise following the method in Behrens et al. [10]. **(B)** Effect of additives and higher adapter concentration. Using deacylated and gel purified human tRNA as substrate, pre-adenylated l2N as adapter and 4°C, 24 h incubation. An irrelevant well has been crossed out to avoid image splicing. **(C)** Effect of ligase type. Using the E.coli tRNA-Lys-CCA oligo as substrate, pre-adenylated l1N as adapter and 4°C, 24 h incubation with 20% DMSO. Wells with "+l1N" were added additional none pre-adenylated adapter. Rnl2tr KQ (T4 RNA Ligase 2, truncated KQ) is the standard ligase used for pre-adenylated adapters whereas Rnl2 (T4 RNA Ligase 2) does not require pre-adenylation of adapters.

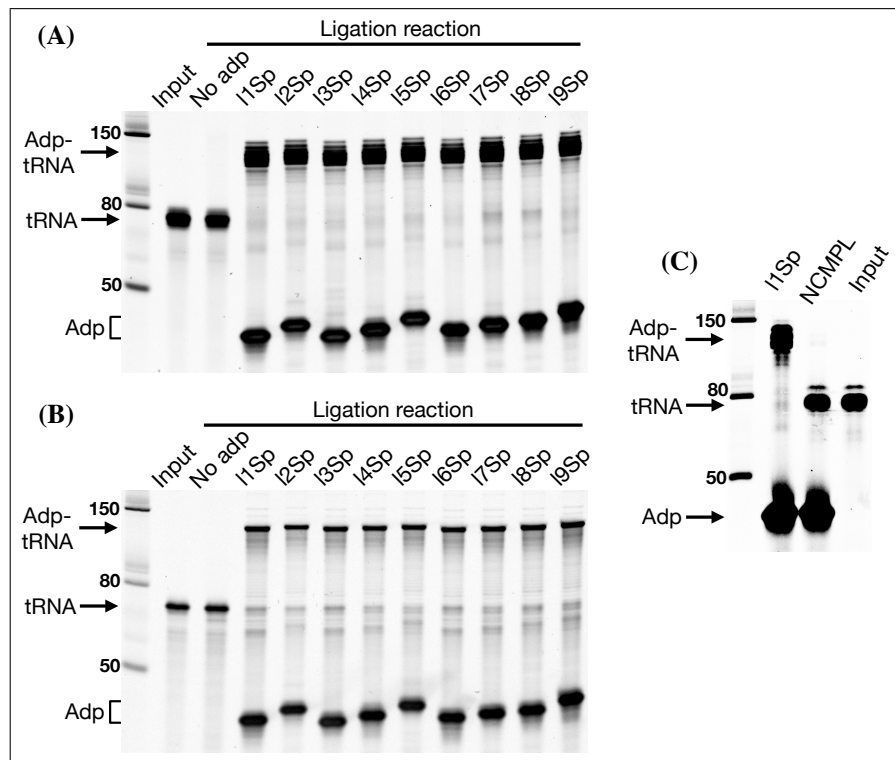


Figure D.5: Ligation efficiency of all the barcoded adapters is high and depends on splint complementarity. **(A)** Ligation reactions using deacylated purified human tRNA as substrate. **(B)** Ligation reactions using E. coli tRNA-Lys-CC oligo as substrate. **(C)** Comparing ligation using a tRNA-end complementary splint (l1Sp lane) vs. a non-complementary splint (NCMPL lane). For both ligations the l1Sp adapter was used. For the non-complementary splint ligation the two standard TGGN and GGN overhang generating splints were swapped by two splints generating CAAC and AAC overhangs.

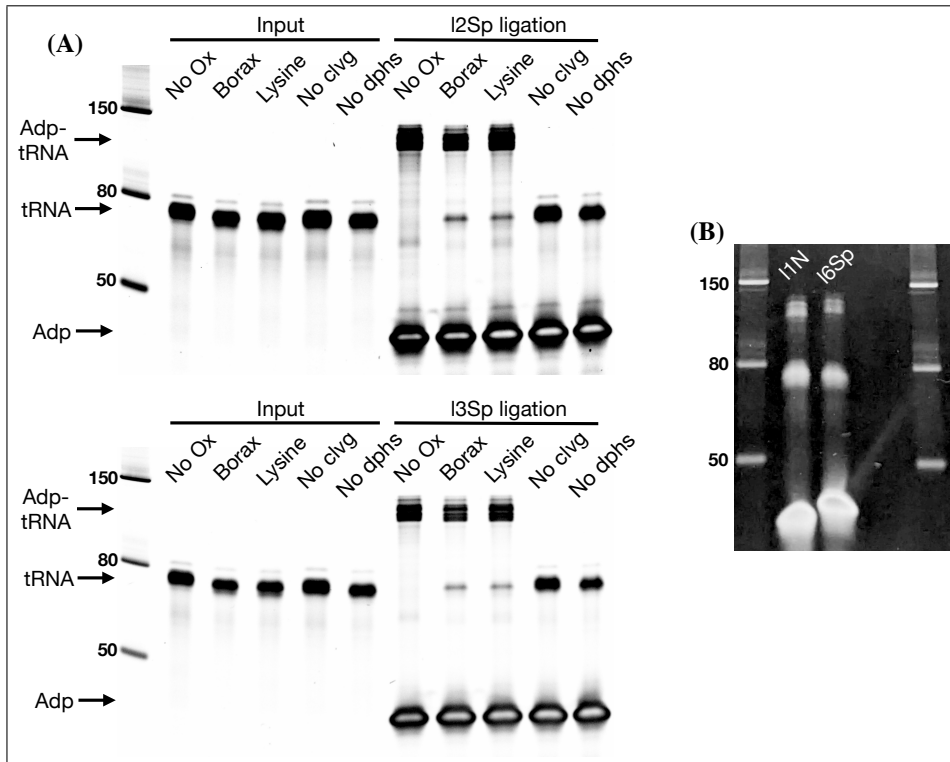


Figure D.6: **(A)** Ligation test comparing the effect of RNA processing. Similar to figure 4.2), panel E but with two different adapters. **(B)** The unligated tRNA that appears after tRNA is oxidized with periodate in panel A is refractory to further ligation. The unligated tRNA was gel purified from enough ligation reactions as shown in panel A to setup two new ligation reactions using either l1N pre-adenylated adapter for blunt end ligation or l6Sp for splint assisted ligation. For l1N, ligation was setup with 35 ng tRNA, 20 pmol adapter, 17.5% PEG-8000, 20% DMSO, 1xT4 RNA ligase buffer, 1 L T4 RNA ligase 2 (truncated KQ) and 1 L SuperaseIn. For l6Sp, the ligation was setup as described in the charge tRNA-Seq protocol.

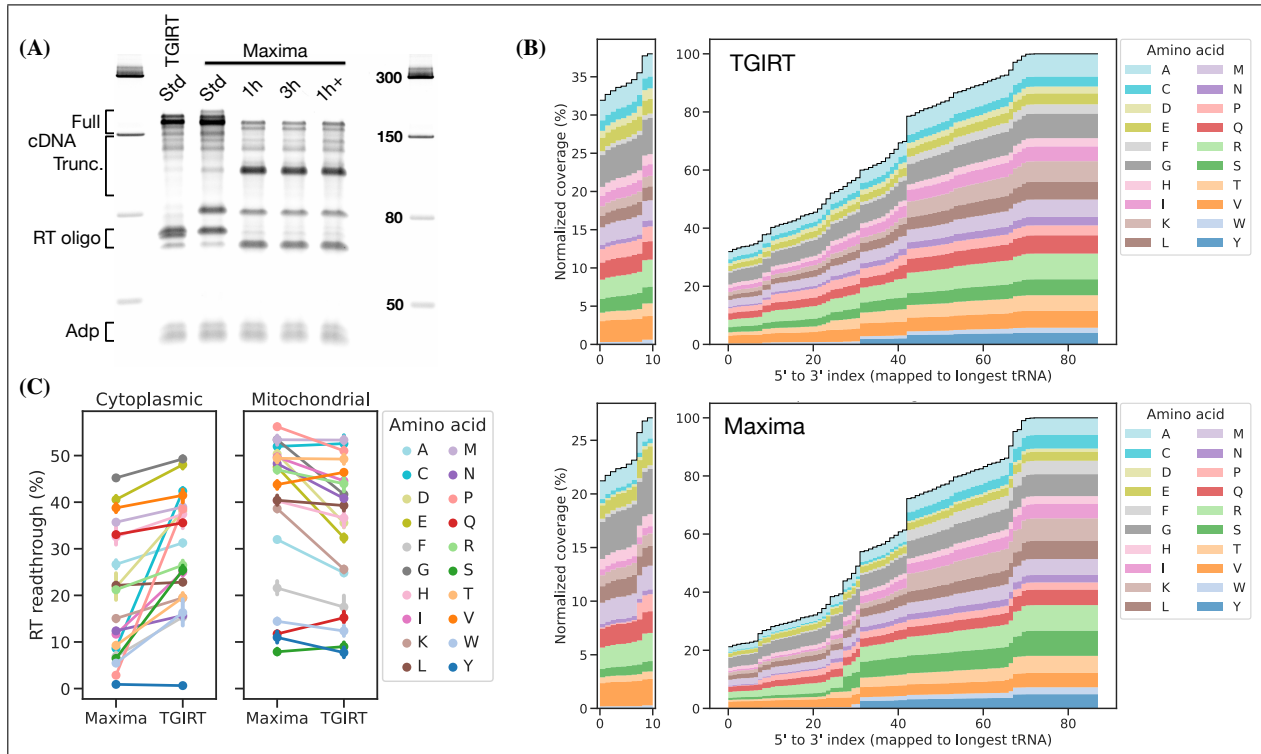


Figure D.7: **(A)** The Maxima RT polymerase produces similar levels of full size cDNA as TGIRT-III under the standard (Std) tRNA-Seq RT-PCR conditions ( $42^{\circ}\text{C}$ , 16 h, suggested by Behrens et al. [10]). For Maxima, other incubation conditions tested are: 1 h at  $60^{\circ}\text{C}$  (similar to Lucas et al. [94]), 3 h at  $60^{\circ}\text{C}$  and 1 h at  $60^{\circ}\text{C}$  followed by 15 h at  $42^{\circ}\text{C}$  (1h<sup>+</sup>). After RT-PCR, the RNA template was removed by NaOH hydrolysis, liberating the DNA adapter annotated on the gel. **(B)** Coverage plots for cytoplasmic tRNA transcripts grouped by cognate amino acid, comparing samples prepared with TGIRT-III or Maxima using standard incubation ( $42^{\circ}\text{C}$ , 16 h). **(C)** Percentage of full length transcripts grouped by cognate amino acid (i.e. left side of plots in panel B). Errorbars are bootstrapped 95% confidence interval of the mean over the 7 individual samples barcoded, pooled and used for RT-PCR template with both TGIRT-III and Maxima.

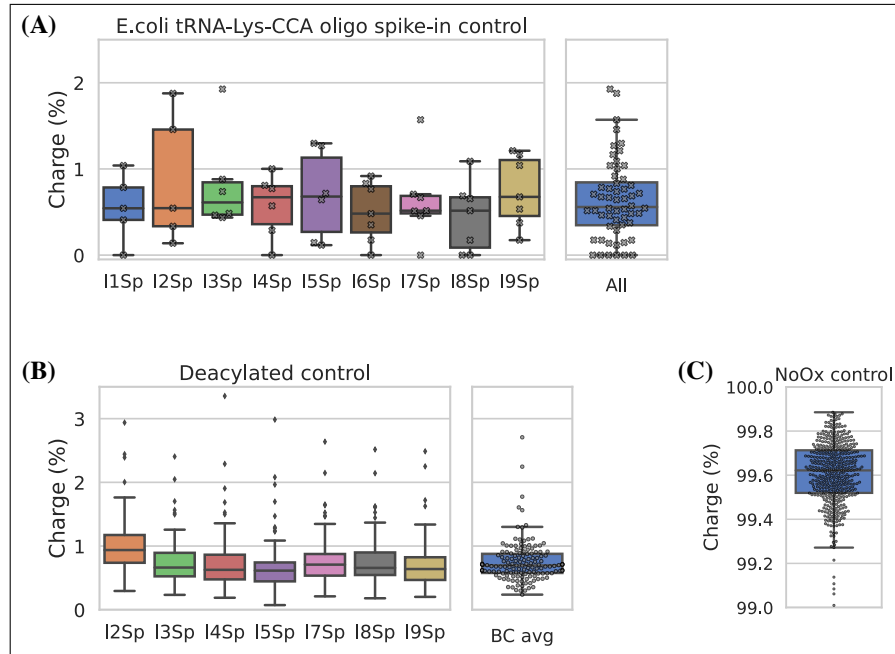


Figure D.8: Charge tRNA-Seq control samples and spike-ins validate the method. **(A)** Cleavage of the 3' adenine on spike-in oligo is near complete and similarly measured across adapters. Using the E.coli tRNA-Lys-CCA oligo as a spike-in control to monitor completion of the Whitfeld reaction. If complete, 100% E.coli tRNA-Lys-CC should be produced and thus appearing as 0% charged. Each dot represents one sample spiked with E.coli tRNA-Lys-CCA oligo before the Whitfeld reaction and processed using the charge tRNA-Seq processing described in the method section. **(B)** Aminoacylation level of human tRNA transcripts after undergoing deacylation by incubation at 45°C for 4 h in 1 M lysine (pH=8). Mitochondrial tRNA<sup>fMet</sup> was excluded because formylated amino acids are known to be highly resistant towards deacylation [128]. **(C)** Aminoacylation level of tRNA transcripts from four samples receiving sham oxidation (NaCl) during the Whitfeld reaction.

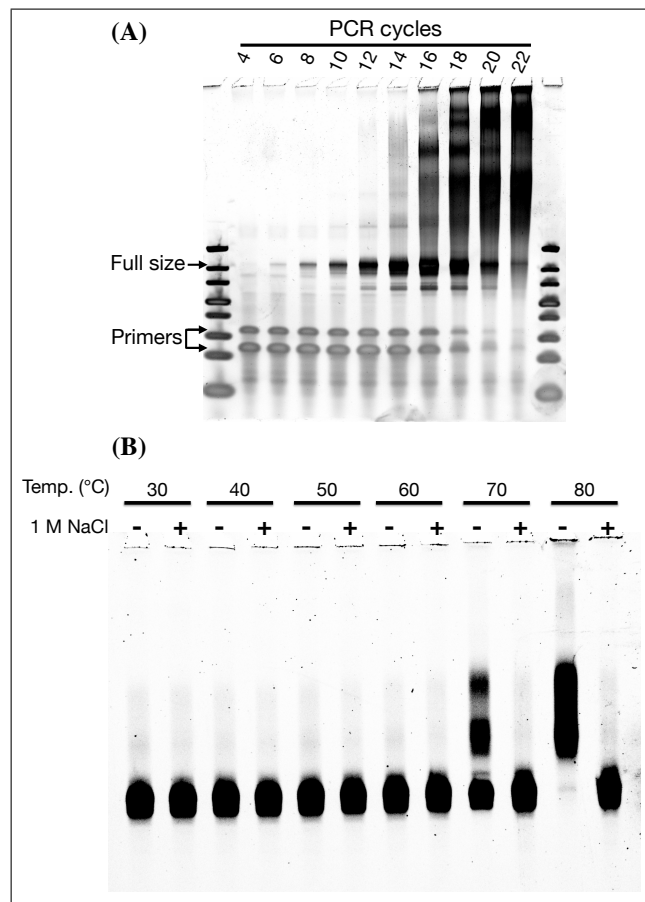


Figure D.9: **(A)** The specificity of the final library PCR step (attaching Illumina P7 and P5 sequences) deteriorates with increasing product-to-primer ratios, probably due to high tRNA homology and PCR crossover [65]. **(B)** tRNA-Seq DNA library reannealing is inhibited by high salt concentrations. A gel purified charge tRNA-Seq DNA library was resuspended in TBE buffer and incubated 30 min at different temperatures with or without 1 M NaCl.

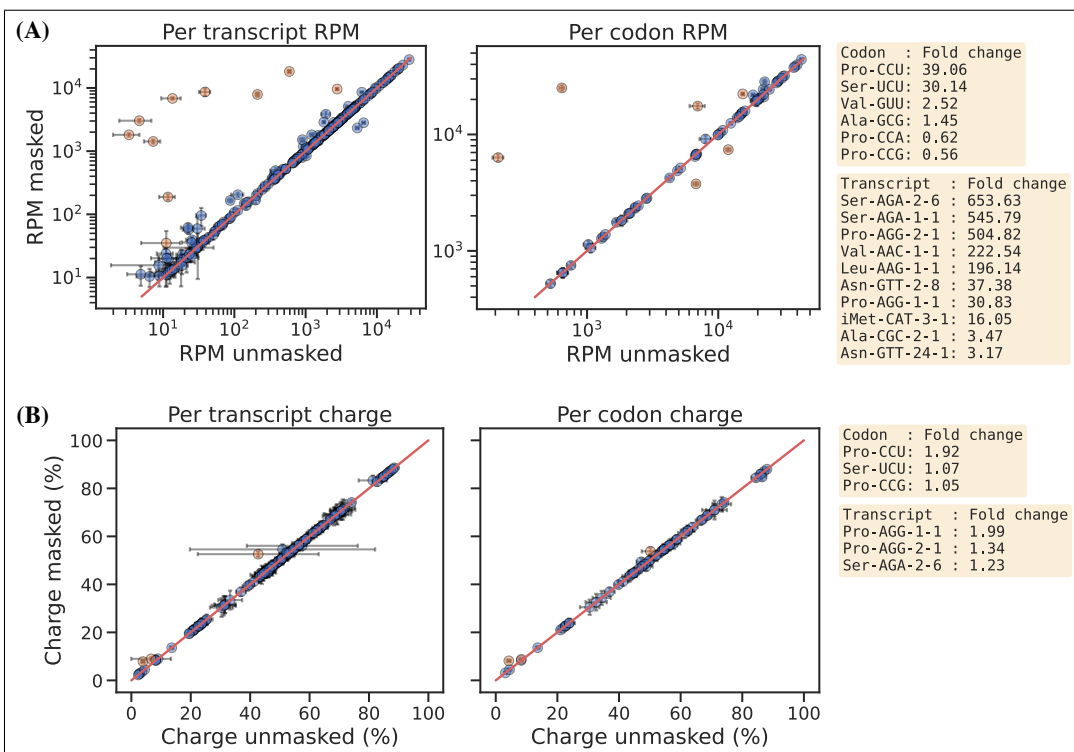


Figure D.10: (A) Reference masking effect on RPM levels per transcript (left) and per codon (right). Transcripts showing  $> 3$ , and codons showing  $> 1.4$ , fold increase or decrease upon reference masking are colored orange and annotated on the right side of the plot. (B) Reference masking effect on charge levels per transcript (left) and per codon (right). Transcripts/codons showing  $> 1.05$  fold increase or decrease upon reference masking are colored orange and annotated on the right side of the plot.

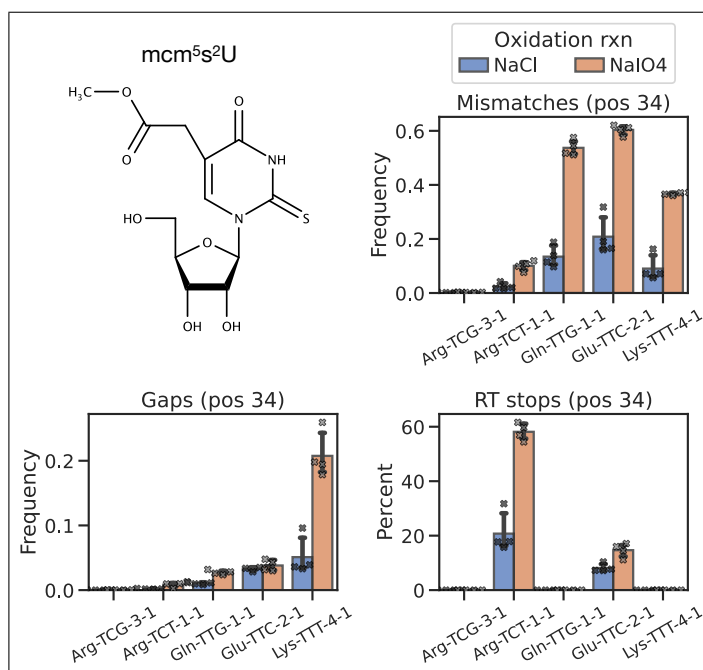


Figure D.11: Mismatch frequency, gap frequency and RT stop percentage is increased upon periodate oxidation for transcripts known to be 5-methoxycarbonylmethyl-2-thiouridine (mcm5s2U) modified. The mcm5s2U modification has been shown to be present on the first anticodon nucleoside (position 34) in human tRNA Lys-UUU, Gln-UUG, Glu-UUC and Arg-UCU, while absent in the similar tRNA Arg-UCG [91].

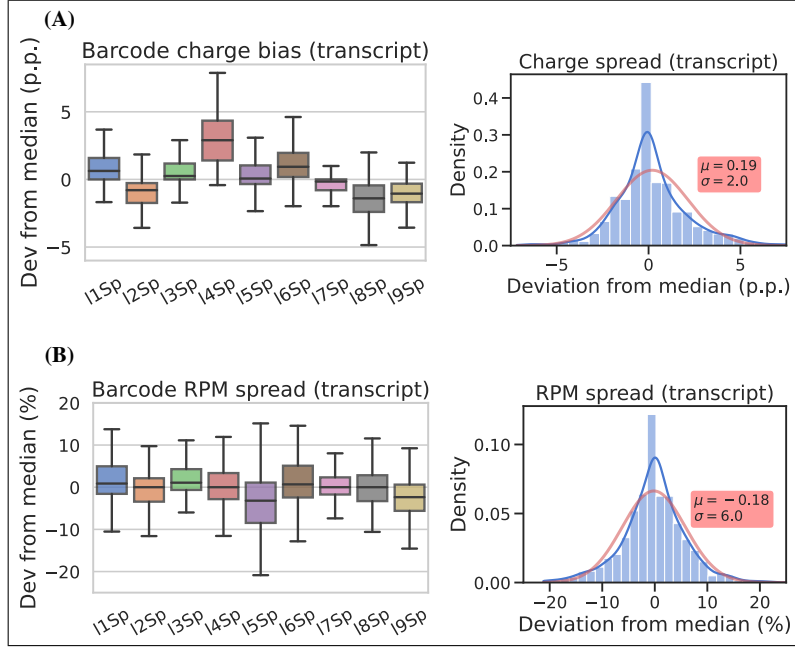
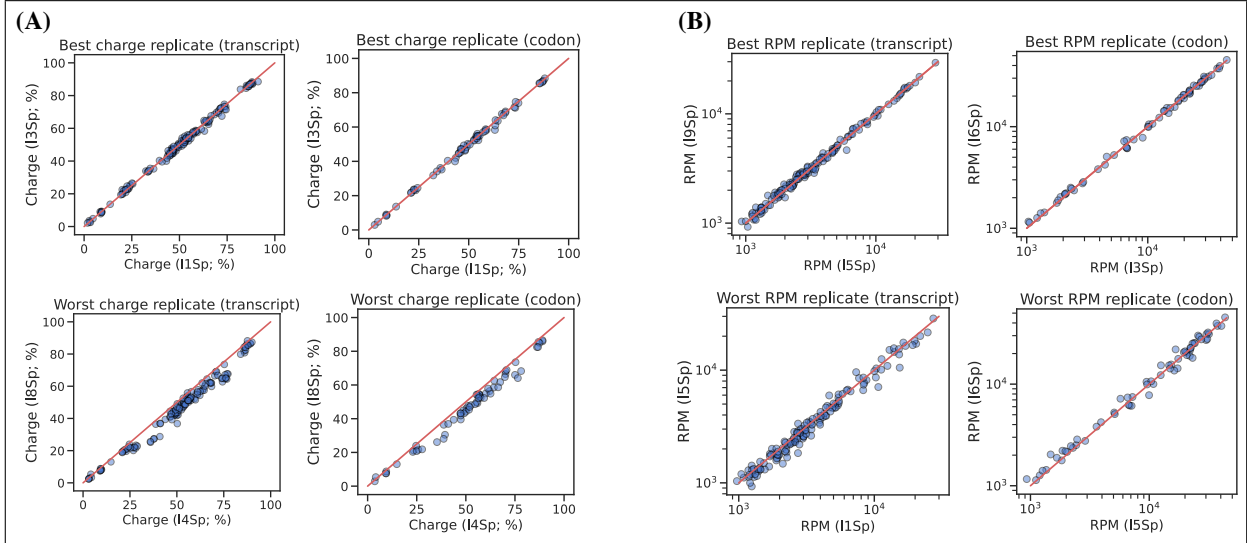


Figure D.12: Similar to figure 4.4), but at the transcript level.

Figure D.13: Best and worst pairwise comparisons between barcode replicates. Sorting pairwise comparisons between barcode replicates according to the sum of squared differences and showing the best and worst either at the transcript or codon level. **(A)** For charge levels, adapter I4Sp tends to overestimate charge. **(B)** For RPM levels. For all plots the red line is proportionality.

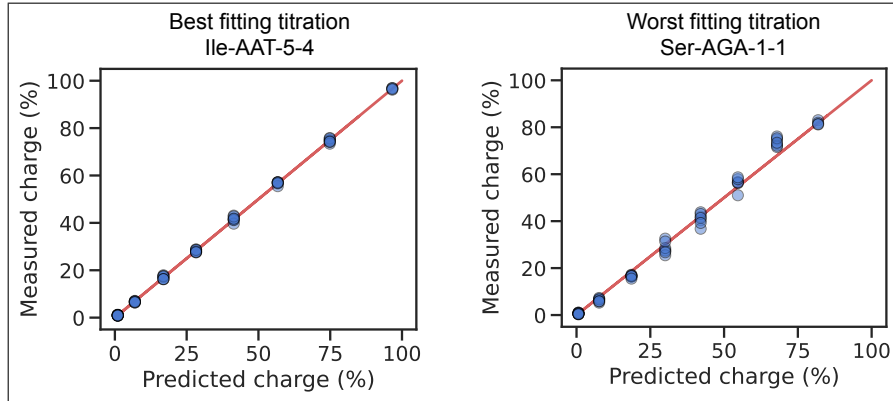


Figure D.14: The best and worst transcript when ranked based on the sum of squared differences between the measured and predicted charge. Related to the representative (i.e. ranked as the median) transcript shown in figure 4.5), panel B.

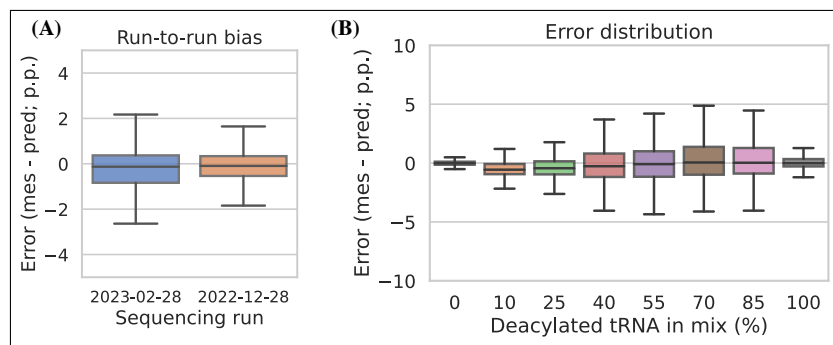


Figure D.15: Charge titration prediction error binned by sequencing run and titration sample. **(A)** Run-to-run bias of two sequencing libraries independently prepared and sequenced on different days. **(B)** Error distribution binned by titration sample. In both panels, error is the percentage point difference between the measured vs. predicted charge for all transcripts in the bin.

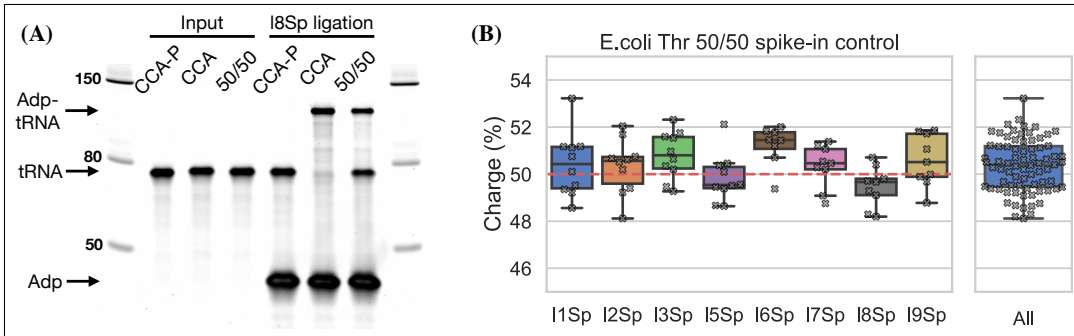


Figure D.16: Spike-in control for 50% charge using the E.coli tRNA-Thr-CGT oligo. **(A)** Ligation between E.coli tRNA-Thr-CCA-Phos and l8Sp is completely blocked indicating ~100% 3' phosphorylation. CCA-P, E.coli tRNA-Thr-CCA-Phos. CCA, E.coli tRNA-Thr-CCA. 50/50, equal mix of CCA-p and CCA. **(B)** E.coli tRNA-Thr spike-in charge measured for samples prepared with an equimolar mix of E.coli tRNA-Thr-CCA-Phos and E.coli tRNA-Thr-CCA. Each dot represents a single charge tRNA-Seq sample. The red dashed line indicates 50% charge.

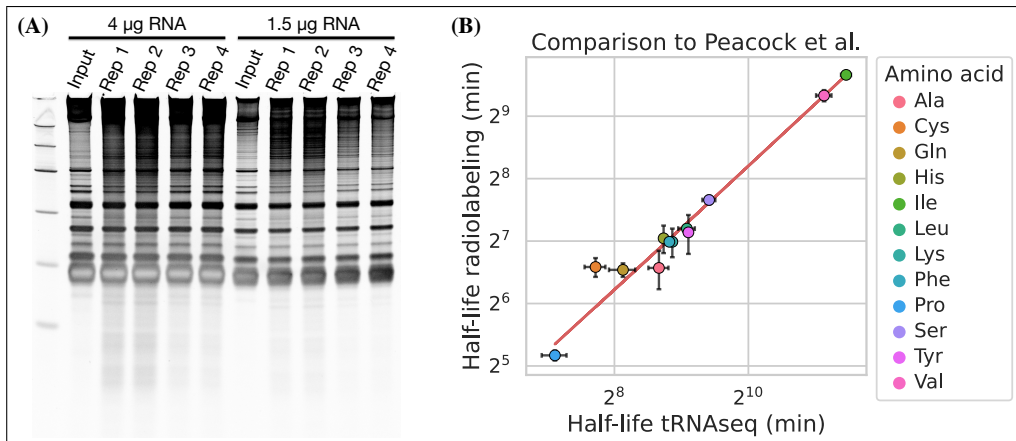


Figure D.17: **(A)** RNA integrity after the last sample was taken (40 h) for the four replicates in the aminoacylation half-life experiment. **(B)** Comparison between aminoacylation half-life estimates grouped by amino acid from this study (tRNAseq) and measurements by Peacock et al. [118] (radiolabeling). Errorbars are +/- standard deviations. A linear regression line is shown as a red line.

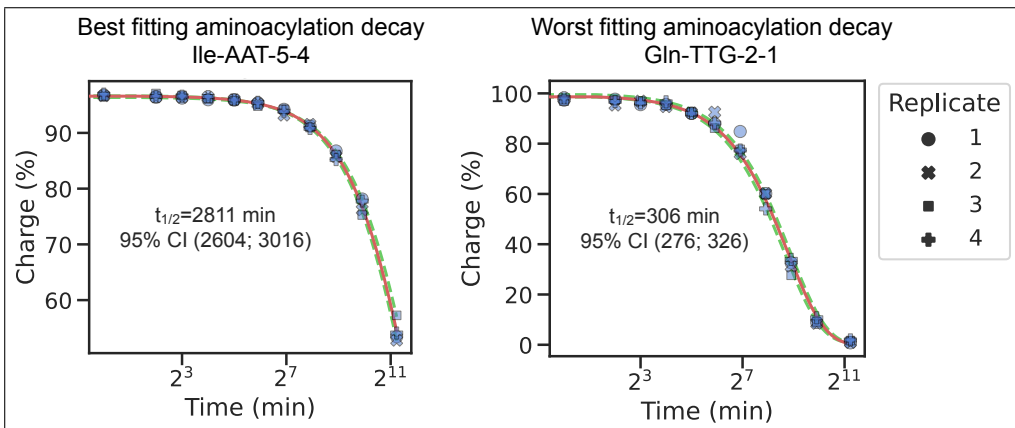


Figure D.18: The best and worst transcript half-life estimates, ranked based on the sum of squared differences between the fitted decay function and the mean charge of the replicates. Related to the representative (i.e. ranked as the median) transcript shown in figure 4.6), panel A.